

COPPER CHALCOGENIDE THIN FILMS BASED ASYMMETRIC SOLID STATE SUPERCAPACITORS

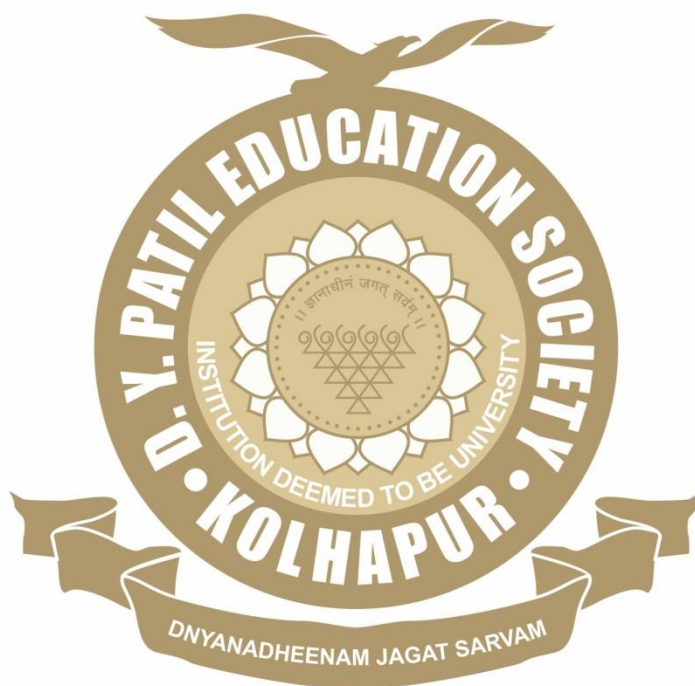
By

Mr. DHANAJI B. MALAVEKAR

Under the Supervision of

Prof. C. D. LOKHANDE

Thesis Submitted to



For the Degree of

Doctor of Philosophy

2021

**COPPER CHALCOGENIDE THIN FILMS
BASED ASYMMETRIC SOLID STATE
SUPERCAPACITORS**

A Thesis Submitted to

**D. Y. PATIL EDUCATION SOCIETY
(DEEMED TO BE UNIVERSITY)**

For the Degree of

DOCTOR OF PHILOSOPHY

In

PHYSICS

By

Mr. DHANAJI B. MALAVEKAR

M. Sc.

Under the Supervision of

Prof. C. D. LOKHANDE

M. Sc., Ph. D.

CENTRE FOR INTERDISCIPLINARY RESEARCH,

D. Y. PATIL EDUCATION SOCIETY

(DEEMED TO BE UNIVERSITY),

KOLHAPUR- 416 006.

2021

DECLARATION

I hereby declare that, the work containing in this thesis entitled, “Copper chalcogenide thin films based asymmetric solid state supercapacitors” has not been previously submitted to meet requirements for an award at this or any other higher education institute in the India or any other country. To the best of my knowledge and belief, the thesis contains no material previously published or written by another person except where due reference is made. Further, I declare that, I have not violated any of the provisions under copyright and piracy/cyber/IPR act amended from time to time.

Research student

Place: Kolhapur

Date: 31/08/2021



Dhanaji Balaso Malavekar

CERTIFICATE OF GUIDE

This is to certify that, the present thesis which is being submitted herewith for the award of Doctor of Philosophy in Physics under the faculty of Center for Interdisciplinary Research (CIR) of D. Y. Patil Education Society, Kolhapur is the result of original research work completed by Mr. Dhanaji Balaso Malavekar under my supervision and guidance and the best of my knowledge and belief, the work embodied in this thesis has not formed earlier the basis for the award of any degree or similar title of this or any other University or examining body.

Research Guide

Place: Kolhapur

Date: 31/08/2021



Prof. C. D. Lokhande

ACKNOWLEDGMENT

Undertaking this PhD has been a truly life-changing experience for me and it would not have been possible to do without the support and guidance that I received from many people.

*I would first like to thank my supervisor, **Prof. C. D. Lokhande** (Dean and Research Director, D. Y. Patil Education Society, Kolhapur), whose expertise was invaluable in formulating the research questions and methodology. I have learnt a lot from his meticulous planning and implementation, dedication and hard work. His insightful feedback pushed me to sharpen my thinking and brought my work to a higher level. My association with him for the past few years was a rewarding experience, which will be cherished by me all along.*

*I would like to express my sincere thanks to Vice-Chancellor **Prof. R. K. Mudgal**, Pro-Vice Chancellor **Dr. Shimpa Sharma** and the Registrar **Dr. V. V. Bhosale** for the inspiration and support. I thank **Dr. U. M. Patil**, **Dr. J. L. Gunjakar**, **Dr. Arvind Gulbake**, and **Dr. Vishwajeet Khot** who helped me to analyse the results with all their empathy and cooperative mind. I also thank **Dr. A. C. Lokhande**, **Dr. V. C. Lokhande**, and **Dr. R. N. Bulakhe** for providing me very important sample characterization data during entire research work.*

*I would like to express sincere thanks to my seniors **Dr. A. M. Patil**, **Dr. T. T. Ghogare**, **Dr. S. B. Kale**, **Dr. P. K. Katkar**, and **Dr. S. J. Marje** for insightful guidance, scientific discussions and valuable suggestions on the present work.*

*I would like to acknowledge my colleagues at Centre for Interdisciplinary Research, **Satyajeet Harugale**, **Satish Jadhav**, **Vikas Mane**, **Sachin Pujari**, **Shivaji Ubale**, **Prity Bagwade**, **Vikas Magdum**, **Yogesh Chitare**, **Akash Patil**, **Suraj Khalate**, **Navnath Padalkar**, **Shrikant Sadavar**, **Rohini Shinde**, **Shirin Kulkarni**, **Ranjit Nikam**, **Sambhaji Khot**, and **Vinod Patil** for their wonderful collaboration. I want to thank them for their support and valuable suggestions during research work.*

*My heartfelt appreciation goes out to my late father **Balaso**, my mother **Anandibai**, and my lovely brother **Tanaji**, for their continuous support and love. I am also thankful to all teaching and nonteaching staff of the Centre for Interdisciplinary Research for their cooperation.*

Place: Kolhapur

~ Dhanaji

LIST OF PATENTS, PUBLICATIONS AND CONFERENCES ATTAINED

Patents: (Granted 01, Published 01)

1. Method of synthesizing reduced graphene oxide-copper selenide films for energy storage application. Prof. C. D. Lokhande, **Mr. D. B. Malavekar**, Dr. V. V. Bhosale, and Mr. V. C. Lokhande, Grant number: **374930**.
2. A method for coating of cerium sulfide-carbon based composite. Prof. C. D. Lokhande, **Mr. D. B. Malavekar**, Dr. V. V. Bhosale, Mr. V. C. Lokhande, Mr. V. J. Mane, Application No: 202021002802.

Articles in International Journals: (Published 11)

1. **D. B. Malavekar**, S. B. Kale, V. C. Lokhande, U. M. Patil, J. H. Kim, C. D. Lokhande, Chemically synthesized Cu_3Se_2 film based flexible solid-state symmetric supercapacitor: effect of reaction bath temperature, J. Phys. Chem. C, 124 (2020) 28395-28406. (**I.F. 4.128**).
2. **D. B. Malavekar**, V. C. Lokhande, V. J. Mane, S. B. Ubale, U. M. Patil, C. D. Lokhande, Enhanced energy density of flexible asymmetric solid state supercapacitor device fabricated with amorphous thin film electrode materials, J. Phys. Chem. Solids, 141 (2020) 109425. (**I.F. 3.995**).
3. **D. B. Malavekar**, V. C. Lokhande, V. J. Mane, S. B. Kale, R. N. Bulakhe, U. M. Patil, I. In, C. D. Lokhande, Facile synthesis of layered reduced graphene oxide-copper sulfide (rGO-CuS) hybrid electrode for all solid-state symmetric supercapacitor, J. Solid State Electrochem., 24 (2020) 2963-2974. (**I.F. 2.647**).
4. **D. B. Malavekar**, R. N. Bulakhe, S. B. Kale, U. M. Patil, I. In, C. D. Lokhande, Synthesis of layered copper selenide on reduced graphene oxide sheets via SILAR method for flexible asymmetric solid-state supercapacitor, J. Alloys Compd. 869 (2021) 159198. (**I.F. 5.316**).
5. S. B. Ubale, R. N. Bulakhe, V. J. Mane, **D. B. Malavekar**, I. In, C. D. Lokhande, Chemical synthesis of nano-grained ytterbium sulfide thin films for supercapacitor application, Appl Nanosci, 10 (2020) 5085-5097. (**I.F. 3.674**).
6. V. J. Mane, **D. B. Malavekar**, S. B. Ubale, R. N. Bulakhe, Insik In, C. D. Lokhande, Binder free lanthanum doped manganese oxide@graphene oxide composite as high energy density electrode material for flexible symmetric solid state supercapacitor, Electrochim. Acta, 335 (2020) 135613. (**I.F. 6.901**).
7. P. P. Bagwade, **D. B. Malavekar**, T. T. Ghogare, S. B. Ubale, V. J. Mane, R. N. Bulakhe, I. In, C. D. Lokhande, A high performance flexible solid-state asymmetric supercapacitor based on composite of reduced graphene oxide@dysprosium sulfide nanosheets and manganese oxide nanospheres, J. Alloys Compd., 859 (2021) 157829. (**I.F. 5.316**).
8. V. J. Mane, **D. B. Malavekar**, S. B. Ubale, V. C. Lokhande, C. D. Lokhande, Manganese dioxide thin films deposited by chemical bath and successive ionic layer adsorption and reaction deposition methods and their supercapacitive performance, Inorg. Chem. Commun., 115 (2020) 107853. (**I.F. 2.495**).
9. S. B. Jadhav, **D. B. Malavekar**, R. N. Bulakhe, U. M. Patil, I. In, C. D. Lokhande, P. N. Pawaskar, Dual-functional electrodeposited vertically grown $\text{Ag-La}_2\text{O}_3$ nanoflakes for non-enzymatic glucose sensing and energy storage application, Surf. Interfaces, 23 (2021) 101018. (**I.F. 4.837**).
10. S. B. Jadhav, **D. B. Malavekar**, S. B. Kale, S. R. Sabale, U. M. Patil, C. D. Lokhande, P. N. Pawaskar, Reliable glucose sensing properties of electrodeposited vertically aligned manganese oxide thin film electrode, Appl. Phys. A, 127 (2021) 391 (**I.F. 2.584**).
11. P. P. Bagwade, **D. B. Malavekar**, S. B. Ubale, T. T. Ghogare, R. N. Bulakhe, I. In, U. M. Patil, C. D. Lokhande, Characterization of Dy_2S_3 thin films deposited by successive ionic layer adsorption and reaction (SILAR) method, Solid State Sci., 119 (2021) 106693 (**I.F. 3.059**).

Conference/Seminar/Workshop Participation & Presentations (05)

1. **D. B. Malavekar**, V. J. Mane, S. B. Kale, U. M. Patil, C. D. Lokhande, “Flexible asymmetric all solid state supercapacitor with high energy and power density.” National Conference on Advanced Materials Synthesis, Characterization and Applications-2018, Department of Physics, Savitribai Phule Pune University, Pune.
2. **D. B. Malavekar**, V. J. Mane, U. M. Patil, C. D. Lokhande, “Flexible, low cost asymmetric supercapacitor based on rGO-CuS and rGO-MnO₂ electrodes.” International Conference on Smart Materials and Nanotechnology-2020, Department of Physics and Chemistry, SKN Sinhgad College of Engineering, Pandharpur.
3. **D. B. Malavekar**, S. B. Ubale, V. J. Mane, U. M. Patil, C. D. Lokhande, “Flexible asymmetric all solid state supercapacitor device.” International Conference on Advancements in Renewable Energy-2020, School of Physical Sciences, Swami Ramanand Teerth Marathwada University, Nanded.
4. **D. B. Malavekar**, C. D. Lokhande, “Flexible asymmetric all solid state supercapacitor device.” West Zone Inter-University Student Research Convention: Anveshan 2018-19, Pacific Academy of Higher Education and Research University, Udaipur.
5. **D. B. Malavekar**, C. D. Lokhande, “Flexible asymmetric solid-state supercapacitor based on MnO₂-GO and CuS-GO electrodes.” West Zone Inter-University Student Research Convention: Anveshan 2019-20” University of Mumbai, Mumbai.

CONTENTS

Candidate's Declaration.....	ii
Certificate of Guide.....	iii
Acknowledgement.....	iv
List of patents, Articles in International Journals and National/international conferences attended	v
Contents.....	vii
List of figures.....	viii
List of tables and charts.....	xii
List of abbreviations.....	xiii
Chapter I: Introduction to supercapacitor and literature review...	1
Chapter II: Theoretical background of successive ionic layer adsorption and reaction (SILAR) method and thin film characterization techniques.....	39
Chapter III: CuS and CuS@rGO thin films by SILAR method: Characterization and electrochemical performance.....	71
Chapter IV: CuSe₂ and CuSe₂@rGO thin films by SILAR method: Characterization and electrochemical performance	107
Chapter V: Synthesis and characterization of MnO₂ thin films...	129
Chapter VI: Fabrication and performance evaluation of FSS- ASCs devices based on CuS@rGO and CuSe₂@rGO thin films...	143
Chapter VII: Summary and conclusions.....	157

List of Figures

Chapter 1	Introduction to supercapacitor and literature review	
Figure 1.1	Ragone plot for various energy storage/propulsion devices and their “charge” time	01
Figure 1.2	Schematic of an electrochemical capacitor.....	04
Figure 1.3	The schematic of FSS-SCs.....	15
Chapter 2	Theoretical background of successive ionic layer adsorption and reaction (SILAR) method and thin film characterization techniques	
Figure 2.1	Schematic of four beaker SILAR method.....	43
Figure 2.2	Bragg’s diffraction.....	47
Figure 2.3	Schematic of X-ray Tube.....	47
Figure 2.4	a) Schematic of X-ray diagram, and b) photograph of Bruker D2 phaser X-ray analyser	48
Figure 2.5	Basic schematic of FT-IR with Michelson interferometer.....	49
Figure 2.6	a) Photograph of ALPHA II compact FT-IR spectrometer, and b) the basic ray diagram of FT-IR system.....	50
Figure 2.7	Energy level diagram showing the states involved in Raman spectra.....	52
Figure 2.8	The basic block diagram of Raman spectrometer.....	53
Figure 2.9	Ray diagram for the emission of different types of electrons after the interaction of primary electrons from source with sample.....	54
Figure 2.10	a) Ray diagram of emission of different types of electrons, and b) photograph of FE-SEM instrument.....	55
Figure 2.11	Atomic model of the working principle of XPS.....	56
Figure 2.12	Schematic diagram of an XPS instrument.....	57
Figure 2.13	a) Photograph of Rame-Hart NRL contact angle meter, and b) contact angle of a liquid in contact with solid sample.....	57
Figure 2.14	Schematic diagram of the dynamic flow method apparatus.....	59
Figure 2.15	Schematics of charge-storage mechanisms for a) an EDLC, and (b-d) different types of pseudocapacitive electrodes: b) surface redox pseudocapacitor, c) intercalation pseudocapacitor, and d) battery-type Faradic reaction.....	62
Figure 2.16	The typical cyclic voltammogram for a reversible single electron transfer reaction.....	62
Figure 2.17	Charge–discharge curves of a supercapacitor.....	63
Figure 2.18	Representative shapes of GCD curves: a) EDLC, b) surface redox capacitance, c) intercalation capacitance, and d) Faradic battery-type.....	64
Figure 2.19	Nyquist plot with electrical equivalent circuit consisting charge R_{ct} in parallel with C	65
Figure 2.20	Nyquist plots with corresponding electrical equivalent circuit a) consisting R_s , R_{ct} and C and b) consisting R_s , R_{ct} , C , and W	66
Chapter 3	CuS and CuS@rGO thin films by SILAR method: Characterization and electrochemical performance	
Figure 3.1	Schematic flow chart of rGO synthesis by Modified Hummer's method.....	74
Figure 3.2	Graphical representation of weight deposited of CuS on SS substrate at 60 (CuS60), 80 (CuS80), 100 (CuS100), and 120 (CuS120) SILAR deposition cycles.....	75
Figure 3.3	The schematic of SILAR method employed for CuS@rGO thin film electrode preparation.....	75
Figure 3.4	Graphical representation of weight deposited of CuS@rGO on SS substrate at various concentration of rGO suspension.....	76

Figure 3.5	a) The electrochemical work station, b) experimental setup, and c) schematic representation of three electrode system.....	77
Figure 3.6	a) The XRD patterns and b) FT-IR spectra of CuS thin films deposited at different cycles.....	79
Figure 3.7	FE-SEM images of a) CuS60, b) CuS80, c) CuS100, and d) CuS120 at the magnification of 10,000 X, and e) CuS60, f) CuS80, g) CuS100, and h) CuS120 at the magnification of 50,000 X.....	80
Figure 3.8	The EDAX spectra of a) CuS60, b) CuS80, c) CuS100, and d) CuS120 thin films (Insets show atomic percentages of constituting elements of CuS thin film).....	81
Figure 3.9	a) The Raman spectrum, b) water contact angle photograph, c) N ₂ sorption isotherms, and d) BJH pore size distribution curve of CuS material deposited at 100 cycles.....	82
Figure 3.10	a) The XRD patterns and b) the FT-IR spectra of CuS@rGO thin films deposited using different concentrations of rGO suspension.....	84
Figure 3.11	FE-SEM images of a) CuS@rGO3, b) CuS@rGO4, c) CuS@rGO5, and d) CuS@rGO6 at the magnification of 20,000 X, and e) CuS@rGO3, f) CuS@rGO4, g) CuS@rGO5, and h) CuS@rGO6 at the magnification of 100,000 X.....	84
Figure 3.12	The EDAX spectra of a) CuS@rGO3, b) CuS@rGO4, c) CuS@rGO5, and d) CuS@rGO6 thin films (Insets show atomic percentages of constituting elements).....	85
Figure 3.13	The XPS spectra of a) CuS@rGO film wide survey scan, b) Cu2p, c) S2p, d) C1s, and e) O1s	86
Figure 3.14	a) The Raman spectrum, b) water contact angle photograph, c) N ₂ sorption isotherms, and d) BJH pore size distribution curve of CuS@rGO thin film deposited at 0.5 mg/mL concentration of rGO suspension.....	87
Figure 3.15	a) Comparative CV curves of CuS thin films at a scan rate of 20 mV s ⁻¹ , b) variation of C _s with the scan rates, and the CV curves at various scan rates from 1-20 mV s ⁻¹ of c) CuS60, d) CuS80, e) CuS100, and f) CuS120 thin film electrodes.....	89
Figure 3.16	a) Plots of log <i>i</i> against log <i>v</i> , b) plots of <i>i/v</i> ^{1/2} against <i>v</i> ^{1/2} for CuS thin film electrodes; and contribution of capacitive and diffusion controlled currents for c) CuS60, d) CuS80, e) CuS100, and f) CuS120 thin film electrodes.....	90
Figure 3.17	a) Comparative GCD curves of CuS thin film electrodes at a current density of 5 A g ⁻¹ , b) variation of C _s with the current densities, and the GCD curves at various current densities from 1-5 A g ⁻¹ of c) CuS60, d) CuS80, e) CuS100, and f) CuS120 thin film electrodes.....	93
Figure 3.18	a) Nyquist plots, b) the fitted equivalent circuit for the EIS data, and c) the stability curves for CuS thin film electrodes.....	94
Figure 3.19	a) Comparative CV curves of rGO and CuS@rGO thin films at a scan rate of 20 mV s ⁻¹ , b) variation of C _s with the scan rate, and the CV curves at various scan rates from 2-20 mV s ⁻¹ of c) CuS@rGO3, d) CuS@rGO4, e) CuS@rGO5, and f) CuS@rGO6 thin film electrodes.....	96
Figure 3.20	a) Plots of log <i>i</i> against log <i>v</i> , b) plots of <i>i/v</i> ^{1/2} against <i>v</i> ^{1/2} of CuS@rGO thin film electrodes; and contribution of capacitive and diffusion controlled currents for c) CuS@rGO3, d) CuS@rGO4, e) CuS@rGO5, and f) CuS@rGO6 thin film electrodes.....	97
Figure 3.21	a) Comparative GCD curves of CuS@rGO thin film electrodes at a current density of 5 A g ⁻¹ , b) variation of C _s with the current densities, and the GCD curves at various current densities from 1-5 A g ⁻¹ of c) CuS@rGO3, d) CuS@rGO4, e) CuS@rGO5, and f) CuS@rGO6 thin film electrodes.....	99

Figure 3.22	a) Nyquist plots of CuS@rGO thin films, b) the fitted equivalent circuit for the EIS data, and c) the stability curves for CuS@rGO thin film electrodes.....	101
Chapter 4	CuSe₂ and CuSe₂@rGO thin films by SILAR method: Characterization and electrochemical performance	
Figure 4.1	Graphical representation of weight deposited of copper selenide on SS substrate at 20 (C1), 30 (C2), 40 (C3), and 50 (C4) SILAR deposition cycles..	108
Figure 4.2	Schematic of SILAR method used for deposition of CuSe ₂ @rGO thin films....	109
Figure 4.3	a, b) Crystal structure of CuSe ₂ plotted using VESTA software, c) unit cell of cubic CuSe ₂ , d) rGO sheet, e) CuSe ₂ @rGO after first SILAR cycle of deposition, f) CuSe ₂ @rGO after multiple SILAR cycles of deposition.....	110
Figure 4.4	The XRD patterns of a) CuSe ₂ and b) CuSe ₂ @rGO thin films	111
Figure 4.5	FT-IR spectra of (i) CuSe ₂ and (ii) CuSe ₂ @rGO thin films.....	112
Figure 4.6	The Raman spectra of a) CuSe ₂ and b) CuSe ₂ @rGO thin films.....	113
Figure 4.7	The FE-SEM images of a-c) CuSe ₂ , and d-f) CuSe ₂ @rGO thin films at various (5,000 X, 25,000 X, and 100,000 X) magnifications.....	114
Figure 4.8	EDAX spectra of a) CuSe ₂ and b) CuSe ₂ @rGO thin films (Insets show atomic percentages of elements).....	115
Figure 4.9	a) The XPS spectrum of CuSe ₂ @rGO electrode, the XPS spectrum of b) Cu2p, c) Se3d, d) C1s, and e) O1s.....	116
Figure 4.10	Water contact angle photographs of a) CuSe ₂ and b) CuSe ₂ @rGO thin films...	117
Figure 4.11	N ₂ adsorption graphs of a) CuSe ₂ , and b) CuSe ₂ @rGO, pore size distribution of c) CuSe ₂ , and d) CuSe ₂ @rGO samples.....	118
Figure 4.12	a) Comparative CV curves of CuSe ₂ , CuSe ₂ @rGO, and rGO at a scan rate of 20 mV s ⁻¹ , the CV curves of b) CuSe ₂ , and c) CuSe ₂ @rGO at various scan rates from 2-20 mV s ⁻¹ , and d) variation of C _s with the scan rate for CuSe ₂ and CuSe ₂ @rGO thin film electrodes.....	119
Figure 4.13	a) Plots of log <i>i</i> verses log <i>v</i> , b) plots of <i>i/v</i> ^{1/2} verses <i>v</i> ^{1/2} of CuSe ₂ , and CuSe ₂ @rGO thin film electrodes, and calculated charge storage by capacitive and diffusion processes for d) CuSe ₂ , and e) CuSe ₂ @rGO thin film electrodes.	120
Figure 4.14	GCD curves of a) CuSe ₂ , b) CuSe ₂ @rGO at different current densities from 2-6 A g ⁻¹ , and c) variation of C _s with charge-discharge current density.....	122
Figure 4.15	a) Nyquist plots of i) CuSe ₂ and ii) CuSe ₂ @rGO thin film electrodes (Inset shows magnified Nyquist plots in higher frequency region), and b) the fitted equivalent circuit for the EIS data.....	123
Figure 4.16	Stability curves of i) CuSe ₂ and ii) CuSe ₂ @rGO thin film electrodes.....	124
Chapter 5	Synthesis and characterization of MnO₂ thin films	
Figure 5.1	a) The XRD pattern, b) FT-IR spectrum, c) Raman spectrum, and d) EDAX spectrum of MnO ₂ thin film (Inset shows atomic percentage of constituent elements).....	133
Figure 5.2	The FE-SEM images at a) 10,000 X, and b) 70,000 X magnifications, c) contact angle photograph, and d) N ₂ sorption curves of MnO ₂ film (Inset shows pore size distribution curve).....	134
Figure 5.3	a) CV curves, b) variation of the C _s with the scan rate, c) GCD plots, and d) Nyquist plot (Inset shows fitted equivalent circuit for the EIS data) of MnO ₂ thin film electrode.....	136
Figure 5.4	Capacitance retention of MnO ₂ thin film electrode (Inset shows CV curves of 2 nd and 5000 th cycles).....	137
Chapter 6	Fabrication and performance evaluation of FSS-ASCs devices based on CuS@rGO and CuSe₂@rGO thin films	
Figure 6.1	a) CV curves, b) GCD curves at different voltage ranges (0 V to 1.6 V), c) CV curves at various scan rates, and d) GCD curves at various current densities of MnO ₂ //CuS@rGO ASC device.....	146

Figure 6.2	Variation of specific capacitance with a) the scan rates and b) the current densities.....	146
Figure 6.3	a) Ragone plot, and b) change in specific capacitance with different bending angles of $\text{MnO}_2//\text{CuS}@r\text{GO}$ ASC device	147
Figure 6.4	a) The Nyquist plot (Inset image shows equivalent circuit), and b) phase angle as a function of frequency of FSS-ASC device.....	148
Figure 6.5	a) Variation of specific capacitance with GCD cycles (Inset image show 2 nd and 6000 th cycles), and b) practical application of $\text{MnO}_2//\text{CuS}@r\text{GO}$ device to glow 201 red LEDs panel.....	148
Figure 6.6	a) Schematic of assembly, and b) photograph of $\text{CuSe}_2@r\text{GO}//\text{CuS}$ ASC device.....	149
Figure 6.7	a) CV curves, and b) GCD plots at various voltages, c) CV curves at different scan rates, and d) GCD curves at various charging current densities of $\text{CuSe}_2@r\text{GO}//\text{CuS}$ ACS device.....	150
Figure 6.8	a) Variation of C_s with a) the scan rates and b) current densities.....	150
Figure 6.9	a) Ragone plot, b) Nyquist plot (Inset image shows equivalent circuit), c) Bode plot, and d) plot of C_s retention over 5000 GCD cycles (Inset image shows 2 nd and 5000 th GCD cycles) of ASC device.....	152
Figure 6.10	a) The selected CV curves at various bending angles, b) retention of specific capacitance with the bending angles, and c) demonstration of two series connected $\text{CuSe}_2@r\text{GO}//\text{CuS}$ ASC devices to illuminate 201 red LEDs.....	153
Chapter 7	Summary and conclusions	
Figure 7.1	a) Photograph in twisted position, and b) thickness measurement of $\text{CuS}@r\text{GO}//\text{MnO}_2$ ASC device, demonstration to illuminate c) table lamp consisting 12 white LEDs, and d) LEDs panel made of 201 red LEDs using two series connected $\text{CuS}@r\text{GO}//\text{MnO}_2$ ASC devices.....	163

List of Tables and Charts

Chart 1.1	Classification of supercapacitors.....	04
Chart 1.2	Classification of supercapacitor electrodes based on charge storage mechanism...	07
Table 1.1	Previous results obtained from FSS–SSCs device.....	17
Table 1.2	Previous results obtained from FSS–ASCs device.....	18
Table 1.3	The literature survey of metal chalcogenide based supercapacitor.....	21
Chart 2.1	General classification of thin film deposition techniques.....	41
Table 3.1	Electrochemical impedance spectroscopic fitted circuit parameters for Nyquist plots of CuS thin film electrodes	95
Table 3.2	Electrochemical impedance spectroscopic fitted circuit parameters for Nyquist plots of CuS@rGO thin film electrodes.....	101
Table 4.1	Electrochemical impedance spectroscopic fitted circuit parameters for Nyquist plots of CuSe ₂ and CuSe ₂ @rGO thin film electrodes.....	123
Table 7.1	The electrochemical parameters of CuS, CuS@rGO, CuSe ₂ , and CuSe ₂ @rGO thin film electrodes in three electrode system	162
Table 7.2	The electrochemical parameters of FSS-ASC devices evaluated using two electrode system.....	162

List of Abbreviations

AC	Activated carbon	PEC	Photoelectrochemical
P	Adsorptive pressure	PV	Photovoltaic
AR	Analytical reagent	PEO	poly (ethylene oxide)
C_a	Areal capacitance	PMMA	Poly (methyl methacrylate)
ASC	Asymmetric supercapacitor	PVA	Poly (vinyl alcohol)
BJH	Barrett-Joyner-Halenda	PVF	Poly (vinylidene fluoride)
BET	Brunauer-Emmett-Teller	PVdF-co-HFP	Poly (vinylidene fluoride-cohexafluoropropylene)
CF	Carbon foam	PAA	Polyacrylate
CNTs	Carbon nanotubes	PAN	Polyacrylonitrile
f₀	Characteristics frequency	PANI	Polyaniline
R_{ct}	Charge transfer resistance	PPy	Polypyrrole
CCD	Charge coupled device	PTh	Polythiophene
CBD	Chemical bath deposition	KOH	Potassium hydroxide
CVD	Chemical vapour deposition	ΔE	Potential window
CV	Cyclic voltammetry	PC	Propylene carbonate
t_a	Discharging time	rGO	Reduced graphene oxide
DDW	Double distilled water	t₀	Relaxation time constant
EDLC	Electric double-layer capacitors	SCE	Saturated calomel electrode
EIS	Electrochemical impedance spectroscopy	P_s	Saturated vapor pressure
ED	Electrodeposition	R_s	Series resistance
E	Energy	S_P	Specific power
EDAX	Energy dispersive X-ray spectroscopy	C_s	Specific capacitance
EMC	Ethyl methyl carbonate	S_E	Specific energy
EC	Ethylene carbonate	S_B	Specific surface area
FE-SEM	Field emission scanning electron microscopy	SS	Stainless steel
FSS-SCs	Flexible solid state supercapacitors	Q	Stored charges
FT-IR	Fourier transform infrared spectroscopy	SILAR	Successive ionic layer adsorption and reaction
FWHM	Full width at half maximum	SCs	Supercapacitors
GCD	Galvanostatic charge-discharge	SSC	Symmetric supercapacitor
GNS	Graphene nanosheets	S_T	Total surface area
GO	Graphene oxide	TMCs	Transition metal chalcogenides
HSC	Hybrid capacitor	W	Warburg impedance
IR	Internal resistance	XRD	X-ray diffraction
LEDs	Light emitting diodes	XPS	X-ray photoelectron spectroscopy
LIBs	Lithium-ion batteries		
Hg/HgO	Mercury/mercury oxide		

CHAPTER – I

**Introduction to supercapacitor and
literature review**

Chapter-I

Introduction to supercapacitor and literature review

1.1	Energy storage systems.....	1
1.2	Supercapacitor.....	2
1.2.1	Evolution of supercapacitor.....	2
1.2.2	Basic working principle.....	3
1.2.3	Types of supercapacitors.....	4
1.2.4	Types of electrode materials.....	7
1.2.5	Electrolytes.....	10
1.3	Flexible solid state supercapacitors (FSS-SCs).....	14
1.4	Literature survey.....	19
1.4.1	Copper sulfide.....	19
1.4.2	Copper selenide.....	20
1.5	Purpose of the research.....	23
	References.....	25

1.1 Energy storage systems

With the technical advancement, production and demand for electrical energy rise tremendously in recent years. This drives research in the energy storage sector at a greater speed among academia and industry to develop a device for electricity storage. Batteries, capacitors, fuel cells, and supercapacitors (SCs) are used to hold charges through different mechanisms. The Ragone plot for various energy storage and propulsion devices with their ‘charge’ times is shown in Figure 1.1. The availability of different materials for the production of different components of energy storage devices such as an electrode, electrolytes, packing materials, and production process are some of the important key points which decide the price of device. Different electrode materials have been extensively investigated with the intention to change production methods, increase energy storage capacity and electrochemical stability. The capacity and stability of electrode material are depending on electrolyte used. Researchers have mainly focused to produce low cost and less hazardous electrode materials [1].

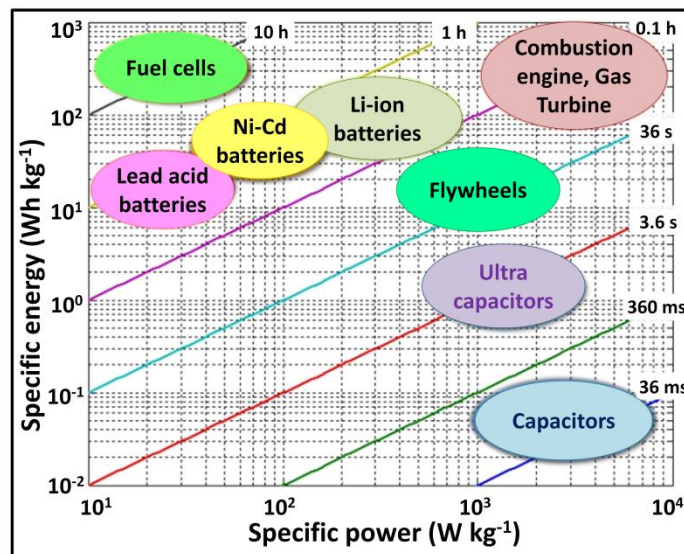


Figure 1.1: Ragone plot for various energy storage and propulsion devices and their ‘charge’ time [2].

Increasing applications of portable and lightweight electronics require a suitable energy storage device possessing long life and flexibility. Lithium-ion batteries (LIBs) and SCs are convenient to use in portable electronics as energy storage devices. Both of them store energy with different mechanisms, the former one via bulk redox reactions, and the latter by electrostatically (for carbon materials) or via

reversible redox reactions taking place at the surface of the electrode (transition metal chalcogenides, silicates, carbides, nitrides, and phosphates) [3].

The SCs are the most promising energy storage device so far as services life, specific power (S_P), and safety are concerned. Various designs of SCs were put forward to improve charge storage capacity. The scientific community is engaged in preparation of materials through different methods for SCs. The electrolytes inside SCs are most important part of the design. The energy stored (E) in the SC can be calculated using relation $E = 0.5C_sV^2$; where C_s is the specific capacitance measured in $F\ g^{-1}$ and V is the operating potential window in V. A feasible way to increase energy storage capacity of the SCs is either to raise C_s or operating potential [4].

Currently, market of SCs is dominated by electric double layer capacitor (EDLC) materials, as it is economical and highly stable. However, considering charge storage capacity, EDLC materials lag behind pseudocapacitive materials. Therefore, it is necessary to investigate pseudocapacitive electrode materials which store more electric energy. The new class of materials was formed by the combination of EDLC and pseudocapacitor materials which store energy via both EDLC and pseudocapacitive mechanisms and capable of operating stably at comparative high voltages with long cycle life [5, 6].

1.2 Supercapacitor

1.2.1 Evolution of supercapacitors

The storage of electrical energy in a double layer formed at the interface of electrode and electrolyte was put forth in the 19th century. The company, General Electric, Boston (USA) reported the first EDLCs in 1957 based on porous carbon electrodes [7]. However, this device was not commercialized because of its impractical flooded battery like storage mechanism in which both the electrodes were required to be dipped in an electrolyte container. Further, in 1966 the Standard Oil Company of Ohio was succeeded in the development of an energy storage device by utilizing high surface area carbon materials in tetraalkylammonium salt electrolyte [8]. In 1988, the Nippon Electric Company (NEC) produced the first world's smallest chip type solid tantalum electrolytic capacitor. Initially, these devices were employed for memory backup systems and later on for various consumers' appliances. In 1980,

Matsushita Electric Industrial Co. (Panasonic) invented “Goldcap”. These devices were also used in memory backup systems. The main difference between Panasonic and NEC devices was the electrolyte. For the construction of SC, NEC used an aqueous electrolyte while Panasonic used a non-aqueous electrolyte. In 1975-1985, Convey developed new conception of charge storage mechanism based on fast and reversible redox reactions occurring near the surface or in the bulk of electrode material. Convey used ruthenium oxide (RuO_2) as a pseudocapacitive material and performed several experiments. In 1987 ELNA had begun to produce a double layer capacitor by the name “Dynacap”. The first high power double layer capacitors were developed by PRI under the name “PRI Ultracapacitor” in 1982 using metal oxide electrodes.

In 1990, the entire research field in SCs becomes more significant to develop high performance SC devices. The US department of energy in 1992 announced its ultracapacitor development program at Maxwell Laboratories. Many companies all over the world like ELTON, CAP-XX, Nippon Chemi-Con Corporation, NessCap, etc., are manufacturing SCs.

1.2.2 Basic working principle

In SCs, electric charges are stored at the interface of electrode and electrolyte, although the electrolyte ions with different charges are organized on the electrolyte side (see Figure 1.2).

The electric charge storage mechanism of ordinary capacitor and SC is same but the difference is in the dielectric and electrolyte material. The C_s of SC devices mainly depends on the specific surface area of electrode plates and the distance between the two plates. The capacitance of electrochemical capacitor is calculated as,

$$C = \frac{\varepsilon A}{d} \quad (1.1)$$

where C is the capacitance of electrochemical capacitor, ε is dielectric constant of the vacuum, d is distance between electrolyte ions and the electrode and A is the specific surface area of the active electrodes. The specific energy (S_E) and specific power (S_P) of electrochemical capacitor can be estimated by the following equations,

$$S_E = \frac{0.5 \times C_s \times \Delta V^2}{3.6}, \quad (1.2), \text{ and} \quad S_P = \frac{3600 \times S_E}{dt} \quad (1.3)$$

where C_s is specific capacitance, ΔV is a potential window of SC, and dt is the discharging time.

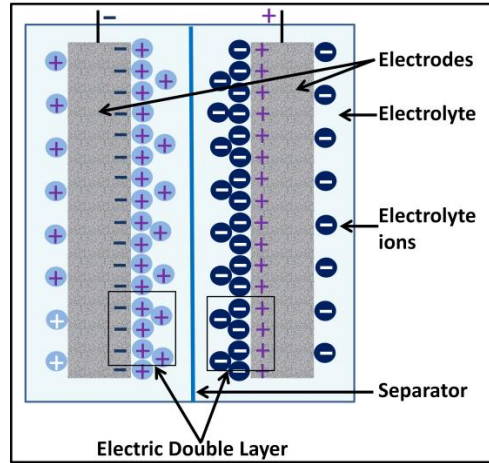


Figure 1.2: Schematic of an electrochemical capacitor.

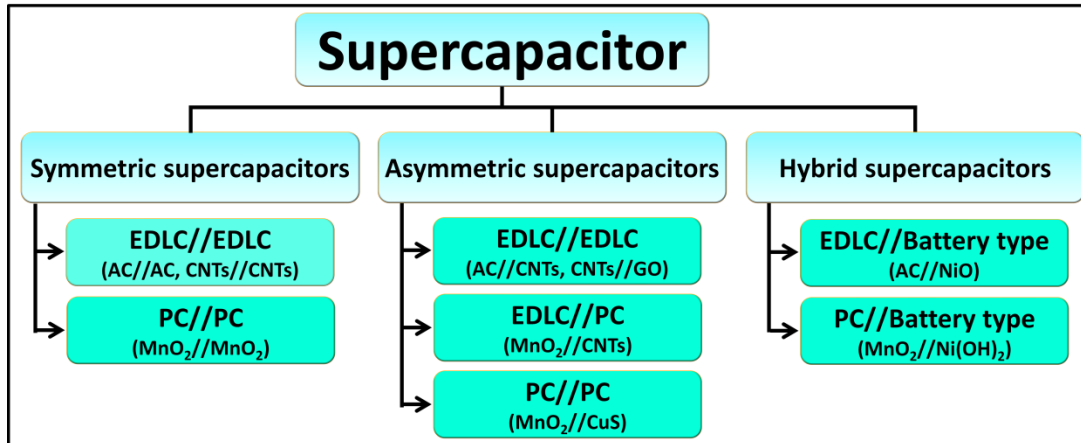


Chart 1.1: Classification of supercapacitors.

1.2.3 Types of supercapacitors

The electric charge storage mechanism divides SCs into different types as symmetric supercapacitor (SSC), asymmetric supercapacitor (ASC), and hybrid capacitor (HSC) [9]. The SCs are administrated by the same fundamental equations as an ordinary conventional capacitor but offer higher specific surface area using a porous surface electrode and polymer gel electrolyte to reach higher C_s . The graphical presentation of different classes of SCs is summarized in Chart 1.1.

1.2.3.1 Symmetric supercapacitors (SSCs)

The combination of two similar types of electrodes to form SC can be termed as SSC. The S_P of SSCs could be lower than the ASCs due to the lower potential window. Carbon nanotubes (CNTs)//CNTs and MnO_2 // MnO_2 are representative examples of SSC devices [10]. As both electrodes are from similar materials, the charge balance can be achieved easily in this case.

1.2.3.2 Asymmetric supercapacitors (ASCs)

The configuration of SC device which uses two dissimilar electrodes is called ASC. This type of configuration is expected to be a promising way to assemble a cell that will provide equivalent S_P as that of SCs. With the combination of the electrodes having different charge storage mechanisms, one can manage to improve the electrochemical properties of the new cell. Usually, the electrodes based on pseudocapacitive and EDLC charge storage mechanisms were assembled. The ASCs can operate at high voltage and provide longer electrochemical stability and high energy density at high current rates. In simple words, the term ASC can be used when both EDLC or one EDLC and one pseudocapacitive or both pseudocapacitive electrodes are in cell assembly. AC//CNTs, AC// MnO_2 [11], and MnO_2 // Fe_2O_3 [12] are few representative examples of the ASCs devices. The final voltage of ASCs is decided by the working voltages of the individual electrodes [13]. To achieve maximum working potential and S_E , the charges stored (Q) on both constituent electrodes must be balanced i.e. $Q_- = Q_+$ [14]. Typically the charges stored are associated with the electroactive mass (m), potential window (ΔE), and C_s of the electrode material. Best mass ratio of the electrodes were calculated from following relation,

$$\frac{m_+}{m_-} = \frac{C_- \times \Delta E_-}{C_+ \times \Delta E_+} \quad (1.4)$$

where the signs + and – indicate the entity for positive and negative electrodes, respectively. The C_s of the electrode material can be calculated theoretically using following relation [15],

$$C = \frac{n.F}{m.\Delta E} \quad (1.5)$$

where F , n , and m are the Faraday's constant (96485 C mol^{-1}), number of transferred electrons and molecular weight (MW) of active material, respectively.

The selection of electrode materials plays a crucial role in deciding final working voltage of ASC device. The selection of electrolyte also plays a vital role in voltage window of the ASC devices. Thermodynamically the oxidation and reduction reactions in materials are associated with the work function of material. Therefore, the electrodes with the largest work function can offer a higher working voltage. Thus the following relation is used to calculate possible working voltage window of ASCs,

$$E = E_0 + \Delta E_1 + \Delta E_2 = \frac{1}{F(\omega^\beta - \omega^\alpha)N_A} + \Delta E_1 + \Delta E_2 \quad (1.6)$$

where ω^β and ω^α are the work functions for the positive and negative electrodes, respectively and N_A is the Avogadro's constant ($6.02 \times 10^{23} \text{ mol}^{-1}$) [16]. For SSCs, $\omega^\beta = \omega^\alpha$ and $\Delta E_1 = -\Delta E_2$; hence, the potential window is limited to their three electrode measurement.

1.2.3.3 Hybrid supercapacitor (HSCs)

The capacitors are high power devices and store a small amount of electricity whereas the batteries are a type of device having high S_E but lacking S_P . These two materials can be brought together in one device to boost both S_E and S_P . Configuration of energy storage devices consisting of one capacitive (carbon) and another battery type (NiO) electrode in one device is called hybrid supercapacitors (HSCs). These types of SCs show deviation from charge storage mechanism of the EDLC and pseudocapacitors. In HSCs, a high working voltage can be achieved to reach the redox potential of pseudocapacitive material which eventually enhances S_E and S_P of the SCs [17]. Despite high capacity and wide operating voltage of HSCs, due to one of the battery type electrodes lead to lesser rate capacity and cycle life.

This problem was mitigated by the fabrication of electrodes with layered and porous nanostructured materials that can ensure easy intercalation/deintercalation of the charges. There are many ways which were put in practice to produce porous nanostructured electroactive electrode. This will reduce charge transport length and increase exposed electroactive surface areas which provide more accessible storage sites. The systematic composition of pseudocapacitive material with highly conductive carbon allotropes such as graphene, CNTs, activated carbons (AC), etc., was proposed to overcome the issue of sluggish kinetics involved in the charge

storage process [18]. The electrochemical characteristics of the HSCs deviate from the capacitive behavior due to hybridization.

1.2.4 Types of electrode materials

The electrode material to be used for charge storage must go under redox reaction or hold charges by non-faradaic charge transfer. To accomplish outstanding charge storage capacity, electrode material must possess good electrical conductivity, surface structure with proper pores size, and high specific surface area. Some of the requirements of electrode material are (a) low synthesis cost, (b) environment friendly or less hazardous, (c) good electrical conductivity, (d) thermally and chemically stable inside the electrolyte being used, and (e) a high specific surface area with appropriate pore size provides more electroactive site for electrochemical redox reactions.

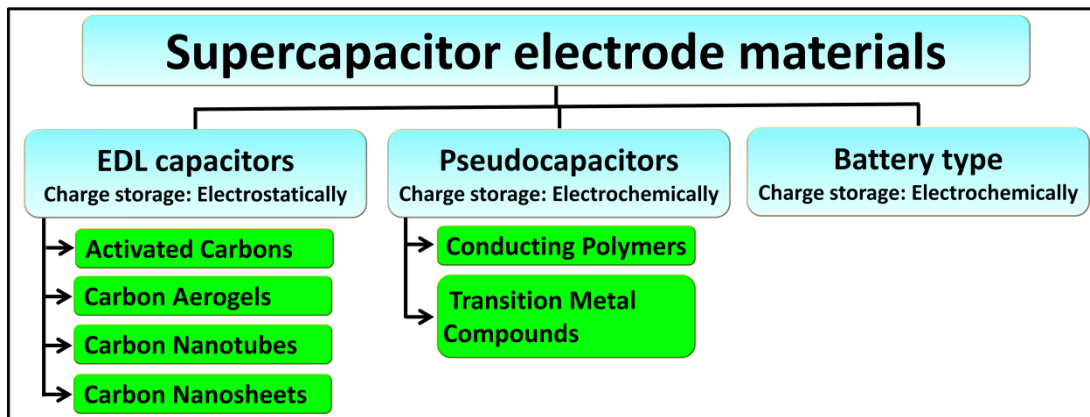


Chart 1.2: Classification of supercapacitor electrodes based on charge storage mechanism.

Although carbon based materials are thermally and chemically stable and offer high conductivity hence become one of the first choices for the EDLC type SC. The pseudocapacitive materials such as metal chalcogenides, hydroxides, nitrides, silicates, carbides, and conducting polymers are applied as pseudocapacitors, due to their ability to undergo reversible redox reactions which can store high charges than EDLC materials [19, 20].

1.2.4.1 Electrochemical double layer capacitor (EDLC)

Carbon based electrode materials are EDLCs type materials. Besides having high power capability than batteries, their charge storing and charge releasing mechanism is efficiently reversible, so they are extremely promising candidates with

long charge/discharge life. Carbon allotropes such as AC, carbon aerogels, graphene, reduced graphene oxide (rGO), graphite paper, and CNTs have been investigated enormously to get high performance of electrode material due to its properties like superior conductivity, excellent thermal and electrochemical stability in all types of electrolytes. Lower cost and larger specific surface area (up to $3000 \text{ m}^2 \text{ g}^{-1}$) make EDLC materials a first choice for the SCs application [21].

1.2.4.2 Pseudocapacitive materials

Transition metal compounds such as chalcogenides, silicates, carbides, nitrides, and polymers such as polyaniline (PANI), polypyrrole (PPy), and polythiophene (PTh), etc., are studied extensively. Among these, transition metal chalcogenides (TMCs) have received well deserved attention due to their excellent electrical conductivity and thermal stability as compared to other mentioned transition metal compounds and polymers owing to achieve high capacitance and S_E for portable energy storage devices [22, 23].

1.2.4.2A Transition metal chalcogenides (TMCs)

Presently, nanostructured TMCs are used as the electroactive material for SC. The metal constituents having different oxidation states affect the electric conductivity of electrode material which is beneficial for high electrochemical performance [24]. Peng et al. [25] were developed a SC electrode composed of CuS microspheres with PPy sheet-like structure to enhance the pseudocapacitive performance. Three layer nanostructure of CuS/rGO/Ni₃S₂ composite was in-situ grown on nickel foam (NF) through a one-step hydrothermal assisted method by Wang et al. [26]. The arrays of CuS ultrafine nanoneedles supported on a CNT backbone were fabricated by template engaged chemical conversion route by Zhu et al. [27]. Bulakhe et al. [28] prepared copper sulfide with different morphologies for high performance SCs using successive ionic layer adsorption and reaction (SILAR) method. A double sided mesh electrode coated with Cu₂S film and carbon nanoparticles was reported by Shi et al. [29]. Hsu et al. [30] testified CuS nanowire array with a hierarchical nanoarchitecture directly on copper foil using a simple and cost effective liquid-solid reaction for SC application. Huang et al. [31] synthesized CuS with different morphologies via a simple one step solvothermal method with or

without surfactants. The solvothermal method used for the preparation of 3D hierarchical covellite CuS microspheres from an ionic liquid precursor was reported by Zhang et al. [32]. Qian et al. [33] achieved a high C_s of 2393 F g⁻¹ at 10 mV s⁻¹ for CuS nanotubes in redox active polysulfide electrolyte through a combination of pseudocapacitance of CuS nanotubes in the electrolyte. Chen et al. [34] reported synthesis of CuS/MWCNT by one step hydrothermal process and C_s of 2831 F g⁻¹ was obtained from the nanotubes structured surface.

1.2.4.2B Conducting polymers

PANI, PPy, and PTh are the polymers used as the electrode material for SCs. The performance of SC is elevated by the better electric conductivity of polymers. Generally, the potential window of these conducting polymers is stationary. Due to the degradation of the polymers in the electrolyte after cycling performance of the polymer based electrodes reduced significantly. Peng et al. [35] reported a C_s of 480 F g⁻¹ for PPy electrodes. Dubal et al. [36] prepared PPy thin films using the electrodeposition method which gives C_s of 586 F g⁻¹. The composite of CNTs and conducting polymers were prepared by Zhou et al. [37] for pseudocapacitor application. Ambade et al. [38] reported synthesis of PTh electrode by electrochemical method and obtained C_s of 425.4 F g⁻¹.

Recently, to increase specific surface area, thermal stability, and electrical conductivity polymers were composited with the EDLC materials in various compositions using different methods of preparations.

1.2.4.2C Other pseudocapacitive materials

The capacitance and energy density of TMCs are much higher than those of carbon based materials. However, the distortion that occurred in the microstructure of TMCs due to the repeated charge discharge process ultimately results in lower cycle life. For practical application along with higher energy density cycling stability becomes crucial for pseudocapacitive materials. Thus, synthesis of material possessing high degree of porosity with outstanding electrochemical performance is crucial for achieving higher S_E and S_P . It is well known that the capacitance of pseudocapacitive materials depend on the number of parameters, such as crystallinity, porosity, specific surface area, and mass loading of the electrode. Therefore, the need

for advanced functional materials is growing. To develop new materials, various transition metal compounds were synthesized and tested for supercapacitive properties. Chodankar et al. [39] fabricated MoN nanoparticles as pseudocapacitive material on phosphorus incorporated carbon fabric and achieved C_s of 400 mF cm^{-2} . Wang et al. [40] prepared MnSi, CoSi, and NiSi by a hydrothermal method and reported C_s of 517.0, 452.8, 66.7 F g^{-1} at 0.5 A g^{-1} , respectively. Rakhi et al. [41] prepared nanocrystalline $\epsilon\text{-MnO}_2$ whiskers on MXene nanosheet surfaces ($\epsilon\text{-MnO}_2/\text{Ti}_2\text{CT}_x$ and $\epsilon\text{-MnO}_2/\text{Ti}_3\text{C}_2\text{T}_x$) to make nanocomposite electrodes for aqueous pseudocapacitors and obtained C_s of 212.1 F g^{-1} at the current density of 1 A g^{-1} . Marje et al. [42] prepared nickel phosphate thin films by chemical bath deposition (CBD) method and reported C_s of 1031 F g^{-1} at a current density of 0.5 mA cm^{-2} . Lokhande et al. [43] reported the hydrothermal synthesis of cobalt tungstate nanocomposite (CNT-CoWO₄) as SC electrode material with C_s of 1486 F g^{-1} at 5 mV s^{-1} .

1.2.5 Electrolytes

The inorganic salt dissolved in perfect ionizing solvent and the resultant solution is electrically conductive called an electrolyte. The conductivity of the electrolyte depends on the amount of salt dissolved in the unit volume of the solvent. The electrolyte plays important role in the electrochemical performance of SC. The type of electrolyte and solvent decides operational potential window of the SC hence, directly impacts on S_E and S_P . Depending upon physical state of electrolytes, there are two classes of electrolytes as liquid and solid state electrolytes (SSEs). Both of these have their advantages and disadvantages. There is another classification of the electrolytes based on the nature of solvent as protic and aprotic electrolytes. Protic electrolytes are the electrolytes in which polar solvent is used to dissolve salt e. g. water. In aprotic electrolyte nonpolar solvent is used to dissolve salt e.g. ethylene carbonate, propylene carbonate [44, 45].

1.2.5.1 Liquid electrolyte

There are two groups of liquid electrolytes depending on the type of solvent used for preparation; the aqueous and organic electrolytes. Usually, water based electrolytes are largely used to fabricate SCs, because of their lower cost, easy

preparation way, less toxic nature, and large ionic conductivity ($\sim 10^{-3} \text{ S cm}^{-1}$) [46]. But dissociation of the water at 1.23 V limits operating potential window and overall performance of SCs. In the case of organic electrolyte, the operating potential window can be extended up to 3.0 V but safety issues associated with it, like flammability and toxic nature of solvents and solutes are of major concern. The higher size of organic molecules (15-20 Å) and lower ionic conductivity are the reasons for lower C_s in the organic electrolyte. Lower C_s values lead to less energy and power density compared to the water based SCs, but this can be compensated by the wide operating potential window.

Both water based and organic electrolyte have their limitations and drawbacks such as high cost of packaging material and requirement of superior techniques to avoid possible leakage of the electrolytes, as most of the electrolytes are highly toxic and corrosive. Fabrication of micro and flexible SCs with liquid electrolytes is complicated. Reduction in energy efficiency due to evaporation of the electrolyte is another limitation of the liquid electrolyte. Therefore, it is necessary to formulate novel electrolyte composition which is more appropriate for flexible and micro SC devices in comparison to the liquid electrolyte. However, to date, there is no known perfect electrolyte suitable for all types of electrodes for achieving high performance next generation SCs.

1.2.5.2 Solid state electrolyte (SSE)

The issues of safety and power density remain with the use of flammable liquid electrolytes. This also restrains scaling up production. The application of SSEs will address these issues. The much higher thermal stability of SSE makes their best choices for next generation energy storage devices. The inorganic SSE can work into a wide range of temperatures (223 K to 473 K or greater). Inorganic SSEs exhibit high ion conductivity of over $10^{-4} \text{ S cm}^{-1}$ with high thermal stability owing to the inflexible crystal structure. But the performance of these electrolytes is very low because of poor interfacial contact between electrolyte and electrode. Another problem faced is the loss of capacity due to mechanical and electrochemical reasons. So, the manufacturing of inorganic SSE compatible for a variety of electrode materials is the need of time [47, 48].

Polymer gel electrolytes have attracted considerable research attentions with the increasing demand for wearable, lightweight, and flexible energy storage devices. Polymer electrolytes used in solid state SCs not only avoid the safety risk such as leakage and volatility but also greatly reduce the cost of encapsulation and provide more design opportunities for novel configuration of devices. They are usually divided into two types: gel polymer electrolytes (consisting of the polymer matrix, plasticizer, and supporting salt) and solid polymer electrolytes (without any solvent). However, given that the ultralow room temperature ionic conductivity of solid polymer electrolytes limits the further utilization in SCs. Gel polymer electrolytes are preferable and have been extensively prepared and investigated for solid state SC applications

The research in the field of gel polymer electrolytes encompasses investigations of the physical and chemical behaviors of the solids with fast ion movement within the bulk as well as their technological aspects. These gel polymer electrolytes are also called the ‘superionic solids’ or ‘fast ion conductors’. The gel polymer electrolytes show tremendous scope to develop solid state mini/micro electrochemical devices viz. batteries, fuel cells, SCs, electrochromic displays, sensors, photoelectrochemical (PEC) solar cells, etc. Mobile ions are the principal charge carriers in SSE. The SSEs have high ionic conductivity in the range of 10^{-2} to 10^{-4} S cm⁻¹. They possess high thermal and electrochemical stability.

The ion transformation in this electrolyte is principally governed by the thermally generated point defects such as Schottky and Frenkel defects. They possess very low room temperature ionic conductivity of an order of 10^{-16} to 10^{-12} S cm⁻¹ and usually, they are considered as an insulator. Many efforts were made to increase the extent of ionic conductivity by aliovalent doping, but with very limited success. However, major breakthrough was achieved in 1973, when materials science introduced the polymer based solid electrolyte [49]. Polymer electrolytes are defined as polymeric membranes which possessing the ion transport property comparable to the liquid electrolyte. The signification of polymer electrolytes with other solid electrolytes is in terms of high mechanical flexibility, ionic conductivity ($\sim 10^{-3}$ S cm⁻¹) at room temperature, and ease of preparation [50]. For reliable solid state

electrochemical application, polymer electrolyte should possess the following features;

- **High ionic conductivity:** To achieve electrochemical performance, comparable to liquid electrolyte the ionic conductivity of polymer electrolyte should be $10^{-3} \text{ S cm}^{-1}$ at room temperature.
- **High chemical, thermal and electrochemical stability:** The SC is fabricated by sandwiching the polymer electrolyte in between two electrodes. To avoid the undesired chemical reactions at the interface of electrode/electrolyte, polymer electrolyte must have high chemical stability. Further, to get a wider operating temperature range for SC, electrolyte must be thermally stable. Additionally, they should have excellent electrochemical stability to get high operating potential window.
- **Mechanical strength:** The polymer electrolyte must have the good mechanical strength to scale up manufacturing.
- **Compatibility:** To achieve the highest performance without depletion, the polymer electrolyte should be compatible with different types of electrode materials.
- **Improved safety:** To improve safety, the polymer electrolyte should be liquid free, so can be packed in plastic container other than metal one to avoid buildup of internal pressure. This will reduce the probability of explosion by a greater amount.
- **Serve as a separator:** In SC, a polymer electrolyte acts as a separator as well as conducting medium in between two electrodes. It avoids the necessity of a separator. Based on physiochemical properties many routes are adopted for the synthesis of polymer electrolytes. They are classified into various groups such as plasticized polymer electrolytes, rubbery electrolytes, and solvent-swollen polymer electrolytes [51].

In last decade, the polymer gel electrolytes are predominately used to develop SCs, as they possess both the cohesive properties of solid and diffusive transport properties of the liquid [52, 53]. Typically, polymer gel electrolytes are prepared by entrapping the liquid electrolyte within the polymeric network. The ionic conduction occurs through the motion of liquid electrolytes, whereas polymer provides the mechanical integrity. Due to their gel like nature and much lower liquid content, it is

expected that the polymer gel electrolytes are less reactive than their liquid electrolyte counterparts [54].

The advantages of polymer gel electrolytes are higher ionic conductivity (comparable to SSEs), sufficient potential window (3.0 V), mechanical flexibility, and interfacial stability. Previously, polyacrylate (PAA) [55], poly (ethylene oxide) (PEO) [56], poly (vinyl alcohol) (PVA), polyacrylonitrile (PAN) [57], poly (vinylidene fluoride) (PVdF), poly (vinylidene fluoride-cohexafluoropropylene) (PVdF-co-HFP) [58] and poly (methyl methacrylate) (PMMA) [59] were used as host polymers for preparing polymer gel electrolytes. Commonly used organic solvents are EC, PC, and ethyl methyl carbonate (EMC), but organic solvents are generally often toxic, flammable, and expensive. Therefore, replacement of organic solvents with aqueous solvents is highly suitable. The aqueous gel electrolytes can also substantially reduce device cost.

1.3 Flexible solid state supercapacitors (FSS-SCs)

Recent scope toward the fabrication of small size portable electronic devices needs a small size flexible electric charge storage device. Nowadays, Li-ion batteries and flexible solid state supercapacitors (FSS-SCs) devices are appropriate in the fabrication of microelectronics. The properties like long cycle life, high S_p , safety, flexibility, and stability of FSS-SCs are beneficial for energy storage applications. The schematic of FSS-SCs is shown in Figure 1.3. The current collector with a thin layer of electroactive material acts as one electrode. If the device is symmetric then the two electrodes are of the same type. For ASCs device two electrodes are of different types. The solid polymer gel electrolyte is used as an electrolyte as well as separator and all this assembly is packed in suitable packaging materials [60].

The earlier reports show the studies of ordinary conventional capacitors in which aqueous, organic or ionic liquids are used as electrolytes. Because of liquid electrolytes, the problems like leakage and electrochemical cycling stability arise. Leakage problem demands a need for proper packaging. It increases the cost of SC devices which limits the use of the device in portable electronics. Furthermore, due to liquid electrolytes, the size of SCs reduces up to a certain limit which restricts the use of such devices in smaller electronic parts. Liquid organic electrolytes are toxic and harmful to human beings. Additionally, aqueous electrolytes evaporate at higher

temperatures. Along with these devices, a new class of energy storage devices like FSS-SCs achieved greater attention due to their higher storage and cycling stability. Also, it has the advantages like small size, light weight, convenient, excellent reliability, high operating potential window and ability to withstand at high temperatures. For fabrication of FSS-SCs devices, flexible electrodes and solid polymer gel electrolytes are required, which can hold their properties even at bending or twisting.

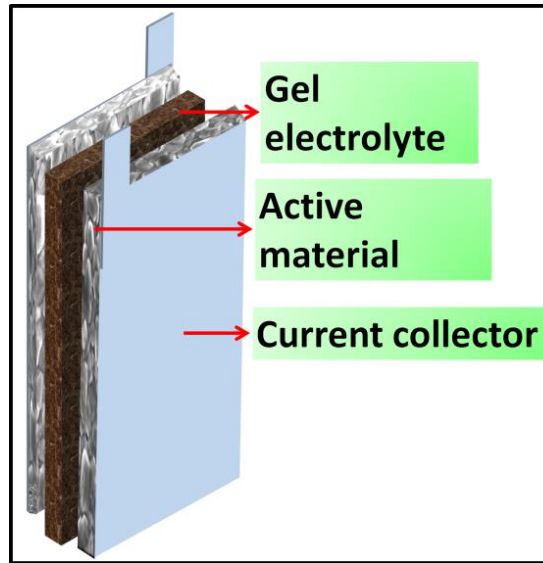


Figure 1.3: The schematic of FSS-SCs.

The FSS-SCs have same positive and negative electrodes sandwiched with polymer gel electrolyte [61]. The overall capacitance of SC device is calculated using the following equation.

$$1/C = 1/C_p + 1/C_n \quad (1.7)$$

where C is the overall capacitance of the device, C_p and C_n are the capacitances of anode and cathode, respectively. Table 1.1 shows the results obtained for symmetric FSS-SCs devices.

The relation between S_E , S_P , and operating voltage of SC states that values of S_E and S_P can be increased with increasing potential window and C_s . The increase in the potential window may cause a reduction in the cycling stability of the SCs due to irreversible chemical reactions that occur at the interface of the electrode and electrolyte. These reactions reduced active material and form a chemically inactive layer at the interface. Fabrication of the FSS-ASCs device is one of the best ways to

increase the working voltage of the SCs. To increase stability of the electrode materials well known way is to composite the pseudocapacitive electrode material with the EDLC material. The electrochemical characteristics of individual electrodes decide the performances of asymmetric FSS-SCs. Table 1.2 shows the results obtained for asymmetric FSS-SCs in previous reports.

Table 1.1: Previous results obtained from FSS–SSCs device.

Sr. No.	Configuration	Electrolyte	Specific capacitance	Energy density	Power density	Electrochemical stability (%) (cycles)	Ref.
1	Ni ₃ S ₂ @rGO//Ni ₃ S ₂ @rGO	PVA-KOH	865 F g ⁻¹	45.8 Wh kg ⁻¹	3700 W kg ⁻¹	92 (30000)	[62]
2	Carbon cloth//Carbon cloth	PVA-H ₂ SO ₄	-----	4.27 mWh cm ⁻³	1.32 W cm ⁻³	93 (5000)	[63]
3	rGO–PMo12//rGO–PMo12	PVA-H ₂ SO ₄	3.18 F cm ⁻³	1.07 mWh cm ⁻³	12 mW cm ⁻³	-----	[64]
4	CuCo ₂ S ₄ //CuCo ₂ S ₄	PVA-KOH	35.83 mF cm ⁻²	7.2 μWh cm ⁻²	599.9 μW cm ⁻²	50 (1500)	[65]
5	MnO ₂ -CNTs-G//MnO ₂ -CNTs-G	PVA-LiCl	31 mF cm ⁻²	3.1 μWh cm ⁻²	120 μW cm ⁻²	82 (10000)	[66]

Table 1.2: Previous results obtained from FSS–ASCs device.

Sr. No.	Configuration	Electrolyte	Specific capacitance	Energy density	Power density	Electrochemical stability (%) (cycles)	Ref.
1	NPG@MnO ₂ //CNT/carbon paper	PVA-LiCl	12 mF cm ⁻² at 0.3 mA cm ⁻²	5.4 μWh cm ⁻²	284 μW cm ⁻²	90 (2000)	[67]
2	CF@MnO ₂ //Fe ₃ O ₄	PVA-LiCl	16 mF cm ⁻² at 0.5 mA	9 μWh cm ⁻²	532.7 μW cm ⁻²	99 (2000)	[68]
3	Co ₃ O ₄ /NiCo ₂ O ₄ //N-rGO	PVA-KOH	251 mF cm ⁻²	75 Wh kg ⁻¹	3000 W kg ⁻¹	94 (10000)	[69]
4	FeCo ₂ O ₄ @polypyrrole//AC	PVA-KOH	194 F g ⁻¹ at 1 A g ⁻¹	68.8 Wh kg ⁻¹	800 W kg ⁻¹	91 (5000)	[70]
5	CuO//CuS	PVA-KOH	123 F g ⁻¹ at 5 mV s ⁻¹	22.8 Wh kg ⁻¹	2.5 W kg ⁻¹	96 (5000)	[71]
6	CoSe ₂ //MnO ₂	PVA-LiCl	1.77 F cm ⁻³ at 1 mA cm ⁻²	0.58 mWh cm ⁻³	0.282 W cm ⁻³	94.8 (2000)	[72]

1.4 Literature Survey

The transition metal sulfides and selenides have attracted great attention due to their excellent physical and electrical properties useful for applications in electronic, optical, and optoelectronic devices [73]. In recent years, nanostructured transition metal sulfides and selenides have been investigated as a new class of energy storage material. The common characteristic of sulfides and selenides is that their metal constituent can appear in two or more valence states [74]. Also, while modeling anodic oxidation reaction of covellite, it was established that the equivalent electrical circuit has to contain one relatively high capacitor. The literature survey of transition metal sulfides and selenides based electrode materials for energy storage is given in Table 1.3.

1.4.1 Copper sulfide

Metal chalcogenides thin films are studied for various applications such as electrochemical SCs, solar cells, electrophotocatalysis, etc., because of their structural, electrical, mechanical properties. Copper chalcogenides belong to I-VI compounds [75]. Copper(II) chalcogenides have general formula CuX where, $\text{X} = \text{O}, \text{S}, \text{Se}, \text{Te}$ and show hexagonal close-packed crystal structure. Though they are not studied very much for energy storage purposes, it is quite competitive material for SC application. Patil et al. [76] synthesized pure hexagonal CuS having porous nanoflower-like morphology which helped in higher electron transfer and shortens ion diffusion pathway. The electrode exhibited C_s of 1818.2 F g^{-1} at a scan rate of 5 mV s^{-1} with electrochemical stability of 92%. Naveed et al. [77] reported template free and facile microwave assisted synthesis of mesoporous copper sulfide nanosheets possessing C_s of 2535 F g^{-1} at a current density of 1 A g^{-1} in an aqueous 2 M KOH electrolyte. Zhao et al. [78] prepared copper sulfide (Cu_2S) microspheres by reducing copper sulfate with ascorbic acid in sodium thiosulfate solution at room temperature exhibited a maximum C_s of 444.2 F g^{-1} at the current density of 1 A g^{-1} . Marimuthu et al. [79] synthesized CuS thin films using hydrothermal method on FTO conductive glass substrate. The C_s of the flower-like morphological electrode was found to be 10.04 mF cm^{-2} . Durga et al. [80] prepared leaf-like nanostructure of copper sulfide using CBD method and found C_s of 1041.36 F g^{-1} at a current density of 4 A g^{-1} . Raj et al. [81] reported C_s of 72.85 F g^{-1} for CuS electrode prepared using CBD method.

Raj et al. [82] reported C_s of 4.9 mF cm^{-2} for CuS based planer SC device. Zhao et al. [83] reported preparation of rGO supported CuS nanoparticles using solvothermal reaction method possessing C_s of $946 \text{ F} \cdot \text{g}^{-1}$ at the scan rate of 10 mV s^{-1} . Kumar et al. [84] synthesized flower-like $\text{Cu}_{1.8}\text{S}$ nanostructures with a C_s of 1050.0 F g^{-1} . Li et al. [85] prepared an array of CuS nanoplatelets on graphene nanosheets with C_s of 497.8 F g^{-1} at a current density of 0.2 A g^{-1} .

1.4.2 Copper selenide

Copper selenide is the other possible copper chalcogenide compound that may be used as electrode material for SC with the support of rGO. Sandoval-Paz et al. [86] prepared copper (I) selenide thin film by using CBD method with the band gap of 2.0 eV . The electrical resistivity was of the order of $10^{-3} \Omega \text{ cm}$. Tan et al. [87] prepared CuSe@rGO/CNTs composites by using hydrothermal method; which exhibited high surface area and excellent conductivity. Pathan et al. [88] reported the preparation of CuSe thin film by SILAR method for solar cell application with a band gap of 2.35 eV and electrical resistivity of the order of $10^{-1} \Omega \text{ cm}$. Hankare et al. [89] synthesized CuSe thin film on glass substrates by CBD method having an electrical conductivity of the order of $10^{-3} \Omega \text{ cm}$. Zardkhoshoui et al. [90] used hydrothermal method for preparation of copper-cobalt selenide hollow spheres with C_s of 1775.4 F g^{-1} at a current density of 1 A g^{-1} . Moosavifard et al. [91] reported nanoporous copper-cobalt selenide hollow spheres prepared through a simple self template procedure exhibited specific capacity of 562 C g^{-1} at current density of 2 A g^{-1} . Pazhamalai et al. [92] prepared CuSe_2 nanoneedles on copper foil possessing C_s of 1037.5 F g^{-1} at a constant current density of 0.25 mA cm^{-2} . Deka et al. [93] synthesized Cu-Co nanowires on carbon fiber using hydrothermal method with C_s of 28.36 F g^{-1} . Zhang et al. [94] reported ternary alkali metal copper chalcogenide KCu_4Se_8 nanowires with C_s of 25.3 F g^{-1} at the scan rate of 5 mV s^{-1} . Wang et al. [95] prepared $\text{Ni}_{4.5}\text{Co}_{4.5}$ -selenide nanowires on carbon cloth exhibiting a specific capacity of 1333 C g^{-1} at a current density of 1.2 A g^{-1} .

Table 1.3: The literature survey of metal chalcogenide based supercapacitor.

Sr. No.	Material	Method of preparation	Surface morphology	Electrolyte	Potential Window	Specific capacitance/capacity	Electrochemical stability (%) (Cycles)	Ref.
1	Ni _{4.5} Co _{4.5} -selenide	Hydrothermal	Nanowires	6 M KOH	−0.1 to 0.6 V	1333 C g ^{−1}	120 (10000)	[95]
2	NiCo ₂ S ₄	Hydrothermal	Core-shell	3 M KOH	0 to 0.5 V	1098 F g ^{−1}	Not reported	[96]
3	NiCoS	Solvothermal	Nanosheets	2 M KOH	0 to 0.6 V	1653 F g ^{−1}	84 (3000)	[97]
4	NiFeS ₂	Solvothermal	Nanosheets	6 M KOH	0 to 0.5 V	1051 F g ^{−1}	90 (1000)	[98]
5	NiCo ₂ S ₄	Hydrothermal	Nanosheets	6 M KOH	0 to 0.45 V	1687 F g ^{−1}	Not reported	[99]
6	Nickel-zinc sulfide	Magnetron co-sputtering	Cone-shaped particles	2 M KOH	0.1 to 0.7 V	134 C g ^{−1}	90 (3500)	[100]
7	NiCoMn-S	Hydrothermal	Nanoparticles	6 M KOH	0 to 0.55 V	661 C g ^{−1}	86 (1000)	[101]
8	Nickel cobalt sulfide	Microwave-assisted	Nanosheets	3 M KOH	0 to 0.6 V	226 mAh g ^{−1}	Not reported	[102]
9	MoS ₂	Hydrothermal	Nanospheres	1 M LiCl	−0.8 to 0.8 V	368 F g ^{−1}	Not reported	[103]
10	MoNiCoS	Electrodeposition	Microspheres	2 M KOH	0 to 0.5 V	1472 F g ^{−1}	98 (5000)	[104]
11	Cu _{1.92} S	Chemical bath deposition	3D-hexagonal	2 M KOH	−1.0 to 0.8 V	1173 F g ^{−1}	99 (3000)	[105]
12	Co ₉ S ₈	Atomic layer deposition	Sheets	2 M KOH	−0.1 to 0.6 V	1645 F g ^{−1}	94 (2000)	[106]
13	Co ₉ S ₈	Self-sacrifice template strategy	Microplate	3 M KOH	0 to 0.6 V	1852 F g ^{−1}	86 (5000)	[107]
14	NiSe	Hydrothermal	Nanosheets	2 M KOH	0 to 0.6 V	1790 F g ^{−1}	70 (1000)	[108]
15	NiSe-CoSe	Solvothermal	Nanosphere	6 M KOH	0 to 0.55 V	584 C g ^{−1}	98 (1000)	[109]
16	NiSe@MoSe ₂	Hydrothermal	Nanosheets	2 M KOH	−0.1 to 0.65 V	223 F g ^{−1}	94 (1000)	[110]
17	(Ni _x Co _{1-x}) _{0.85} Se	Hydrothermal	Nanoparticles	6 M KOH	−1.0 to 0.4 V	172 F g ^{−1}	91 (2000)	[111]
18	Ni _{0.85} Se	Solvothermal	Nanoparticles	2 M KOH	0 to 0.8 V	115 mA h g ^{−1}	74 (5000)	[112]
19	Ni _{0.85} Se	Solvothermal	Nanoflower	2 M KOH	0 to 0.8 V	1010 F g ^{−1}	91 (1000)	[113]
20	(Ni _x Co _{1-x}) _{0.85} Se	Hydrothermal + cation exchange	Nanosheets	3 M KOH	0 to 0.5 V	431 mA h g ^{−1}	85 (3000)	[114]

21	(Ni, Co)Se ₂	Solvothermal	Microspheres	2 M KOH	−0.1 to 0.65 V	106 mAh g ^{−1}	85 (5000)	[115]
22	NiCoSe	Thermodynamic	Spear	3 M KOH	0 to 0.6 V	211 mAh g ^{−1}	90 (5000)	[116]
23	NiCo ₂ Se ₄ /rGO	Hydrothermal	Needle-like	6 M KOH	−1.0 to 0 V	1776 F g ^{−1}	86 (3000)	[117]
24	Ni ₃ Se ₂	Electrodeposition	Nanorods	1 M KOH	0 to 0.43 V	581.1 F g ^{−1}	90 (10000)	[118]
25	NiSe	Electrodeposition	Nanorods	1 M KOH	0 to 0.43 V	1645 F g ^{−1}	75 (10000)	[118]
26	Ni _{0.67} Co _{0.33} Se ₂	Hydrothermal	Nanosheets	6 M KOH	0 to 0.6 V	447 C g ^{−1}	97 (5000)	[119]
27	CoSe	Electrodeposition	Sheets	1 M KOH	0 to 0.4 V	510 F g ^{−1}	91 (5000)	[120]
28	Co _{0.85} Se	Microwave-assisted	Nanosheets	2 M KOH	0 to 0.6 V	1580 F g ^{−1}	Not reported	[121]
29	FeSe ₂	KCl-templated solvothermal technique	Flower	1 M LiPF ₆	−1.2 to −0.2 V	701 mAh g ^{−1}	99 (100)	[122]
30	MnSe	Solvothermal	Microflowers	1 M LiCl	0 to 1 V	1896 F g ^{−1}	99 (10000)	[123]
31	Zinc-cobalt selenide	Heat-treatment	Nanowires	3 M KOH	0 to 0.6 V	1419 C g ^{−1}	83 (5000)	[124]
32	Nickel sulfide/rGO	Hydrothermal	Nanosphere	2 M KOH	0.15 to 0.55 V	1169 F g ^{−1}	78 (1000)	[125]
33	NiS/graphene nanosheets (GNS)	dip and dry” and electrodeposition	Microfibers	6 M KOH	0 to 0.6 V	775 F g ^{−1}	88 (2000)	[126]
34	Ni ₃ S ₂ -rGO	Hydrothermal	Nanorods	6 M KOH	0 to −0.75 V	988 F g ^{−1}	98 (3000)	[127]
35	Co ₃ S ₄ -rGO	Hydrothermal	Nanosheets	6 M KOH	0 to 0.55 V	1369 F g ^{−1}	97 (3000)	[127]
36	NiS on N-doped graphene	Hydrothermal	Nanoflakes	6 M KOH	−0.5 to 0.4 V	1120 F g ^{−1}	82 (3000)	[128]
37	NiS ₂ @regenerative graphene oxide	Hydrothermal	Nanoflower	6 M KOH	0 to 0.4 V	1932 F g ^{−1}	83 (10000)	[129]
38	NiCo ₂ S ₄ @rGO	Solvothermal	Nanospheres	6 M KOH	0 to 0.45 V	2418 F g ^{−1}	Not reported	[130]
39	CoS@rGO	Ultrasound-assisted soaking	Nanosheets	2 M KOH	0 to 0.55 V	773 F g ^{−1}	90 (3000)	[131]
40	Cobalt sulfide/rGO	Hydrothermal	Nanoflowers	3 M KOH	0 to 0.6 V	697 F g ^{−1}	93 (20000)	[132]
41	NiSe ₂ /rGO	Solvothermal	Nanoparticles	2 M KOH	0 to 0.7 V	138 mAh g ^{−1}	81 (2500)	[133]

1.5 Purpose of the research

In the last few decades, a lot of efforts have been carried out to improve electrochemical performance and design of the SCs in such a way that can efficiently power up portable and flexible electronic devices. Equivalent series resistance (ESR) of SCs arises from electrode and electrolyte prevents from attaining higher possible power densities. Several methods have been adopted for reducing the ESR and are developing, such as the rough surface of the collector, and direct growth of electroactive material on the current collector. The overall performance of an efficient SC generally arises from a high surface area as well as fast and reversible redox reactions of active materials. Hence, to enhance the performance of SCs, new electrode material with more conductive nature, higher redox potential of cations, and large surface area with porous electrode is required. The extensive applications of SCs mainly depend on low cost as well as excellent electrochemical performance of the electrode material along with cycling life. To increase the performance of the SC, it is worth noting that the performance of the SCs depends on electrode material and electrolyte being used. Electrode stability and C_s mainly depend on the electrolyte used. Therefore, there are a lot of possibilities in the development of active material for SC and development of electrolyte.

There are three types of electrode materials classified according to the nature of charge storage mechanism they have in different electrolytes such as carbon based EDLC materials, conducting polymer, and transition metal compounds (collectively called pseudocapacitive materials) electrodes. Among all these, EDLCs and transition metal oxides are largely explored as an active electrode material, in which copper chalcogenides are the most studied material and have very promising potential towards addressing the issues in the area of SCs. The present work is focused on the fabrication of FSS-SCs device using the composite nanostructured CuS@rGO and Cu₂Se@rGO thin films as an active electrode material and polymer gel electrolyte as an electrolyte. The intention behind the fabrication of FSS-SCs device is to check the usefulness of active electrode material at a device level and also to assess the limitations of liquid electrolyte.

Nanostructured CuS@rGO and Cu₂Se@rGO thin films will be prepared by SILAR method, which can accomplish the electrochemical properties of SC

electrodes. This method is superior to control the different preparative parameters such as the concentration of reactants, number of deposition cycles, pH, and nature of the complexing agent, temperature, and time to get desired surface morphology and thickness. The SILAR is the simple and cheaper method to prepare the large area thin films on different supporting substrates with diverse nanostructures at the low reaction temperature. It gives the binder less and additive free thin films by improving the interfacial contact of active electrode material and supporting substrate. Further, the effects of different preparative parameters will be systematically studied to get well adherent and uniform thin films.

The characterization is an imperative stair in the exotic materials. The complete characterization of material includes phase analysis, structural elucidation, compositional, surface, and microstructural analysis, which defines the different properties of material. The X-ray diffraction (XRD) technique will be employed for the phase identification of the material. The surface morphology of film will be visualized by the field emission scanning electron microscopy (FE-SEM) technique. The Raman and Fourier transform infrared spectroscopy (FT-IR) spectroscopy of the samples will be carried out to investigate the chemical bonding and confirmation of phase formation. Oxidation states of constituent elements of material will be analyzed by X-ray photoelectron spectroscopy (XPS). Further, to examine the specific surface area and pore size distribution of the electrode material surface area analysis will be carried out using Brunauer-Emmett-Teller (BET) measurement.

The electrochemical features of CuS@rGO and Cu₂Se@rGO electrodes will be studied by cyclic voltammetry (CV), galvanostatic charge-discharge (GCD) measurement, and electrochemical impedance spectroscopy (EIS) on the electrochemical workstation. This will include CuS@rGO or Cu₂Se@rGO as a working electrode, SCE or Hg/HgO as reference electrode, and platinum sheet as a counter electrode. The performance of CuS@rGO and Cu₂Se@rGO thin films will be evaluated through different parameters such as C_s , electrochemical stability, and equivalent series resistance (R_s). In the next step, FSS-ASCs devices will be fabricated and the electrochemical performance of FSS-ASCs devices will be evaluated out in terms of C_s , S_E , S_P and electrochemical stability, and R_s . In addition to this, the effect of bending on the electrochemical performance of the solid state device will be studied to check the applicability in various portable electronic devices.

Lastly, the conclusions will be drawn based on electrochemical performance asymmetric FSS-SCs device in terms of C_s , operating potential window, S_E , S_P , and electrochemical stability of FSS-ASCs device.

References:

- [1] W. H. Low, P. S. Khiew, S. S. Lim, C. W. Siong, E. R. Ezeigwe, Recent development of mixed transition metal oxide and graphene/mixed transition metal oxide based hybrid nanostructures for advanced supercapacitors, *J. Alloys Compd.*, 775 (2019) 1324-1356, DOI: 10.1016/j.jallcom.2018.10.102.
- [2] S. J. Moura, J. B. Siegel, D. J. Siegel, H. K. Fathy, A. G. Stefanopoulou, IEEE Vehicle power and propulsion conference, 2010.
- [3] P. Pazhamalai, K. Krishnamoorthy, S. Sahoo, V. K. Mariappan, S. J. Kim, Copper tungsten sulfide anchored on Ni-foam as a high-performance binder free negative electrode for asymmetric supercapacitor, *Chem. Eng. J.*, 359 (2019) 409-418, DOI: 10.1016/j.cej.2018.11.153.
- [4] N. Bardi, T. Giannakopoulou, A. Vavouliotis, C. Trapalis, Electrodeposited films of graphene, carbon nanotubes, and their mixtures for supercapacitor applications, *ACS Appl. Nano Mater.*, 3 (2020) 10003-10013, DOI: 10.1021/acsanm.0c02002.
- [5] C. Wu, S. Yang, J. Cai, Q. Zhang, Y. Zhu, K. Zhang, Activated microporous carbon derived from almond shells for high energy density asymmetric supercapacitors, *ACS Appl. Mater. Interfaces*, 8 (2016) 15288-15296, DOI: 10.1021/acsami.6b02942.
- [6] J. Ren, W. Bai, G. Guan, Y. Zhang, H. Peng, Flexible and weaveable capacitor wire based on a carbon nanocomposite fiber, *Adv. Mater.*, 25 (2013) 5965-5970, DOI: 10.1002/adma.201302498.
- [7] <https://www.powerelectronics.com/technologies/alternative-energy/article/21864122>.
- [8] R. A. Rightmire, Electrical energy storage apparatus. U.S., Patent 3288641 (1966).
- [9] P. Simon, Y. Gogotsi, B. Dunn, Where do batteries end and supercapacitors begin? *Science*, 343 (2014) 1210-1211, DOI: 10.1126/science.1249625.
- [10] J. W. Long, D. Bélanger, T. Brousse, W. Sugimoto, M. B. Sassin, O. Crosnier, Asymmetric electrochemical capacitors-stretching the limits of aqueous electrolytes, *MRS Bull.*, 36 (2011) 513-522, DOI: 10.1557/mrs.2011.137.
- [11] F. Chen, H. Wang, S. Ji, V. Linkov, R. Wang, High-performance all-solid-state asymmetric supercapacitors based on sponge-like NiS/Ni₃S₂ hybrid nanosheets, *Mater. Today Energy* 11 (2019) 211-217, DOI: 10.1016/j.mtener.2018.12.002.

- [12] H. Pang, Y. Zhang, W. Y. Lai, Z. Hu, W. Huang, Lamellar $K_2CO_3(P_2O_7)_2 \cdot 2H_2O$ nanocrystal whiskers: High-performance flexible all-solid-state asymmetric micro-supercapacitors via inkjet printing, *Nano Energy*, 15 (2015) 303-312, DOI: 10.1016/j.nanoen.2015.04.034.
- [13] Y. Wang, Y. Song, Y. Xia, Electrochemical capacitors: mechanism, materials, systems, characterization and applications, *Chem. Soc. Rev.*, 45 (2016) 5925-5950, DOI: 10.1039/C5CS00580A.
- [14] M. Huang, F. Li, F. Dong, Y. X. Zhang, L. L. Zhang, MnO_2 -based nanostructures for high-performance supercapacitors, *J. Mater. Chem. A*, 3 (2015) 21380-21423, DOI: 10.1039/C5TA05523G.
- [15] U. M. Patil, R. R. Salunkhe, K. V. Gurav, C. D. Lokhande, Chemically deposited nanocrystalline NiO thin films for supercapacitor application, *Appl. Surf. Sci.*, 255 (2008) 2603-2607, DOI: 10.1016/j.apsusc.2008.07.192.
- [16] G. A. Snook, P. Kao, A. S. Best, Conducting polymer based supercapacitor devices and electrodes, *J. Power Sources*, 196 (2011) 1-12, DOI: 10.1016/j.jpowsour.2010.06.084.
- [17] T. Brousse, D. Bélanger, J. W. Long, To be or not to be pseudocapacitive? *J. Electrochem. Soc.*, 162 (2015) A5185-A5189, DOI: 10.1149/2.0201505jes.
- [18] X. Wang, Y. Liu, Y. Wang, L. Jiao, CuO quantum dots embedded in carbon nanofibers as binder-free anode for sodium ion batteries with enhanced properties, *Small*, 12 (2016) 4865-4872, DOI: 10.1002/sml.201601474.
- [19] Q. Ke, C. Guan, X. Zhang, M. Zheng, Y. W. Zhang, Y. Cai, H. Zhang, J. Wang, Surface-charge-mediated formation of $H-TiO_2@Ni(OH)_2$ heterostructures for high-performance supercapacitors, *Adv. Mater.*, 29 (2017) 1604164, DOI: 10.1002/adma.201604164.
- [20] P. Yu, Z. Zhang, L. Zheng, F. Teng, L. Hu, X. Fang, A novel sustainable flour derived hierarchical nitrogen-doped porous carbon/polyaniline electrode for advanced asymmetric supercapacitors, *Adv. Energy Mater.*, 6 (2016) 1601111, DOI: 10.1002/aenm.201601111.
- [21] J. Wei, Y. Li, D. Dai, F. Zhang, H. Zou, X. Yang, Y. Ji, B. Li, X. Wei, Surface roughness: A crucial factor to robust electric double layer capacitors, *ACS Appl. Mater. Interfaces*, 12 (2020) 5786-5792, DOI: 10.1021/acsami.9b18799.
- [22] K. S. Kumar, N. Choudhary, Y. Jung, J. Thomas, Recent advances in two-dimensional nanomaterials for supercapacitor electrode applications, *ACS Energy Lett.*, 3 (2018) 482-495, DOI: 10.1021/acsenergylett.7b01169.
- [23] A. M. Bryan, L. M. Santino, Y. Lu, S. Acharya, J. M. D'Arcy, Conducting polymers for pseudocapacitive energy storage, *Chem. Mater.*, 28 (2016) 5989-5998, DOI: 10.1021/acs.chemmater.6b01762.

-
- [24] B. Guan, Y. Li, B. Yin, K. Liu, D. Wang, H. Zhang, Synthesis of hierarchical NiS microflowers for high performance asymmetric supercapacitor, *Chem. Eng. J.*, 308 (2017) 1165-1173, DOI: 10.1016/j.cej.2016.10.016.
- [25] H. Peng, G. Ma, K. Sun, J. Mu, H. Wang, Z. Lei, High-performance supercapacitor based on multi-structural CuS@polypyrrole composites prepared by in situ oxidative polymerization, *J. Mater. Chem. A*, 2 (2014) 3303-3307, DOI: 10.1039/C3TA13859C.
- [26] K. Wang, C. Zhao, Z. Zhang, S. Min, X. Qian, A facile one-step route to synthesize the three-layer nanostructure of CuS/RGO/Ni₃S₂ and its high electrochemical performance, *RSC Adv.*, 6 (2016) 16963-16971, DOI: 10.1039/C5RA26428F.
- [27] T. Zhu, B. Xia, L. Zhou, X. W. Lou, Arrays of ultrafine CuS nanoneedles supported on a CNT backbone for application in supercapacitors, *J. Mater. Chem.*, 22 (2012) 7851-7855, DOI: 10.1039/c2jm30437f.
- [28] R. N. Bulakhe, S. Sahoo, T. T. Nguyen, C. D. Lokhande, C. Roh, Y. R. Lee, J. Shim, Chemical synthesis of 3D copper sulfide with different morphologies for high performance supercapacitors application, *RSC Adv.*, 6 (2016) 14844-14851, DOI: 10.1039/C5RA25568F.
- [29] C. Shi, H. Dong, R. Zhua, H. Lia, Y. Sun, D. Xu, Q. Zhao, D. Yu, An “all-in-one” mesh-typed integrated energy unit for both photoelectric conversion and energy storage in uniform electrochemical system, *Nano Energy*, 13 (2015) 670-678, DOI: 10.1016/j.nanoen.2015.03.032.
- [30] Y. K. Hsu, Y. C. Chen, Y. G. Lin, Synthesis of copper sulfide nanowire arrays for high-performance supercapacitors, *Electrochim. Acta*, 139 (2014) 401-407, DOI: 10.1016/j.electacta.2014.06.138.
- [31] K. J. Huang, J. Z. Zhang, Y. Fan, One-step solvothermal synthesis of different morphologies CuS nanosheets compared as supercapacitor electrode materials, *J. Alloys Compd.*, 625 (2015) 158-163, DOI: 10.1016/j.jallcom.2014.11.137.
- [32] J. Zhang, H. Feng, J. Yang, Q. Qin, H. Fan, C. Wei, W. Zheng, Solvothermal synthesis of three-dimensional hierarchical CuS microspheres from a Cu-based ionic liquid precursor for high-performance asymmetric supercapacitors, *ACS Appl. Mater. Interfaces*, 7 (2015) 21735-21744, DOI: 10.1021/acsami.5b04452.
- [33] L. Qian, X. Tian, L. Yang, J. Mao, H. Yuan, D. Xiao, High specific capacitance of CuS nanotubes in redox active polysulfide electrolyte, *RSC Adv.*, 3 (2013) 1703-1708, DOI: 10.1039/C2RA22257D.
- [34] H. Chen, J. Li, C. Long, T. Wei, G. Ning, J. Yan, Z. Fan, Nickel sulfide/graphene/carbon nanotube composites as electrode material for the supercapacitor application in the sea flashing signal system, *J. Mar. Sci. Appl.*, 13 (2014) 462-466, DOI: 10.1007/s11804-014-1279-1.
- [35] C. Peng, D. Hua, G. Z. Chen, Theoretical specific capacitance based on charge storage mechanisms of conducting polymers: Comment on ‘Vertically oriented
-

- arrays of polyaniline nanorods and their super electrochemical properties', *Chem. Commun.*, 47 (2011) 4105-4107, DOI: 10.1039/C1CC10675A.
- [36] D. P. Dubal, S. H. Lee, J. G. Kim, W. B. Kim, C. D. Lokhande, Porous polypyrrole clusters prepared by electropolymerization for a high performance supercapacitor, *J. Mater. Chem.*, 22 (2012) 3044-3052, DOI: 10.1039/C2JM14470K.
- [37] H. Zhou, G. Han, One-step fabrication of heterogeneous conducting polymers-coated graphene oxide/carbon nanotubes composite films for high-performance supercapacitors, *Electrochimica Acta*, 192 (2016) 448-455, DOI: 10.1016/j.electacta.2016.02.015.
- [38] R. B. Ambade, S. B. Ambade, N. K. Shrestha, Y. Nah, S. H. Han, W. Lee, S. H. Lee, Polythiophene infiltrated TiO₂ nanotubes as high-performance supercapacitor electrodes, *Chem. Commun.*, 49 (2013) 2308-2310, DOI: 10.1039/c3cc00065f.
- [39] D. P. Dubal, S. Abdel-Azeim, N. R. Chodankar, Y. Han, Molybdenum nitride nanocrystals anchored on phosphorus-incorporated carbon fabric as a negative electrode for high-performance asymmetric pseudocapacitor, *iScience*, 16 (2019) 50-62, DOI: 10.1016/j.isci.2019.05.018.
- [40] Q. Wang, Y. Zhang, H. Jiang, X. Li, Y. Cheng, C. Meng, Designed mesoporous hollow sphere architecture metal (Mn, Co, Ni) silicate: a potential electrode material for flexible all solid-state asymmetric supercapacitor, *Chem. Eng. J.* 362 (2019) 818-829, DOI: 10.1016/j.cej.2019.01.102.
- [41] R. B. Rakhi, B. Ahmed, D. Anjum, H. N. Alshareef, Direct chemical synthesis of MnO₂ nanowhiskers on transition-metal carbide surfaces for supercapacitor applications, *ACS Appl. Mater. Interfaces*, 8 (2016) 18806-18814, DOI: 10.1021/acsami.6b04481.
- [42] S. J. Marje, P. K. Katkar, S. S. Pujari, S. A. Khalate, P. R. Deshmukh, U. M. Patil, Effect of phosphate (anion) precursor on structural and morphology behavior of nickel phosphate thin films and its supercapacitive performance, *Mater. Sci. Eng., B*, 261 (2020) 114641, DOI: 10.1016/j.mseb.2020.114641.
- [43] V. Lokhande, S. J. Lee, A. Lokhande, J. H. Kim, T. Ji, 1.5 V symmetric supercapacitor device based on hydrothermally synthesized carbon nanotubes and cobalt tungstate nanocomposite electrodes, *Mater. Chem. Phys.*, 211 (2018) 214-224, DOI: 10.1016/j.matchemphys.2018.02.039.
- [44] J. Gai, F. Ma, Z. Zhang, D. Sun, Y. Jin, Y. Guo, W. Kim, Flexible organic-inorganic composite solid electrolyte with asymmetric structure for room temperature solid-state Li-ion batteries, *ACS Sustainable Chem. Eng.*, 7 (2019) 15896-15903, DOI: 10.1021/acssuschemeng.9b01869.
- [45] W. Luo, Y. Gong, Y. Zhu, K. K. Fu, J. Dai, S. D. Lacey, C. Wang, B. Liu, X. Han, Y. Mo, E. D. Wachsman, L. Hu, Transition from superlithiophobicity to

- superlithiophilicity of garnet solid-state electrolyte, *J. Am. Chem. Soc.*, 138 (2016) 12258-12262, DOI: 10.1021/jacs.6b06777.
- [46] C. Zhong, Y. Deng, W. Hu, J. Qiao, L. Zhangd, J. Zhang, A review of electrolyte materials and compositions for electrochemical supercapacitors, *Chem. Soc. Rev.*, 44 (2015) 7484-7539, DOI: 10.1039/C5CS00303B.
- [47] Y. Zheng, Y. Yao, J. Ou, M. Li, D. Luo, H. Dou, Z. Li, K. Amine, A. Yu, Z. Chen, A review of composite solid-state electrolytes for lithium batteries: fundamentals, key materials and advanced structures, *Chem. Soc. Rev.*, *Chem. Soc. Rev.*, 49 (2020) 8790-8839, DOI: 10.1039/d0cs00305k.
- [48] K. Fu, Y. Gong, B. Liu, Y. Zhu, S. Xu, Y. Yao, W. Luo, C. Wang, S. D. Lacey, J. Dai, Y. Chen, Y. Mo, E. Wachsman, L. Hu, Toward garnet electrolyte-based Li metal batteries: An ultrathin, highly effective, artificial solid-state electrolyte/metallic Li interface, *Sci. Adv.*, 3 (2017) e1601659, DOI: 10.1126/sciadv.1601659.
- [49] D. E. Fenton, J. M. Parker, P. V. Wright, Complexes of alkali metal ions with poly(ethylene oxide), *Polymer*, 14 (1973) 589, DOI: 10.1016/0032-3861(73)90146-8.
- [50] S. S. Sekhon, Conductivity behaviour of polymer gel electrolytes: Role of polymer, *Bull. Mater. Sci.*, 26 (2003) 321-328, DOI: 10.1007/BF02707454.
- [51] C. M. Yang, H. S. Kim, B. K. Na, K. S. Kum, B. W. Cho, Gel type polymer electrolytes with different types of ceramic fillers and lithium salts for lithium-ion polymer batteries, *J. Power Sources*, 156 (2006) 574-580, DOI: 10.1016/j.jpowsour.2005.06.018.
- [52] C. W. Liew, S. Ramesh, A. K. Arof, Good prospect of ionic liquid based-poly(vinyl alcohol) polymer electrolytes for supercapacitors with excellent electrical, electrochemical and thermal properties, *Int. J. Hydrogen Energ.*, 39 (2014) 2953-2963, DOI: 10.1016/j.ijhydene.2013.06.061.
- [53] R. C. Agrawal and G. P. Pandey, Solid polymer electrolytes: materials designing and all-solid-state battery applications: an overview, *J. Phys. D: Appl. Phys.*, 41 (2008) 223001, DOI: 10.1088/0022-3727/41/22/223001.
- [54] G. P. Pandey, A. C. Rastogi, C. R. Westgate, All-solid-state supercapacitors with poly(3,4-ethylenedioxythiophene)-coated carbon fiber paper electrodes and ionic liquid gel polymer electrolyte, *J. Power Sources*, 245 (2014) 857-865, DOI: 10.1016/j.jpowsour.2013.07.017.
- [55] P. Sivaraman, A. Thakur, R. K. Kushwaha, D. Ratna, A. B. Samui, Poly(3-methyl thiophene)-activated carbon hybrid supercapacitor based on gel polymer electrolyte, *Electrochem. Solid State Lett.*, 9 (2006) A435, DOI: 10.1149/1.2213357.
- [56] Y. S. Lee, S. H. Ju, J. H. Kim, S. S. Hwang, J. M. Choi, Y. K. Sun, H. Kim, B. Scrosati, D. W. Kim, Composite gel polymer electrolytes containing core-shell

- p>structured SiO
- ₂
- (Li
- ⁺
-) particles for lithium-ion polymer batteries,
- Electrochim. Comm.*
- , 17 (2012) 18-21, DOI: 10.1016/j.elecom.2012.01.008.
- [57] C. Meng, C. Liu, L. Chen, C. Hu, S. Fan, Highly flexible and all-solid-state paperlike polymer supercapacitors, *Nano Lett.*, 10 (2010) 4025-4031, DOI: 10.1021/nl1019672.
- [58] S. K. Tripathi, A. Kumar, S. A. Hashmi, Electrochemical redox supercapacitors using PVdF-HFP based gel electrolytes and polypyrrole as conducting polymer electrode, *Solid State Ionics*, 177 (2006) 2979-2985, DOI: 10.1016/j.ssi.2006.03.059.
- [59] S. Chandra, S. S. Sekhon, N. Arora, PMMA based protonic polymer gel electrolytes, *Ionics*, 6 (2000) 112-118, DOI: 10.1007/BF02375554.
- [60] N. R. Chodankar, D. P. Dubal, G. S. Gund, C. D. Lokhande, Bendable all-solid-state asymmetric supercapacitors based on MnO₂ and Fe₂O₃ thin films, *Energy Technol.*, 3 (2015) 625-631, DOI: 10.1002/ente.201402213.
- [61] N. R. Chodankar, H. D. Pham, A. K. Nanjundan, J. F. S. Fernando, K. Jayaramulu, D. Golberg, Y. Han, D. P. Dubal, True meaning of pseudocapacitors and their performance metrics: asymmetric versus hybrid supercapacitors, *small*, 16 (2020) 2002806, DOI: 10.1002/sml.202002806.
- [62] C. Zhang, Y. Huang, S. Tang, M. Deng, Y. Du, High-energy all-solid-state symmetric supercapacitor based on Ni₃S₂ mesoporous nanosheet-decorated three-dimensional reduced graphene oxide, *ACS Energy Lett.*, 2 (2017) 759-768, DOI: 10.1021/acsenergylett.7b00078.
- [63] Z. Miao, Y. Huang, J. Xin, X. Su, Y. Sang, H. Liu, J. Wang, High-performance symmetric supercapacitor constructed using carbon cloth boosted by engineering oxygen-containing functional groups, *ACS Appl. Mater. Interfaces*, 11 (2019) 18044-18050, DOI: 10.1021/acsami.9b04426.
- [64] D. P. Dubal, J. Suarez-Guevara, D. Tonti, E. Enciso, P. Gomez-Romero, A high voltage solid state symmetric supercapacitor based on graphene–polyoxometalate hybrid electrodes with a hydroquinone doped hybrid gel-electrolyte, *J. Mater. Chem. A*, 3 (2015) 23483-23492, DOI: 10.1039/C5TA05660H.
- [65] J. Qi, X. Liu, Y. Sui, Y. He, Y. Ren, Q. Meng, F. Wei, X. Zhang, High performance fiber-shaped all-solid-state symmetric supercapacitor based on mesoporous CuCo₂S₄ nanosheets, *J. Mater. Sci.: Mater. Electron.*, 30 (2019) 667-676, DOI: 10.1007/s10854-018-0335-z.
- [66] Q. Kang, J. Zhao, X. Li, G. Zhu, X. Feng, Y. Ma, W. Huang, J. Liu, A single wire as all-inclusive fully functional supercapacitor, *Nano Energy*, 32 (2017) 201-208, DOI: 10.1016/j.nanoen.2016.12.020.
- [67] H. Xu, X. Hu, Y. Sun, H. Yang, X. Liu, Y. Huang, Flexible fiber-shaped supercapacitors based on hierarchically nanostructured composite electrodes, *Nano Res.*, 8 (2015) 1148-1158, DOI: 10.1007/s12274-014-0595-8.

-
- [68] G. H. Li, R. C. Li, W. J. Zhou, A wire shaped supercapacitor in micrometer size based on Fe_3O_4 nanosheet arrays on Fe wire, *Nano-Micro Lett.*, 9 (2017) 46, DOI: 10.1007/s40820-017-0147-3.
- [69] M. K. Paliwal, S. K. Meher, $\text{Co}_3\text{O}_4/\text{NiCo}_2\text{O}_4$ perforated nanosheets for high-energy-density all-solid-state asymmetric supercapacitors with extended cyclic stability, *ACS Appl. Nano Mater.*, 3 (2020) 4241-4252, DOI: 10.1021/acsanm.0c00419.
- [70] X. He, Y. Zhao, R. Chen, H. Zhang, J. Liu, Q. Liu, D. Song, R. Li, J. Wang, Hierarchical FeCo_2O_4 @polypyrrole core/shell nanowires on carbon cloth for high-performance flexible all-solid-state asymmetric supercapacitors, *ACS Sustain. Chem. Eng.*, 6, (2018) 14945-14954, DOI: 10.1021/acssuschemeng.8b03440.
- [71] A. M. Patil, V. C. Lokhande, T. Ji, C. D. Lokhande, New design of all-solid state asymmetric flexible supercapacitor with high energy storage and long term cycling stability using m-CuO/FSS and h-CuS/FSS electrodes, *Electrochim. Acta*, 307 (2019) 30-42, DOI: 10.1016/j.electacta.2019.03.108.
- [72] N. Yu, M. Zhu, D. Chen, Flexible all-solid-state asymmetric supercapacitors with three-dimensional CoSe_2 /carbon cloth electrodes, *J. Mater. Chem. A*, 3 (2015) 7910-7918, DOI: 10.1039/C5TA00725A.
- [73] S. Shen, Q. Wang, Rational tuning the optical properties of metal sulfide nanocrystals and their applications, *Chem. Mater.*, 25 (2013) 1166-1178, DOI: 10.1021/cm302482d.
- [74] R. Barik, P. P. Ingole, Challenges and prospects of metal sulfide materials for supercapacitors, *Curr. Opin. Electrochem.*, 21 (2020) 327-334, DOI: 10.1016/j.coelec.2020.03.022.
- [75] H. M. Pathan, C. D. Lokhande, Deposition of metal chalcogenide thin films by successive ionic layer adsorption and reaction (SILAR) method, *Bull. Mater. Sci.*, 27 (2004) 85-111, DOI: 10.1007/BF02708491.
- [76] A. M. Patil, A. C. Lokhande, N. R. Chodankar, P. A. Shinde, J. H. Kim, C. D. Lokhande, Interior design engineering of CuS architecture alteration with rise in reaction bath temperature for high performance symmetric flexible solid state supercapacitor, *J. ind. eng. chem.*, 46 (2017) 91-102, DOI: 10.1016/j.jiec.2016.10.019.
- [77] M. Naveed, W. Younas, Y. Zhu, S. Rafai, Q. Zhao, M. Tahir, N. Mushtaq, C. Cao, Template free and facile microwave-assisted synthesis method to prepare mesoporous copper sulfide nanosheets for high-performance hybrid supercapacitor, *Electrochim Acta*, 319 (2019) 49-60, DOI: 10.1016/j.electacta.2019.06.169.
- [78] T. Zhao, X. Peng, X. Zhao, J. Hu, W. Yang, T. Li, I. Ahmad, Facile preparation and high capacitance performance of copper sulfide microspheres as
-

- supercapacitor electrode material, *Composites Part B*, 163 (2019) 26-35, DOI: 10.1016/j.compositesb.2018.11.023.
- [79] T. Marimuthu, N. Anandhan, R. Panneerselvam, K. P. Ganesan, A. A. Roselin, Synthesis and characterization of copper sulfide thin films for quantum dot sensitized solar cell and supercapacitor applications, *Nano-Struct. Nano-Objects*, 17 (2019) 138-147, DOI: 10.1016/j.nanoso.2018.12.004.
- [80] I. K. Durga, S. S. Rao, A. E. Reddy, C. V. V. M. Gopi, H. Kim, Achieving copper sulfide leaf like nanostructure electrode for high performance supercapacitor and quantum-dot sensitized solar cells, *Appl. Surf. Sci.*, 435 (2018) 666-675, DOI: 10.1016/j.apsusc.2017.11.171.
- [81] C. Raj, B. Kim, W. Cho, W. Lee, Y. Seo, K. Yu, Electrochemical capacitor behavior of copper sulfide (CuS) nanoplatelets, *J. Alloys Compd.*, 586 (2014) 191-196, DOI: 10.1016/j.jallcom.2013.10.056.
- [82] C. J. Raj, M. Rajesh, R. Manikandan, W. Lee, K. Yu, B. C. Kim, Direct fabrication of two-dimensional copper sulfide nanoplates on transparent conducting glass for planar supercapacitor, *J. Alloys Compd.*, 735 (2018) 2378-2383, DOI: 10.1016/j.jallcom.2017.12.031.
- [83] T. Zhao, W. Yang, X. Zhao, X. Peng, J. Hu, C. Tang, T. Li, Facile preparation of reduced graphene oxide/copper sulfide composite as electrode materials for supercapacitors with high energy density, *Composites, Part B*, 150 (2018) 60-67, DOI: 10.1016/j.compositesb.2018.05.058.
- [84] D. R. Kumar, S. Kesavan, M. L. Baynosa, J. J. Shim, Flower-like Cu_{1.8}S nanostructures for high-performance flexible solid-state supercapacitors, *Appl. Surf. Sci.*, 448 (2018) 547-558, DOI: 10.1016/j.apsusc.2018.03.247.
- [85] X. Li, K. Zhou, J. Zhou, J. Shen, M. Ye, CuS nanoplatelets arrays grown on graphene nanosheets as advanced electrode materials for supercapacitor applications, *J. Mater. Sci. Technol.*, 34 (2018) 2342-2349, DOI: 10.1016/j.jmst.2018.06.013.
- [86] M. G. Sandoval-Paz, C. A. Rodríguez, P. F. Porcile-Saavedra, C. Trejo-Cruz, Study of the crystallographic phase change on copper (I) selenide thin films prepared through chemical bath deposition by varying the pH of the solution, *J. Solid State Chem.*, 239 (2016) 106-112, DOI: 10.1016/j.jssc.2016.04.026.
- [87] L. Tan, N. Li, S. Chen, Z. Q. Liu, Self-assembly synthesis of CuSe@graphene-carbon nanotubes as efficient and robust oxygen reduction electrocatalysts for microbial fuel cells, *J. Mater. Chem. A*, 4 (2016) 12273-12280, DOI: 10.1039/C6TA02891H.
- [88] H. M. Pathan, C. D. Lokhande, D. P. Amalnerkar, T. Seth, Modified chemical deposition and physico-chemical properties of copper(I) selenide thin films, *Appl. Surf. Sci.*, 211 (2003) 48-56, DOI: 10.1016/S0169-4332(03)00046-1.
- [89] P. P. Hankare, A. S. Khomane, P. A. Chate, K. C. Rathod, K. M. Garadkar, Preparation of copper selenide thin films by simple chemical route at low

- temperature and their characterization, *J. Alloys Compd.*, 469 (2009) 478-482, DOI: 10.1016/j.jallcom.2008.02.062.
- [90] A. M. Zardkhoshoui, S. S. H. Davarani, Construction of complex copper-cobalt selenide hollow structures as an attractive battery-type electrode material for hybrid supercapacitors, *Chem. Eng. J.*, 402 (2020) 126241, DOI: 10.1016/j.cej.2020.126241.
- [91] S. E. Moosavifard, F. Saleki, A. Mohammadi, A. Hafizi, M. R. Rahimpour, Construction of hierarchical nanoporous bimetallic copper-cobalt selenide hollow spheres for hybrid supercapacitor, *J. Electroanal. Chem.*, 871 (2020) 114295, DOI: 10.1016/j.jelechem.2020.114295.
- [92] P. Pazhamalai, K. Krishnamoorthy, S. J. Kim, Hierarchical copper selenide nanoneedles grown on copper foil as a binder free electrode for supercapacitors, *Int. J. Hydrogen Energy*, 41 (2016) 14830-14835, DOI: 10.1016/j.ijhydene.2016.05.157.
- [93] B. K. Deka, A. Hazarika, J. Kim, N. Kim, H. E. Jeong, Y. Park, H. W. Park, Bimetallic copper cobalt selenide nanowire-anchored woven carbon fiber-based structural supercapacitors, *Chem. Eng. J.*, 355 (2019) 551-559, DOI: 10.1016/j.cej.2018.08.172.
- [94] K. Zhang, H. chen, X. Wang, D. Guo, C. Hu, S. Wang, J. Sun, Q. Leng, Synthesis and structure determination of potassium copper selenide nanowires and solid-state supercapacitor application, *J Power Sources*, 268 (2014) 522-532, DOI: 10.1016/j.jpowsour.2014.06.079.
- [95] C. Wang, Z. Song, H. Wan, X. Chen, Q. Tan, Y. Gan, P. Liang, J. Zhang, H. Wang, Y. Wang, X. Peng, P. A. van Aken, H. Wang, Ni-Co selenide nanowires supported on conductive wearable textile as cathode for flexible battery-supercapacitor hybrid devices, *Chem. Eng. J.*, 400 (2020) 125955, DOI: 10.1016/j.cej.2020.125955.
- [96] Y. Liu, G. Jiang, Z. Huang, Q. Lu, B. Yu, U. Evariste, M. Pian Pian, Decoration of hollow mesoporous carbon spheres by NiCo_2S_4 nanoparticles as electrode materials for asymmetric supercapacitors, *ACS Appl. Energy Mater.*, 2 (2019) 8079-8089, DOI: 10.1021/acsaem.9b01569.
- [97] T. Liu, J. Liu, L. Zhang, B. Cheng, J. Yu, Construction of nickel cobalt sulfide nanosheet arrays on carbon cloth for performance-enhanced supercapacitor, *J. Mater. Sci. Technol.*, 47 (2020) 113-121, DOI: 10.1016/j.jmst.2019.12.027.
- [98] A. Ansari, R. A. Badhe, S. S. Garje, One pot synthesis of bimetallic transition metal sulfide NiFeS_2 nanocomposite and its use as a high performance supercapacitor material, *Mater. Lett.*, 281 (2020) 128636, DOI: 10.1016/j.matlet.2020.128636.
- [99] X. Hong, J. Li, G. Zhu, H. Xu, X. Zhang, Y. Zhaoa, J. Zhang, D. Yana, A. Yu, Cobalt–nickel sulfide nanosheets modified by nitrogen-doped porous reduced

- graphene oxide as high-conductivity cathode materials for supercapacitor, *Electrochim. Acta*, 362 (2020) 137156, DOI: 10.1016/j.electacta.2020.137156.
- [100] G. S. Kaliaraj, A. Ramadoss, Nickel–zinc sulfide nanocomposite thin film as an efficient cathode material for high-performance hybrid supercapacitors, *Mater. Sci. Semicond. Process.*, 105 (2020) 104709, DOI: 10.1016/j.mssp.2019.104709.
- [101] J. Cao, Y. Hu, Y. Zhu, H. Cao, M. Fan, C. Huang, K. Shu, M. He, H. C. Chen, Synthesis of mesoporous nickel-cobalt-manganese sulfides as electroactive materials for hybrid supercapacitors, *Chem. Eng. J.*, 405 (2021) 126928, DOI: 10.1016/j.cej.2020.126928.
- [102] F. Zhao, D. Xie, X. Song, H. Wu, Q. Zhang, J. Zou, X. Zeng, Construction of hydrangea-like nickel cobalt sulfide through efficient microwave-assisted approach for remarkable supercapacitors, *Appl. Surf. Sci.*, 539 (2021) 148260, DOI: 10.1016/j.apsusc.2020.148260.
- [103] M. S. Javed, S. Dai., M. Wang, D. Guo, L. Chen, X. Wang, C. Hu, Y. Xi., High performance solid state flexible supercapacitor based on molybdenum sulfide hierarchical nanospheres, *J. Power sources*, 285 (2015) 63-69, DOI: 10.1016/j.jpowsour.2015.03.079.
- [104] U. Evariste, G. Jianga, B. Yu, Y. Liu, P. Ma, One-step electrodeposition of molybdenum nickel cobalt sulfides on ni foam for high-performance asymmetric supercapacitors, *J. energy storage*, 29 (2020) 101419, DOI: 10.1016/j.est.2020.101419.
- [105] S. Shaikh, M. K. Rabinal, Rapid ambient growth of copper sulfide microstructures: Binder free electrodes for supercapacitor, *J. energy storage*, 28 (2020) 101288, DOI: 10.1016/j.est.2020.101288.
- [106] H. Li, Y. Gao, Y. Shao, Y. Su, X. Wang, Vapor-phase atomic layer deposition of Co_9S_8 and its application for supercapacitors, *Nano Lett.*, 15 (2015) 6689-6695, DOI: 10.1021/acs.nanolett.5b02508.
- [107] J. Li, Q. Li, J. Sun, Y. Ling, K. Tao, L. Han, Controlled preparation of hollow and porous Co_9S_8 microplate arrays for high-performance hybrid supercapacitors, *Inorg. Chem.*, 59 (2020) 11174-11183, DOI: 10.1021/acs.inorgchem.0c01768.
- [108] C. Tang, Z. Pu, Q. Liu, A. M. Asiri, X. Sun, Y. Luo, Y. He, In situ growth of NiSe nanowire film on nickel foam as an electrode for high-performance supercapacitors, *ChemElectroChem*, 2 (2015) 1903-1907, DOI: 10.1002/celec.201500285.
- [109] H. Chen, M. Fan, C. Li, G. Tian, C. Lv, D. Chen, K. Shu, J. Jiang, One-pot synthesis of hollow NiSe-CoSe nanoparticles with improved performance for hybrid supercapacitors, *J. Power Sources*, 329 (2016) 314-322, DOI: 10.1016/j.jpowsour.2016.08.097.

-
- [110] H. Peng, J. Zhou, K. Sun, G. Ma, Z. Zhang, E. Feng, Z. Lei, High-performance asymmetric supercapacitor designed with a Novel NiSe@MoSe₂ nanosheet array and nitrogen-doped carbon nanosheet, *ACS Sustainable Chem. Eng.*, 5 (2017) 5951-5963, DOI: 10.1021/acssuschemeng.7b00729.
- [111] L. Wu, L. Shen, T. Wang, X. Xu, Y. Sun, Y. Wang, Y. Zhao, Y. Du, W. Zhong, Component-controllable bimetallic nickel cobalt selenides (Ni_xCo_{1-x})_{0.85}Se for high performance supercapacitors, *J. Alloys Compd.*, 766 (2018) 527-535, DOI: 10.1016/j.jallcom.2018.06.353.
- [112] S. Wu, Q. Hu, L. Wu, J. Li, H. Peng, Q. Yang, One-step solvothermal synthesis of nickel selenide nanoparticles as the electrode for high-performance supercapacitors, *J. Alloys Compd.*, 784 (2019) 347-353, DOI: 10.1016/j.jallcom.2019.01.026.
- [113] Q. Yang, X. Chen, H. Zhan, S. Wu, Q. Hub, R. Zhou, Y. Xue, Mixing solvothermal synthesis of surfactant free nanoflower-sphere-like nickel selenide for supercapacitor application, *Synth. Met.*, 257 (2019) 116167, DOI: 10.1016/j.synthmet.2019.116167.
- [114] L. Du, W. Du, Y. Zhao, N. Wang, Z. Yao, S. Wei, Y. Shi, B. Zhang, Ternary nickel-cobalt selenide nanosheet arrays with enhanced electrochemical performance for hybrid supercapacitors, *J. Alloys Compd.*, 778 (2019) 848-857, DOI: 10.1016/j.jallcom.2018.11.105.
- [115] H. Lei, J. Zhou, R. Zhao, H. Peng, Y. Xu, F. Wang, H. A. Hamouda, W. Zhang, G. Ma, Design and assembly of a novel asymmetric supercapacitor based on all-metal selenides electrodes, *Electrochim. Acta*, 363 (2020) 137206, DOI: 10.1016/j.electacta.2020.137206.
- [116] H. Liu, H. Guo, N. Wu, W. Yao, R. Xue, M. Wang, W. Yang, Rational design of nickel-cobalt selenides derived from multivariate bimetal metal-organic frameworks for high-performance asymmetric supercapacitor, *J. Alloys Compd.*, 856 (2020) 156535, DOI: 10.1016/j.jallcom.2020.156535.
- [117] S. Ghosh, P. Samanta, N. C. Murmu, T. Kuila, Investigation of electrochemical charge storage in nickel-cobalt-selenide/reduced graphene oxide composite electrode and its hybrid supercapacitor device, *J. Alloys Compd.*, 835 (2020) 155432, DOI: 10.1016/j.jallcom.2020.155432.
- [118] H. Li, J. Gong, J. Li, X. Zhang, C. Tanga, H. Yao, Q. Ding, Synthesis of nickel selenide thin films for high performance all-solid-state asymmetric supercapacitors, *Chin. Chem. Lett.*, 31 (2020) 2275-2279, DOI: 10.1016/j.ccllet.2020.03.010.
- [119] Y. Hu, C. Huang, S. Jiang, Y. Qin, H. C. Chen, Hierarchical nickel-cobalt selenide nanoparticles/nanosheets as advanced electroactive battery materials for hybrid supercapacitors, *J. Colloid Interface Sci.*, 558 (2020) 291-300, DOI: 10.1016/j.jcis.2019.09.115.
-

- [120] X. Zhang, J. Gong, K. Zhang, W. Zhu, J. Li, Q. Ding, All-solid-state asymmetric supercapacitor based on porous cobalt selenide thin films, *J. Alloys Compd.*, 772 (2019) 25-32, DOI: 10.1016/j.jallcom.2018.09.023.
- [121] W. Younas, M. Naveed, C. Cao, S. Khalid, S. Rafai, Z. Wang, Y. Wu, L. Yang, Rapid and simplistic microwave assisted method to synthesize cobalt selenide nanosheets; a prospective material for high performance hybrid supercapacitor, *Appl. Surf. Sci.*, 505 (2020) 144618, DOI: 10.1016/j.apsusc.2019.144618.
- [122] P. Santhoshkumar, G. Nagaraju, N. Shaji, G. S. Sim, M. Nanthagopal, S. C. Sekhar, J. S. Yu, C. W. Lee, Hierarchical iron selenide nanoarchitecture as an advanced anode material for high-performance energy storage devices, *Electrochim. Acta*, 356 (2020) 136833, DOI: 10.1016/j.electacta.2020.136833.
- [123] M. S. Javed, S. S. A. Shah, S. Hussain, S. Tane, W. Mai, Mesoporous manganese-selenide microflowers with enhanced electrochemical performance as a flexible symmetric 1.8 V supercapacitor, *Chem. Eng. J.*, 382 (2020) 122814, DOI: 10.1016/j.cej.2019.122814.
- [124] L. Cheng, S. Chen, Q. Zhang, Y. Li, J. Chen, Y. Lou, Hierarchical sea-urchin-like bimetallic zinc-cobalt selenide for enhanced battery-supercapacitor hybrid device, *J. Energy Storage*, 31 (2020) 101663, DOI: 10.1016/j.est.2020.101663.
- [125] Z. Xing, Q. Chu, X. Ren, J. Tian, A. M. Asiri, K. A. Alamry, A. O. Al-Youbi, X. Sun, Biomolecule-assisted synthesis of nickel sulfides/reduced graphene oxide nanocomposites as electrode materials for supercapacitors, *Electrochem. Commun.* 32 (2013) 9-13, DOI: 10.1016/j.elecom.2013.03.033.
- [126] Y. Li, K. Ye, K. Cheng, J. Yin, D. Cao, G. Wang, Electrodeposition of nickel sulfide on graphene-covered make-up cotton as a flexible electrode material for high-performance supercapacitors, *J. Power Sources*, 274 (2015) 943-950, DOI: 10.1016/j.jpowsour.2014.10.156.
- [127] D. Ghosh, C. K. Das, Hydrothermal growth of hierarchical Ni_3S_2 and Co_3S_4 on a reduced graphene oxide hydrogel@Ni foam: A high-energy-density aqueous asymmetric supercapacitor, *ACS Appl. Mater. Interfaces*, 7 (2015) 1122-1131, DOI: 10.1021/am506738y.
- [128] B. J. Reddy, P. Vickraman, A. S. Justin, Electrochemical performance of nitrogen-doped graphene anchored nickel sulfide nanoflakes for supercapacitors, *Appl. Surf. Sci.*, 483 (2019) 1142-1148, DOI: 10.1016/j.apsusc.2019.03.292.
- [129] L. Zhanga, H. Guoa, R. Xue, L. Yue, Q. Li, H. Liu, W. Yang, X. Wang, W. Yang, In-situ facile synthesis of flower shaped NiS_2 @regenerative graphene oxide derived from waste dry battery nano-composites for high-performance supercapacitors, *J. Energy Storage*, 31 (2020) 101630, DOI: 10.1016/j.est.2020.101630.
- [130] Y. Zhao, H. Zhang, Y. Lin, J. Chen, K. Li, A. Cheng, Design and construction of nickel-cobalt-sulfide nanoparticles in-situ grown on graphene with enhanced

performance for asymmetric supercapacitors, *Diamond Relat. Mater.*, 108 (2020) 107925, DOI: 10.1016/j.diamond.2020.107925.

- [131] X. Song, L. Tan, X. Wang, L. Zhu, X. Yi, Q. Dong, Synthesis of CoS@rGO composites with excellent electrochemical performance for supercapacitors, *J. Electroanal. Chem.*, 794 (2017) 132-138, DOI: 10.1016/j.jelechem.2017.04.014.
- [132] Z. Ji, N. Li, M. Xie, X. Shen, W. Dai, K. Liu, K. Xu, G. Zhu, High-performance hybrid supercapacitor realized by nitrogen-doped carbon dots modified cobalt sulfide and reduced graphene oxide, *Electrochim Acta*, 334 (2020) 135632, DOI: 10.1016/j.electacta.2020.135632.
- [133] S. Wu, T. Cui, Q. Hu, F. Yin, Q. Feng, S. Zhou, Q. Su, L. Wu, Q. Yang, Mixing solvothermal synthesis nickel selenide on the surface of graphene for high-efficiency asymmetric supercapacitors, *Synth. Met.*, 268 (2020) 116490, DOI: 10.1016/j.synthmet.2020.116490.

CHAPTER – II

**Theoretical background of successive ionic
layer adsorption and reaction (SILAR)
method and thin film characterization
techniques**

Chapter-II

Theoretical background of successive ionic layer adsorption and reaction (SILAR) method and thin film characterization techniques

2.1	Introduction.....	39
2.2	Theoretical background of successive ionic layer adsorption and reaction (SILAR) method.....	40
2.2.1	Effect of preparative parameters.....	44
2.3	Thin film characterization techniques.....	46
2.3.1	Physico-chemical characterization techniques.....	46
2.3.1.1	<i>X-ray diffraction (XRD)</i>	46
2.3.1.2	<i>Fourier transforms infra-red spectroscopy (FT-IR)</i>	49
2.3.1.3	<i>Raman spectroscopy</i>	51
2.3.1.4	<i>Field emission scanning electron microscopy (FE-SEM)</i> ..	53
2.3.1.5	<i>X-ray photoelectron spectroscopy (XPS)</i>	55
2.3.1.6	<i>Contact angle measurement</i>	57
2.3.1.7	<i>Brunauer-Emmett-Teller (BET) analysis</i>	58
2.3.2	Electrochemical characterization techniques.....	60
2.3.2.1	<i>Cyclic voltammetry (CV)</i>	62
2.3.2.2	<i>Galvanostatic charge-discharge (GCD)</i>	63
2.3.2.3	<i>Electrochemical impedance spectroscopy (EIS)</i>	64
	References.....	66

2.1 Introduction

Significant change in physical and chemical properties of the material with change in dimensions attracts attention of academics and scientist around the world. Development of sophisticated instrumentation for material synthesis and structural analysis further accelerated research in the field of low dimensional material synthesis [1]. From last decade, computer based simulation using various computational methods complement preparation methods while studying materials and material systems at diverse dimensions [2]. Nowadays, the most widely used approach in nearly all the fields is the application of thin films to improve the physical and chemical characteristics of materials. Due to wide variety of functions, solid thin films have been adapted in many types of engineering systems, for example photovoltaic (PV), sensors and transducers, energy storage systems, electronics, different types of catalysis systems and in biological applications [3]. The reliability and performance of these devices depend on the characteristics of material used to fabricate these devices. Control over different preparative parameters and post deposition treatments gives wide scope to modify specific properties of material in solid thin film form. Most of technologies make use of fact that the properties can be controlled by variation of thickness. Materials thickness varies from few nanometres to several micrometres can be called thin film of that material. Notwithstanding, it should be stressed that there is no perfect definition of the thickness below which a film becomes thin. The primary reason for this is that variation of properties with the thickness differs from material to material. The properties of the material in thin film form are changed predominantly from their bulk counterpart. The cause behind is the nanocrystalline nature of thin film which offers reduction in density and thermal conductivity, rise in volume to mass ratio, electrical conductivity are the major causes of the characteristic changes. Furthermore, film preparation method greatly affects properties of thin film such as crystal structure, crystallinity, roughness, morphology, and reactivity, etc. [4, 5].

The major deposition methods are classified into physical methods like vacuum evaporation and sputtering and chemical methods including chemical vapour deposition (CVD), photo CVD, laser CVD, metal organo-chemical vapour deposition (MOCVD) and plasma enhanced CVD, CBD, electrodeposition, SILAR, hydrothermal, anodization, spin coating, spray pyrolysis, liquid phase epitaxy, sol gel method, etc. The general classification of thin film deposition methods are presented

in Chart 2.1. The necessity of sophisticated instruments which can create high vacuum, temperature makes physical methods costlier. Simplicity of instrumentation, inexpensiveness, scalability, lower working temperature, ability to deposit materials on large substrates and variety of substrate choices makes chemical deposition methods more favourable compared to physical methods [6-8]. Various kinds of substrates can be employed to deposit thin films due to lower working temperature. Prohibition of oxidation of metallic substrates is another advantage of lower working temperature [9].

The structural, morphological and elemental characterization techniques such as XRD, FT-IR, Raman spectroscopy, FE-SEM, energy dispersive X-ray spectroscopy (EDAX), XPS, and contact angle measurements are carried out to determine surface properties of thin films. The specific surface area of materials and pore size distribution are measured employing BET technique and Barrett-Joyner-Halenda (BJH) analysis, respectively. The electrochemical characteristics of films of CuS, CuS@rGO, CuSe₂, CuSe₂@rGO, and MnO₂ are evaluated using various techniques like CV, GCD and EIS.

2.2 Theoretical background of successive ionic layer adsorption and reaction (SILAR) method.

The SILAR method is a facile and cost efficient method used for deposition of numerous materials in thin film form. One advantage of SILAR method is great control over deposition parameters while deposition proceeds. Mechanism of SILAR method was first reported by Ristov et al. in 1985 [10] and Nicolau et al. [11] referred name as SILAR for the method. The method is useful for deposition of numerous chemical compounds and composite films. The SILAR method is also called as modified CBD method. Generally, SILAR method involves adsorption, reaction and rinsing in between them.

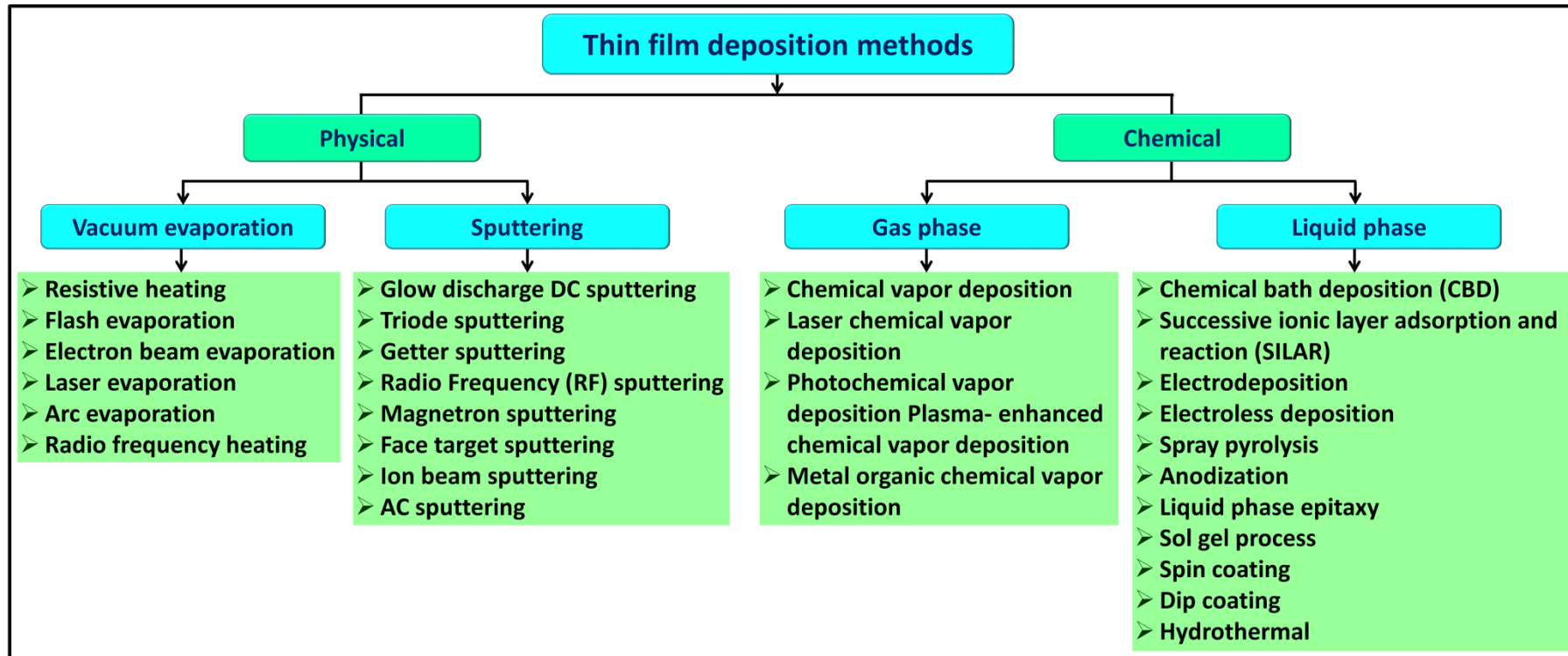
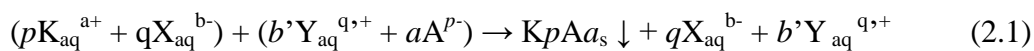


Chart 2.1: General classification of thin film deposition methods.

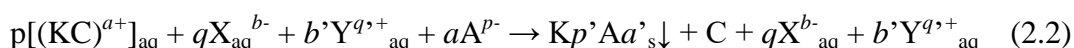
The SILAR is based on sequential reactions at the substrate surface followed by rinsing. Rinsing enables uniform growth of solid phase. This method is intended to grow thin films of water insoluble ionic or ion covalent compounds of the type $KpAa$ by heterogeneous chemical reaction at solid solution interface between adsorbed cations, pK_a^+ and anions, aA_p^- . The reaction can be represented by following relation.



with $ap = bq = b'q'$

where K represents cations (Zn^{2+} , Fe^{2+} , Co^{2+} , Fe^{3+} , Cu^{2+} , Ni^{2+} , etc), p represents the number of cations, a represents the numerical value of charge on cation, X is a ion in cationic precursors having negative charge ($X = SO_4^{2-}$, Cl^- , NO_3^- , etc), q represents number of X in cationic precursors and b the numerical value of charges on X. Y ion is attached to chalcogen ion, b' is the number of Y in anionic solution, q' is the numerical value of charge on Y. A is the chalcogen ion and a is the number of anions.

In the presence of complexing agent, above reaction can be written as,



where C is complexing agent. The basic representation of four beaker SILAR method is shown in Figure 2.1. The different processes involved in SILAR method are elaborated below.

(a) Adsorption:

It is an initial step of deposition process, where positive ions get adsorbed on the surface of the substrate to form the Helmholtz electric double layer. Two layers of ions formed on the surface of substrate due to Vander Waals forces. The inner layer is composed of positively charged ions and the outer layer is of counter layer of an anions.

(b) First rinsing:

The loosely adsorbed cations on the substrate surface are removed in this process. Rinsing has significant influence on morphology, particle size, crystallinity and the adherence of the thin film to the substrate. Generally, double distilled water (DDW) is used as rinsing solution.

(c) Reaction:

This is the third step where the anions from anionic precursor solution get in the reaction process. Due to high reactivity between cations and anions, a solid substance possessing chemical composition $KpAa$ forms at the interface. This step

involves irreversible chemical reaction between preadsorbed cations (pK^{a+}) and anions (aA^{p-}) from the solution.

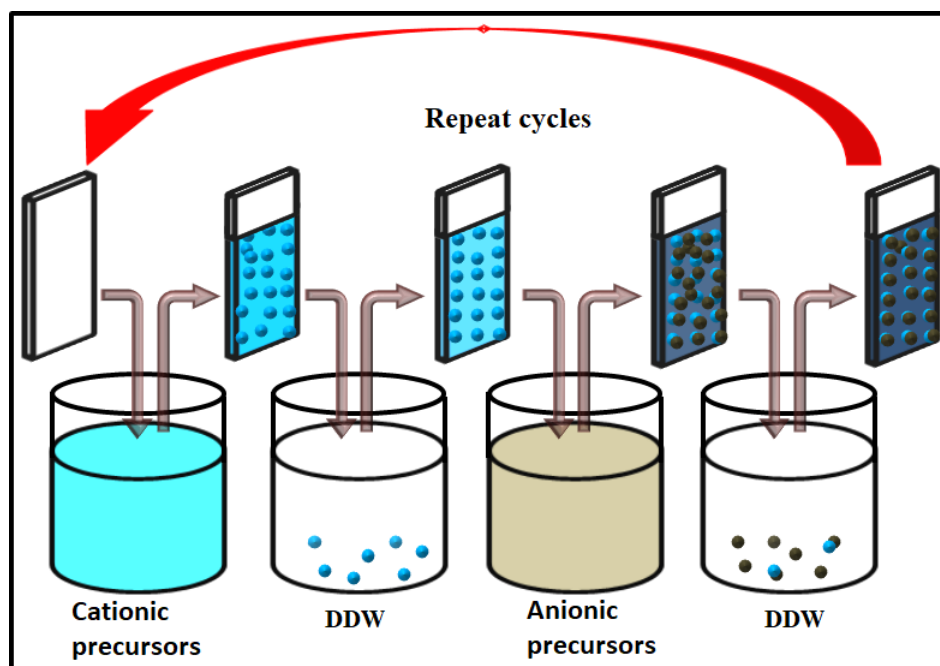


Figure 2.1: Schematic of four beaker SILAR method.

(d) Second Rinsing:

This is last step of SILAR deposition method used to remove unreacted, excess species, and secondary products of the reaction (aA^{p-} , X, Y) from the diffusion layer. As like in step second, DDW is used as rinsing solution. Thin film growth rate largely depend on various preparative parameters such as temperature of solutions, number of repeated cycles, pH of the solutions, concentration of cationic and anionic precursors, rinsing time, adsorption and reaction time, type and concentration of complexing agent, etc.

Advantages of SILAR method

Apart from saving material cost, preparation of thin films using SILAR method has the following advantages:

- (i) SILAR is a simple, inexpensive method and it is efficient for deposition over a large area.
- (ii) Various kinds of substrates like metals, semiconductors, insulators, and polymers can be used, because it is a low temperature process. This prevents corrosion or oxidation of metallic substrates.
- (iii) This method is very feasible to dope any element with the required proportion in the film.

- (iv) The deposition rate, morphology, and film thickness can be efficiently manipulated by varying the preparative conditions.
- (v) A comparatively uniform film can be deposited on any kind of substrate having a complex configuration.
- (vi) Drawbacks like contamination, interdiffusion, and dopant redistribution, due to high temperature deposition techniques can be avoided in this low temperature deposition method.

Along with the above advantages, SILAR has attractive features that material can be directly deposited from aqueous and nonaqueous baths and used to produce binary metal phosphate materials.

2.2.1 Effect of preparative parameters

The growth kinetics depends on the concentration of ion, nucleation and growth process on immersed substrates. The nature of the counter ions (viz. SO_4^{2-} and Na^+), the nature of solvent, presence of impurities giving more insoluble compounds than that to be deposited, the added complexing agents, the substrate polishing and etching, the substrate solubility also play a role. Effects of various parameters are given below.

(i) Concentration of precursors

Concentration of the precursor solutions affects the growth rate of film formation, in almost all chemical deposition methods. Rate of adsorption and reaction is depends on the concentration of the precursor solutions. If concentration of cations is above the certain concentration, the rate of adsorption becomes high thickness of film observed and if concentration of anionic precursor increases reaction rate becomes higher and large particle growth is observed. The higher reaction rate results in nonadherent and a nonhomogeneous film thickness. Higher precursor concentrations lead to formation of maximum film thickness and probability of formation of insoluble impurities in the film becomes high [12]. The optimum concentration of the both precursors should be experimentally determined.

(ii) pH

The pH of solutions plays an important role. Extreme pH values affect substrate surface state and solubility of desired compound, impurities and even substrate, also. At certain pH level reaction rate becomes faster and at certain pH level ionic product of metal and chalcogenide becomes less than the solubility product of

metal chalcogenide and a film will not be formed. pH value of cationic solution can be altered using complexing agent.

(iii) Temperature

The variations of film thickness can possible using varying temperature of solution bath. The dissociation of complex and the anion of the compound depend on the temperature. At the higher temperature, dissociation is greater and results higher rate of deposition. At room or lower temperatures the film formation rate becomes slow. The thickness is increased with increase in temperature linearly.

(iv) Complexing agent

The metal ion concentration, in the solution can be controlled with addition of complexing agent. The complexing agents are also called ligands. They have one or more donor atoms which can form coordination covalent bond with metal ion from the solution. The compound formed by metal ion and complexing agent is called as coordination compound. Added complexing agents introduce a supplementary activated kinetic step of decomplexation, thus increasing surface relaxation time that promotes a regular growth. The concentration of complexing agent decreases concentration of active metal ions. Therefore, the rate of reaction and precipitate formation is reduced leading to larger terminal thickness of the film. The deposition of thin film on surface of substrate is an only adsorption phenomenon. The thin film formation occurs by combination of released metal ion form complex metal ion source and chalcogen source. The complexing agents are classified on the basis of number of binding sites. Ammonia (NH_3 ; monodentate), ethylenediaminetetraacetic acid ($\text{C}_{10}\text{H}_{16}\text{N}_2\text{O}_8$; hexadentate), ethylenediamine ($\text{C}_2\text{H}_4(\text{NH}_2)_2$; bidentate), triethanolamine ($\text{N}(\text{CH}_2\text{CH}_2\text{OH})_3$; monodentate), polyvinyl alcohol ($\text{C}_2\text{H}_4\text{O}$)_x; monodentate/bidentate), etc. are some of the common complexing agents used in chemical deposition methods.

(v) Number of cycles

As each repeated cycle of deposition adds up few layers of the material on the substrate, increased number of cycles gives higher thickness of film. Large number of cycles results in formation of cluster of particles. Hence after critical number of cycles thin film starts to peel off.

(vi) Rinsing time

The hydrodynamics of the rinsing affects formation of thin film as in rinsing weakly adsorbed ions are removed. Formation of metal hydroxide with other

chalcogenides is another source of the impurities. The optimum rinsing time after adsorption and reaction should be experimentally determined. This helps to avoid formation of cluster of particles and uniform thin film can be deposited.

2.3 Thin film characterization techniques

2.3.1 Physico-chemical characterization techniques

The physicochemical properties such as crystal structure, specific surface area, surface texture, conductivity, and elemental composition are strongly correlated with its electrochemical properties. Therefore, the characterizations of material through different techniques and thorough analysis of the results to explain the relationship between different properties is a major work in the research field. This helps to decide proper material and its application. These methods also make it easier to check modifications in materials. Thus, the thin film electrodes in the present study were analyzed through different material characterization techniques. The comprehensive description of the basic principle, instrumentation, and working of these techniques are covered in this section.

2.3.1.1 X-ray diffraction (XRD)

In the field of materials science, XRD is a very primary, well-established, and widely used powerful nondestructive characterization technique to obtain information on the atomic scale structure of various substances in a variety of states [13]. The technique also provides information on unit cell dimensions. The XRD is a best and common technique used for the determine crystallite size (D) and to calculate lattice strain, chemical composition, state of ordering and to determine phase diagrams as well.

Working principle

The XRD analysis is mainly based on constructive interference of monochromatic X-rays from crystalline sample. The interatomic distance in materials is on the order of few Angstroms (\AA). This distance corresponds to wavelength of X-rays (energy between 3- 8 keV). Hence, when crystalline materials are exposed to the X-rays, constructive and destructive interference patterns are observed. When the intensity of diffracted X-rays measured as a function of scattering angle, a diffraction pattern is obtained. According to Bragg's condition (Figure 2.2), the constructive interference of diffracted X-rays observed when path difference $((AC+CB)-AB)$ equals to the wavelength of X-rays (λ). From Figure 2.2, the above condition can be written mathematically as [14],

$$d\sin\theta + d\sin\theta = n\lambda \quad \text{Or} \quad 2d\sin\theta = n\lambda \quad (2.3)$$

where n is the order of diffraction, θ is the glancing angle or Bragg's angle, and d is the interplaner distance.

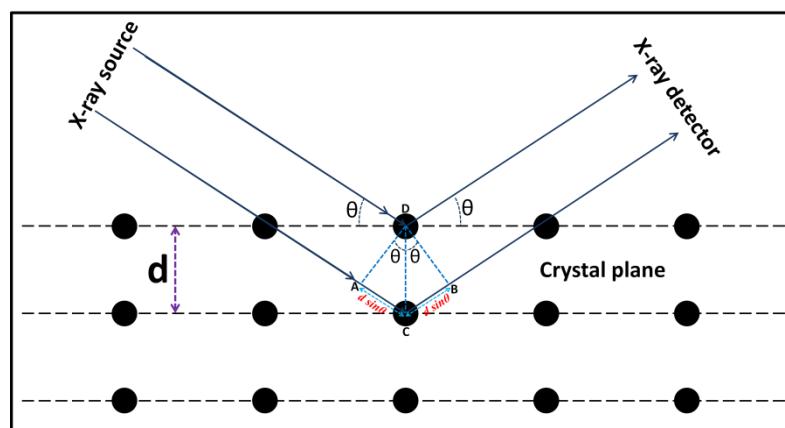


Figure 2.2: Bragg's diffraction.

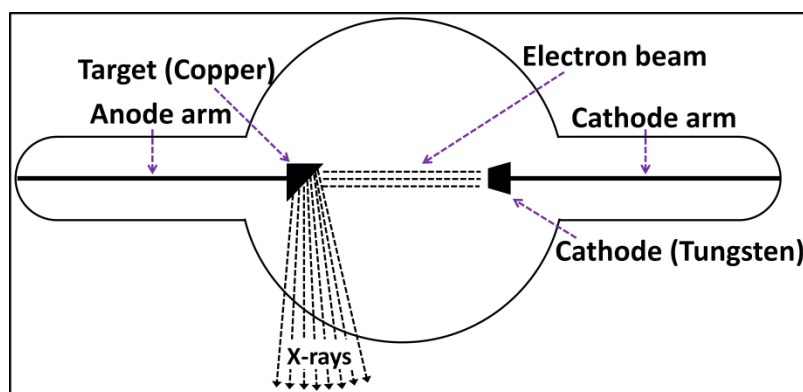


Figure 2.3: Schematic of X-ray tube.

Working of instrument

The X-Ray diffractometer consists of three major components; a monochromatic source of X-ray, specimen holder and X-ray detector. The X-ray generator is called cathode ray tube, made of a cathode, monochromator and target material enclosed in glass or ceramic container at vacuum (Figure 2.3). The cathode is heated to produce electrons; generally it is of tungsten filament. These electrons were accelerated towards target material (Cu, Fe, Mo, Cr) by applying a voltage. If electrons have enough energy to eject inner shell electrons of the target element, the outer electrons from target element jump into inner shells and to compensate energy difference the radiation is emitted. This radiation is the characteristics of target material. For copper as a target material, radiation consisting K_α and K_β lines are emitted. This radiation undergoes filtering process to produce monochromatic X-rays. The wavelength for copper radiation is $\text{CuK}_\alpha = 1.5418 \text{ \AA}$. Now, monochromatic X-

rays were collimated and directed towards desired specimen to be characterised. As specimen and detector are rotating, when Bragg's condition satisfy, peaks in the X-ray intensity is recorded. The schematic of X-ray instrument is shown in Figure 2.4a. The detector records the signals and converts it into count rate and provided to output instrument (computer) for further analysis.

Three methods available to determine crystal structure of sample are Laue method, rotating crystal, and powder method.

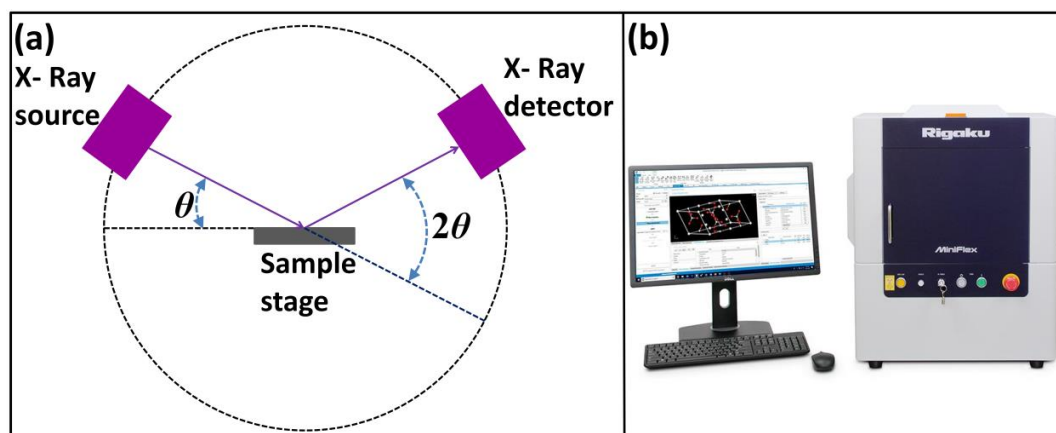


Figure 2.4: a) Schematic of X-ray instrument [15], and b) photograph of RIGAKU MiniFlex600 diffractometer [16].

In order to simply analyse crystal structure of sample, powder method is commonly used. Laue method is the oldest method used for the determination of crystal structure, where continuous spectrum of X-ray is used and angle of incidence is fixed. This method gives faster diffraction than other methods in which monochromatic X-rays used. Therefore, it is used to observe dynamic process in crystal structure. If the angle of incidence is fixed and wavelength is variable then that method is called rotating crystal method. In rotating crystal method, a monochromatic beam of hard X-rays allowed to fall on sample which is rotated at a constant angular velocity. In case of powder method, wavelength is taken as a fixed and angle of incidence is variable. Figure 2.4b shows the photograph of Bruker D2 phaser X-ray diffractometer. One very important use of XRD when dealing with nanocrystals is to estimate crystal dimensions through the Scherrer relationship [17]:

$$D = \frac{0.9\lambda}{\beta \cos \theta} \quad (2.4)$$

where β is full width at half maximum (FWHM) of the diffraction peak, θ is peak position in radians.

In the present study, XRD patterns of deposited thin film electrodes are recorded using RIGAKU MiniFlex600 diffractometer with Cu $K\alpha$ characteristic radiations ($\lambda = 1.5406 \text{ \AA}$) operated at 30 kV in $\theta/2\theta$ mode.

2.3.1.2 Fourier transforms infra-red spectroscopy (FT-IR)

The FT-IR spectroscopy offers qualitative information about the chemical bonding in materials. This is a nondestructive analysis. This can be used for analysis of solids, liquids and gases. The FT-IR denotes Fourier transforms infra-red and the technique is called infrared spectroscopy, name itself suggest the way data is collected and converted from interference pattern to the spectrum.

Working principle

Molecular bonds vibrate at certain frequencies depending on the type of bond and elements involved in bonding. According to quantum mechanics, these frequencies correspond to the ground state and several excited states. When these bonds absorb light energy of certain frequency they can be excited to upper possible state of energy. For any given transition between two states the light energy must be equal or greater than the difference in the energy between ground state and the first excited state. The wavelength absorbed by the bond is the characteristics of chemical bond and can be seen in spectrum. The range of mid-infrared region is 4000 to 200 cm^{-1} . The schematic of FT-IR instrument with Michelson interferometer is shown in Figure 2.5 [18].

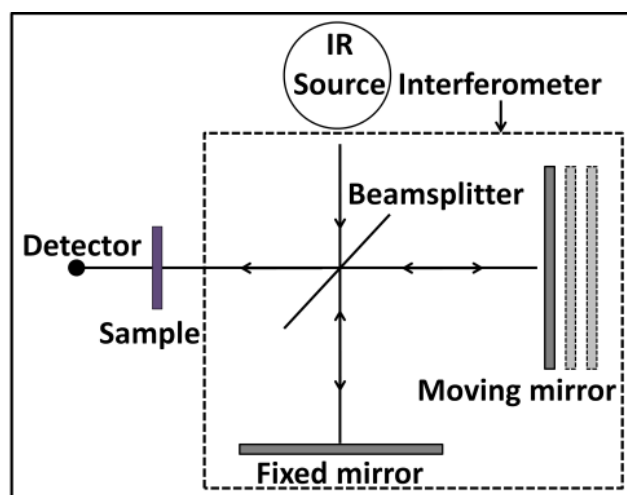


Figure 2.5: Basic schematic of FT-IR with Michelson interferometer.

Working of instrument

A common FT-IR spectrometer consists of a source, interferometer, sample compartment, detector, amplifier, A/D convertor, and a computer. Figure 2.6a depicts

photograph of ALPHA II compact FT-IR spectrometer. The schematic diagram of the basic FT-IR system coupled with amplifier and necessary electronics for conversion of acquired data is presented in Figure 2.6b. The IR spectrum is a graph of infrared light absorbance by the substance on the vertical axis and the frequency (wavenumber) on the horizontal axis. Silicon carbide rod, nichrome and kanthanol wire coils, Nernst glowers and carbon arcs are used as the source of IR radiation. The beam splitter is made of a material that reflects half of the radiation striking it and transmits the other half. Out of these two beams, one is transmitted to moving mirror and other to stationary mirror. Again, these beams reflected back and undergo splitting and only one beam directed towards sample and other to source. The stationary mirror is made of highly reflecting material. The simplicity of FT-IR design lies in moving mirror. This mirror produces path length difference between two beams from stationary mirror and moving mirror and forms interference pattern.

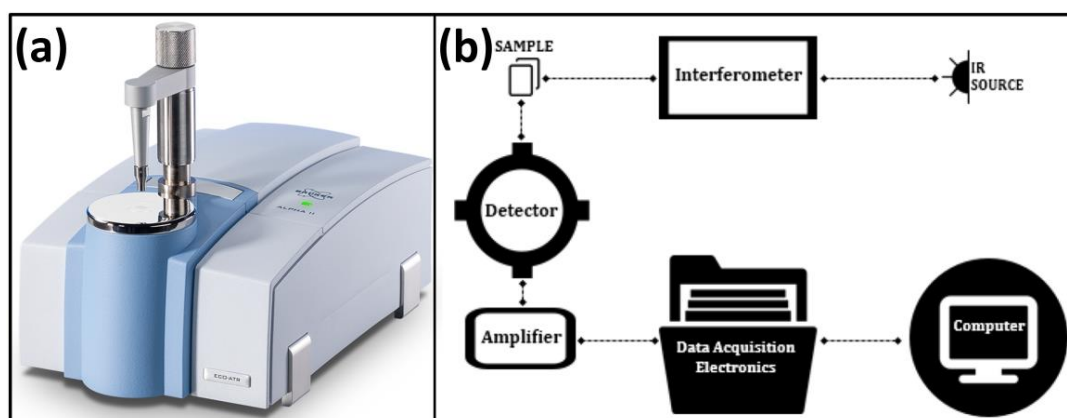


Figure 2.6: a) Photograph of ALPHA II compact FT-IR spectrometer [19], and b) the basic ray diagram of FT-IR system [20].

The sample for FT-IR must be thin so the IR radiations must pass through it. This serves as one of the advantage of FT-IR analysis as it requires very small sample. When IR radiation is passed through a sample, some of the radiation is absorbed by the sample and remaining transmitted. The detectors are of two types; thermal and quantum detectors. Thermal detectors treat received light as heat, while quantum detector as light. Hence, quantum detectors are highly sensitive. Then the obtained data in terms of intensities are processes by Fourier transform and plotted against wavenumber. For analysis purpose, observed data is compared with available reference patterns. There are no two unique molecular structures, that can yield similar infrared spectrum. In this way infrared spectroscopy is useful for several types of analysis. Using FT-IR spectroscopy the following information is obtained [21],

- Identification of unknown materials.
- Determination of the quality or consistency of a thin film sample.
- Determination of amount of components in a mixture.

In the present study, the FT-IR spectra of synthesised materials are recorded using ALPHA II interferometer with diode laser as an IR source.

2.3.1.3 Raman spectroscopy

Raman spectroscopy is a highly versatile technique that provides a simple, fast and nondestructive analysis of both organic and inorganic materials [22]. It uses the interaction of light with the material to gain insight into characteristics of material and its constituents. It measures different modes of molecules such as rotational, vibrational, and other low frequency modes [23].

Working principle

Raman scattering is a two photon process. Electrons have different vibrational levels which are defined by specific energy differences (Figure 2.7). When an incident monochromatic light interacts with an electron in the sample, the electron absorbs energy from an incident photon and goes to a higher state of energy. The electron falls back to an energy level by losing energy. When the energy lost equal to the energy of the incident photon, electron falls back to its initial level and loses one photon. Hence the molecule doesn't have any Raman active modes. This secondary photon has the same frequency as the incident photon and Rayleigh scattering occurs. However, sometimes electrons while losing energy from the virtual state can fall back to a different vibrational level.

In this case, the energy loses by the electron is different than the energy absorbed from the incident photon. As a result, the emitted photon has energy different than the incident photon. In this case, the frequency of the emitted photon is not equal to the incident photon. This gives the Raman scattering. Depending on the final vibrational level of electron Raman scattering is separated into stokes line and antistokes lines. The radiation having lower energy as compared to the incident radiation is called stocks lines, while the radiation having higher energy than incident radiations are called antistocks lines [24].

The Raman shift $\Delta\nu$ is positive for stokes and negative for anti-stokes and is a characteristic feature of material undergoing Raman shift. The Raman spectrum gives the molecular fingerprint and it is different for different molecules. By studying the

Raman spectra one can identify the rotational levels and thus a particular molecule. This will help to analyse the sample qualitatively. Similarly, the intensity of a particular Raman line helps to determine the concentration of a molecule in the sample.

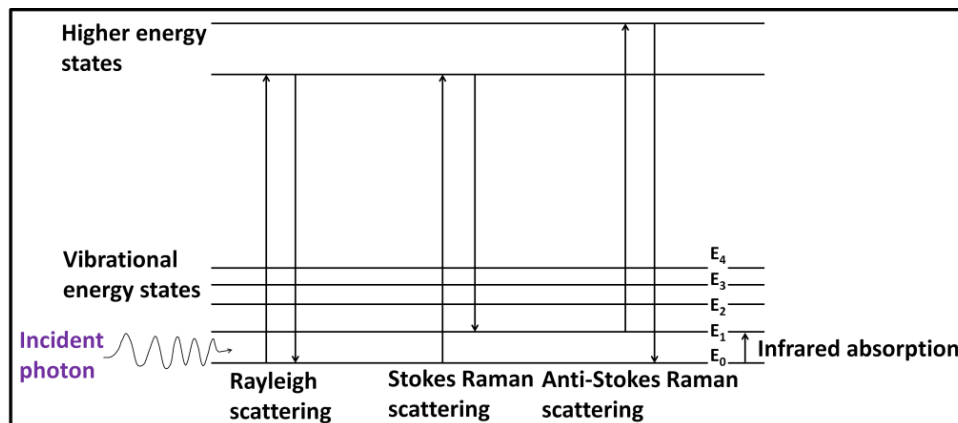


Figure 2.7: Energy level diagram showing the states involved in Raman spectra.

Working of instrument

There are three primary components to any Raman spectrometer: an excitation source, a sampling apparatus, and a detector. The basic block diagram of Raman spectrometer is shown in Figure 2.8. In Raman spectroscopy a monochromatic excitation source is employed. Generally, a laser with extremely stable and narrow bandwidth used as an excitation light source. The laser source must have certain characteristics, such as small form factor, low power consumption, narrow line width, a stable power output and a stable wavelength output. For organic molecules it is important to shift the laser wavelength into the near infrared to minimize fluorescence while not exceeding CCD spectral detection limits. Due to availability and the maximum fluorescence reduction without the sacrifice of spectral range or resolution 785 nm diode lasers have become more favourable. For highly colored or strong fluorescence samples, 1064 nm laser is the best choice. For inorganic molecules, 532 nm laser is the best choice as it offers increased sensitivity. The second component is the sample interface for which fiber optic probe is used. It usually provides the flexible sampling interface. The flexibility afforded by fiber optics not only allows for the probe to be taken to a solid sample, but also allows it to be immersed in liquids or slurries in both laboratory and process environments. It can also be connected to microscopes, cuvette holders. The spectrometer is the next component and has some characteristic such as small form factor, high resolution, low power consumption, and

low noise to detect very weak Raman scattering [25]. Further, the desired detector is required and is depends upon the type of excitation laser being used. Majority times, charge coupled device (CCD) are used as the detector for Raman spectroscopy. For very low concentrations or weak Raman scatters, it may be necessary to use a back thinned CCD to further increase the sensitivity of the spectrometer [26, 27].

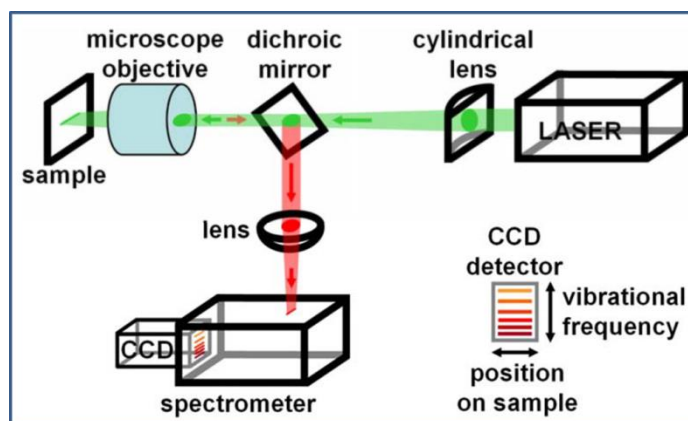


Figure 2.8: The basic block diagram of Raman spectrometer [28].

2.3.1.4 Field emission scanning electron microscopy (FE-SEM)

The FE-SEM microscope is a dominant instrument used for the analysis of surface microstructure at high resolution. It employs electrons instead of photons for imaging process. These electrons are liberated by a field emission source. The FE-SEM provides topographical and elemental information at magnifications of 10 X to 300,000 X, with virtually unlimited depth of field.

Working principle

The FE-SEM images a sample surface by raster scanning over it with a high energy beam of electrons. The primary electrons liberated from a field emission source are accelerated in the electric field. Using electromagnetic lenses, a narrow beam is produced by focusing these primary electrons. The beam is allowed to strike the sample. After interaction, primary electrons lose their energy inside the sample, due to this; different types of electrons are produced as shown in Figure 2.9. This causes the emission of secondary electrons from the sample. The electrons interact with the atoms comprising the sample to produce secondary electrons that contain information about surface topography, composition. By processing these electrons, detector generates an electric signal which is further amplified and transformed into an image.

Working of instrument

The schematic diagram of the FE-SEM instrument is shown in Figure 2.10a. An electron gun, an anode (accelerator), magnetic lenses, sample holder and detector are the main parts of a FE-SEM instrument.

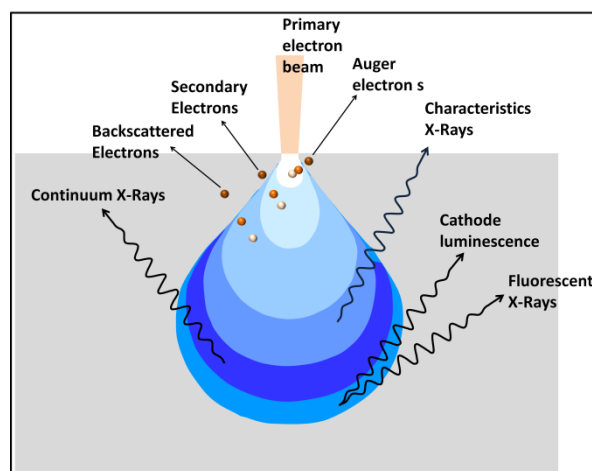


Figure 2.9: Ray diagram for the emission of different types of electrons after the interaction of primary electrons from source with sample.

The whole assembly is mounted on a desk. For operation, the gun head, column and specimen chamber have to be evacuated. Column chamber valve remains closed until the detected pressure is not ready for operation. After vent command, column chamber valve closes and N_2 gas flows into the specimen chamber through vent valve. Sample preparation is also one of the parts of FE-SEM characterization technique. For FE-SEM, the sample must be conductive. Before mounting on a special holder, the samples are first made conductive by coating them with ultrathin layer electrically conducting metal such as gold (Au), platinum (Pt), gold/palladium (Au/Pd), chromium (Cr), silver (Ag), or iridium (Ir) [29]. The conductive layer of metal on the sample prevents charging of the specimen, reduces thermal damage and increases the amount of secondary electrons therefore increases the signal to noise ratio.

In FE-SEM, high-energy electrons (termed as primary electrons) are generated by placing a filament of tungsten fashioned into a sharp point; in a huge electrical potential gradient (cathode). The voltage difference between anode and cathode allows generated electrons to accelerate towards the sample. The voltage is in the order of magnitude of 0.5 to 30 kV, and the high vacuum ($\sim 10^{-6}$ Pa) in the column of the microscope is maintained. The electron beam is focused by the electromagnetic lenses to a tiny sharp spot. The condenser lens controls the amount of magnification. Objective lens focuses the electron beam onto the specimen. Objective lens consists of electromagnetic and electrostatic lens. Deflection system consists of a set of scan

coils to move the electron beam in a point-to-point scan process. Once the focused electron beam bombards on the surface of the sample, it penetrates the sample up to a few microns and interacts in different ways [30]. The scattering of electrons and volume of interaction depends on the atomic number, the concentration of atoms of sample and the energy of primary electrons. The high energy of primary electrons increases interaction volume and scattering process. While the high concentration of atoms and the atomic number will decrease the interaction volume and scattering.

All these signals are gathered by a detector and separated based on their energy values. The backscattered and secondary electrons are used for the creation of a sample image by amplifying and transforming the signals. When primary electrons interact with electrons at the inner shell and knock it out, the electron from a higher energy level jumps to lower energy by losing some energy. This extra energy is loosed in the form of X-rays. Therefore, each element in the sample produces a characteristic X-ray. All these characteristic X-rays from all elements are used to identify the elemental composition of the sample by energy-dispersive X-ray spectroscopy (EDAX) coupled to the FE-SEM instrument [31]. Photograph of FE-SEM instrument is shown in Figure 2.10b.

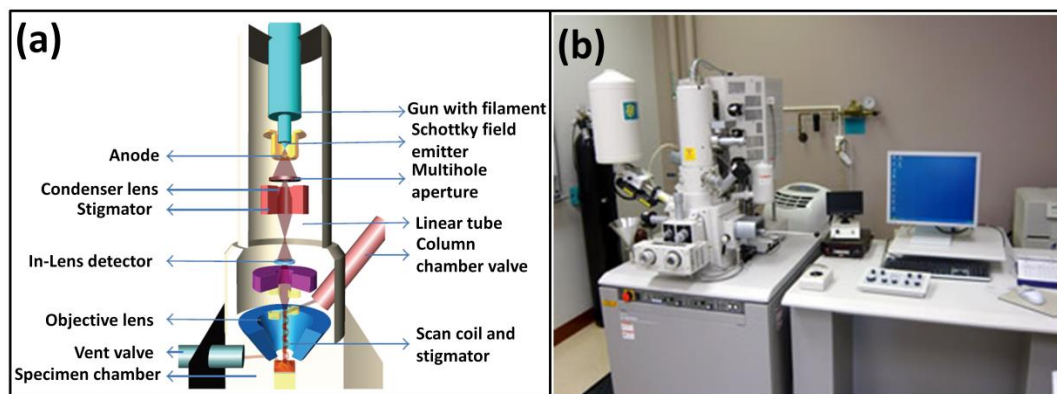


Figure 2.10: a) Schematic of FE-SEM [32], and b) photograph of FE-SEM instrument [33].

In the present study, FE-SEM and EDAX are performed on Philips SEM-XL30S microscope (Netherlands) coupled with an energy-dispersive X-ray spectroscopy (EDAX) analyzer.

2.3.1.5 X-ray photoelectron spectroscopy (XPS)

The XPS is a chemical analysis technique mainly used for analyzing surface composition of a material and oxidation state of elements present in it. The XPS can characterize only 1-10 nm depth of the sample. The XPS technique is based on the

photoelectric effect described by Einstein, which states that when electromagnetic radiation hits a material, electrons are emitted. These emitted electrons are also called photoelectrons.

Working principle

When an incident X-ray has sufficient energy, it will be absorbed by an atom and by the phenomenon of the photoelectric effect, an inner shell electron will be ejected as demonstrated in Figure 2.11. The kinetic energy of photoelectrons is collected. As the energy of an incident X-ray is known, the binding energy of photoelectron is calculated by the below formula:

$$E_{binding} = E_{photon} - (E_{kinetic} + \varphi) \quad (2.5)$$

where φ is the work function of the element.

By measuring the count of photoelectrons as a function of binding energy, the composition of the sample and the various oxidation states of elements present in it can be calculated.

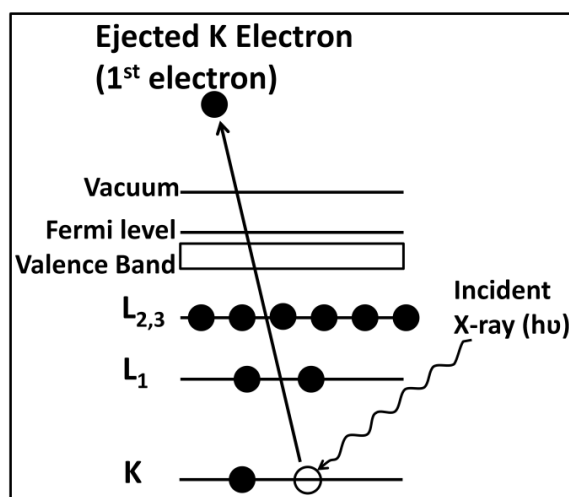


Figure 2.11: Atomic model of the working principle of XPS.

Working of instrument

In XPS an X-ray source generates X-rays (typically MgK α and AlK α) which are monochromatized using a monochromator in a high vacuum. These X-rays incident on the sample and excite the electrons inside the atoms present on the surface of the sample. These photoelectrons go to the electron detector where the detector counts the incoming electrons as well as the kinetic energy of these electrons. Finally, this kinetic energy is represented in the form of a spectrum where particular energy represents an element present in the sample. The X-ray photoelectron spectroscope, K-alpha XPS system of Thermo Fisher Scientific, U. K. is used in the present study.

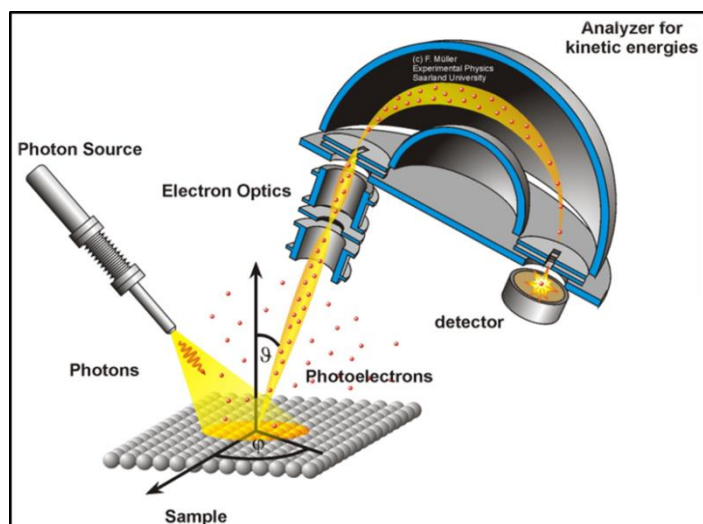


Figure 2.12: Schematic diagram of an XPS instrument [34].

2.3.1.6 Contact angle measurement

The contact angle is an important tool used to measure the contact angle and surface wettability of thin film surface. Also, it is possible to calculate surface free energy. The wettability measure the ability of material to interact with liquid. Figure 2.13a shows photograph of Rame-Hart NRL contact angle meter and Figure 2.13b shows contact angle image of a liquid sample on a solid thin film surface.

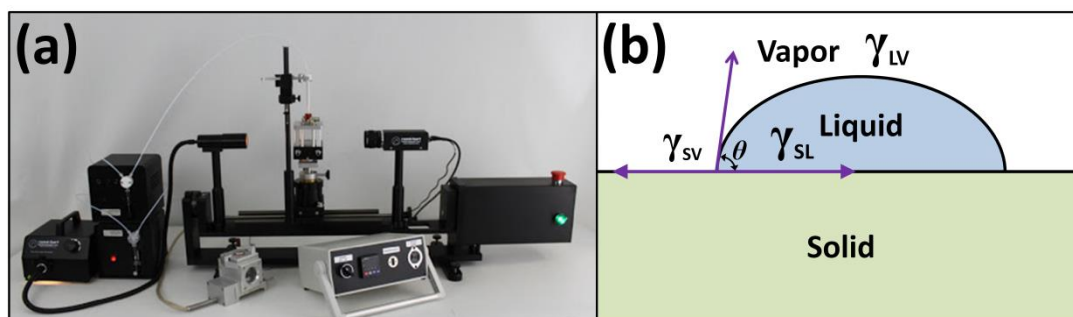


Figure 2.13: a) Photograph of Rame-Hart NRL contact angle meter [35], and b) contact angle of a liquid in contact with solid sample.

The contact angle is the angle between surface of a solid and tangent drawn to the liquid surface, measures inside the liquid. If the contact angle is greater than 90° then it is hydrophobic in nature and surface is less wettable. Super hydrophobic surface means contact angle is above 170° [36]. If the contact angle is less than 90° , solid surface is hydrophilic and wettable. In case of super hydrophilic condition, the contact angle is less than 5° and surface is more wettable. The different methods are used to measure contact angle. If the three phases are in equilibrium condition, then net force is zero. The contact angle (θ) is calculated by the Young's relation [37].

$$\gamma_{s,v} = \gamma_{s,l} + \gamma_{l,v} \cos\theta \quad (2.6)$$

where $\gamma_{s,v}$ is the solid-vapour, $\gamma_{s,l}$ is the solid-liquid and $\gamma_{l,v}$ is the liquid-vapour interfacial energies.

In the present study, contact angle images of deposited thin film electrodes are recorded using Rame-Hart goniometer (modal 260).

2.3.1.7 Brunauer-Emmett-Teller (BET) analysis

The physical adsorption of a gas on the surface of thin film material and the amount of adsorbate gas gives a specific surface area of a prepared sample. The film formed with gas adsorption on the surface of the specimen. The gas also adsorbs to the surface as well as in the pores of the specimen. The pore size structure of the sample is determined by measuring the amount of gas adsorbed at provided pressure. Commonly, the nitrogen gas is used for BET measurement [38]. The specific surface area in the $\text{m}^2 \text{g}^{-1}$ provides significant information about the effect of surface porosity and particle size.

Working principle

The gravimetric or volumetric method is used to measure the adsorption isotherm. In both methods the adsorbent is held at a constant temperature (near the boiling point of the adsorptive). The adsorptive pressure is increased step wise and held constant for a period of time to allow the adsorption to occur and the temperature of the adsorbent to reequilibrate. In the case of the volumetric system, the pressure change was measured and compared with expected pressure change in absence of adsorbent. For the gravimetric measurement the mass gain indicated amount of adsorbent. The isotherm is a plot of the amount adsorbed versus the adsorptive pressure. The pressure is expressed as a ratio of the adsorptive pressure (P) to the saturated vapor pressure (P_0). As being simple and relatively inexpensive, volumetric method is the most common measurement of the isotherm. Uncertainty in the results is the drawback of this method. The gravimetric method is more accurate and precise, however such instrumentation is costly. There are six types of isotherms but, each adsorbent–adsorbate combination has its own standard curve. Type I isotherm is obtained when chemisorption or physisorption take place on a material that has extremely fine pores. For nonporous and macroporous materials, if the energy of adsorption is high then type II isotherm and for low energy of adsorption type III isotherm is obtained. For mesoporous material with high energy of adsorption type IV

and with low energy of adsorption type V isotherms are observed. Type VI of isotherm is attributed to several possibilities the most likely being, if the temperature is below the adsorptive triple point, that the adsorbate is more like a solid forming a structured layer. Other possible explanations include multiple pore sizes. The phenomenon of desorption isotherm being different from the adsorption isotherm is called hysteresis. According to IUPAC, four types of hysteresis loops are H1, H2, H3, and H4. Below certain relative pressure (P/P_0) hysteresis does not occur. The value is 0.42 for nitrogen adsorption. To evaluate specific surface area (A_s) from cross sectional area of adsorbate molecule (a) and number of mole of adsorbate in a monolayer (n_m),

$$A_s = n_m N_A a \quad (2.7)$$

where $a = (M/\rho)^{2/3} N_A^{1/3}$, M is the molar mass (g mol^{-1}), ρ is the liquid density (gm^{-3}), and N_A is Avogadro's number ($6.022 \times 10^{23} \text{ mol}^{-1}$).

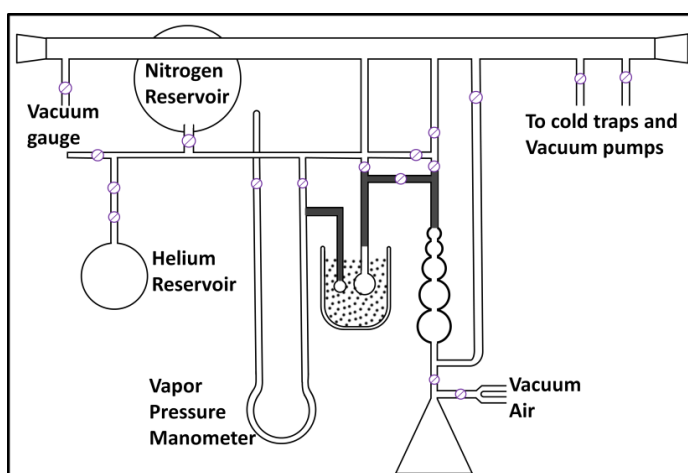


Figure 2.14: Schematic diagram of the dynamic flow method apparatus [39].

Working of instrument

As stated previously, there are two methods (volumetric and gravimetric) used to determine surface area by physisorption. In both methods, the adsorption is performed in a temperature and pressure range just below the boiling point of the gas. The amount of a gas that adsorbs on the surface is measured as a function of the pressure. From the amount of gas adsorbed and the pressure, the surface area, strength of forces causing adsorption, porosity was calculated. The basic volumetric method is shown schematically in Figure 2.14. System parts are not to scale. Sample chambers are usually constructed from Pyrex.

The total surface area (S_T) and a specific surface area (S_B) are projected by below countenance;

$$S_T = \frac{v_m N S}{V}, \quad (2.8), \text{ and} \quad S_B = \frac{S_T}{a} \quad (2.9)$$

where S is the adsorption cross section of the adsorbing species, N is Avogadro's number, V_m is the molar volume of the adsorbate gas, and a is the mass of the adsorbent [40].

2.3.2 Electrochemical characterization techniques

Need of development of diverse electrical energy storage devices specifically designed for certain purposes such as wearable and portable electronics, health care systems, etc., have increased interest of scientific community in electrochemical energy storage. Ragone plot (Figure 1.1) showing performance of electrochemical energy storage devices suggests S_E of fuel cells are very high and S_P of capacitors are higher compared to batteries and SCs. Along with batteries, SCs bridge the gap between fuel cell and capacitors [41]. Taking in to account that diversity of electrode materials, electrolytes, and ability to support various designs according to requirement in many fields (aerospace, medical, military, transportation etc.) SCs, often called supercapacitors have attracted research interest globally. The SCs are classified according to mechanism of charge storage or configuration or physical state of electrolyte into various classes. Based on charge storage mechanism, SC electrodes are classified as EDLCs (non-Faradic mechanism), pseudocapacitors (Faradic mechanism), and battery type. The SCs are classified as symmetric and asymmetric in which configuration is considered and second one is liquid-state and solid-state, based on physical state of electrolytes [42]. Common configuration of SC consists of two conducting electrodes separated by porous membrane immersed in relevant electrolyte. The specific capacitance (C_s), specific capacity (C) and areal capacitance (C_a) of such device are determined by the following relations;

$$\text{Specific capacitance } (C_s) = \frac{1}{m \Delta V} \int_{V_1}^{V_2} I(V) dV \quad (\text{CV study}) \quad (2.10)$$

$$\text{Areal capacitance } (C_a) = \frac{1}{a \Delta V} \int_{V_1}^{V_2} I(V) dV \quad (\text{CV study}) \quad (2.11)$$

$$C_s = \frac{I \times t}{m \times \Delta V} \quad (\text{GCD study}) \quad (2.12)$$

$$C_a = \frac{I \times t}{a \times \Delta V} \quad (\text{GCD study}) \quad (2.13)$$

$$\text{Specific capacity } (C) = \frac{C_s \times \Delta V}{3600} \quad (2.14)$$

where $\int_{V_1}^{V_2} I(V)dV$ is the area enclosed in a CV curve, m (g) is deposited mass of material on both electrodes, v ($V s^{-1}$) is the potential scan rate, ΔV (V) is an operational potential window, and I (A) is the current response, a (cm^2) is area of the SC. Furthermore, the S_E and S_P of the SC are calculated using the Eq. (1.4) and (1.5), respectively. To achieve higher values of S_E and S_P , the working voltage and C_s of SC must be large with lower interfacial resistance [43]. However, C_s and working voltage depend on the combination of electrode and electrolyte used in SC fabrication.

Generally, EDLC type materials can operate up to 1 V in water based electrolytes, while in organic electrolytes potential window can be extended to 2.5 V (sometimes up to 3.0 V). In EDLCs, the electrically conducting electrode and ionically conducting electrolyte, in which electric double layer is formed at the interface. The electric charge storage in EDLCs type SC shown in Figure 2.15a can be written as,



where E_{s1} and E_{s2} are corresponding to the specific surface area of negative and positive electrodes. The symbol // indicates the electric double layer, where charges are stored on either side and K^+ and A^- are cations and anions present in the electrolyte, respectively. The process of adsorption and desorption is accountable for charging and discharging of EDLCs, consequently no charge transfer occurs around the interface. Hereafter, the active electrodes are chemically inert; so this process is called as non-Faradaic [44].

The fast and reversible redox reactions with double layer capacitance give pseudocapacitance. The charge stored in pseudocapacitor is due to the Faradaic reaction at an interface of electrode and electrolyte. The schematic of different charge storage mechanisms observed in the pseudocapacitive materials is shown in Figure 2.15b-d. In Faradaic process, during charging discharging, the charges are transmitted on the electrode material as well as in the bulk of electrode material [45]. The charge storage in pseudocapacitor is done by two way process. In the first step accumulation of charges on the electrode material surface takes place. In second process, the redox reaction takes place in electrode surface as well as in the bulk of electrode material. Above two processes are mainly dependent on the applied potential, so the pseudocapacitance is also dependent on potential. To better understand the electrochemical properties of the electrode material, the measurements such as CV,

GCD and EIS are necessary. Consequently, for application of thin films as an active electrode for SC devices, the electrochemical features are significant.

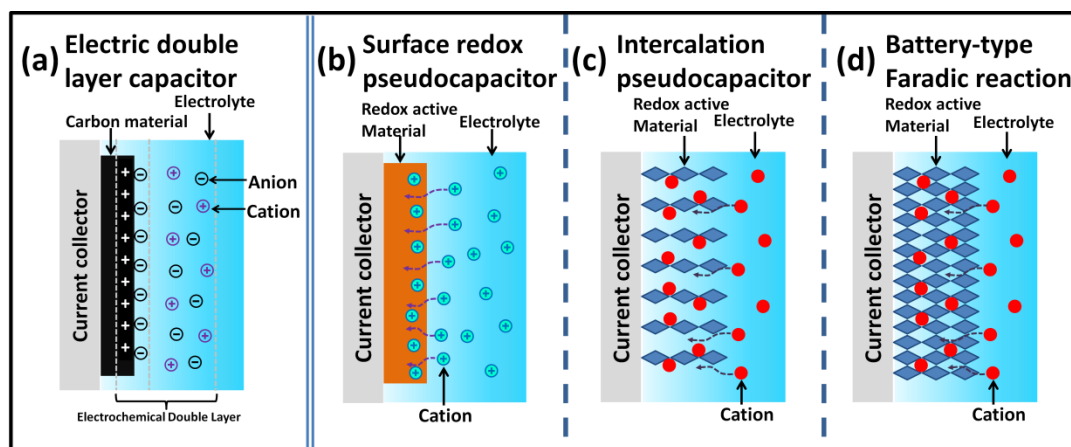


Figure 2.15: Schematics of charge-storage mechanisms for a) an EDLC [46] and (b–d) different types of pseudocapacitive electrodes: b) surface redox pseudocapacitor, c) intercalation pseudocapacitor, and d) battery-type Faradaic reaction [47].

2.3.2.1 Cyclic voltammetry (CV)

The CV offers a plentiful experimental information and insights into both thermodynamic and the kinetic details of many chemical systems. This is a fundamental characterization technique which provides information about electroactivity of electrode in various electrolytes. The reversal linear scan voltammetry carried out by switching direction of the scan at certain potentials is called CV. In CV measurement, the stationary electrode with 1 cm^2 area is used, which immersed in an electrolyte solution. The three electrode system is beneficial for minimization of ohmic resistance of electrode. The potential is applied between the working electrode and reference electrode, simultaneously the current measured between the working electrode and counter electrode.

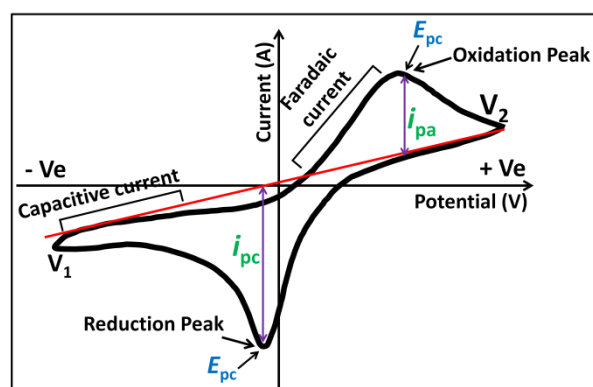


Figure 2.16: The typical cyclic voltammogram for a reversible single electron transfer reaction [48].

In CV measurement, the potential is swept between given potential range, nevertheless, when the voltage reaches maximum potential limit then scan is reversed and the voltage is swept back to the minimum voltage range. Figure 2.16 illustrates CV curve for a reversible single electrode transfer reaction in the potential limit of V_2 to V_1 . The I_{pc} and I_{pa} are cathodic and anodic peak currents, while E_{pc} and E_{pa} are cathodic and anodic peak voltages of the electrode material. In CV measurement, the selection of potential limit is important due to the oxidation and reduction positions of CV curve. One state of electrode material change to another during charging, while at reverse direction the electrode material achieves an initial state with reduction process.

There are many fields in which CV technique is used extensively. These include metal-ligand interaction, in which electron pair transfer to form complex compound. Other applications include analysis of solids [49], solutions, polymers media with and without added supporting electrolyte, membrane [50], frozen solutions [51], emulsions and suspensions [52], and liquid-liquid systems [53], and biological systems such as enzymes [54].

2.3.2.2 Galvanostatic charge-discharge (GCD)

In GCD technique, constant current is applied to the working electrode. The corresponding potential is measured against the reference electrode as a function of time. At initial the potential is suddenly changed because of the potential drop afterwards slowly changes in potential. Figure 2.17 shows charge discharge curve of SC. This is due to the concentration of the reactant exhausted at the electrode surface [55, 56].

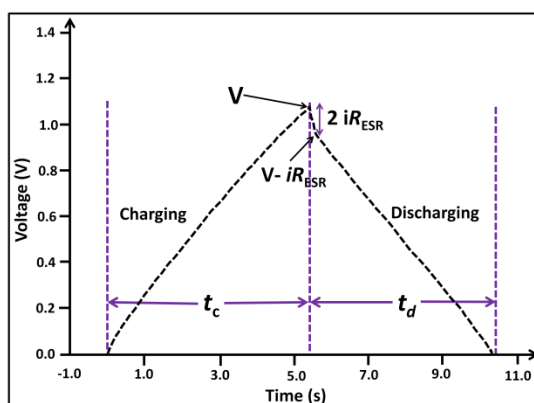


Figure 2.17: Charge discharge curves of a SC [57].

During discharging potential drop due to the solution and interfacial resistance, which can be corrected through the constant potential offset. From the nature of the

charge discharge curve, the type of charge storage mechanism for sample electrode is confirmed. The symmetric shape of the charge discharge curve indicates the charge storage mainly due to the double layer mechanism if not then charge storage due to the pseudocapacitive mechanism [58, 59]. Additionally, GCD analysis is important to determine the S_E and S_P of the SC.

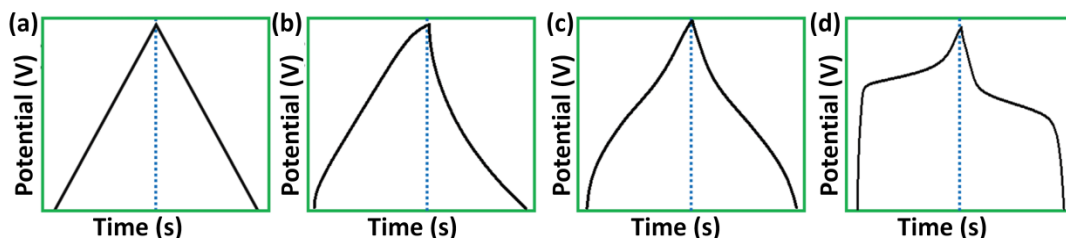


Figure 2.18: Representative shapes of GCD curves: a) EDLC, b) surface redox capacitance, c) intercalation capacitance, and d) Faradic battery-type [60].

2.3.2.3 Electrochemical impedance spectroscopy (EIS)

The charge storage mechanism at an electrode electrolyte interface is studied using EIS technique which is also called as an AC impedance spectroscopy. EIS works on a wide range of frequencies beneficial for accurate determination of resistances at an electrode electrolyte interface. The small AC signal (5 to 10 mV) is applied to the SC cell over a wide range of frequency from 1 mHz to 1 MHz. The output signals are the current response to the applied AC signals. The plot of imaginary impedance against real impedance is called as the Nyquist plot [61, 62]. The EIS method is useful to record frequency independent and dependent resistive parameters of the system. If the input signals of a sinusoidal voltage $V(\omega) = V_0 \sin \omega t$ and $I(\omega) = I_0 \sin(\omega t + \phi)$ be its output response, then the impedance of the electrode material is given by,

$$Z(\omega) = \frac{V(\omega)}{I(\omega)} = \frac{V_0 \sin(\omega t)}{I_0 \sin(\omega t + \phi)} = Z_0 \frac{\sin(\omega t)}{\sin(\omega t + \phi)} \quad (2.16)$$

The impedance is expressed in terms of magnitude, Z_0 and phase shift ϕ . The imaginary and real parts of impedance are depicted in the Nyquist plot shown in Figure 2.19. The inset diagram displays a general equivalent circuit (Randles cell) associated with the Nyquist plot.

In this Figure, R_{ct} is the charge transfer resistance (Figure 2.19). Transfer of these charges has fixed kinetics depend on reaction type, temperature, concentration, and potential of reaction products. As the series resistance (R_s) of the electrochemical cell is negligible, Nyquist plot intercept at origin of the Z_{re} axis. But for the every

electrochemical cell, there is small internal resistance. Hence, first intercept of Nyquist plot on is on the positive side of Z_{re} -axis. This gives value of equivalent R_s (Figure 2.20a). This resistance is in series with R_{ct} . The resistance offered to the diffusion of electrolyte ions takes place in lower frequency region, indicated by the straight line in Figure 2.20b. This adds a more component in the equivalent circuit in series with R_{ct} called Warburg impedance (W). The Warburg impedance is smaller at higher frequencies, because the diffusing reactant does not need to go very far [63]. The value of capacitance as a function of frequency can be evaluated using EIS.

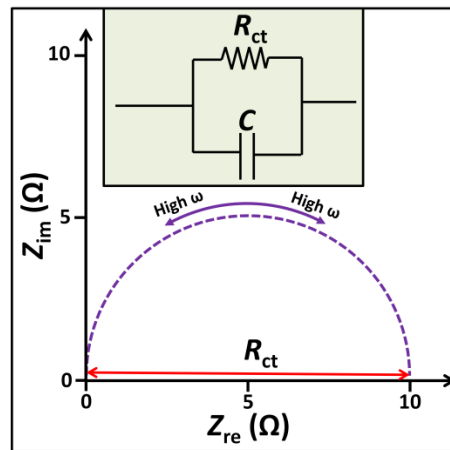


Figure 2.19: Nyquist plot with electrical equivalent circuit consisting charge R_{ct} in parallel with C [64].

A SC behaves as a pure resistor and capacitor at low and high frequencies, respectively. Moreover, in the medium frequency range, the physical and morphological properties of electroactive material play a crucial role in achieving the capacitance value and serving as an association of resistors and capacitors. The obtained data fitted with different interface parameters and attained algorithms. Inset circuit shows equivalent circuit corresponding to Nyquist plot. The sinusoidal voltage and current signals are written as,

$$V(\omega) = V_0 e^{i\omega t} \quad (2.17)$$

$$I(\omega) = I_0 e^{i\omega t - \phi} \quad (2.18)$$

The complex quantity is written as,

$$Z(\omega) = Z_0 e^{i\phi} = Z_0 e^{(\cos\phi + i \sin\phi)} \quad (2.19)$$

The expression for $Z(\omega)$ is composed of a real and an imaginary part.

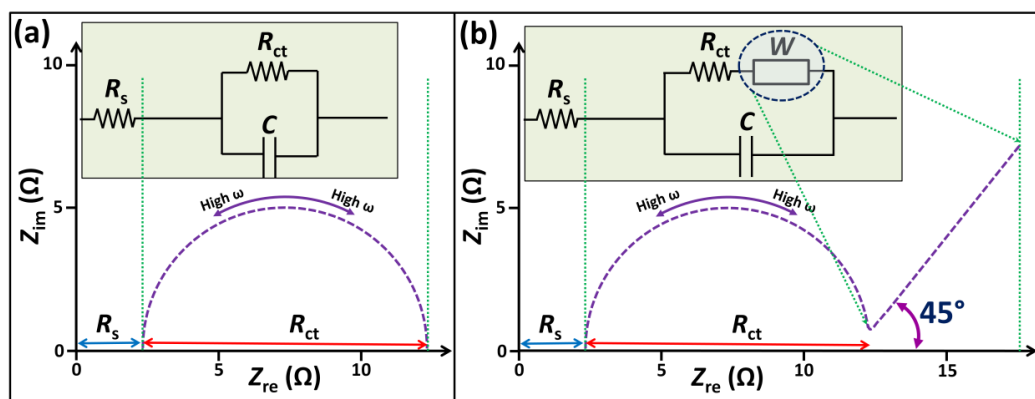


Figure 2.20: Nyquist plots with corresponding electrical equivalent circuit a) consisting R_s , R_{ct} and, C , and b) consisting R_s , R_{ct} , C , and W .

All electrochemical tests mentioned above (section 2.4.2) were analysed using ZIVE MP1 electrochemical workstation. The collected data was utilized to evaluate electrochemical properties such as C_s , S_E , S_P , R_s and R_{ct} . The EIS measurement was performed at AC amplitude of 5 mV in between frequency range of 0.01 Hz to 0.1 MHz at bias potential of open circuit potential. To analyse EIS data and obtain equivalent circuit “ZSimpWin” editor was used.

References:

- [1] S. V. Ganachari, N. R. Banapurmath, B. Salimath, J. S. Yaradoddi, A. S. Shettar, A. M. Hunashyal, A. Venkataraman, P. Patil, H. Shoba, Gurusiddesh B. Hiremath, Handbook of ecomaterials. Springer, Cham. (2017) 1-21.
- [2] L. E. Murr, Handbook of materials structures, Properties, Processing and Performance, (2016) 1–15.
- [3] M. Benelmekkia, A. Erbe, Nanostructured thin films, 14 (2019) 1-24.
- [4] R. D. Gould, S. Kasap, A. K. Ray, Thin Films, Springer Handbook of Electronic and Photonic Materials (2017), DOI: 10.1007/978-3-319-48933-9-28.
- [5] L. B. Freund, S. Suresh, Thin film materials, Cambridge University Press, Cambridge, UK, 2008.
- [6] A. Rockett, The materials science of semiconductors, Springer US, Boston, (2008) 289–356, DOI: 10.1007/978-0-387-68650-9.
- [7] C. D. Lokhande, Chemical deposition of metal chalcogenide thin films, Mater. Chem. Phys., 28 (1991) 45-149, DOI: 10.1016/0254-0584(91)90158-Q.
- [8] Z. Cao, Thin Film Growth, Woodhead publishing series in electronic and optical materials, (2011) 185-210 DOI: 10.1533/9780857093295.2.185.

-
- [9] J. L. Robins, Thin film nucleation and growth kinetics, *Appl. Surf. Sci.*, 33/34 (1988) 379-394, DOI: 10.1016/0169-4332(88)90330-3.
- [10] M. Ristov, G. J. Sinadinovski, I. Grozdanov, Chemical deposition of Cu₂O thin films, *Thin solid films*, 123 (1985) 63-67, DOI: 10.1016/0040-6090(85)90041-0.
- [11] Y. F. Nicolau, J. C. Menard, Solution growth of ZnS, CdS and Zn_{1-x}Cd_xS thin films by the successive ionic-layer adsorption and reaction process; growth mechanism, *J. Cryst. Growth*, 92 (1988) 128-142, DOI: 10.1016/0022-0248(88)90443-5.
- [12] Y. F. Nicolau, Solution deposition of thin solid compound films by a successive ionic-layer adsorption and reaction process, *Appl. Surf. Sci.*, 22/23 (1985) 1061-1074, DOI: 10.1016/0378-5963(85)90241-7.
- [13] M. Birkholz, P. F. Fewster, C. Genzel, *Thin film analysis by X-ray scattering*, Wiley-VCH, 2006, 1-30.
- [14] V. Petkov, Nanostructure by high-energy X-ray diffraction, *Mater. Today*, 11 (2008) 28-38, DOI: 10.1016/S1369-7021(08)70236-0.
- [15] <http://xrd.co/component-parts-x-ray-diffractometer>.
- [16] <https://www.rigaku.com/products/xrd/miniflex>.
- [17] B. D. Cullity, "Elements of X-rays Diffraction", Second ed., Addison-Wesley, London (1978).
- [18] <https://www.findlight.net/blog/2019/03/27/ftir-principles-applications/>
- [19] <https://www.sigmaaldrich.com/technical-documents/articles/biology/ir-spectrum-table.html#ir-table-by-compound>.
- [20] <https://www.bruker.com/products/infrared-near-infrared-and-raman-spectroscopy/ft-ir-routine-spectrometers/compact-ftir-alpha-ii.html>.
- [21] A. Munajad, C. Subroto, Suwarno, Fourier transform infrared (FTIR) spectroscopy analysis of transformer paper in mineral oil-paper composite insulation under accelerated thermal aging, *Energies*, 11 (2018) 364, DOI: 10.3390/en11020364.
- [22] https://en.wikipedia.org/wiki/Raman_spectroscopy.
- [23] I. J. D. Ebenezar, S. Ramalingam, C. R. Raja, P. C. J. Prabakar, Vibrational spectroscopic [IR and Raman] analysis and computational investigation [NMR, UV-Visible, MEP and Kubo gap] on L-Valinium Picrate, *J. Nano. Adv. Mat.*, 2 (2014) 11-25, DOI: 10.12785/jnam/020102.
- [24] J. A. Breier, S. N. White, C. R. German, Mineral-microbe interactions in deep-sea hydrothermal systems: a challenge for Raman spectroscopy, *Phil. Trans. R. Soc. A*, 368 (2010) 3067-3086, DOI: 10.1098/rsta.2010.0024.
-

- [25] A. Downes, A. Elfick, Raman spectroscopy and related techniques in biomedicine, *Sensors*, 10 (2010) 1871-1889, DOI: 10.3390/s100301871.
- [26] <https://bwtek.com/raman-components-of-a-raman-spectrometer/>
- [27] https://www.mt.com/in/en/home/applications/L1_AutoChem_Applications/Raman-Spectroscopy.html
- [28] H. Vašková, International journal of mathematical models and methods in applied sciences, 5 (2011) 1205-1212, <https://www.naun.org/main/NAUN/ijmmas/17-120.pdf>.
- [29] <https://www.thermofisher.com/blog/microscopy/sputter-coating-for-sem-how-this-sample-preparation-technique-assists-your-imaging/>
- [30] Morphological Characterization of Nanomaterials, A. Mayeen, L. K. Shaji, A. K. Nair, N. Kalarikkal, *Advances and key technologies, micro and nano technologies*, 2018, 335-364, DOI: 10.1016/B978-0-08-101973-3.00012-2
- [31] <https://www.hitachi-hightech.com/global/science/products/microscopes/electron-microscope/fe-sem/>.
- [32] http://mcff.mtu.edu/acmal/electronmicroscopy/FE_Form_Function.html.
- [33] Y. Jusman, S. C. Ng, N. A. A. Osman, Investigation of CPD and HMDS sample preparation techniques for cervical cells in developing computer-aided screening system based on FE-SEM/EDX, *Sci. World J.*, 2014 (2014) 1-11, DOI: 10.1155/2014/289817.
- [34] https://epm.univie.ac.at/fileadmin/user_upload/p_epm/xps-machine.png.
- [35] <http://www.ramehart.com/790.htm>.
- [36] M. M. Vadiyar, S. C. Bhise, S. K. Patil, S. S. Kolekar, A. Shelke, N. Deshpande, J. Chang, K. Ghule, A. V. Ghule, Contact angle measurements: a preliminary diagnostic tool for evaluating the performance of ZnFe₂O₄ nano-flake based supercapacitors, *Chem. Commun.*, 52 (2016) 2557-2560, DOI: 10.1039/C5CC08373G.
- [37] T. T. Chau, W. J. Bruckard, P. T. L. Koh, A. V. Nguyen, A review of factors that affect contact angle and implications for flotation practice, *Adv. Colloid Interface Sci.*, 150 (2009) 106-115, DOI: 10.1016/j.cis.2009.07.003.
- [38] P. Sinha, A. Datar, C. Jeong, X. Deng, Y. G. Chung, L. Lin, Surface area determination of porous materials using the Brunauer–Emmett–Teller (BET) method: Limitations and improvements, *J. Phys. Chem. C*, 123 (2019) 20195-20209, DOI: 10.1021/acs.jpcc.9b02116.
- [39] http://www.pharmacopeia.cn/v29240/usp29nf24s0_c846.html.

-
- [40] D. P. Lapham, J. L. Lapham, BET surface area measurement of commercial magnesium stearate by krypton adsorption in preference to nitrogen adsorption, *Int J Pharm.*, 568 (2019) 118522, DOI: 10.1016/j.ijpharm.2019.118522.
- [41] A. C. Forse, C. Merlet, J. M. Griffin, C. P. Grey, New perspectives on the charging mechanisms of supercapacitors, *J. Am. Chem. Soc.*, 138 (2016) 5731-5744, DOI: 10.1021/jacs.6b02115.
- [42] A. Afif, S. M. Rahman, A. T. Azad, J. Zaini, M. A. Islan, A. K. Azad, Advanced materials and technologies for hybrid supercapacitors for energy storage – A review, *J. Energy Storage*, 25 (2019) 100852, DOI: 10.1016/j.est.2019.100852.
- [43] Y. Wu, C. Cao, The way to improve the energy density of supercapacitors: Progress and perspective, *Sci. China Mater.*, 61 (2018) 1517-1526, DOI: 10.1007/s40843-018-9290-y.
- [44] J. Park, B. Kim, Y. Yoo, H. Chung, W. Kim, Energy density enhancement of carbon-nanotube-based supercapacitors with redox couple in organic electrolyte, *ACS Appl. Mater. Interfaces*, 6 (2014) 19499-19503, DOI: 10.1021/am506258s.
- [45] S. D. Perera, X. Ding, A. Bhargava, R. Hovden, A. Nelson, L. F. Kourkoutis, R. D. Robinson, Enhanced supercapacitor performance for equal Co-Mn stoichiometry in colloidal $\text{Co}_{3-x}\text{Mn}_x\text{O}_4$ nanoparticles, in additive-free electrodes, *Chem. Mater.*, 27 (2015) 7861-7873, DOI: 10.1021/acs.chemmater.5b02106.
- [46] Y. Shao, M. F. El-Kady, J. Sun, Y. Li, Q. Zhang, M. Zhu, H. Wang, B. Dunn, R. B. Kaner, Design and mechanisms of asymmetric supercapacitors, *Chem. Rev.*, 118 (2018) 9233-9280, DOI: 10.1021/acs.chemrev.8b00252.
- [47] V. Augustyn, P. Simon, B. Dunn, Pseudocapacitive oxide materials for high-rate electrochemical energy storage, *Energy Environ. Sci.*, 7 (2014) 1597-1614, DOI: 10.1039/c3ee44164d.
- [48] V. Climent, J. M. Feliu, Single crystal electrochemistry as an in situ analytical characterization tool, *Annu. Rev. Anal. Chem.*, 13 (2020) 201-222, DOI: 10.1146/annurev-anchem-061318-115541.
- [49] M. V. Portales, A. R. L. Fraga, A. M. D. García, O. García-Zaldívar, A. P. Barranco, M. A. A. Frutis, Cyclic voltammetry and impedance spectroscopy analysis for graphene-modified solid-state electrode transducers, *J. Solid State Electrochem.*, 22 (2018) 471–478, DOI: 10.1007/s10008-017-3776-z.
- [50] A. Wardak, H. T. Tien, Cyclic voltammetry studies of bilayer lipid membranes deposited on platinum by self assembly, *Bioelectrochem. Bioenerg.*, 24 (1990) 1-11, DOI: 10.1016/0302-4598(80)85001.
- [51] H. Qu, M. Harada, T. Okada, Voltammetry of Viologens Revealing Reduction of Hydrophobic Interaction in Frozen Aqueous Electrolyte Solutions, *ChemElectroChem*, 4 (2017) 35-38, DOI: 10.1002/celec.201600560.
- [52] C. Peng, G. A. Snook, D. J. Fray, M. S. P. Shaffer, G. Z. Chen, Carbon nanotube stabilised emulsions for electrochemical synthesis of porous nanocomposite
-

- coatings of poly[3,4-ethylene-dioxythiophene], *Chem. Commun.*, 44 (2006) 4629-4631, DOI: 10.1039/B609293D.
- [53] R. J. Bushby, O. R. Lozman, L. A. Mason, N. Taylor, S. Kumar, *Cyclic Voltammetry Studies of Discotic Liquid Crystals*, *Mol. Cryst. Liq. Cryst.*, 410 (2004) 171-181, DOI: 10.1080/15421400490436313.
- [54] D. Qazzazie, O. Yurchenko, S. Urban, J. Kieninger, G. Urban, *Platinum nanowires anchored on graphene-supported platinum nanoparticles as a highly active electrocatalyst towards glucose oxidation for fuel cell applications*, *Nanoscale*, 9 (2017) 6436-6447, DOI: 10.1039/C7NR01391D.
- [55] R. R. Salunkhe, Y. V. Kaneti, Y. Yamauchi, *Metal-organic framework-derived nanoporous metal oxides toward supercapacitor applications: progress and prospects*, *ACS Nano*, 11 (2017) 5293-5308, DOI: 10.1021/acsnano.7b02796.
- [56] P. Veerakumar, A. Sangili, S. Manavalan, P. Thanasekaran, K. Lin, *Research progress on porous carbon supported metal/metal oxide nanomaterials for supercapacitor electrode applications*, *Ind. Eng. Chem. Res.*, 59 (2020) 6347-6374, DOI: 10.1021/acs.iecr.9b06010.
- [57] B. K. Kim, S. Sy, A. Yu, J. Zhang, *Handbook of Clean Energy Systems*, (2015) 1-25, DOI: 10.1002/9781118991978.hces112.
- [58] K. S. Kumar, N. Choudhary, Y. Jung, J. Thomas, *Recent advances in two-dimensional nanomaterials for supercapacitor electrode applications*, *ACS Energy Lett.*, 3 (2018) 482-495, DOI: 10.1021/acsenerylett.7b01169.
- [59] K. Breitsprecher, C. Holm, S. Kondrat, *Charge me slowly, I am in a hurry: optimizing charge-discharge cycles in nanoporous supercapacitors*, *ACS Nano*, 12 (2018) 9733-9741, DOI: 10.1021/acsnano.8b04785.
- [60] N. R. Chodankar, H. D. Pham, A. K. Nanjundan, J. F. S. Fernando, K. Jayaramulu, D. Golberg, Y. Han, D. P. Dubal, *True meaning of pseudocapacitors and their performance metrics: asymmetric versus hybrid supercapacitors*, *small*, 16 (2020) 2002806, DOI: 10.1002/sml.202002806.
- [61] B. Mei, O. Munteshari, J. Lau, B. Dunn, L. Pilon, *Physical interpretations of nyquist plots for edlc electrodes and devices*, *J. Phys. Chem. C*, 122 (2018) 194-206, DOI: 10.1021/acs.jpcc.7b10582.
- [62] D. K. Kampouris, X. Ji, E. P. Randviira, C. E. Banks, *A new approach for the improved interpretation of capacitance measurements for materials utilised in energy storage*, *RSC Adv.*, 5 (2015) 12782-12791, DOI: 10.1039/C4RA17132B.
- [63] A. R. C. Bredar, A. L. Chown, A. R. Burton, B. H. Farnum, *Electrochemical impedance spectroscopy of metal oxide electrodes for energy applications*, *ACS Appl. Energy Mater.*, 3 (2020) 66-98, DOI: 10.1021/acsaem.9b01965.
- [64] B. Mei, J. Lau, T. Lin, S. H. Tolbert, B. S. Dunn, L. Pilon, *Physical interpretations of Nyquist plots for EDLC electrodes and devices*, *J. Phys. Chem. C*, 122 (2018) 24499-24511, DOI: 10.1021/acs.jpcc.7b10582.

CHAPTER – III

**CuS and CuS@rGO thin films by SILAR
method: Characterization and
electrochemical performance**

Chapter-III

CuS and CuS@rGO thin films by SILAR method: Characterization and electrochemical performance

3.1	Introduction.....	71
3.2	Synthesis of CuS and CuS@rGO thin films.....	72
3.2.1	Introduction	72
3.2.2	Experimental details	73
3.2.2.1	<i>Cleaning of substrate.....</i>	73
3.2.2.2	<i>Chemicals.....</i>	73
3.2.2.3	<i>Synthesis of rGO</i>	73
3.2.2.4	<i>Synthesis of CuS thin films.....</i>	74
3.2.2.5	<i>Synthesis of CuS@rGO thin films.....</i>	75
3.3	Material characterizations.....	76
3.3.1	Physico-chemical characterizations.....	76
3.3.2	Electrochemical characterizations.....	76
3.4	Results and discussion.....	77
3.4A	Physico-chemical characterizations.....	77
3.4A.1	<i>Physico-chemical characterizations of CuS thin films.....</i>	77
3.4A.2	<i>Physico-chemical characterizations of CuS@rGO thin films.....</i>	82
3.4B	Electrochemical characterizations.....	88
3.4B.1	<i>Electrochemical characterizations of CuS thin films.....</i>	88
3.4B.2	<i>Electrochemical characterizations of CuS@rGO thin films.....</i>	95
3.5	Conclusions.....	101
	References.....	101

3.1 Introduction

Increasing applications of portable and lightweight electronics require a suitable energy storage device with long life, flexibility, safety, and environment friendly nature. The LIBs and SCs are convenient to use in portable electronics as energy storage devices. Both of them store energy with different mechanisms, the former via bulk redox reactions, and the latter by electrostatically, (carbon materials) [1] or via reversible redox reactions, (transition metal chalcogenides, silicates, carbides, nitrides, and phosphates) [2].

The SCs are most promising energy storage device so far as life, S_p , and safety are concerned. The scientific community is engaged in uplifting the charge storage capability of the SCs by employing the large number of materials prepared through different methods of synthesis, electrolytes used in SCs, and the most important, design of the SCs. A feasible way is to increase the working potential of the SCs, as the energy stored (E) is $E = 0.5C_s V^2$; where C_s is the specific capacitance and V is the operating potential window of the SCs device. Currently, the market of SCs is dominated by EDLC materials, as it is economical and highly stable. However, considering charge storage capacity, EDLC materials lag behind pseudocapacitive materials. Therefore, it is necessary to investigate the composite electrode material which stores energy via both EDLC and pseudocapacitive mechanisms and capable of operating stably at high voltage with long life cycles [3, 4].

In the past few years, composite materials based on carbon allotropes (graphene oxide (GO), rGO, graphene foam, and CNTs) and transition metal chalcogenides (MnO_2 , Co_2S_3 , Fe_2O_3 , NiO, CuS, etc.) [5] have shown great potential as supercapacitive electrode material. The rGO provides large surface area for growth of the pseudocapacitive nanoparticles which produces many electroactive sites of an electrode and also a lateral path for electron conduction. The optimization of the EDLC and pseudocapacitive materials, the size of nanoparticles, and surface microstructure via synthesis method is required for better electron transfer [6]. Construction of successive layered structure of rGO and metal chalcogenide nanomaterials to provide the stable interactive surface of the electrode is the current need of the SCs device [7]. The layered structural growth of the material attracts more attention due to high thermodynamic stability, more accessible active sites and

superior control over the thickness of electrode which impact S_E and S_P of the SC device [8-10].

Earlier, several chemical deposition methods such as hydrothermal [11, 12], CBD [13], SILAR [14], electrodeposition [15], and chemical conversion route [16] are used to prepare CuS thin films with various morphologies. Huang et al. [17] prepared CuS nanosheets by hydrothermal method assisted with or without surfactants. The high C_s and good cycling stability are shown by CuS prepared without surfactants. Hollow copper sulfide nanosphere/GO core shell nanocomposite synthesized by Han et al. [18] using template assisted approach for drug delivery application. Jin et al. [19] electrodeposited CuS nanosheets on carbon cloth composite which displayed outstanding C_a of 4676 mF cm^{-2} at 2 mA cm^{-2} . Xu et al. [20] fabricated spherical clusters composed of CuS nanosheets and obtained a high C_s of 276 F g^{-1} at the scan rate of 5 mV s^{-1} . Yang et al. [21] prepared CuS coated multiwalled CNTs and compared their supercapacitive performance in NaOH and Na_2SO_4 electrolyte and observed that CuS and CuS/MWCNT show high C_s and excellent cyclic stability in Na_2SO_4 electrolyte.

The present chapter deals with the synthesis of CuS and CuS@rGO thin films by SILAR method and their characterization.

3.2 Synthesis of CuS and CuS@rGO thin films

3.2.1 Introduction

The electrode material to be used in SC must have good electrical conductivity, appropriate pore size, high surface area, chemical, and thermal stability. The preparation method of electrode material is low cost and scalable to commercialize SCs in large scale applications. From these points of view, CuS and CuS@rGO films are fabricated on flexible stainless steel (SS) substrate. The porous electrode structure can be prepared by compositing rGO sheets with CuS nanoparticles grown by the SILAR method. Subsequently, CuS and CuS@rGO films were characterized using different techniques like XRD for structural analysis, FT-IR and Raman for chemical bonding study, XPS to determine chemical states, FE-SEM for surface microstructural studies, EDAX for elemental composition, and BET for determination of specific surface area of thin film material. Also, the wettability

measurement was carried out to study the interaction between CuS or CuS@rGO thin film electrodes with DDW.

3.2.2 Experimental details

3.2.2.1 Cleaning of substrate

In chemical methods, the substrate surface with extreme cleanness is an essential requirement to obtain good quality thin films. Furthermore, the impurity of any material acts as a nucleation centre on the substrate surface. The conducting substrate is the prime requirement of SCs. The SS substrate is suitable for SC because of its high electrical conductivity and low cost. The substrate preparation includes polishing, washing through acetone, and DDW, and ultrasonication. The SS substrates were polished by zero grade polish paper, followed by successive cleaning using acetone and DDW. Then, substrates were ultrasonically cleaned for 10 min. Finally, substrates were air dried and used for the deposition of material.

3.2.2.2 Chemicals

Analytical reagent (AR) grade copper sulfate pentahydrate ($\text{CuSO}_4 \cdot 5\text{H}_2\text{O}$) and sodium sulfide (Na_2S) were used as received from Thomas Baker Chemicals Pvt. Ltd., India, without further purification. The commercially available flexible SS of thickness 0.3 mm (304 grade) was used as substrate. The DDW was used as a solvent throughout the experiment.

3.2.2.3 Synthesis of rGO

To prepare rGO, graphite was exfoliated to form GO suspension followed by chemical reduction. The GO suspension was prepared according to the previously reported method. 2 g graphite flakes of average diameter 100 μm and 100 mL concentrated H_2SO_4 were taken in 500 mL conical flask and kept into an ice bath with continuous stirring followed by addition of 1 g NaNO_3 . A 8 g KMnO_4 was slowly added to this mixture to maintain reaction temperature below 293 K. After complete addition, the reaction mixture was kept at room temperature with continuous stirring for 12 h. Then, 100 mL DDW was added followed by an additional 300 mL DDW and 8 mL H_2O_2 (30%) after 1.5 h. This makes the solution yellowish. Then, the mixture was washed through 5% HCl for a couple of times followed by DDW for

several times to obtain 6.5 pH. The concentration of GO slurry was determined using the gravimetric weight difference method and suspension of 0.1 mg mL^{-1} of GO was prepared which was sonicated for 4 h followed by the addition of 5 mL of hydrazine hydrate in 1000 mL of prepared solution. The prepared solution was kept at 368 K for 3 h to reduce graphene oxide sheets. The prepared dispersion of rGO was washed with DDW for several times to remove unwanted traces of hydrazine hydrate. The slurry of rGO was used for further deposition of thin film and characterization purpose. The whole process of synthesis of the rGO is schematically represented in Figure 3.1.

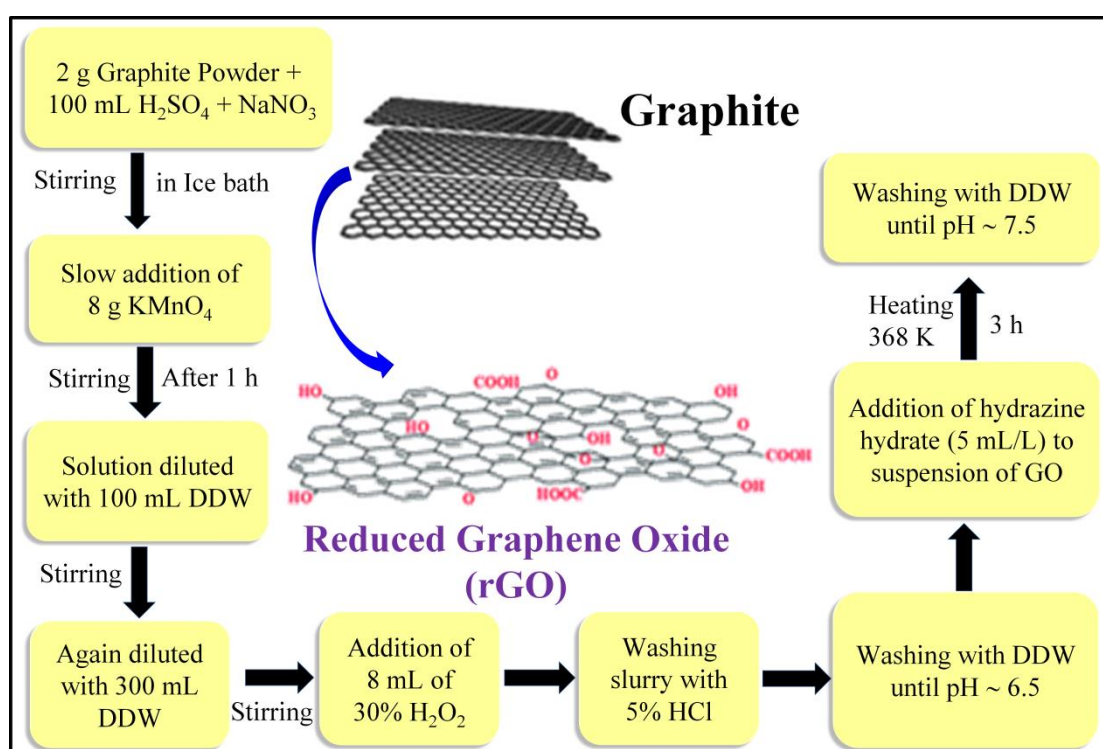


Figure 3.1: Schematic flow chart of rGO synthesis.

3.2.2.4 Synthesis of CuS thin films

To deposit CuS thin film; solutions of 0.1 M CuSO_4 (50 mL) and 0.05 M Na_2S (50 mL) were used as cationic and anionic source, respectively. The SS substrate was immersed in the cationic precursor for 30 s, followed by 25 s rinsing in DDW. The same substrate was immersed in an anionic precursor for 30 s for reaction purposes and further rinsed in DDW for 25 s to remove loosely bounded CuS molecules. Thus a single cycle of SILAR forms a monolayer of CuS; further, such 60, 80, 100, and 120 cycles were repeated to get different weight per unit area of CuS on SS substrate. The

mass loading of these films (Figure 3.2) was 0.0079 ± 0.001 , 0.0084 ± 0.001 , 0.0091 ± 0.001 , and $0.0093 \pm 0.001 \text{ mg cm}^{-2}$, respectively.

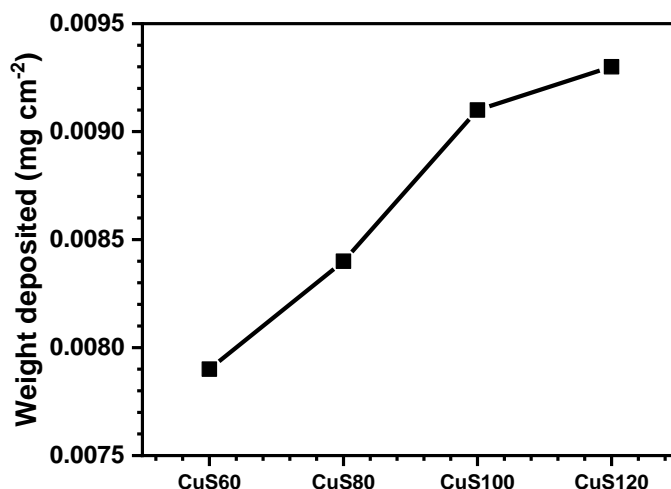


Figure 3.2: Graphical representation of weight deposited of CuS on SS substrate at 60 (CuS60), 80 (CuS80), 100 (CuS100), and 120 (CuS120) SILAR deposition cycles.

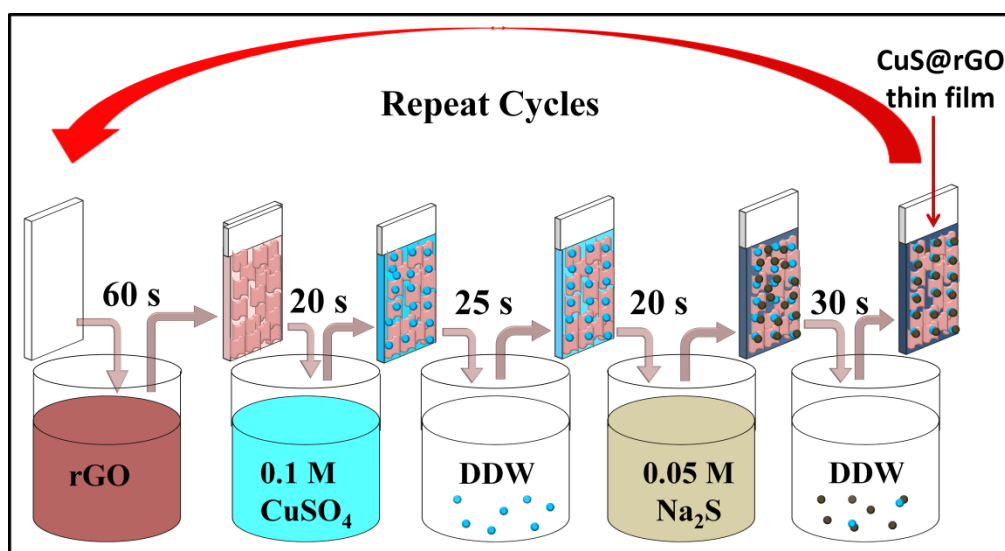


Figure 3.3: The schematic of SILAR method employed for CuS@rGO thin film electrode preparation.

3.2.2.5 Synthesis of CuS@rGO thin films

The concentration of rGO suspension was calculated by drying 1 mL of rGO solution at temperature of 373 K and then measuring weight. From the determined concentration, dispersions of rGO with concentration of 0.3, 0.4, 0.5, and 0.6 mg mL^{-1} were prepared in DDW. The rGO sheets were deposited on SS substrate using layer by layer method followed by single deposition cycle of CuS nanoparticles using the SILAR method. The schematic of CuS@rGO thin film preparation is shown in Figure

3.3, where, the SS substrate was dipped in rGO solution for 60 s for adsorption of rGO sheets, followed by insertion in cationic solution for 20 s, to adsorb Cu^{2+} ions. In this process, some Cu^{2+} species may react with extraplanar hydroxyl or carboxyl groups of rGO sheets. To remove loosely bound Cu^{2+} ions, SS substrate was rinsed in DDW for 25 s subsequently, and dipped in the anionic precursor (S^{2-}) for 20 s for reaction and again rinsed in DDW for 30 s. In this way, a cycle of CuS@rGO deposition was completed and 100 such cycles were repeated with different concentrations of rGO suspension. The process of deposition was carried out using an automated SILAR coating system (HOLMARC-HO-TH-03A) [22, 23]. Thin film growth becomes uniform as both rGO sheets and CuS have hexagonal structure. Thin film prepared with 0.3, 0.4, 0.5, and 0.6 mg mL^{-1} concentrations of rGO suspension are denoted as CuS@rGO3, CuS@rGO4, CuS@rGO5, and CuS@rGO6, respectively and mass loading of these films (Figure 3.4) was 0.0120 ± 0.001 , 0.0132 ± 0.001 , 0.0137 ± 0.001 , and $0.0140 \pm 0.001 \text{ mg cm}^{-2}$, respectively.

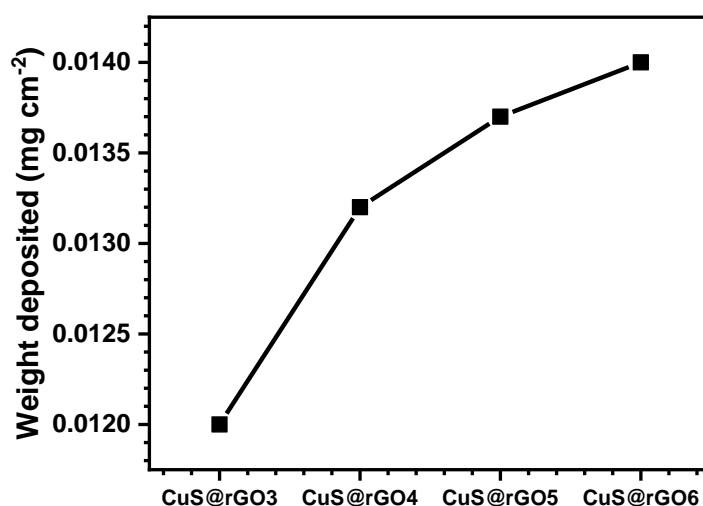


Figure 3.4: Graphical representation of weight deposited of CuS@rGO on SS substrate at various concentration of rGO suspension.

3.3 Material characterizations

3.3.1 Physico-chemical characterizations

The crystal structure and purity of the prepared thin films were analyzed using Rigaku miniflex-600 with Cu-K α radiation ($\lambda=1.5418 \text{ \AA}$) working at 30 kV, and the functional groups present in the synthesized material were analyzed using Bruker Tensor 27 FT-IR instruments. The surface structure of the samples was determined using FE-SEM (JEOL JEM 2100). Energy dispersive X-ray spectroscopy (EDAX)

attached to FE-SEM was employed to analyze the elemental composition. VG Multilab 2000, Thermo VG Scientific, UK with monochromatic Mg-K α (1253.6 eV) radiation source X-ray photoelectron spectroscope was used for the surface chemical composition of CuS@rGO film. The Raman analysis was performed using JASCO NRS-5100 with the $\lambda = 514.4$ nm. The contact angle measurement was carried out using the Rame-Hart instrument. The specific surface area and pore size distribution details were collected by Brunauer, Emmett, and Teller (BET) and Barrett-Joyner-Halenda (BJH) analysis model using Quantachrome Instruments v11.02.

3.3.2 Electrochemical characterizations

For investigation of electrochemical properties of various CuS and CuS@rGO thin films, the three electrode system was used which consists of CuS or CuS@rGO as a working electrode, saturated calomel electrode (SCE), and platinum sheet as a reference and counter electrode. All the measurements were carried out in 1 M LiClO₄ electrolyte at ambient temperature. 1 cm² area of the working electrode was exposed to the electrolyte. Figure 3.5 shows the electrochemical work station (Figure 3.5a), experimental setup (Figure 3.5b), and schematic for the electrochemical study (Figure 3.5c). The supercapacitive behavior of electrodes was evaluated in terms of C_s , electrochemical stability, R_s and R_{ct} . The CV, GCD, and EIS measurements were carried out using an electrochemical workstation (ZIVE MP1).

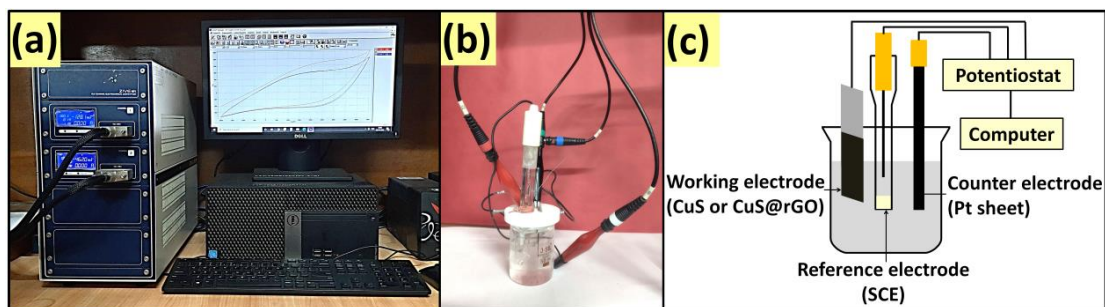


Figure 3.5: a) The electrochemical work station, b) experimental setup, and c) schematic representation of three electrode system.

3.3.2.1 Cyclic voltammetry (CV) study

The CV is an important technique for deciding redox potentials and electronic transfer redox reactions. It is used to determine C_s of electrode materials. The CV study was carried out in the potential window of -0.2 V to -1.1 V/SCE for CuS and

CuS@rGO thin film electrodes. The C_s of electrode material is calculated using Eq. 2.10. The charge storage mechanism was analyzed using power law.

3.3.2.2 Galvanostatic charge discharge (GCD) study

The GCD study was carried out in the same potential window as that of CV for CuS and CuS@rGO thin film electrodes. The nature of charge storage is determined by the shape of GCD curves. The C_s values of thin film electrodes are calculated using Eq. 2.12.

3.3.2.3 Electrochemical impedance spectroscopy (EIS)

The EIS analysis was carried out to understand the resistive parameters of electrode-electrolyte interface. The EIS measurement was used to characterize the interface quality between the electrode and electrolyte, by the electrochemical workstation (ZIVE MP1). The EIS study was performed with 5 mV potential amplitude in the frequency range of 0.01 Hz to 0.1 MHz at a bias of open circuit potential.

3.4 Results and discussion

3.4A Physico-chemical characterizations

3.4A.1 Physico-chemical characterizations of CuS thin films

3.4A.1.1 XRD study

The XRD patterns of CuS thin films deposited at different cycles are represented in Figure 3.6a. The diffraction peaks are assigned to (101), (103), (008), and (110) crystallographic planes, respectively. The observed planes correspond to hexagonal crystal structure with lattice parameter of $a = 3.77 \text{ \AA}$, $b = 3.77 \text{ \AA}$ and $c = 16.27 \text{ \AA}$ and intensities of these peaks are in good agreement with JCPDS card no. 01-078-0877. The crystallite size estimated along (110) plane was 26 nm using Scherrer's formula (Eq. 2.4). The XRD peaks highlighted by the symbol * correspond to SS substrate. No other diffraction peak was observed indicating the absence of any other impurity.

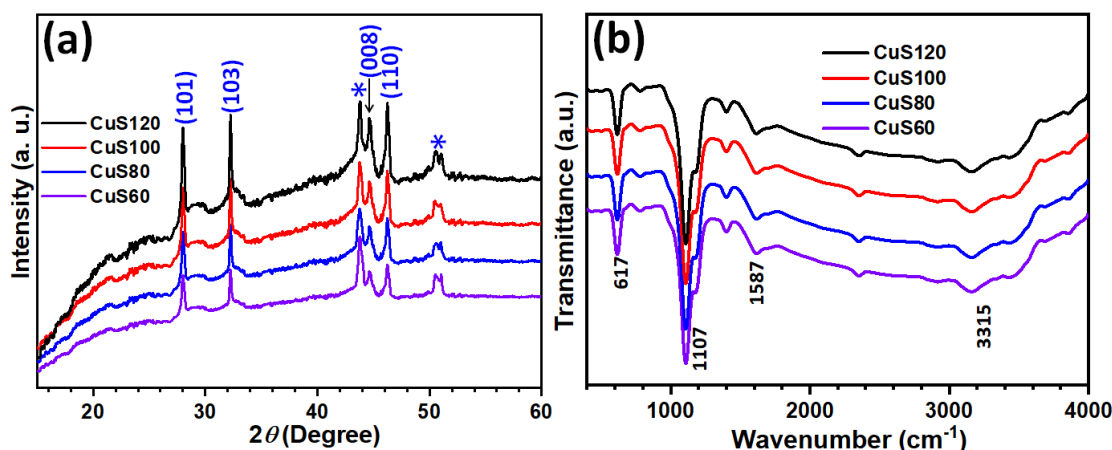


Figure 3.6: a) The XRD patterns and b) FT-IR spectra of CuS thin films deposited at different cycles.

3.4A.1.2 FT-IR study

The molecular bond vibrations in CuS thin films deposited at 60, 80, 100, and 120 cycles were investigated using FT-IR. The FT-IR absorption spectra in the wavenumber range of $4000\text{--}400\text{ cm}^{-1}$ of CuS are shown in Figure 3.6b. The strong absorption bands at 617 and 1107 are assigned to the characteristic absorption of CuS [24]. The broad absorption peak at 1587 cm^{-1} indicates the presence of -OH bond of adsorbed H_2O ; also, broad peak at 3315 cm^{-1} are associated with bonded and nonbonded -OH groups from adsorbed water molecules [25, 26]. The results of FT-IR study confirm presence of adsorbed water in the prepared CuS thin films. From the results, formation of CuS on SS substrate was confirmed.

3.4A.1.3 FE-SEM study

It is known that, the performance of active material is extensively related to morphology of electrode material. The material with microstructured morphology may improve specific surface area allowing easy adsorption/desorption of electrolytic ions and it enhances electrochemical performance of the electrode. The FE-SEM images of CuS thin films deposited at different cycles on the SS substrate at two different magnifications (10,000 X and 50,000 X) are shown in Figure 3.7. The FE-SEM images reveal the correlation between the deposition cycles and surface morphology. The random arrangement of particles is attributed to the higher reaction rate in the alkaline bath in which nucleation and grain growth take place simultaneously. The FE-SEM images of CuS60 film shown in Figure 3.7a and e,

indicate sponge like porous structure consists of uniform nanoparticles. The FE-SEM images of CuS80 electrode are shown in Figure 3.7b and f indicate increased deposition cycles affected microstructure of thin film. Figure 3.7f reveals a nanoflakes-like structure overgrown on spongy base. Also, these nanoflakes are connected to each other resulting in interconnected networks. With the increase in the deposition cycles of CuS thin film (for CuS100 thin film), nanoflakes like morphology with some individual overgrown particles is obtained (Figure 3.5c and g).

Similarly, CuS120 thin film (Figure 3.7d and h)) shows a cluster of nanoflowers, indicating that the sample consists of overgrown nanoparticles with an uneven porous structure having compact morphology. Most importantly, the nanoflakes are interconnected with each other, which help efficiently to carry electrons from active material to the current collector.

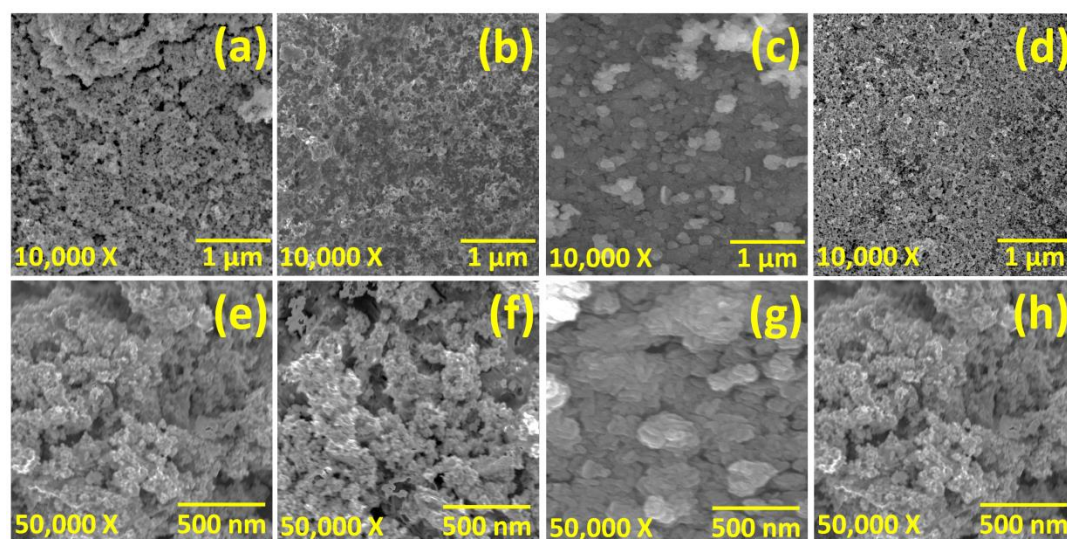


Figure 3.7: FE-SEM images of a) CuS60, b) CuS80, c) CuS100, and d) CuS120 at the magnification of 10,000 X, and e) CuS60, f) CuS80, g) CuS100, and h) CuS120 at the magnification of 50,000 X.

3.4A.1.4 EDAX study

The chemical composition of CuS thin films was investigated by EDAX and presented in Figure 3.8a-d. The EDAX spectra confirm the presence of Cu and S elements in a material without any other impurity. The atomic percentage of Cu in CuS100 thin film is 49.37% and that of S is 50.63%. The atomic percentage of constituting elements for CuS thin films is shown in inset of each image. The observed Cu:S atomic ratios for CuS60, CuS80, CuS100, and CuS120 thin film

electrodes are 0.9:1, 0.92:1, 0.97:1, and 0.97:1, respectively. The CuS thin film formation was confirmed from the EDAX analysis.

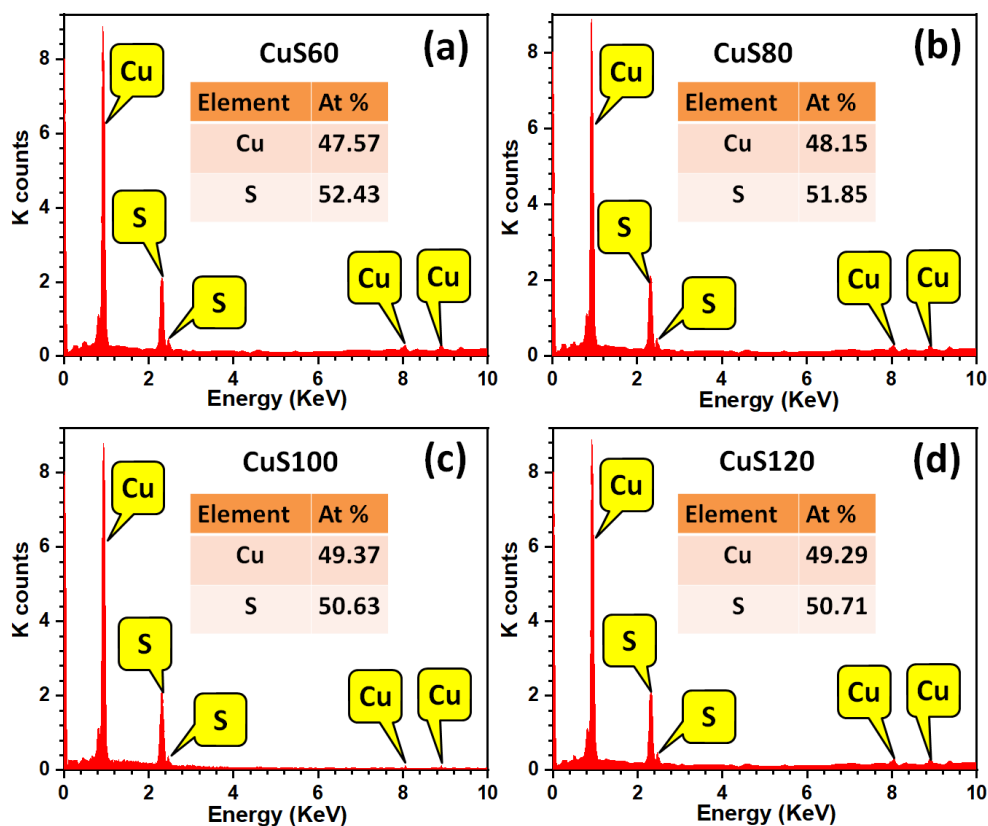


Figure 3.8: The EDAX spectra of a) CuS60, b) CuS80, c) CuS100, and d) CuS120 thin films (Insets show atomic percentages of constituting elements of CuS thin film).

3.4A.1.5 Raman study

The Raman spectroscopic study of CuS100 thin film was carried out using Ar laser with an excitation wavelength of 532 nm which explores the chemical bonding of the material. The Raman spectrum of CuS100 thin film recorded over 200-800 cm^{-1} is shown in Figure 3.9a. The sharp peak at wavenumber 473 cm^{-1} corresponds to S-S bonding in CuS film. Bulakhe et al. [27] and Tang et al. [28] reported similar results for Cu_2S compound.

3.4A.1.6 Contact angle measurement

The nature of surface structure of solid film creates considerable impact on the wettability of the water based electrolytes with film surface. The smaller contact angle and higher surface energy has profoundly positive influence on the electrochemical performance of the material. The particle shape, particle size, purity, roughness,

cleanliness of surface and heterogeneity affect the contact angle values [29-31]. The hydrophilic nature is suitable for SCs application as it provides more interface for electrolyte ions with active electrode. The water contact angle image of CuS film is shown in Figure 3.9b. The contact angle of CuS100 thin film is 47° . The porous surface of CuS100 film is beneficial for lower water contact angle. The hydrophilic nature of the thin film surface helps to create intimate contact with the water based electrolyte which may result in the lower resistances [32, 33].

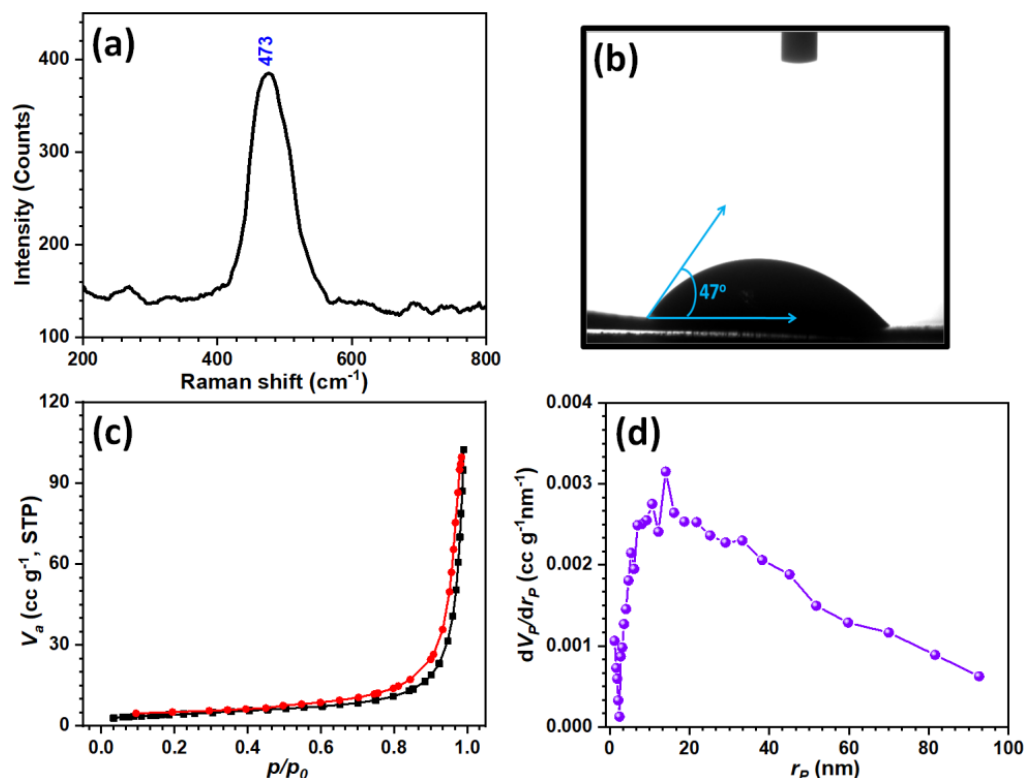


Figure 3.9: a) The Raman spectrum, b) photograph of water contact angle, c) N_2 sorption isotherms, and d) BJH pore size distribution curve of CuS100 thin film.

3.4A.1.7 BET study

It is well known that as the specific surface area of the electrode material increases, the charge accumulation on the electrode increase in proportion. The specific surface area and average pore size distribution of material scratched from the CuS100 thin film electrode were measured by N_2 sorption isotherms. CuS100 thin film exhibits type IV isotherms (Figure 3.9c) having a H3-type hysteresis curve in the range of 0.40 to 1.0 of relative pressure, indicating the presence of meso and micropores. The average pore diameter of the electrodes was analysed by Barrett-Joyner-Halenda (BJH) method and results are provided in Figure 3.9d. The BET

specific surface area of CuS100 sample is $32.4 \text{ m}^2 \text{ g}^{-1}$ and observed average pore diameter is 29 nm.

3.4A.2 Physico-chemical characterizations of CuS@rGO thin films

3.4A.2.1 XRD study

The XRD patterns of CuS@rGO3, CuS@rGO4, CuS@rGO5, and CuS@rGO6 thin films are shown in Figure 3.10a. Intense peaks correspond to (004), (102), (103), and (110) planes of hexagonal crystal structure of CuS (JCPDS card no. 01-078-0877). The variation in the peak intensity at $2\theta = 32.77^\circ$ indicates that the concentration of rGO affects the growth rate of CuS nanoparticles on rGO sheet. The orientation of CuS nanoparticles along the crystallographic plane (103) increases from CuS@rGO3 to CuS@rGO6 thin films. The calculated d values (from Eq. 2.3) match well with standard d value which confirms the hexagonal crystal structure of CuS in CuS@rGO thin films. The prominent diffraction peaks observed for CuS@rGO thin films are different from that of CuS thin films (Figure 3.6a). The crystallite size calculated using Scherrer's formula (Eq. 2.4) along (102) plane was 31 nm. Compared to the crystallite size of CuS, crystallite size of CuS@rGO is higher. The XRD peaks highlighted by the symbol * correspond to the SS substrate. No other diffraction peak is observed indicating the absence of any other impurity. XRD study confirms that composition of rGO with CuS affects growth of CuS particles.

3.4A.2.2 FT-IR study

The FT-IR absorption spectra in the wavenumber range of $4000\text{--}400 \text{ cm}^{-1}$ of rGO-CuS3 to rGO-CuS6 thin films are shown in Figure 3.10b. The strong bond absorptions at around 815 and 1107 cm^{-1} are assigned to the characteristic absorption of CuS. The absorption peak at 1324 cm^{-1} corresponds to -COOH symmetric stretch. The broad absorption peak at 1599 cm^{-1} indicates the presence of sp^2 bond of C-C in rGO; also, peaks at 3326 cm^{-1} is associated with bonded and nonbonded -OH groups from adsorbed water molecules. Compared to FT-IR spectrum of CuS thin films, additional absorption bands from the rGO is observed in the CuS@rGO thin films. From the results, the formation of CuS@rGO on SS substrate can be confirmed.

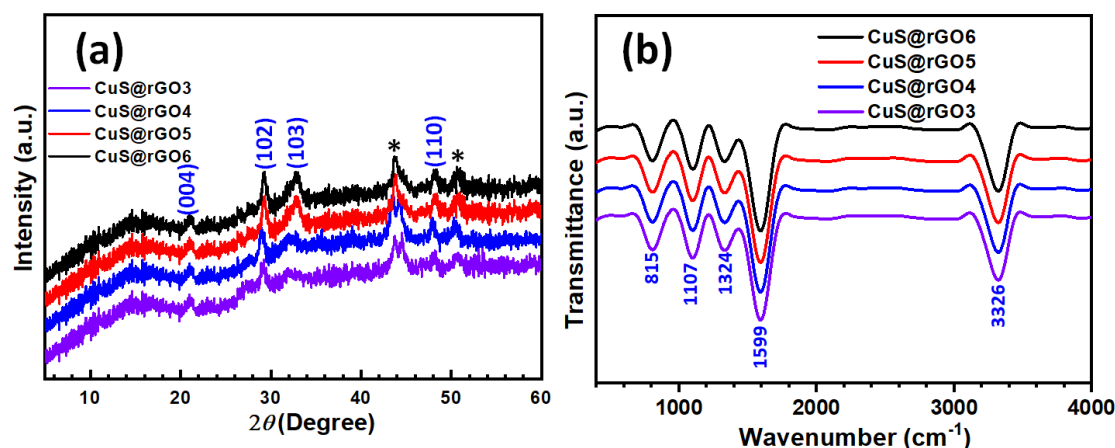


Figure 3.10: a) The XRD patterns and b) the FT-IR spectra of CuS@rGO thin films deposited using different concentrations of rGO suspension.

3.4A.2.3 FE-SEM study

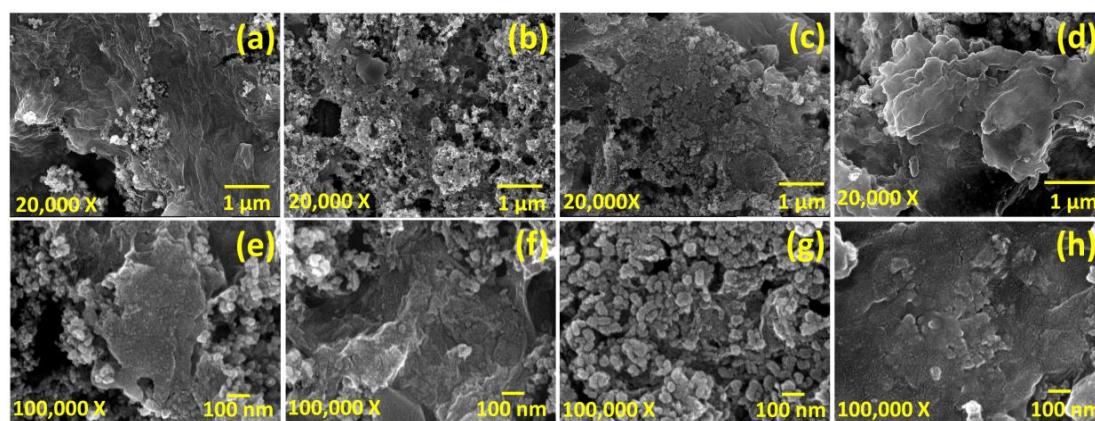


Figure 3.11: FE-SEM images of a) CuS@rGO3, b) CuS@rGO4, c) CuS@rGO5, and d) CuS@rGO6 at the magnification of 20,000 X, and e) CuS@rGO3, f) CuS@rGO4, g) CuS@rGO5, and h) CuS@rGO6 at the magnification of 100,000 X.

Microstructures of CuS@rGO thin films observed from FE-SEM at different magnifications are shown in Figure 3.11a-h. Figures 3.11a-d show images of the CuS@rGO thin films at 20,000 X magnification, displaying a discontinuous and irregularly arranged rGO sheets structure. Figures 3.11e-h show FE-SEM images at 100,000 X magnification which indicate rGO network is interconnected by CuS nanoparticles sandwiched between rGO sheets. The rGO sheets are uniformly coated with CuS nanoparticles in all thin films prepared at various concentration of rGO suspension. These nanoparticles prevent the staking of rGO sheets and also provide easy access to electrolyte ions at the bulk of electrode material through diffusion. Compared to FE-SEM images of CuS thin films (Figure 3.7), the pores are observed on topography of CuS@rGO thin films. These pores are beneficial for diffusion of electrolyte.

3.4A.2.4 EDAX study

The chemical composition of CuS@rGO thin films deposited using different concentrations of rGO suspension was investigated by the EDAX. The EDAX spectra of CuS@rGO thin films are shown in Figure 3.12a-d. The atomic percentages of C, O, S, and Cu elements are shown in the inset of each spectrum, which confirm the composite nature of the thin films. The approximately similar atomic percentage of Cu and S indicates the possible formation of CuS on rGO sheets. Slightly higher content of oxygen shows effective oxidation of the graphite flakes into rGO sheets. The rGO sheets have nonplaner oxygen containing groups which allow the growth of CuS nanoparticles, and also, these groups provide more active sites for interaction with Li^+ ions from electrolyte, which may increase the energy storage capacity of a composite thin film.

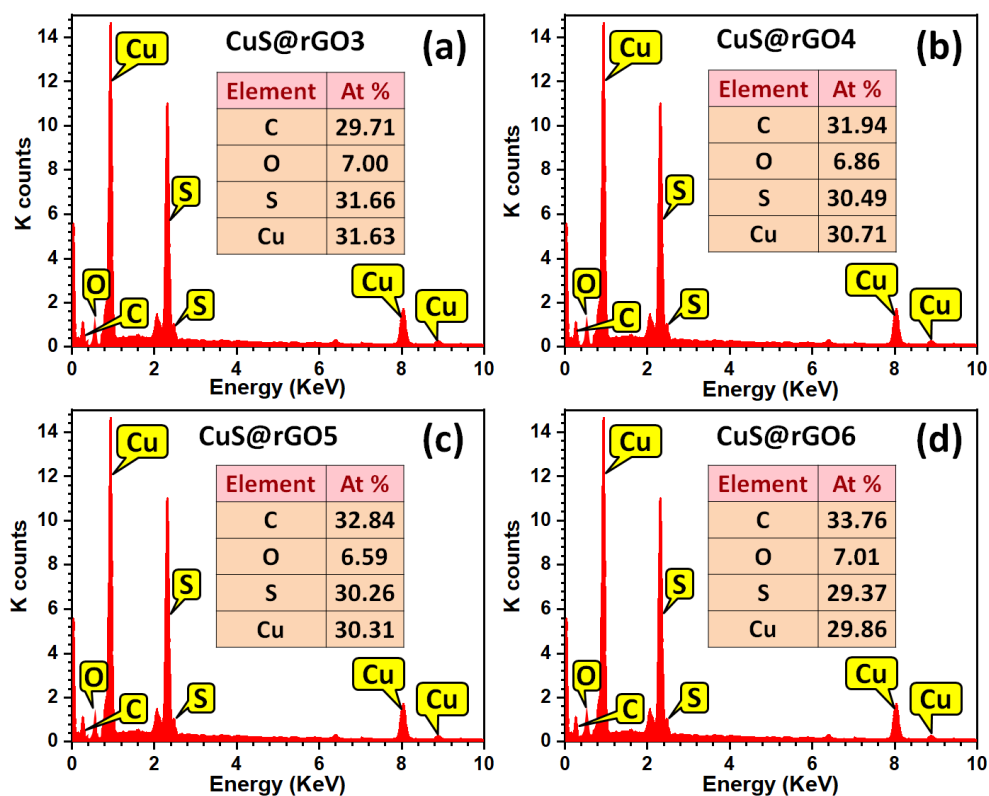


Figure 3.12: The EDAX spectra of a) CuS@rGO3, b) CuS@rGO4, c) CuS@rGO5, and d) CuS@rGO6 thin films (Insets show atomic percentages of constituting elements).

3.4A.2.5 XPS study

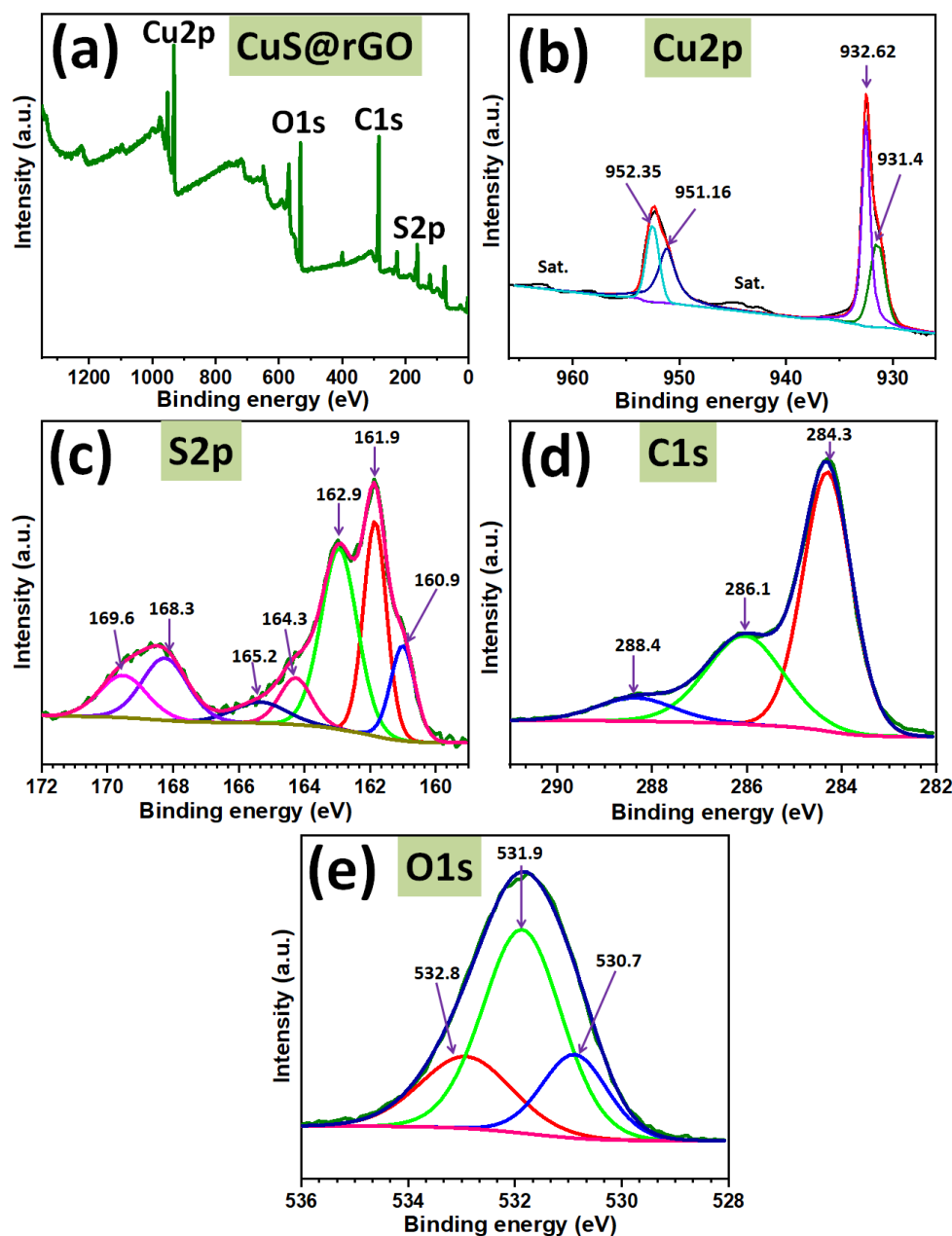


Figure 3.13: The XPS spectra of a) CuS@rGO film wide survey scan, b) Cu2p, c) S2p, d) C1s, and e) O1s.

The surface elemental composition and oxidation states of CuS@rGO film were investigated by the XPS. A wide survey scan of the XPS spectrum taken in the range of 0–1350 eV is displayed in Figure 3.13a. The observed peaks from elements Cu, S, O and C indicates possible formation of CuS@rGO composite thin film on SS substrate. The XPS of Cu2p peaks is deconvoluted in the binding energies of Cu2p_{1/2} (951.15 eV) and Cu2p_{3/2} (932.62 eV) as shown in Figure 3.13b. These peaks are deconvoluted into two components which are assigned to Cu²⁺ and Cu⁺ [34, 35]. The peaks at binding energies 931.4 and 951.16 eV are assigned to Cu and peaks at 932.62 and 952.35 eV correspond to Cu²⁺ states of Cu. Small satellite peaks correspond to

major peaks are observed. The XPS spectra of S2p (Figure 3.13c) indicate presence of sulfur in different chemical states. The peaks at 160.9, 161.9, and 162.9 eV are assigned to sulfide (S^{2-}), peaks at 164.3 and 165.2 eV to sulfite (S^{4+}), and peaks at 168.3 and 169.6 eV to sulfate (S^{6+}) species [36]. The XPS spectrum of C1s from rGO (Figure 3.13d) indicate three components that are related to C atoms in different functional groups; the peak at 284.3 eV indicates (C=C) ring of rGO, the peak at 286.1 eV indicates C-O bond confirming hydroxyl group attached to the rGO sheet, and peak of C (C=O) at 288.4 eV also confirms carboxylic group [37].

As shown in Figure 3.13e, the atomic percentage of O on the surface of the sample is very high, which is attributed to various oxidation states based on the differences in the position and shape of O1s peaks. The O1s signal of CuS@rGO could be deconvoluted into three Gaussian peaks. The peak at binding energy 531.9 eV attributed to lattice oxygen confirms formation of O-C bond, and other two peaks at 530.7 and 532.8 eV are attributed to nonlattice oxygen from the carboxyl, sulfonyl, and hydroxyl groups, respectively [38, 40]. The XPS study lights up the possible presence of Cu=S, C=S=O, C=O, O-Cu-S, C=C, C-C=O(OH), C=S(O)=O bonds in a composite CuS@rGO thin film [41].

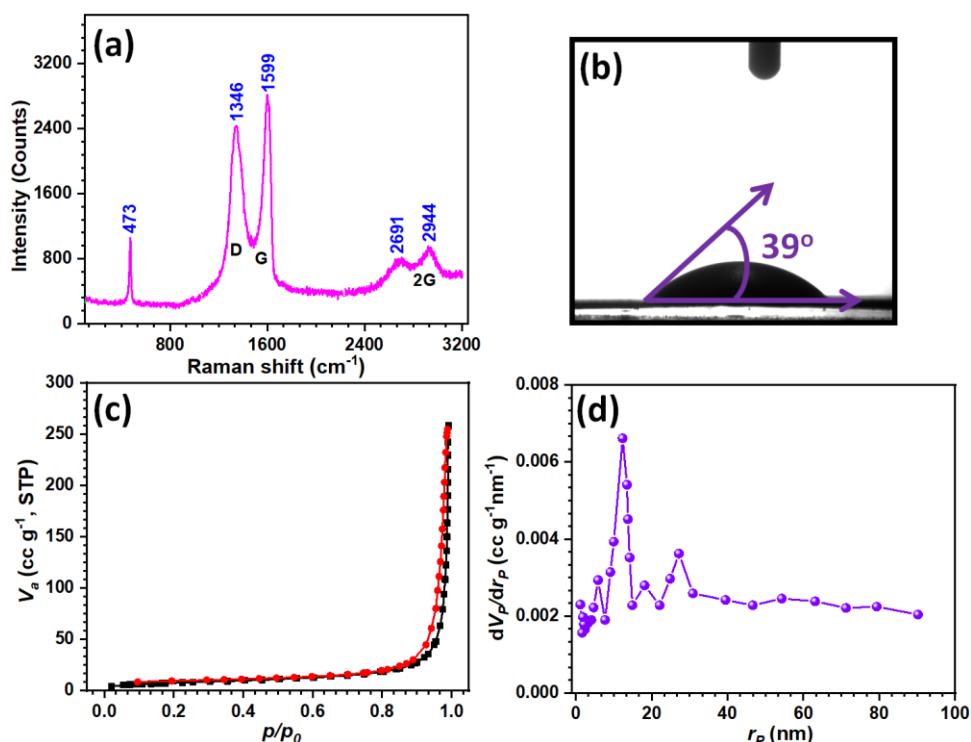


Figure 3.14: a) The Raman spectrum, b) water contact angle photograph, c) N₂ sorption isotherms, and d) BJH pore size distribution curve of CuS@rGO thin film deposited at 0.5 mL⁻¹ concentration of rGO suspension.

3.4A.2.6 Raman study

The Raman spectroscopic study of CuS@rGO5 film was carried out using Ar laser with an excitation wavelength of 532 nm which explores the chemical bonding of the material. The Raman spectrum of CuS@rGO thin film is shown in Figure 3.14a. The sharp peak at wavenumber 473 cm^{-1} corresponds to S-S bonding in CuS@rGO film. The sharpness of the peak confirms the formation of the crystallite form of CuS on the rGO sheets. Other peaks present at 1346 , 1599 cm^{-1} , and broad peaks at 2691 and 2944 cm^{-1} are related to the D, G, and 2D peaks of rGO sheets, respectively. More intensity of the D band indicates comparatively large defects in the rGO sheet which distorts the sp^2 hybridization to the sp^3 . This supports the results obtained from the FT-IR study of the samples.

The G peak helps in the quantitative analysis of the rGO sheet. The results obtained from the equation $I(\text{G})/I(2\text{D})$ indicate the mechanism of formation of CuS@rGO composite thin film. The broad 2D peak at 2692 cm^{-1} suggests formation of multilayered rGO sheets separated by CuS nanoparticles. The stacked rGO sheets with sp^2 hybridization provide an easy lateral path to conduct the electrons. This could decrease R_s of the thin film electrodes.

3.4A.2.7 Contact angle measurement

The contact angle with DDW for CuS@rGO5 thin film is shown in Figure 3.14b. The value of contact angle for CuS@rGO5 thin film electrode was 39° , indicate hydrophilic nature of films. The hydrophilic nature of thin film surface helps to create intimate contact with the water based electrolyte.

3.4A.2.8 BET study

To measure specific surface area and pore size distribution of thin films, BET and BJH techniques were employed, and N_2 adsorption-desorption isotherms of CuS@rGO5 is shown in Figure 3.14c. The specific surface area of CuS@rGO5 sample is $77.5\text{ m}^2\text{ g}^{-1}$. The BJH analysis gives a pore size distribution (Figure 3.14d) for the CuS@rGO5 sample with a mean pore size of 22 nm, indicating a mesoporous structure of thin films.

3.4B Electrochemical characterizations

3.4B.1 Electrochemical characterizations of CuS thin films

3.4B.1.1 CV study

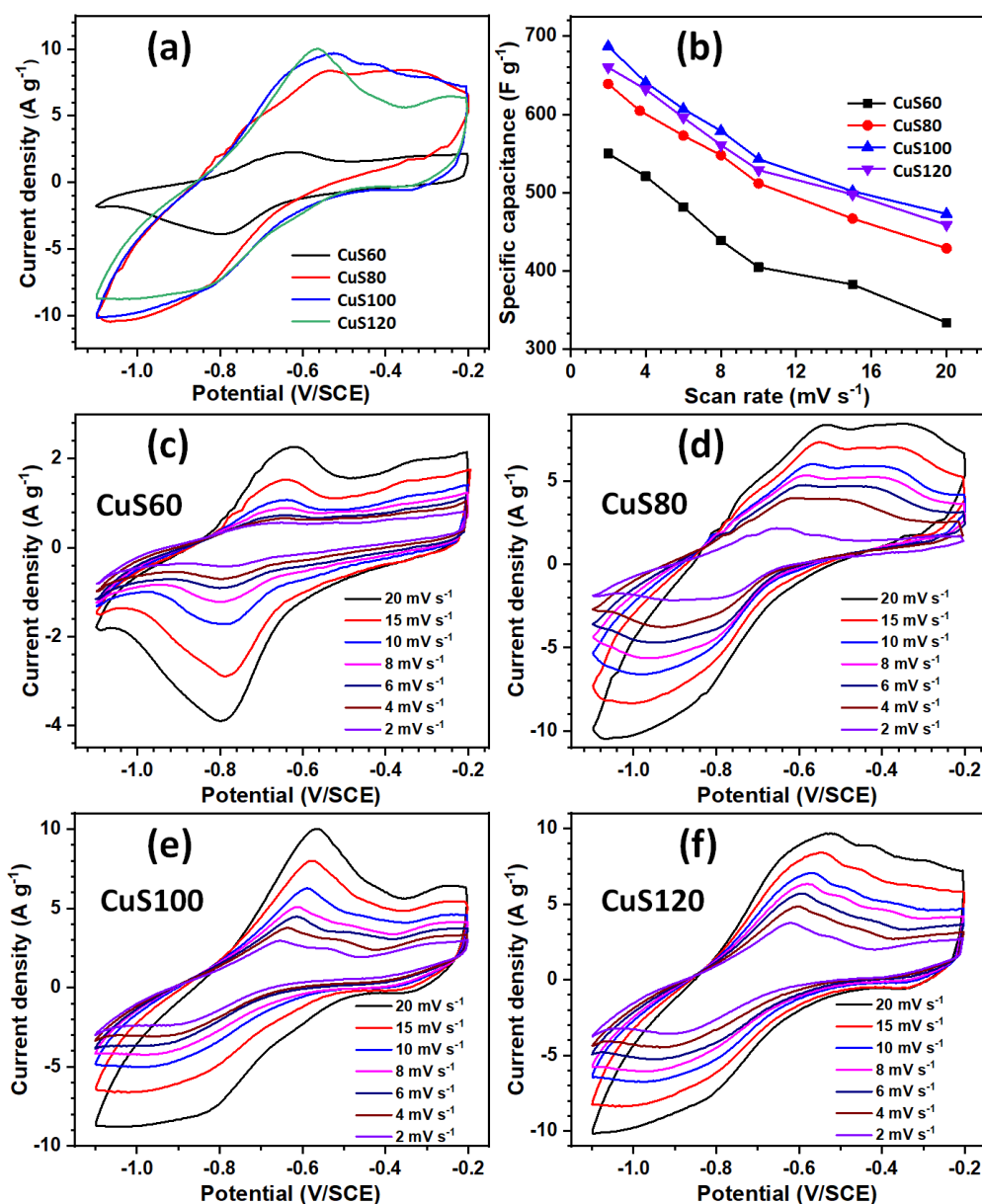


Figure 3.15: a) Comparative CV curves of CuS thin films at a scan rate of 20 mV s⁻¹, b) variation of C_s with the scan rates, and the CV curves at various scan rates from 2-20 mV s⁻¹ of c) CuS60, d) CuS80, e) CuS100, and f) CuS120 thin film electrodes.

The electrochemical evaluation of CuS thin films was carried out in an aqueous 1 M LiClO₄ electrolyte. The potential window for CuS electrode is -0.2 to -1.1 V/SCE. The CV curves for CuS thin films deposited at various cycles are shown in Figure 3.15a. From CV curves, it is seen that strong oxidation and reduction peaks for CuS arise at a potential of -0.57 and -0.79 V/SCE, respectively. The area under CV curves is directly proportional to the scan rate. The current response of CuS100

film electrode in CV curves is more, indicating CuS100 may facilitate fast electronic and ionic transport. The change of oxidation states of Cu^{2+} at an interface of CuS and electrolyte is shown in the following equation,

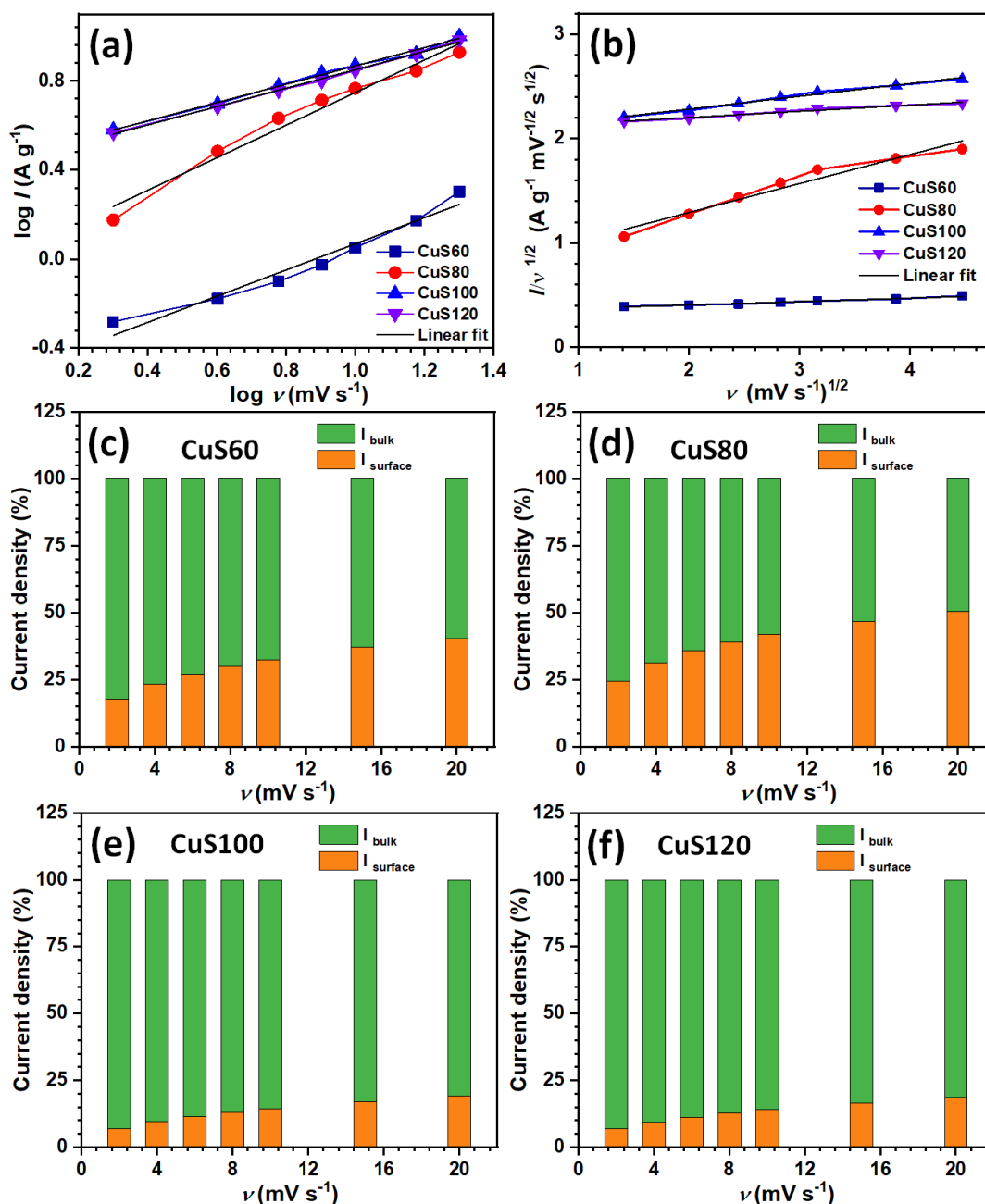


Figure 3.16: a) Plots of $\log I$ against $\log \nu$, b) plots of $I/\nu^{1/2}$ against $\nu^{1/2}$ for CuS thin film electrodes; and contribution of capacitive and diffusion controlled currents for c) CuS60, d) CuS80, e) CuS100, and f) CuS120 thin film electrodes.

The Li^+ ions from electrolyte adsorbed on the CuS surface get oxidised at desired potential, converting Cu^{2+} to Cu^+ . In the reverse scan these $\text{Cu}^{(\text{I})}\text{S} \cdot \text{Li}_x^+$ species get reduced to form Cu^{2+} (CuS). The shape of CV curves of CuS film electrode is of

typical pseudocapacitive material type. The highest C_s value of CuS60, CuS80, CuS100, CuS120 film electrodes at scan rate of 2 mV s^{-1} are 550, 639, 687, and 660 F g^{-1} , respectively.

The graph of variation of C_s with scan rate for CuS thin films displayed in Figure 3.15b. At a lower scan rate, Li^+ ions from LiClO_4 electrolyte take more time for intercalation/deintercalation reaction, which gives more charge transfer during a low scan rate compared with higher scan rates. The decrease in C_s with a rise in a scan rate is due to the least time available for reversible redox reactions at higher scan rates. At higher scan rate, all the electrolyte ions do not undergo reversible redox reaction due to time constraint so C_s decreases with the scan rate. The rate capacity of CuS100 electrode is 60%. The CV curves of CuS60, CuS80, CuS100, and CuS120 thin film electrodes at different scan rates from 2 to 20 mV s^{-1} are shown in Figure 3.15c-f. The increase in current response with the scan rate is observed for all thin film electrodes. From the CV curves one can conclude that CuS thin film electrodes can be used as an electrode material at various current ratings.

The amount of total charge stored by the electrode is ascribable to the contribution of capacitive and diffusion processes. Capacitive charge storage is associated with the electroadsorption of the electrolyte ions on the surface of the electrode followed by the surface redox reactions. In diffusion charge storage process, insertion of electrolyte ions inside the electrode structure takes place where they undergo redox reactions. The charge storage kinetics of CuS is studied using the power law,

$$I_p = a\nu^b \quad (3.2)$$

where I (mA) is the maximum current, ν (mV s^{-1}) represents the scan rate, and 'a' and 'b' are coefficients. If $b \cong 0.5$, then the maximum charge storage is by diffusion controlled processes, and on the other hand, if $b \cong 1$, the maximum charge storage is due to the capacitive processes. From the slope of graph $\log(I)$ versus $\log(\nu)$ (Figure 3.16a), the values of 'b' found to be 0.66, 0.61, 0.57, and 0.56 for CuS60, CuS80, CuS100, and CuS120 thin film electrodes, respectively, indicate that maximum quantity of charge stored is through the diffusion process. To find out the exact contribution by capacitive process and diffusion controlled process in total current

response, further analysis of the CV response is carried out by using Eq. (3.3) as below:

$$I(v) = k_1v + k_2v^{1/2} = I_{\text{surface}} + I_{\text{bulk}} \quad (3.3)$$

where k_1v and $k_2v^{1/2}$ are the contributions from the capacitive process and diffusion-controlled processes, respectively. The slope and intercept of the linear fit of the graph of $I/v^{1/2}$ versus $v^{1/2}$ give values of k_1 and k_2 , respectively, as shown in Figure 3.16b. The capacitive and diffusion controlled currents calculated from Eq. (3.3) and their contributions are shown in Figure 3.16c–f for different CuS electrodes. It is seen that as the scan rate decreases, the contribution from the diffusion controlled process increases and results in a larger value of C_s . At a scan rate of 20 mV s^{-1} , approximately 40% of charge is stored through the capacitive process in CuS60 which decreases to just 19% for CuS120 thin film. A large contribution from the diffusion controlled process is due to the increased thickness of film which allows easy penetration of electrolyte inside film. For CuS100 and CuS120 thin films, similar charge storage contribution from capacitive and diffusion controlled processes is observed. This indicates that with increase in thickness above CuS120 will not affect charge storage capacity of CuS thin films.

3.4B.1.2 GCD study

The GCD curves at a current density of 5 A g^{-1} for CuS electrodes deposited at 60, 80, 100, and 120 cycles are shown in Figure 3.17a. The GCD profile of CuS film electrode is nontriangular suggesting charge storage from the surface redox reactions [42–44]. The values of C_s calculated using Eq. 2.12 are 535, 625, 672, and 645 F g^{-1} for CuS60, CuS80, CuS100, and CuS120 film electrodes at charge discharge current density of 1 A g^{-1} . The easy ion transfer path is delivered by the surface of the electrode, which changes the intercalation/deintercalation rate by decreasing the internal resistance (IR) of material [45]. Variation of C_s with the current density is shown in Figure 3.17b. An increase in IR and time constraint for the reversible redox reactions at higher applied current densities cause a decrease in C_s with rising applied current density. The GCD plots of CuS60, CuS80, CuS100, and CuS120 thin film electrodes at different current densities are shown in Figures 3.17c–f. The nontriangular GCD profiles suggest that charge storage is of the pseudocapacitive

type. The highest discharge time is observed for CuS100 electrode compared with other electrodes, which indicate excellent electrochemical performance.

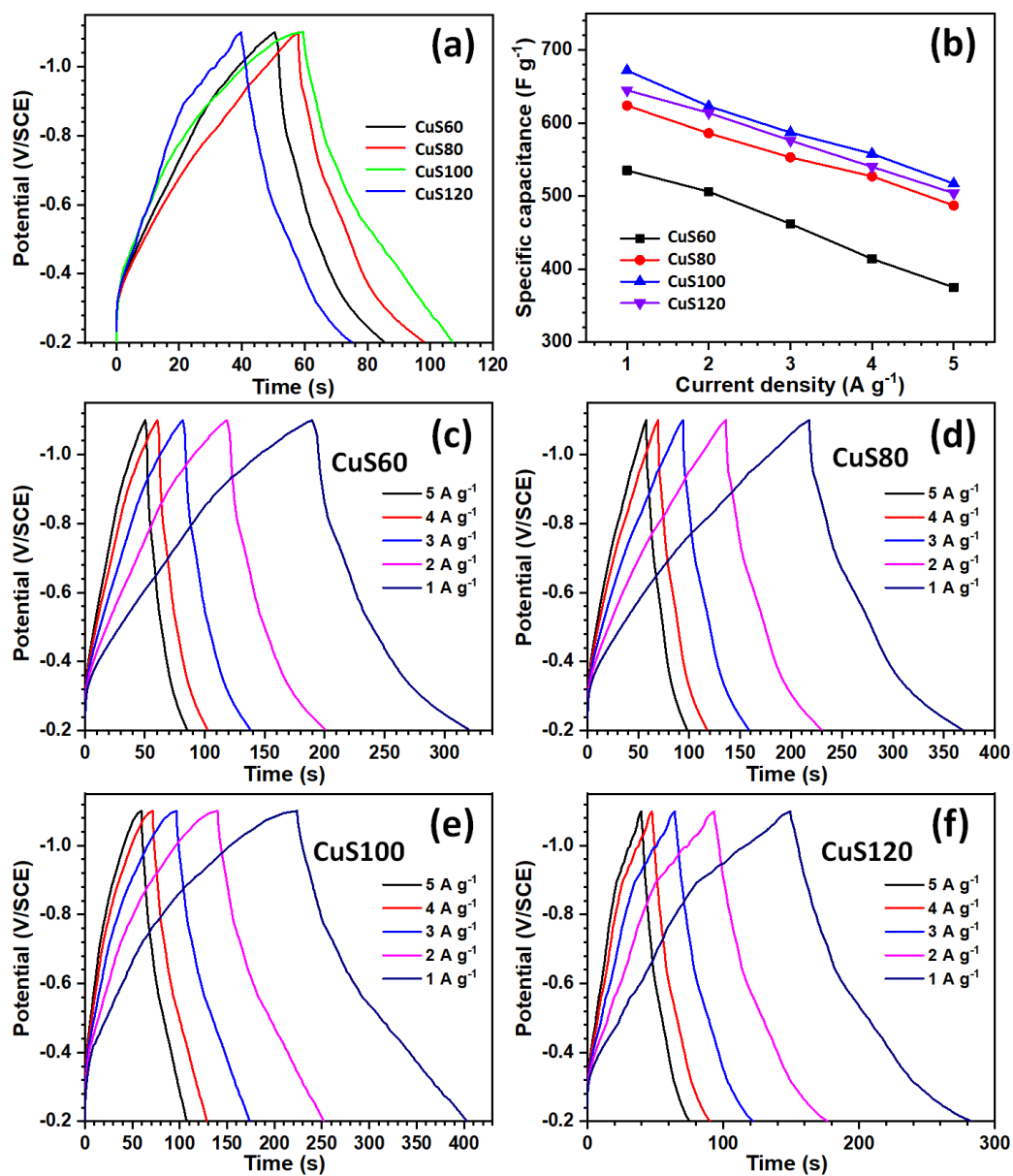


Figure 3.17: a) Comparative GCD curves of CuS thin film electrodes at a current density of 5 A g⁻¹, b) variation of C_s with the current densities, and the GCD curves at various current densities from 1-5 A g⁻¹ of c) CuS60, d) CuS80, e) CuS100, and f) CuS120 thin film electrodes.

The nonlinear behavior of the charge and discharge curves reveals the surface redox reactions of CuS thin film electrodes. Moreover, good symmetrical features of GCD curves explain that CuS material produces excellent electrochemical potential and redox reversibility during charge discharge over total range of potential. The better electrochemical capacitive performance of CuS100 electrode is originated from optimized thickness of the film and high surface area provided by nanoflower-like

morphology. Moreover, the decreasing trend of capacitance with increasing current density indicates that the inner surface of electrode material is not accessible at a higher current density.

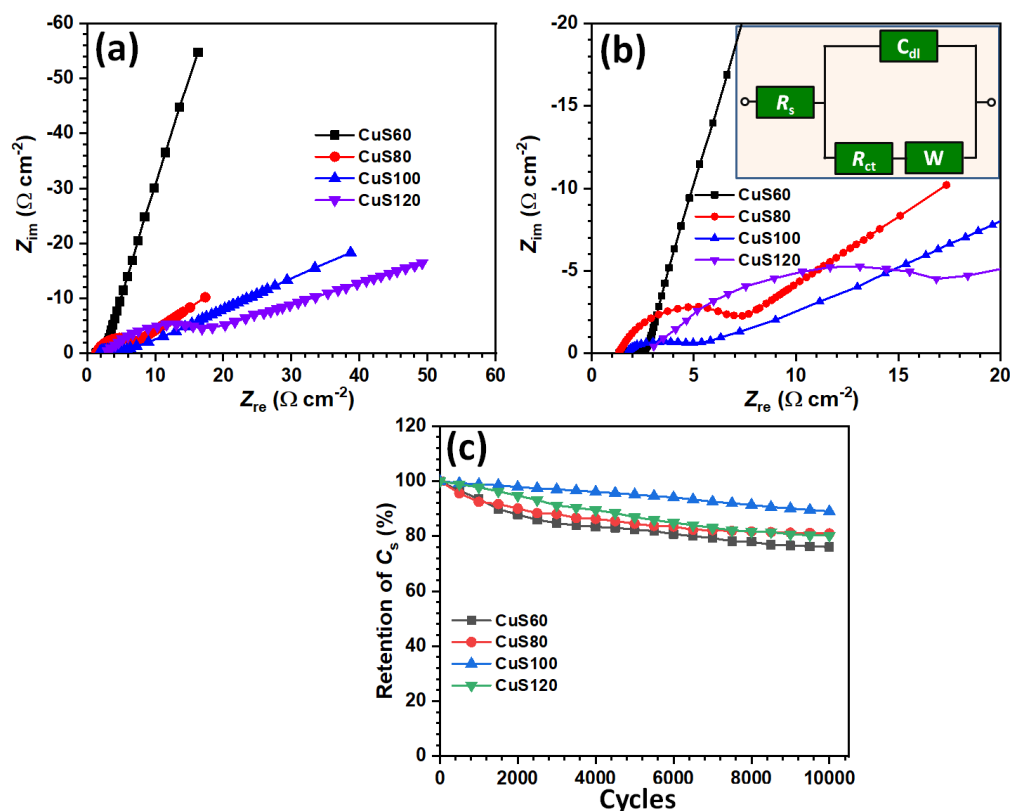


Figure 3.18: a) Nyquist plots, b) the fitted equivalent circuit for the EIS data, and c) the stability curves for CuS thin film electrodes.

3.4B.1.3 EIS study

In the Nyquist plot, semicircle appears in high frequency region and straight line in low frequency region. The semicircle in the high frequency region represents the R_{ct} that arises due to faradaic reactions and double layer capacitance at the interface of electrode/electrolyte. The R_s was obtained by pointing the intersection of the Nyquist plot to the real axis, which is a combination of electrolyte resistance and contact resistance at the interface between electrode and electrolyte. The diameter of the semicircle at high frequency region gives the R_{ct} value and it is related to the faradaic leakage current. The Nyquist plots of CuS films are shown in Figure 3.18a confirm supercapacitive nature with low R_s and R_{ct} . The electrolytic ion diffusion in the active material is responsible for the straight line in the low frequency region and it corresponds to W . The EIS data reveals that CuS100 film electrode has lower resistance and better electrochemical performance [46, 47].

The fitted equivalent circuit for the EIS data of CuS film electrodes is shown in inset of Figure 3.18b. The circuit consists of R_s , R_{ct} , W , and C_{dl} notations are the series resistance, charge transfer resistance, Warburg impedance and double layer capacitance, respectively. The values of fitted circuit parameters are tabulated in Table 3.1. The best performing CuS100 electrode show fitted values of R_s , R_{ct} , W , and C_{dl} are $1.34 \Omega \text{ cm}^{-2}$, $3.54 \Omega \text{ cm}^{-2}$, 0.92 mF , and 0.95Ω , respectively.

Table 3.1: Electrochemical impedance spectroscopic fitted circuit parameters for Nyquist plots of CuS thin film electrodes.

Sample	$R_s (\Omega \text{ cm}^{-2})$	$R_{ct} (\Omega \text{ cm}^{-2})$	$C_{dl} (\text{mF})$	$W (\Omega)$
CuS60	1.77	1.20	0.89	0.56
CuS80	1.36	5.91	0.85	0.76
CuS100	1.34	3.54	0.92	0.95
CuS120	2.96	13.82	0.91	1.28

3.4B.1.4 Stability study

The stability was investigated for all CuS electrodes over 10,000 GCD cycles at a current density of 5 A g^{-1} and the corresponding capacitive retention plot is presented in Figure 3.18c. The capacitive retention for CuS60, CuS80, CuS100, CuS120 electrodes are 74, 79, 89, and 80%, respectively. As the thickness of film electrode increases, more electrochemical stability of the film electrodes was observed. But for CuS120 film electrode, the capacitance drops due to low adherence of film to the substrate [48].

3.4B.2 Electrochemical characterizations of CuS@rGO thin films

3.4B.2.1 CV study

The electrochemical evaluation of rGO and CuS@rGO thin films was carried out in aqueous 1 M LiClO_4 electrolyte in the potential window -0.2 to -1.1 V/SCE . The CV curves of thin film electrodes at a scan rate of 20 mV s^{-1} shown in Figure 3.19a indicate that there is more current response for the CuS@rGO5 thin film compared with CuS@rGO3, CuS@rGO4, and CuS@rGO6 thin film electrodes. Area enclosed by the CV curve of rGO was too smaller compared to CuS@rGO electrodes.

The specific capacitance of rGO (23 F g^{-1}) is very low compared to CuS@rGO5 (790 F g^{-1}) at the scan rate of 20 mV s^{-1} . Hence, further electrochemical characterization of rGO does not reported in further study. This shows that CuS@rGO5 thin film electrode may facilitate fast electronic and ionic transport which raises the current response capacity of the electrode.

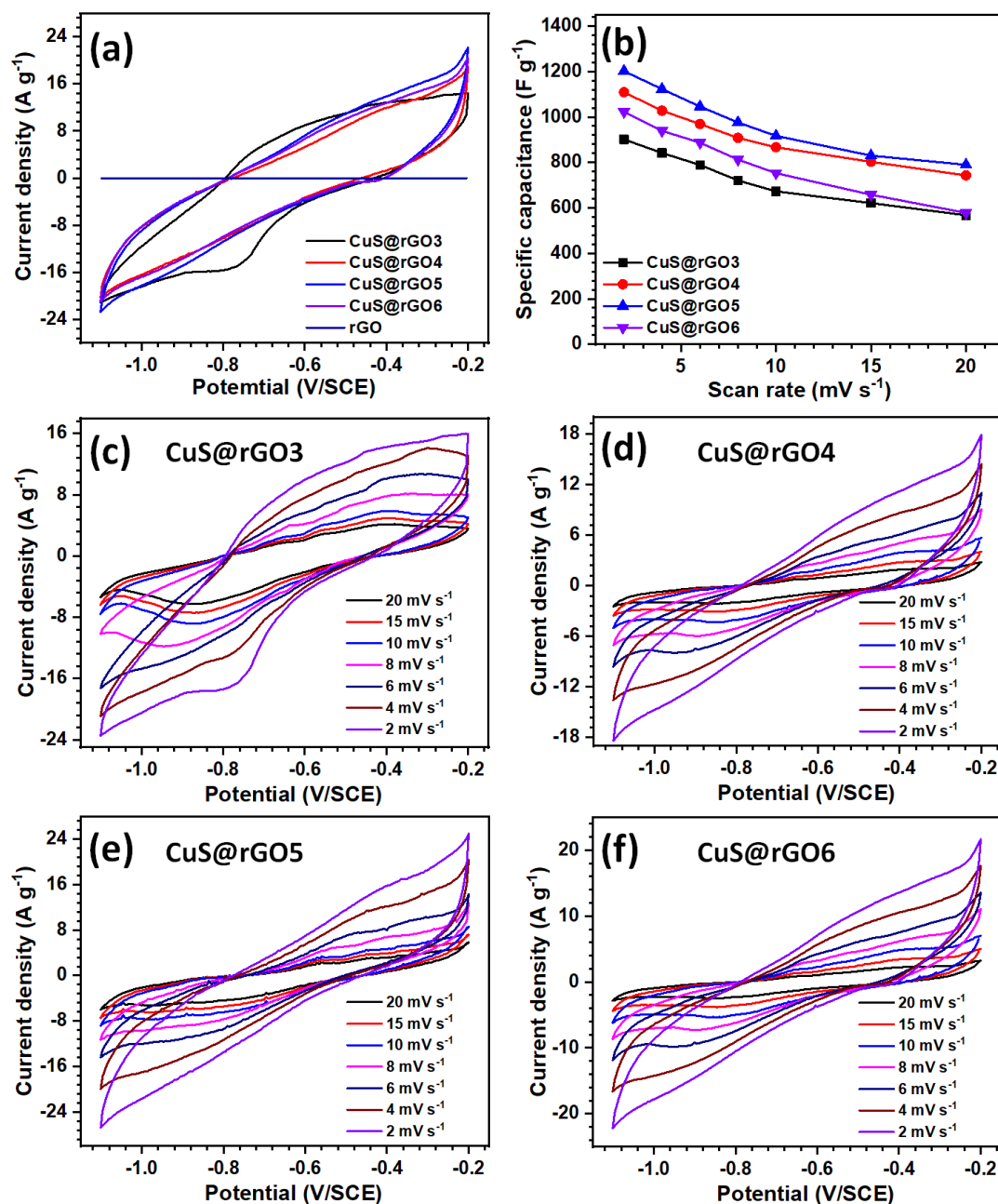


Figure 3.19: a) Comparative CV curves of rGO and CuS@rGO thin films at a scan rate of 20 mV s^{-1} , b) variation of C_s with the scan rate, and the CV curves at various scan rates from 2-20 mV s^{-1} of c) CuS@rGO3, d) CuS@rGO4, e) CuS@rGO5, and f) CuS@rGO6 thin film electrodes.

The nonrectangular shape of the CV curves confirms the presence of a pseudocapacitive charge storage mechanism. The C_s values of film electrodes calculated using Eq. 2.10 at a scan rate of 2 mV s^{-1} are 901.6, 1109.1, 1201.8, and 1022.9 F g^{-1} for CuS@rGO3, CuS@rGO4, CuS@rGO5, and CuS@rGO6 thin film electrodes, respectively.

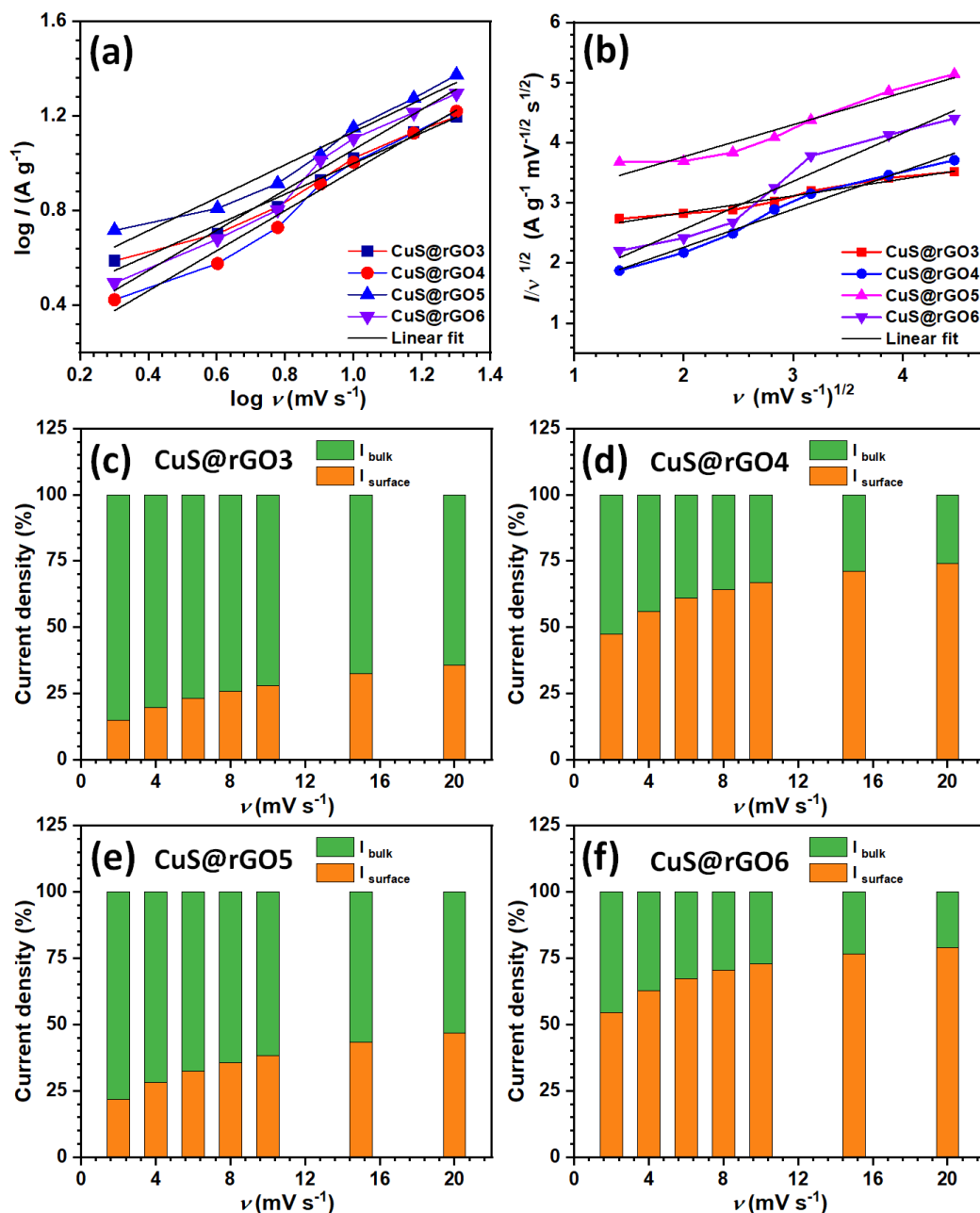


Figure 3.20: a) Plots of $\log I$ against $\log v$, b) plots of $I/v^{1/2}$ against $v^{1/2}$ of CuS@rGO thin film electrodes; and contribution of capacitive and diffusion controlled currents for c) CuS@rGO3, d) CuS@rGO4, e) CuS@rGO5, and f) CuS@rGO6 thin film electrodes.

The graphs of variation of C_s with the scan rate for all films displayed in Figure 3.19b show a decrease in C_s with a higher scan rate due to least time for reversible redox reactions to happen. At a higher scan rate, all the electrolyte ions do not undergo reversible redox reaction due to time constraint so C_s decreases with the scan rate. A decrease of 55% of capacitance is observed from scan rate 2 to 20 mV s^{-1} in the case of CuS@rGO5 electrode. The CV curves of CuS@rGO3, CuS@rGO4, CuS@rGO5, and CuS@rGO6 thin film electrodes at different scan rates from 2 to 20 mV s^{-1} are shown in Figure 3.19c-f. From the CV curves one can conclude that CuS thin film electrodes can be used as an electrode material at various current ratings.

The amount of total charge stored by the electrode is ascribable to the contribution of capacitive and diffusion processes. The charge storage kinetics of CuS@rGO is studied using the power law (Eq. (3.2)). From the slope of graph $\log(I)$ versus $\log(v)$ (Figure 3.20a), the values of “b” are found to be 0.63, 0.67, 0.62, and 0.74 for CuS@rGO3, CuS@rGO4, CuS@rGO5, and CuS@rGO6 thin film electrodes, respectively. This indicates that maximum quantity of charge stored is through the diffusion process. To find out exact contribution by capacitive process and diffusion controlled process in total current response, further analysis of the CV is carried out by using Eq. (3.3).

The slope and intercept of the linear fit of graph of $I/v^{1/2}$ versus $v^{1/2}$ give values of k_1 and k_2 , respectively, as shown in Figure 3.20b. The capacitive and diffusion controlled currents calculated from Eq. (3.3) and their contributions are shown in Figure 3.20c–f for different CuS@rGO electrodes. It is seen that as the scan rate decreases, the contribution from the diffusion controlled process increases and results in a larger value of C_s . Approximately 47% of charge is stored through the capacitive process in CuS@rGO5 at a scan rate of 20 mV s^{-1} which decreases to just 22% at a scan rate of 2 mV s^{-1} . A large contribution from the diffusion controlled process is due to the layered structure which allows easy penetration of electrolyte itself.

3.4B.2.2 GCD study

The GCD curves at a current density of 5 A g^{-1} for CuS@rGO electrodes are shown in Figure 3.21a. The values of C_s calculated using Eq. 2.12 are 872.5, 1091.5, 1132.9, and 1022.8 F g^{-1} for CuS@rGO3, CuS@rGO4, CuS@rGO5, and CuS@rGO6 thin films, respectively, at a current density of 1 A g^{-1} . Variation of C_s with the

current density is shown in Figure 3.21b. An increase in IR and time constraint for the reversible redox reaction at higher applied current densities causes a decrease in C_s with rising applied current density.

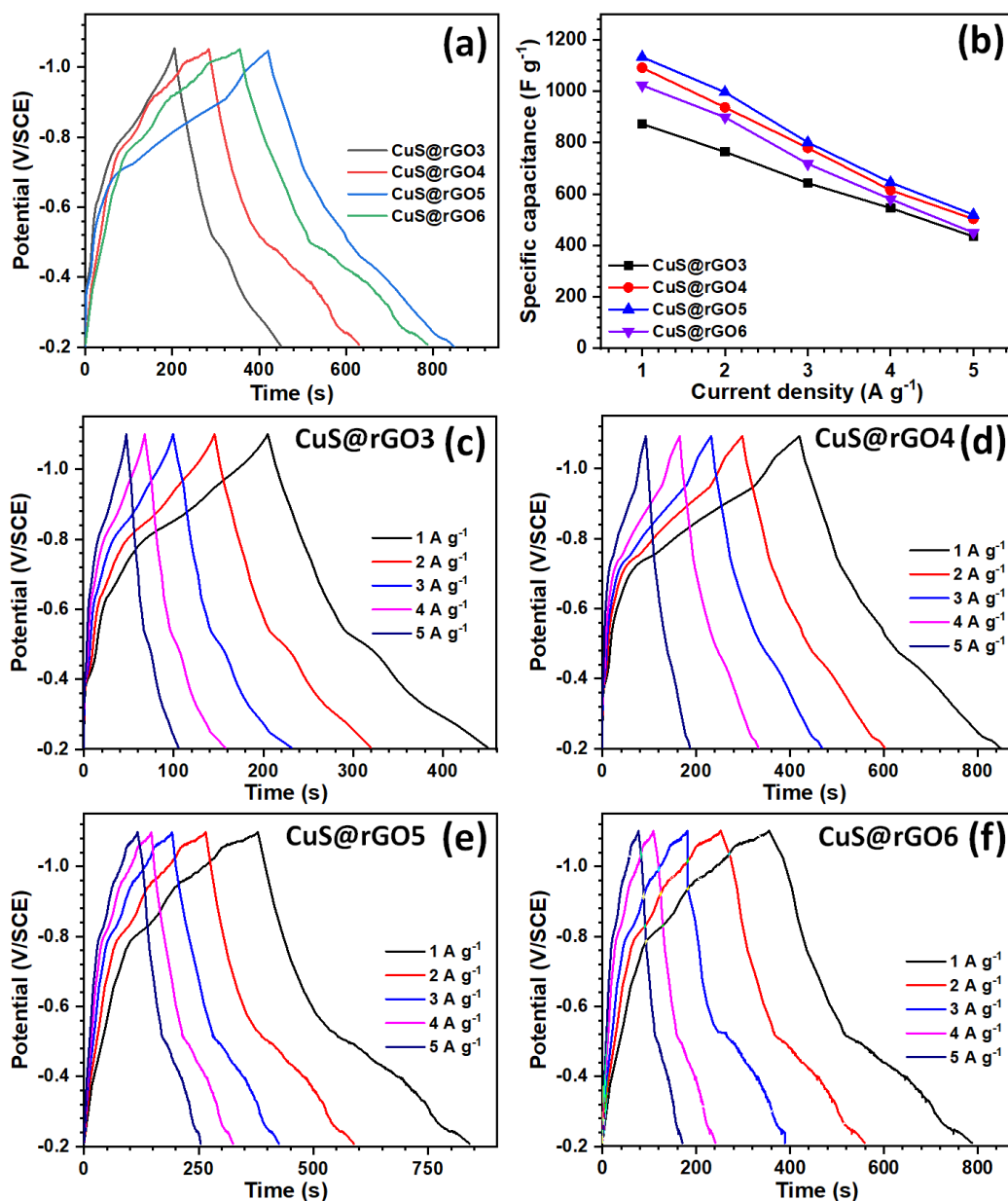


Figure 3.21: a) Comparative GCD curves of CuS@rGO thin film electrodes at a current density of 5 A g⁻¹, b) variation of C_s with the current densities, and the GCD curves at various current densities from 1-5 A g⁻¹ of c) CuS@rGO3, d) CuS@rGO4, e) CuS@rGO5, and f) CuS@rGO6 thin film electrodes.

The GCD plots of CuS@rGO3, CuS@rGO4, CuS@rGO5, and CuS@rGO6 electrodes at different current densities shown in Figures 3.21c-f, suggest an increase in the internal resistance with the rise of the current density of charging. The GCD profile is nontriangular and much different from the GCD profile of pristine CuS. This

suggests that charge storage is from the combination of pseudocapacitive type CuS and EDLC type rGO. The highest discharge time was observed for CuS@rGO5 electrode compared with other electrodes, which indicate excellent electrochemical performance. The nonlinear (quasi triangular) behavior of the charge and discharge curves revealed the intercalation pseudocapacitive characteristic of CuS@rGO thin films [49].

The GCD profiles of all CuS@rGO thin film electrodes show intercalated pseudocapacitive behavior. Moreover, good symmetrical features of GCD curves explain that CuS@rGO composite material produces excellent electrochemical potential and redox reversibility during charge discharge for the total range of potential. The better electrochemical capacitive performance of CuS@rGO5 electrode is originated from optimized thickness and amount of rGO concentration used for composition of the film and high surface area provided by nanosheet-like morphology.

3.4B.2.3 EIS study

The EIS spectra of CuS@rGO thin film electrodes plotted in Figure 3.22a confirm a supercapacitive nature with low R_s and R_{ct} . The EIS plot at higher frequencies is shown in Figure 3.22b. The values of R_s are 3.34, 2.75, 2.78, and 4.13 $\Omega \text{ cm}^{-2}$ and those of R_{ct} 19.2, 21.3, 20.8, and 43.92 $\Omega \text{ cm}^{-2}$ for CuS@rGO3, CuS@rGO4, CuS@rGO5, and CuS@rGO6 thin film electrodes, respectively. The values of R_s , R_{ct} , C_{dl} , and W of CuS@rGO electrodes are determined by fitting measured data with the equivalent circuit (inset of Figure 3.22b), and the observed values are given in Table 3.2. The EIS data reveals that CuS@rGO5 thin film electrode has good conductivity and better electrochemical performance. The appropriate concentration of rGO with CuS forms a binder free stoichiometric thin film which facilitates better conducting properties with electrochemical reactions. Such type of properties was observed in the case of CuS@rGO5 thin film, as the concentration of rGO increases further and then, rise in R_s and R_{ct} is observed, while at low concentration of rGO which may be due to lack of appropriate active sites, values of R_s and R_{ct} are higher [50].

Table 3.2: Electrochemical impedance spectroscopic fitted circuit parameters for Nyquist plots of CuS@rGO thin film electrodes.

Sample	$R_s (\Omega \text{ cm}^{-2})$	$R_{ct} (\Omega \text{ cm}^{-2})$	$C_{dl} (\text{mF})$	$W (\Omega)$
CuS@rGO3	3.34	22.21	1.03	0.36
CuS@rGO4	2.75	21.30	1.23	0.35
CuS@rGO5	2.78	20.80	1.37	0.41
CuS@rGO6	4.13	43.92	1.45	0.58

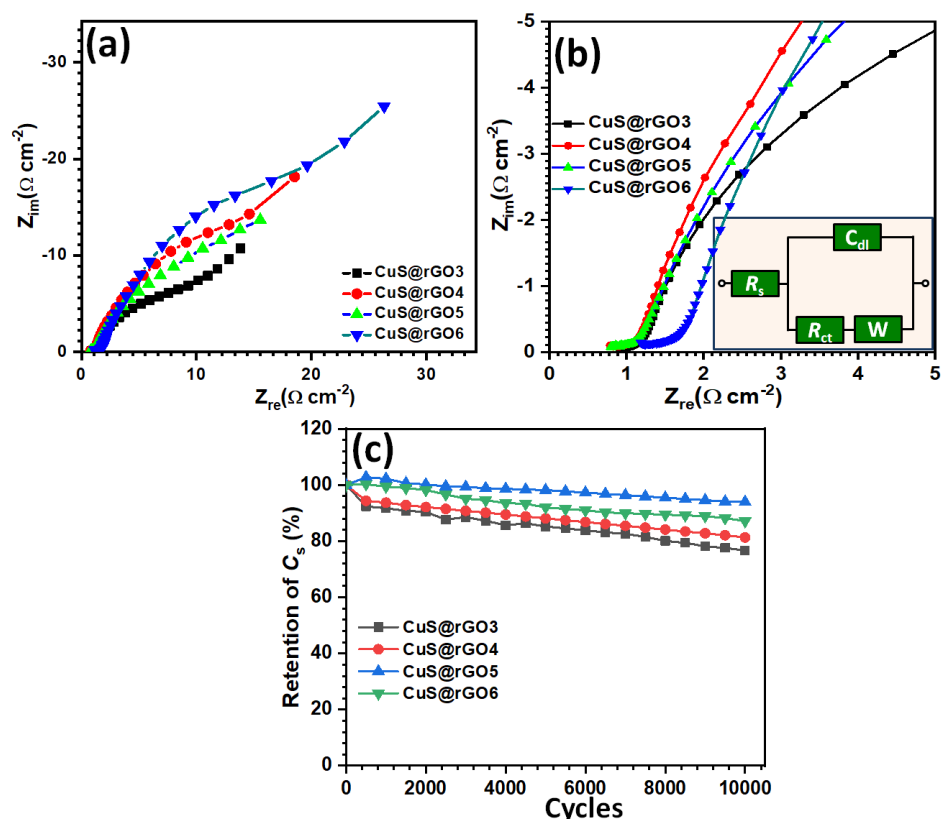


Figure 3.22: a) Nyquist plots of CuS@rGO thin films, b) the fitted equivalent circuit for the EIS data, and c) the stability curves for CuS@rGO thin film electrodes.

3.4B.2.4 Electrochemical stability

The stability of CuS@rGO thin film electrodes was carried out by repeating 10,000 GCD cycles at an applied current density of 5 A g^{-1} . The capacitance retention of electrodes with the GCD cycles is shown in Figure 3.22c. The capacitance retentions for CuS@rGO3, CuS@rGO4, CuS@rGO5, and CuS@rGO6 thin film electrodes were 76, 81, 94, and 87%, respectively. The excellent electrochemical

characteristics were due to the layered architecture of the electrodes providing more electroactive sites to electrochemical reactions and randomly distributed vertical paths for electron conduction and ion diffusion.

3.5 Conclusions

In conclusion, SILAR method is developed to prepare sequential layered CuS@rGO composite thin film electrodes directly on SS substrate. The layered structure of CuS and rGO shows maximum C_s of 1201.8 F g^{-1} at the scan rate of 2 mV s^{-1} in 1 M LiClO_4 electrolyte. The value of R_s is decreased for CuS@rGO electrode compared to pristine CuS but value of R_{ct} increases with the introduction of rGO. The electrochemical cycling stability of CuS@rGO5 film electrode (94%) is more compared to CuS film electrode (89%). These electrochemical investigations indicate CuS@rGO as a future electrode material in SCs.

References:

- [1] C. Liu, Y. Liu, T. Yi, C. Hu, Carbon materials for high-voltage supercapacitors, *Carbon*, 145 (2019) 529-548, DOI:10.1016/j.carbon.2018.12.009.
- [2] D. Dubal, J. Kim, Y. Kim, R. Holze, C. Lokhande, W. Kim, Supercapacitors based on flexible substrates: An overview, *Energy Technol.*, 2 (2014) 325-341, DOI: 10.1002/ente.201300144.
- [3] V. Sharma, I. Singh, A. Chandra, Hollow nanostructures of metal oxides as next generation electrode materials for supercapacitors, *Sci. Rep.*, 8 (2018) 1307, DOI: 10.1038/s41598-018-19815-y.
- [4] Y. Jiang, J. Liu, Definitions of pseudocapacitive materials: A brief review, *Energy Environ. Mater.*, 2 (2019) 30-37, DOI: 10.1002/eem2.12028.
- [5] J. Theerthagiri, K. Karuppusamy, G. Durai, A. U. H. S. Rana, P. Arunachalam, K. Sangeetha, P. Kuppusami, H. Kim, Recent advances in metal chalcogenides (MX; X = S, Se) nanostructures for electrochemical supercapacitor applications: A brief review, *Nanomaterials*, 8 (2018) 256, DOI: 10.3390/nano8040256.
- [6] A. González, E. Goikolea, J. Barrena, R. Mysyk, Review on supercapacitors: Technologies and materials, *Renewable sustainable energy rev.*, 58 (2016) 1189-1206, DOI: 10.1016/j.rser.2015.12.249.
- [7] Y. Zhao, W. Ran, J. He, Y. Huang, Z. Liu, W. Liu, Y. Tang, L. Zhang, D. Gao, F. Gao, High-performance asymmetric supercapacitors based on multilayer MnO_2 /graphene oxide nanoflakes and hierarchical porous carbon with enhanced cycling stability, *small*, 11 (2015) 1310-1319, DOI: 10.1002/smll.201401922.

-
- [8] H. Zhang, M. Chhowalla, Z. Liu, 2D nanomaterials: Graphene and transition metal dichalcogenides, *Chem. Soc. Rev.*, 47 (2018) 3015-3017, DOI: 10.1039/C8CS90048E.
- [9] B. Pandit, D. Dubal, P. Gómez-Romero, B. Kale, B. Sankapal, V₂O₅ encapsulated MWCNTs in 2D surface architecture: Complete solid-state bendable highly stabilized energy efficient supercapacitor device, *Sci. Rep.*, 7 (2017) 43430, DOI: 10.1038/srep43430.
- [10] R. Hou, G. Gund, K. Qi, P. Nakhanivej, H. Liu, F. Li, B. Y. Xia, H. Park, Hybridization design of materials and devices for flexible electrochemical energy storage, *Energy Storage Mater.*, 19 (2019) 212-241, DOI: 10.1016/j.ensm.2019.03.002.
- [11] K. J. Huang, J. Z. Zhang, K. Xing, One-step synthesis of layered CuS/multi-walled carbon nanotube nanocomposites for supercapacitor electrode material with ultrahigh specific capacitance, *Electrochim. Acta.*, 149 (2014) 28-33, DOI: 10.1016/j.electacta.2014.10.079.
- [12] K. Krishnamoorthy, G. K. Veerasubramani, A. N. Rao, S. J. Kim, One-pot hydrothermal synthesis, characterization and electrochemical properties of CuS nanoparticles towards supercapacitor applications, *Mater. Res. Express*, 1 (2014) 035006, DOI: 10.1088/2053-1591/1/3/035006.
- [13] Y. Lu, X. Meng, G. Yi, J. Jia, In situ growth of CuS thin films on functionalized self-assembled monolayers using chemical bath deposition, *J. Colloid Interface Sci.*, 356 (2011) 726-733, DOI: 10.1016/j.jcis.2011.01.031.
- [14] S. D. Sartale, C. D. Lokhande, Growth of copper sulphide thin films by successive ionic layer adsorption and reaction (SILAR) method, *Mater. Chem. Phys.*, 65 (2000) 63-67, DOI: 10.1016/S0254-0584(00)00207-8.
- [15] S. S. Dhasade, J. S. Patil, J. H. Kim, S. H. Han, M. C. Rath, V. J. Fulari, Synthesis of CuS nanorods grown at room temperature by electrodeposition method, *Mater. Chem. Phys.*, 137 (2012) 353-358, DOI: 10.1016/j.matchemphys.2012.09.033.
- [16] Y. F. Zhu, D. H. Fan, and W. Z. Shen, A general chemical conversion route to synthesize various ZnO-based core/shell structures, *J. Phys. Chem. C*, 112 (2008) 10402–10406, DOI: 10.1021/jp802545e.
- [17] K. Huang, J. Zhang, Y. Fan, One-step solvothermal synthesis of different morphologies CuS nanosheets compared as supercapacitor electrode materials, *J. Alloys Compd.*, 625 (2015) 158-163, DOI: 10.1016/j.jallcom.2014.11.137.
- [18] L. Han, Y. Hao, X. Wei, X. Chen, Y. Shu, J. Wang, Hollow copper sulfide nanosphere–doxorubicin/graphene oxide core-shell nanocomposite for photothermo-chemotherapy, *ACS Biomater. Sci. Eng.*, 3 (2017) 3230–3235, DOI: 10.1021/acsbiomaterials.7b00643.
- [19] K. Jin, M. Zhou, H. Zhao, S. Zhai, F. Ge, Y. Zhao, Z. Cai, Electrodeposited CuS nanosheets on carbonized cotton fabric as flexible supercapacitor electrode for
-

- high energy storage, *Electrochim. Acta*, 295 (2019) 668-676, DOI: 10.1016/j.electacta.2018.10.182.
- [20] W. Xu, Y. Liang, Y. Su, S. Zhu, Z. Cui, X. Yang, A. Inoue, Q. Wei, C. Liang, Synthesis and properties of morphology controllable copper sulphide nanosheets for supercapacitor application, *Electrochim. Acta*, 211 (2016) 891-899, DOI: 10.1016/j.electacta.2016.06.118.
- [21] Y. J. Yang, Fullerenes, Nanotubes, Facile preparation of CuS-coated multiwalled carbon nanotubes for supercapacitor application: A study on the effect of electrolyte, *Carbon Nanostruct.*, 25 (2017) 497-503, DOI: 10.1080/1536383X.2017.1344836.
- [22] F. Luan, G. Wang, Y. Ling, X. Lu, H. Wang, Y. Tong, X. Liu, Y. Li, High energy density asymmetric supercapacitors with a nickel oxide nanoflake cathode and a 3D reduced graphene oxide anode, *nanoscale*, 17 (2013) 7984-7990, DOI: 10.1039/C3NR02710D.
- [23] S. Eigler and P. Feicht, Defects in graphene oxide as structural motifs, *ChemNanoMat*, 4 (2018) 244-252, DOI: 10.1002/cnma.201700357.
- [24] A. M. Patil, A. C. Lokhande, N. R. Chodankar, P. A. Shinde, J. H. Kim, C. D. Lokhande, Interior design engineering of CuS architecture alteration with rise in reaction bath temperature for high performance symmetric flexible solid state supercapacitor, *J. Ind. Eng. Chem.*, 46 (2017) 91-102, DOI: 10.1016/j.jiec.2016.10.019.
- [25] A. Naveen, S. Selladurai, Novel low temperature synthesis and electrochemical characterization of mesoporous nickel cobaltite-reduced graphene oxide (RGO) composite for supercapacitor application, *Electrochim. Acta*, 173 (2015) 290–301, DOI: 10.1016/j.electacta.2015.05.072.
- [26] F. Johra, W. Jung, RGO-TiO₂-ZnO composites: Synthesis, characterization, and application to photocatalysis, *Appl. Catal. A*, 491 (2015) 52–57, DOI: 10.1016/j.apcata.2014.11.036
- [27] R. N. Bulakhe, S. Sahoo, T. Nguyen, C. D. Lokhande, C. Roh, Y. R. Lee, J. Shim, Chemical synthesis of 3D copper sulfide with different morphologies for high performance supercapacitors application, *RSC Adv.*, 6 (2016) 14844-14851, DOI: 10.1039/C5RA25568F.
- [28] H. Tang, Y. He, B. Li, J. Jung, C. Zhang, X. Liu, Z. Lin, Continuous crafting of uniform colloidal nanocrystals using an inert-gas-driven microflow reactor, *Nanoscale*, 7 (2015) 9731-9737, DOI: 10.1039/C5NR01492A.
- [29] H. Wang, Y. Wang, X. Cao, M. Feng, G. Lan, Vibrational properties of graphene and graphene layers, *J. Raman Spectrosc.*, 40 (2009) 1791-1796, DOI: 10.1002/jrs.2321.
- [30] Y. Huang, C. Chang, M. Lin, Magnetoabsorption spectra of bilayer graphene ribbons with Bernal stacking, *Phys. Rev. B*, 78 (2008) 115422, DOI: 10.1103/PhysRevB.78.115422.

-
- [31] O. Fesenko, G. Dovbeshko, A. Dementjev, R. Karpicz, T. Kaplas, Y. Svirko, Graphene-enhanced Raman spectroscopy of thymine adsorbed on single-layer graphene, *Nanoscale Res. Lett.*, 10 (2015) 163, DOI: 10.1186/s11671-015-0869-4.
- [32] L. Malard, J. Nilsson, D. Elias, J. Brant, F. Plentz, E. Alves, A. Castro Neto, M. Pimenta, Probing the electronic structure of bilayer graphene by Raman scattering, *Phys. Rev. B*, 76 (2007) 201401, DOI: 10.1103/PhysRevB.76.201401.
- [33] J. Wu, M. Lin, X. Cong, H. Liu, P. Tan, Raman spectroscopy of graphene-based materials and its applications in related devices, *Chem. Soc. Rev.*, 47 (2018) 1822-1873, DOI: 10.1039/C6CS00915H
- [34] A. Bollero, M. Grossberg, B. Asenjo, M. Gutiérrez, CuS-based thin films for architectural glazing applications produced by co-evaporation: Morphology, optical and electrical properties, *Surf. Coat. Technol.*, 204 (2009) 593-600, DOI: 10.1016/j.surfcoat.2009.08.037.
- [35] P. Ganesan, A. Sivanantham, S. Shanmugam, Inexpensive electrochemical synthesis of nickel iron sulphides on nickel foam: super active and ultra-durable electrocatalysts for alkaline electrolyte membrane water electrolysis, *J. Mater. Chem. A*, 4 (2016) 16394-16402, DOI: 10.1039/C6TA04499A.
- [36] F. Xiao, S. Yang, Z. Zhang, H. Liu, J. Xiao, L. Wan, J. Luo, S. Wang, Y. Liu, Scalable synthesis of freestanding sandwich-structured graphene/polyaniline/graphene nanocomposite paper for flexible all-solid-state supercapacitor, *Sci. Rep.*, 5 (2015) 9359, DOI: 10.1038/srep09359.
- [37] D. Rosenthal, M. Ruta, R. Schlogl, L. Kiwi-Minsker, Combined XPS and TPD study of oxygen-functionalized carbon nanofibers grown on sintered metal fibers, *Carbon*, 48 (2010) 1835-1843, DOI: 10.1016/j.carbon.2010.01.029.
- [38] J. Han, W. Liu, T. Zhang, K. Xue, W. Li, F. Jiao, W. Qin, Mechanism study on the sulfidation of ZnO with sulfur and iron oxide at high temperature, *Sci. Rep.*, 7 (2017) 42536, DOI: 10.1038/srep42536.
- [39] T. T. Chau, W. J. Bruckard, P. T. L. Koh, A. V. Nguyen, A review of factors that affect contact angle and implications for flotation practice, *Adv. Colloid Interface Sci.*, 150 (2009) 106-115, DOI: 10.1016/j.cis.2009.07.003.
- [40] M. A. Quetzeri-Santiago, A. A. Castrejón-Pita, J. R. Castrejón-Pita, The effect of surface roughness on the contact line and splashing dynamics of impacting droplets, *Sci Rep.*, 9 (2019) 15030, DOI: 10.1038/s41598-019-51490-5.
- [41] J. Wang, Y. Wu, Y. Cao, G. Li, Y. Liao, Influence of surface roughness on contact angle hysteresis and spreading work, *Colloid Polym Sci.*, 298 (2020) 1107-1112, DOI: 10.1007/s00396-020-04680-x.
- [42] C. Raj, B. Kim, W. Cho, W. Lee, Y. Seo, K. Yu, Electrochemical capacitor behavior of copper sulfide (CuS) nanoplatelets, *J. Alloys Compd.*, 586 (2014) 191-196, DOI: 10.1016/j.jallcom.2013.10.056.
-

- [43] H. Peng, G. Ma, J. Mu, K. Sun, Z. Lei, Controllable synthesis of CuS with hierarchical structures via a surfactant-free method for high-performance supercapacitors, *Mater Lett*, 122 (2014) 25-28, DOI: 10.1016/j.matlet.2014.01.173.
- [44] S. K. Meher, P. Justin, G. R. Rao, Nanoscale morphology dependent pseudocapacitance of NiO: Influence of intercalating anions during synthesis, *Nanoscale*, 3 (2011) 683, DOI: 10.1039/C0NR00555J.
- [45] V. Pototskaya, O. Gichan, On the origin of phase angle in Warburg finite length diffusion impedance, *Int. J. Electrochem. Sci.*, 14 (2019) 8195-8205, DOI: 10.20964/2019.08.97.
- [46] C. Peng, J. Jin, G. Chen, A comparative study on electrochemical co-deposition and capacitance of composite films of conducting polymers and carbon nanotubes, *Electrochim. Acta*, 53 (2007) 525-537, DOI: 10.1016/j.electacta.2007.07.004.
- [47] D. Kampouris, X. Ji, E. Randviir, C. Banks, A new approach for the improved interpretation of capacitance measurements for materials utilized in energy storage, *RSC Adv.*, 5 (2015) 12782-12791, DOI: 10.1039/C4RA17132B.
- [48] A. Khosrozadeh, G. Singh, Q. Wang, G. Luo, M. Xing, Supercapacitor with extraordinary cycling stability and high rate from nano-architected polyaniline/graphene on Janus nanofibrous film with shape memory, *J. Mater. Chem. A*, 6 (2018) 21064-21077, DOI: 10.1039/C8TA07426G.
- [49] S. Lehtimäki, A. Railanmaa, J. Keskinen, M. Kujala, S. Tuukkanen, D. Lupo, Performance, stability and operation voltage optimization of screen-printed aqueous supercapacitors, *Sci. Rep.*, 7 (2017) 46001, DOI: 10.1038/srep46001.
- [50] Y. Ko, D. Shin, B. Koo, S. W. Lee, W. Yoon, J. Cho, Ultrathin supercapacitor electrodes with high volumetric capacitance and stability using direct covalent-bonding between pseudocapacitive nanoparticles and conducting materials, *Nano Energy*, 12 (2015) 612-625, DOI: 10.1016/j.nanoen.2015.01.002.

CHAPTER – IV

**CuSe₂ and CuSe₂@rGO thin films by SILAR
method: Characterization and
electrochemical performance**

CHAPTER-IV

CuSe₂ and CuSe₂@rGO thin films by SILAR method: Characterization and electrochemical performance

4.1	Introduction.....	107
4.2	Synthesis and characterizations of CuSe ₂ and CuSe ₂ @rGO thin films.....	107
4.2.1	Introduction	107
4.2.2	Experimental details.....	107
4.2.2.1	<i>Chemicals</i>	107
4.2.2.2	<i>Preparation of CuSe₂ thin films</i>	108
4.2.2.3	<i>Synthesis of CuSe₂@rGO thin films</i>	108
4.2.2.4	<i>Material characterizations</i>	109
4.3	Results and discussion.....	109
4.3.1	Growth mechanism of CuSe ₂ and CuSe ₂ @rGO thin films.....	109
4.3.2	Physico-chemical characterizations of CuSe ₂ and CuSe ₂ @rGO thin films.....	110
4.3.3	Electrochemical characterizations of CuSe ₂ and CuSe ₂ @rGO thin films	118
4.4	Conclusions.....	123
	References.....	124

4.1. Introduction

The composition of pseudocapacitive materials with modified graphenes (rGO and GO) has been widely studied due to their exceptional characteristics, particularly high surface area, moderate electrical conductivity, and good thermal stability [1]. Different morphologies can be achieved by employing composition. Also, the composition of pseudocapacitive materials with EDLC materials shows an effective way to enhance electrochemical cycling stability. The functional groups attached to the rGO such as -COOH, -OH, -CHO, etc., provide excellent defect sites for the growth of pseudocapacitive material [2]. However, the binder free synthesis of the composite electrode on the conducting current collector is still a challenge [3].

Considering the above viewpoints, herein structural characteristics and electrochemical analysis of SILAR deposited copper selenide and copper selenide composited with rGO thin films are presented. Layer structured material consisting rGO sheets with numerous interlinked copper selenide nanoparticles with mesopores morphology were prepared. Furthermore, the charge storage mechanism of the bare and composite electrodes was identified. A FSS-ASC device with configuration of $\text{CuSe}_2\text{@rGO//CuS}$ was fabricated and the electrochemical features were studied.

4.2. Synthesis and characterization of CuSe_2 and $\text{CuSe}_2\text{@rGO}$ thin films

4.2.1 Introduction

The preparation method of electrode material must be facile and scalable. From these points of view, CuSe_2 and $\text{CuSe}_2\text{@rGO}$ thin films are fabricated on flexible SS substrates using SILAR method at room temperature. The porous electrode structure can be achieved by compositing rGO sheets with CuSe_2 nanoparticles. The present section deals with the synthesis of CuSe_2 and $\text{CuSe}_2\text{@rGO}$ thin films.

4.2.2 Experimental details

4.2.2.1 Chemicals

The required chemicals such as AR grade copper pentahydrate ($\text{CuSO}_4\cdot 5\text{H}_2\text{O}$) and KOH were purchased from Thomas Baker Chemicals Pvt. Ltd., India, and sodium selenide (Na_2Se) were purchased from Sigma Aldrich used without further purification. The commercially available flexible SS of thickness 0.3 mm (304 grade) was used as substrate. The DDW was used as a solvent throughout the experiment.

4.2.2.2 Preparation of CuSe_2 thin films

To synthesis copper selenide thin film; 50 mL of 0.1 M $\text{CuSO}_4 \cdot 5\text{H}_2\text{O}$ and 0.05 M Na_2Se were utilized as a source of Cu^{2+} ions and source of Se^{2-} ions, respectively. Well cleaned SS substrate was immersed in the cationic precursor for 20 s and then in DDW for 15 s to remove loosely adsorbed Cu^{2+} ions from SS substrate. Further, SS substrate was immersed in anionic precursor where preadsorbed Cu^{2+} ions react with Se^{2-} ions to form copper selenide. Excessive and unreacted species were removed by 15 s rinsing in DDW. These immersions in different precursor solutions along with rinsing in DDW complete a cycle of deposition and such 20, 30, 40, and 50 cycles were repeated to get sufficient thickness of thin films. The films prepared at 20, 30, 40, and 50 SILAR cycles are denoted as C1, C2, C3, and C4, respectively. The mass loading of film measured through the gravimetric weight difference method was 0.082 (± 0.001), 0.087 (± 0.001), 0.091 (± 0.001), and 0.093 (± 0.001) mg cm^{-2} for C1, C2, C3, and C4 thin films, respectively. The variation in mass loading of copper selenide thin films is graphically shown in Figure 4.1. The physico-chemical and electrochemical characterizations of the thin film showing the best electrochemical performance than others are provided in this chapter to maintain the flow of the chapter.

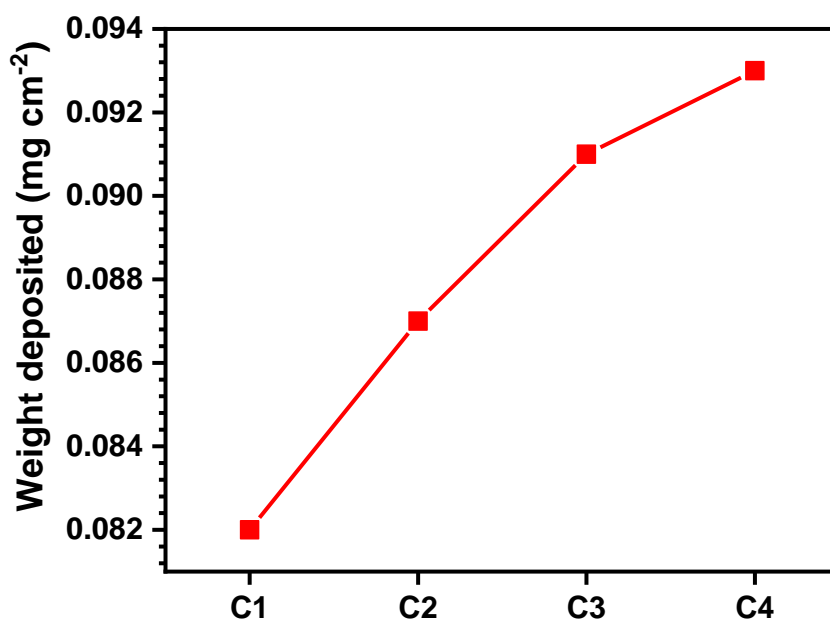


Figure 4.1: Graphical representation of weight deposited of copper selenide on SS substrate at 20 (C1), 30 (C2), 40 (C3), and 50 (C4) SILAR deposition cycles.

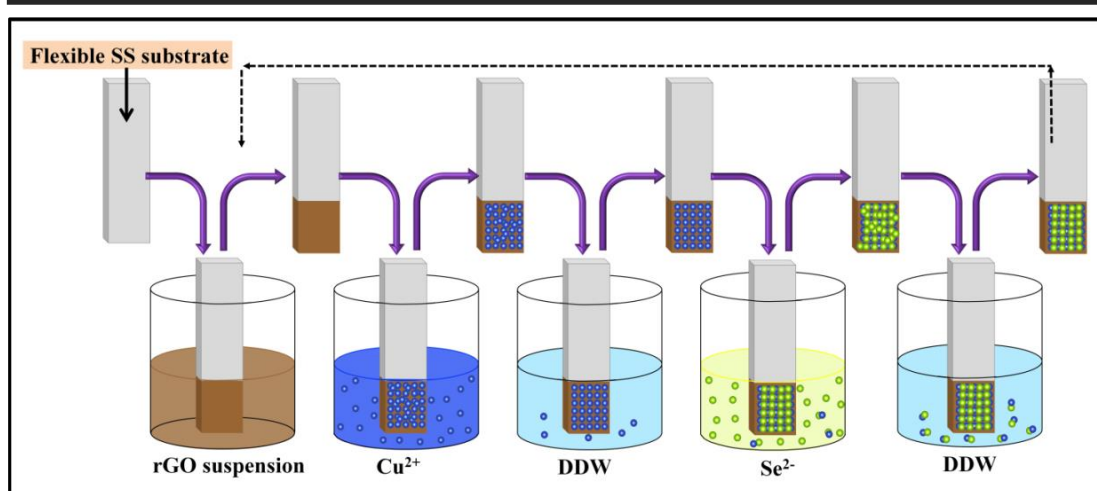


Figure 4.2: Schematic of SILAR method used for deposition of CuSe₂@rGO thin films.

4.2.2.3 Synthesis of CuSe₂@rGO thin films

The rGO suspension of the desired concentration was prepared using a top-down approach (Hummers method) from graphite flakes obtained from the Sigma-Aldrich company [4]. From the results of previous chapter, the optimised concentration of rGO suspension (0.5 mg mL^{-1}) was used to deposit a layer of rGO sheets on the SS substrate through layer-by-layer (LBL) method. The synthesis process of CuSe₂@rGO was carried out as follows; SS substrate was immersed in rGO suspension for 60 s and then dried for 30 s at room temperature; followed by the deposition of copper selenide as described above in section 4.2.2.2. Total 40 cycles were repeated to get the appropriate thickness of CuSe₂@rGO thin films. The mass loading of the films was $0.106 (\pm 0.001) \text{ mg cm}^{-2}$. It was noted that the addition of rGO increases mass loading of CuSe₂@rGO thin film. The schematic of SILAR deposition method adopted to prepare CuSe₂@rGO composite thin films is shown in Figure 4.2. Thin films of rGO were prepared using LBL method repeated for 40 cycles. This thin film was used for comparative electrochemical study.

4.2.2.4 Material characterizations

4.2.2.4A Physico-chemical characterizations

All the physico-chemical characterizations of CuSe₂ and CuSe₂@rGO thin films were performed as mentioned in section 3.3.1.

4.2.2.4B Electrochemical characterizations

For investigation of electrochemical properties of CuSe_2 and CuSe_2/rGO thin films, three electrode system was used with CuSe_2 or CuSe_2/rGO as a working electrode, mercury/mercury oxide (Hg/HgO), and platinum sheet as a reference and counter electrodes, respectively. All the measurements were carried out in 1 M KOH electrolyte.

4.3 Results and discussion

4.3.1 Growth mechanism of CuSe_2 and CuSe_2/rGO thin films

CuSe_2 and CuSe_2/rGO were deposited on the SS substrate by employing SILAR method. In SILAR method, water soluble precursors in separate beakers were converted into the desired solid substance in a phased manner by a heterogeneous chemical reaction at the solid-liquid interface of the substrate. This is followed by crystal growth on the substrate. Cu^{2+} and Se^{2-} ions are generated in aqueous solutions of CuSO_4 and Na_2Se due to the dissociation process as



In SILAR method, preadsorbed Cu^{2+} ions from CuSO_4 solution react with Se^{2-} ions from Na_2Se solution and form CuSe_2 as

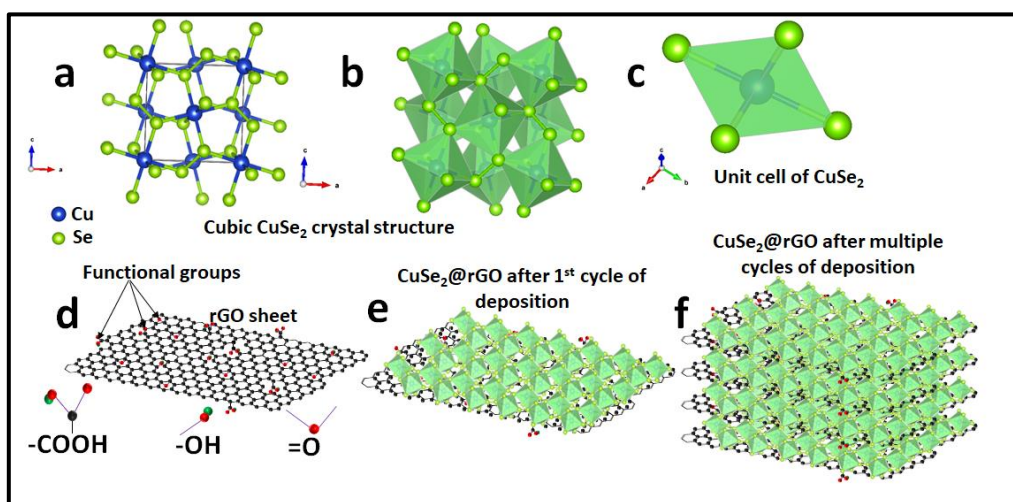


Figure 4.3: a, b) Crystal structure of CuSe_2 plotted using VESTA software, c) unit cell of CuSe_2 , d) rGO sheet, e) CuSe_2/rGO after first SILAR cycle of deposition, f) CuSe_2/rGO after multiple SILAR cycles of deposition.

The crystal structure of CuSe_2 is shown in Figure 4.3a-b. The Cu^{2+} ion is surrounded by six Se^{2-} ions. The unit cell of CuSe_2 is shown in Figure 4.3c. In preparation process of rGO by Hummer's method, defects and wrinkles are formed on rGO sheets. Such defects and wrinkles act as nucleation sites for crystal growth. The rGO nanosheet has a negative charge on itself because of the surface hydroxyl and carboxyl group (Figure 4.3d). The introduction of rGO makes the deposition of CuSe_2 easy and speedy. In this reaction, Cu^{2+} ions were adsorbed electrostatically on rGO sheets. Then the 'oriented attachment' can guide crystal growth. The cubic structured CuSe_2 deposited on rGO nanosheet after single cycle of deposition is shown in Figure 4.3e. Several repeated cycles create a layered structure of CuSe_2 nanoparticles and rGO sheets as presented in Figure 4.3f.

4.3.2 Physico-chemical characterizations of CuSe_2 and CuSe_2 @rGO thin films

4.3.2.1 XRD studies

The XRD patterns of bare CuSe_2 (Figure 4.4a) and CuSe_2 @rGO (Figure 4.4b) thin films are used to obtain information on the crystal structures of deposited material. The XRD pattern of CuSe_2 shows mixed phases of CuSe_2 , Cu_3Se_2 , and elemental Se. The crystallographic planes (001) and (220) are indexed to the standard pattern (JCPDS card no. 72-1421) of tetragonal crystal structure of Cu_3Se_2 . The plane (001) corresponds to metallic Se (JCPDS card no. 86-2246) which may be present at the surface of the film [5, 6]. The sharp peaks corresponding to planes (200), (211), and (221) belong to cubic crystal structure of CuSe_2 (JCPDS card no. 01-071-0047). A similar crystal structure of CuSe_2 was synthesized using thermal evaporation technique by Helan et al. [7].

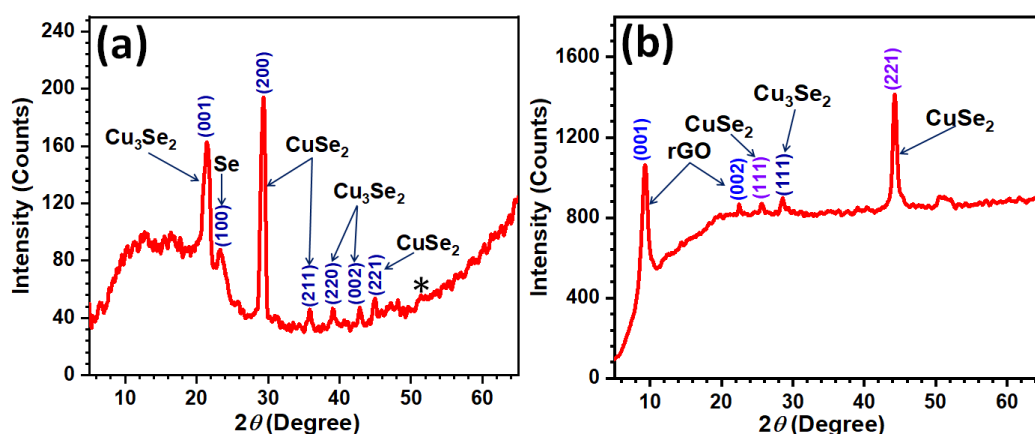


Figure 4.4: The XRD patterns of a) CuSe_2 and b) CuSe_2 @rGO thin films.

The crystallographic planes (001) and (002) correspond to rGO are observed in the XRD pattern of CuSe_2 @rGO thin film. The interplanar distance calculated for (001) plane is 0.93 nm. The (002) plane at $2\theta = 25.79^\circ$ confirms formation of rGO [8]. The planes (111) and (221) are in good accord with the standard diffraction pattern of cubic crystal structure of CuSe_2 (JCPDS card no. 01-071-0047). With the composition of CuSe_2 with rGO, the crystal structure of CuSe_2 remains similar but the crystal orientation takes place along (221) plane. A crystallographic plane (111) at $2\theta = 28.7^\circ$ belongs to tetragonal crystal structure of Cu_3Se_2 . It is noted that the peaks from metallic Se disappeared from the diffraction pattern of the composite film indicating that, the incorporation of rGO in the copper selenide has an impact on the crystal structure and growth mechanism of CuSe_2 . The peak denoted by * corresponds to SS substrate.

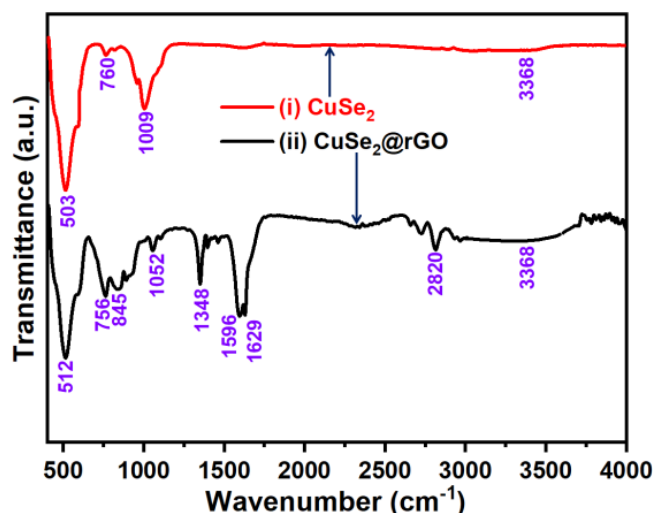


Figure 4.5: FT-IR spectra of (i) CuSe_2 and (ii) CuSe_2 @rGO thin films.

4.3.2.2 FT-IR studies

The FT-IR spectra of CuSe_2 and CuSe_2 @rGO thin films are shown in Figure 4.5. For CuSe_2 thin film, a broad and weak peak was found in between 3368 cm^{-1} attributed to O-H stretching. The band located at 1009 cm^{-1} is due to Se-O bond. The band at 760 cm^{-1} corresponds to Se-Se bonding and the band for Cu-Se stretching vibrations is located at 503 cm^{-1} . Compared with CuSe_2 , In FT-IR spectrum of CuSe_2 @rGO some extra bands located at 2820 cm^{-1} (aromatic sp^2 C-H stretching), 1629 cm^{-1} (C=O stretching vibrations) and 1596 cm^{-1} (COO- asymmetric stretching vibrations), 1348 cm^{-1} (C-OH vibrations) are observed. The observed bands confirm presence of hydroxyl, carboxylic functional groups on the rGO sheet [9-12]. The band

located at 1052 cm^{-1} is due to Se-O bond. The bands at 845 and 756 cm^{-1} correspond to Se-Se bonding vibrations. The absorption band at 512 cm^{-1} corresponds to Cu-Se bond vibrations. The FT-IR study concludes formation of CuSe_2 and $\text{CuSe}_2@\text{rGO}$ composite thin films.

4.3.2.3 Raman studies

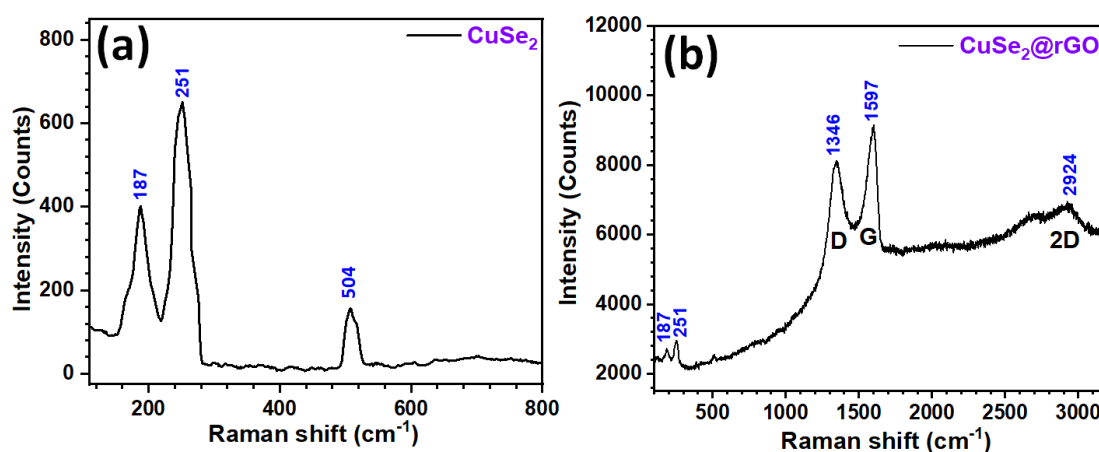


Figure 4.6: The Raman spectra of a) CuSe_2 and b) $\text{CuSe}_2@\text{rGO}$ thin films.

The Raman spectra of CuSe_2 and $\text{CuSe}_2@\text{rGO}$ composite materials are shown in Figure 4.6a and b, respectively. The peaks at 187 and 251 cm^{-1} correspond to Cu-Se bonding and Se-Se bonding, respectively. The peak at 504 cm^{-1} is the overtone of the peak at 251 cm^{-1} . In the Raman spectrum of $\text{CuSe}_2@\text{rGO}$ composite thin film, peaks at 187 and 251 cm^{-1} indicate vibrations of Cu-Se and Se-Se bonding, respectively. Peiris et al. [13] reported Se-Se bond vibrations at 270 cm^{-1} . The peaks at 1346 , 1597 , and 2924 cm^{-1} belong to D, G, and 2D bands of rGO, respectively. The relative intensity ratio $I(\text{D})/I(\text{G})$ for $\text{CuSe}_2@\text{rGO}$ of 0.88 suggests the formation of few-layer rGO in $\text{CuSe}_2@\text{rGO}$ thin film [14, 15]. The relative ratio $I(2\text{D})/I(\text{G})$ (0.76) also supports the formation of few layer rGO [16]. The Raman study confirms formation of composite material as $\text{CuSe}_2@\text{rGO}$.

4.3.2.4 FE-SEM studies

The FE-SEM images of CuSe_2 and $\text{CuSe}_2@\text{rGO}$ electrodes are shown in Figure 4.7a-f at different magnifications ($5,000\text{ X}$, $25,000\text{ X}$, and $100,000\text{ X}$). For CuSe_2 thin film, at a magnification of $5,000\text{ X}$ (Figure 4.7a) smaller particles are uniformly coated on the surface of SS substrate. At the magnification of $10,000\text{ X}$ (Figure 4.7b), petal-like particles interconnected to each other are observed. The surface topography

of CuSe_2 electrode consists of small petal-like particles with an average size of 95 nm (Figure 4.7c) are uniformly distributed on the substrate. All these petals are interconnected to each other and horizontally aligned on the SS substrate.

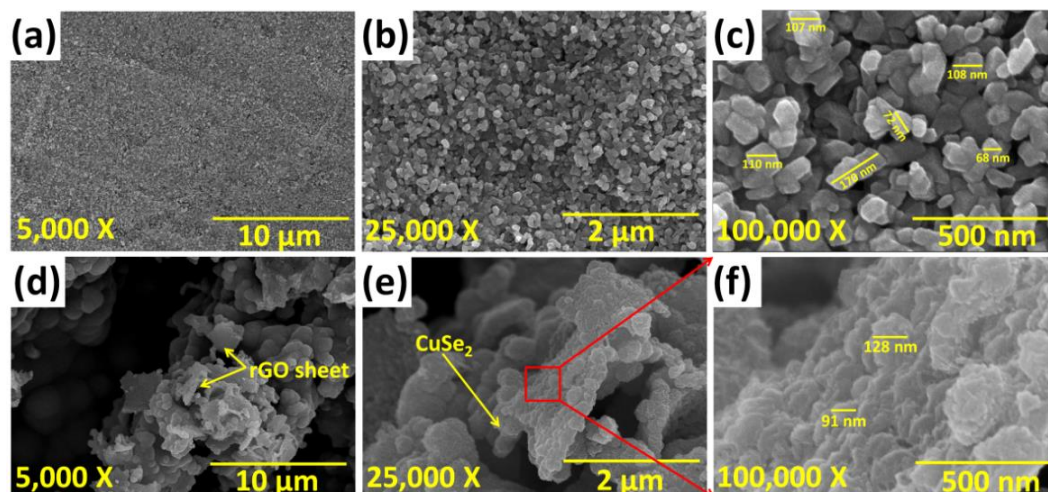


Figure 4.7: The FE-SEM images of a-c) CuSe_2 , and d-f) $\text{CuSe}_2@\text{rGO}$ thin films at various (5,000 X, 25,000 X, and 100,000 X) magnifications.

Interestingly, $\text{CuSe}_2@\text{rGO}$ electrode surface morphology looks very different; the surface consists of rGO sheets covered with nanospheres of CuSe_2 , as shown in Figure 4.7d. At higher magnification (Figure 4.7e and f), these spheres consist of smaller petal-like particles. In $\text{CuSe}_2@\text{rGO}$ electrode pores are created due to the heterogeneous layered structure of rGO sheets. It is seen that the nanostructure of CuSe_2 is effectively tuned from the dense nano-petals to highly porous architecture using rGO sheets. These modulated porous microstructures can promote interaction between the electrolyte and the electrodes. The rGO layer deposited on SS affects the nucleation, aggregation, and coalescence process which leads to variation in surface morphology of $\text{CuSe}_2@\text{rGO}$ from CuSe_2 .

4.3.2.5 EDAX studies

The EDAX spectra for CuSe_2 and $\text{CuSe}_2@\text{rGO}$ samples are shown in Figure 4.8a and b, respectively. The EDAX spectrum confirms presence of Cu and Se in CuSe_2 thin film. The peaks from Cu, Se, C, and O elements are observed in the EDAX spectrum of $\text{CuSe}_2@\text{rGO}$ thin film. The atomic percentages of Cu and Se elements in CuSe_2 film are 34.9 and 65.1%, respectively. The elemental ratio of Cu:Se is 1:1.86. In copper selenide film, Cu and Se are present in the form of Cu_3Se_2 , Se, and CuSe_2 , as observed from the XRD pattern hence atomic ratio deviates from

the ideal value (1:2). For CuSe₂@rGO film, the atomic percentages of Cu, Se, C, and O are 20.33, 43.27, 29.18, 7.20%, respectively. The XRD and EDAX results confirm the formation of CuSe₂ and CuSe₂@rGO composite thin films.

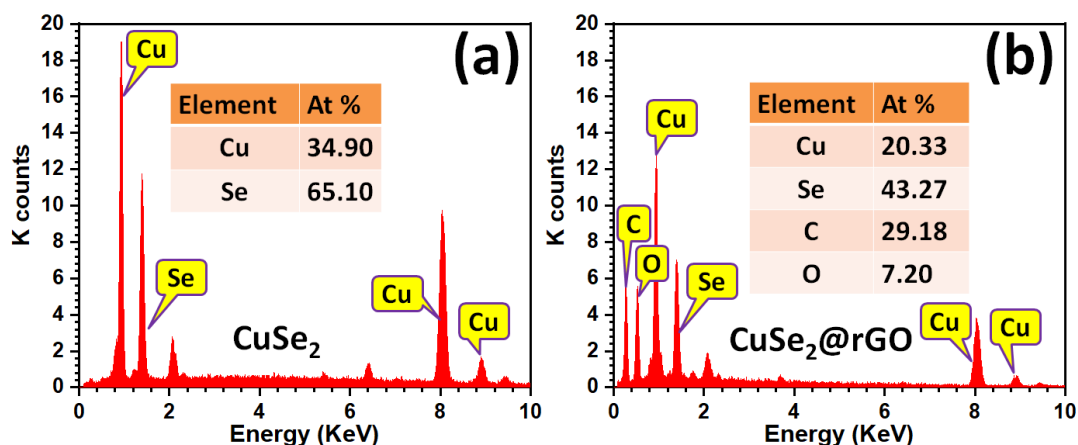


Figure 4.8: EDAX spectra of a) CuSe₂ and b) CuSe₂@rGO thin films (Insets show atomic percentages of elements).

4.3.2.6 XPS studies

To identify oxidation states and possible bonding between Cu and Se elements, the XPS analysis was carried out and results for CuSe₂@rGO film are presented in Figure 4.9a. The peaks from Cu, Se, C and O confirm presence of these elements at the film surface. The XPS spectrum of Cu2p is shown in Figure 4.9b. The peaks at the binding energies 934.1 and 954.5 eV correspond to Cu2p_{3/2} and Cu2p_{1/2} of Cu²⁺, respectively. However, two weak satellite peaks at approximately 943.6 and 962.8 eV indicate paramagnetic chemical state of Cu²⁺. The peaks at 931.7 and 952.2 eV belong to Cu⁺¹ and peaks at 941.1 and 961.1 eV are satellite peaks of Cu⁺¹ [17, 18]. The high resolution spectrum of Se3d is presented in Figure 4.9c. The peaks at binding energies of 54.7 and 55.8 eV correspond to Se3d_{5/2} and Se3d_{3/2}, respectively in CuSe₂ confirm the presence of Se⁻² state, which is in agreement with the literature [19, 20].

The XPS spectra of C1s from rGO (Figure 4.9d) indicate three components that are related to C atoms in different functional groups; the peak at 284 eV indicates non-oxygenated (C=C) sp² hybridized ring of rGO, the peak at 285.9 eV indicates C–O bond confirming hydroxyl group attached to the rGO sheet, and peak of C (C=O) at 288.1 eV confirms carboxylic group [21].

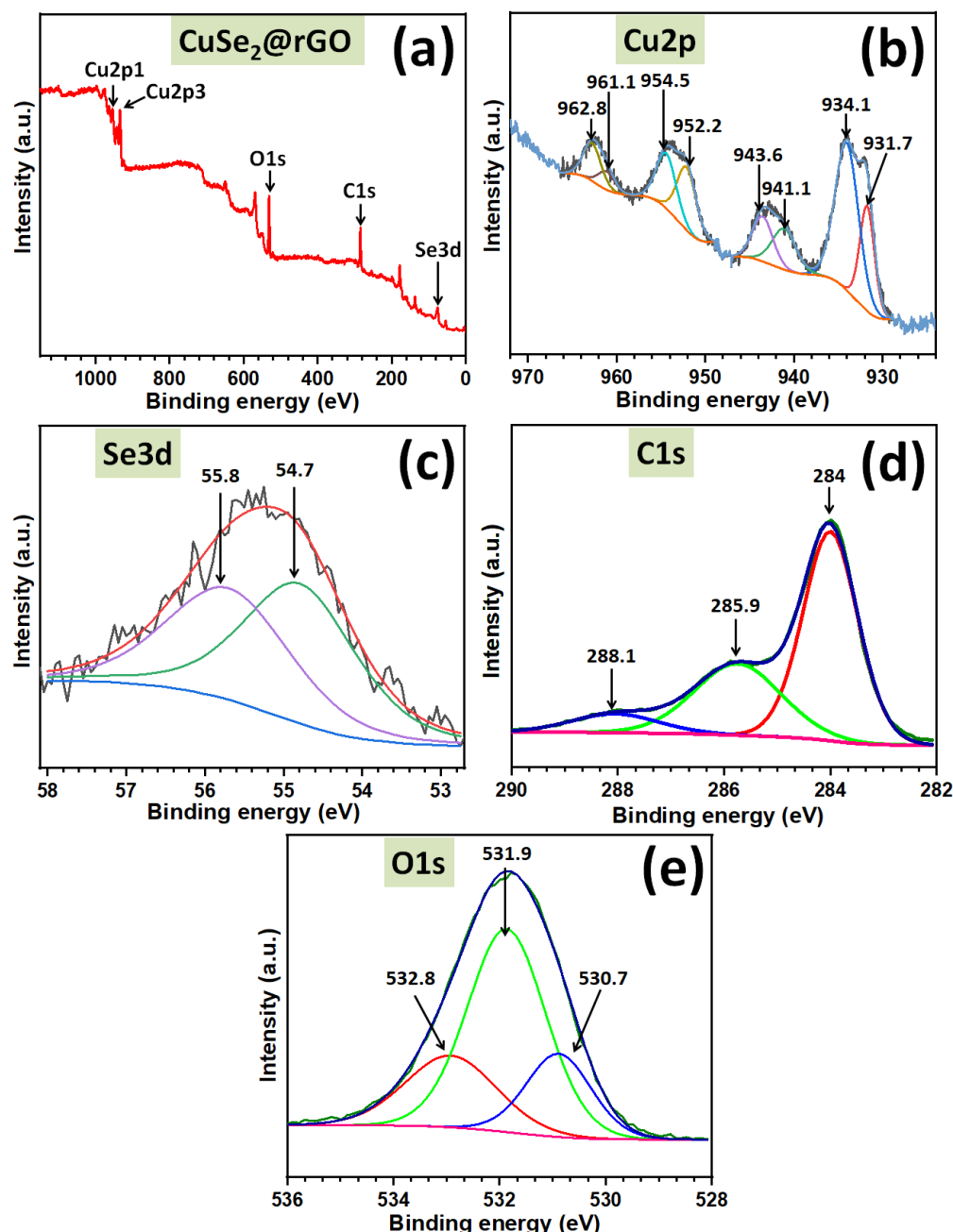


Figure 4.9: a) The XPS spectrum of $\text{CuSe}_2@\text{rGO}$ electrode, the XPS spectrum of b) $\text{Cu}2p$, c) $\text{Se}3d$, d) $\text{C}1s$, and e) $\text{O}1s$.

As shown in Figure 4.9e, the atomic percentage of O on the surface of the sample is very high, which is attributed to various oxidation states based on the differences in the position and shape of $\text{O}1s$ peaks. The $\text{O}1s$ signal of $\text{CuSe}_2@\text{rGO}$ could be deconvoluted into three Gaussian peaks. The peak at binding energy 531.9 eV is attributed to lattice oxygen confirms the formation of O-C bond, and the other two peaks at 532.8 eV and 530.7 eV are attributed to nonlattice oxygen from the carboxyl group and hydroxyl group, respectively [22, 23]. The XPS study lights up

the possible presence of Cu=Se, Se=O, C=O, O-Cu, Cu=C C=C, and C-C=O(OH) bonds in a composite CuSe₂@rGO thin film.

4.3.2.7 Contact angle studies

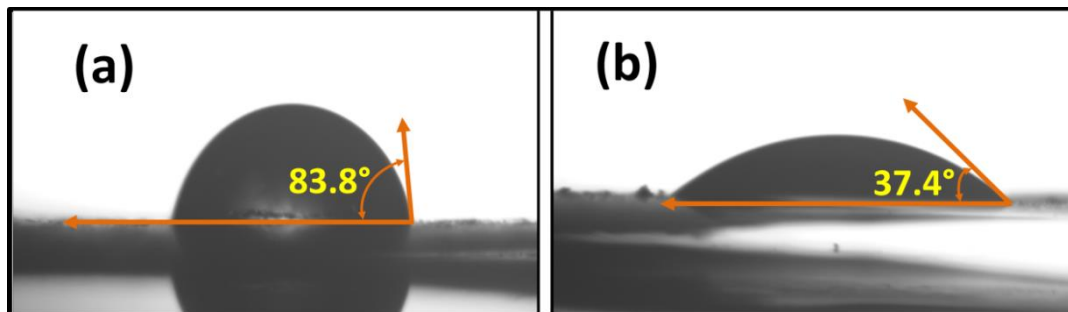


Figure 4.10: Water contact angle photographs of a) CuSe₂ and b) CuSe₂@rGO thin films.

The wettability of the electrolyte on the surface of the electrode has been regarded as an important issue to raise the effective surface area and to improve C_s . The contact angle images of CuSe₂ and CuSe₂@rGO (Figure 4.10) show the values as 83.8° and 37.4°, respectively. The contact angle depends on chemical and physical factors. The particle shape, particle size, purity, roughness, and cleanliness of the surface, and heterogeneity affect the contact angle. With the introduction of rGO, the change in surface topography (as observed in FE-SEM) affects the wettability of the electrodes. The presence of hydroxyl and carboxylic groups in the CuSe₂@rGO film electrode results in a decrease in smaller contact angle. The hydrophilic samples can create good contact with the aqueous electrolyte which may result in least R_{ct} and improvement in S_p of SCs [24].

4.3.2.8 BET and BJH studies

It is well known that as specific surface area of the electrode material raises the charge accumulation on the electrode surges in proportion. The specific surface area and average pore size distribution of materials scratched from the corresponding electrodes were measured by N₂ sorption isotherms. CuSe₂ and CuSe₂@rGO electrodes exhibit type IV isotherms having an H3-type hysteresis curve in the range of 0.45 to 1.0 of relative pressure as shown in Figures 4.11a and b, indicating presence of meso and micropores [25].

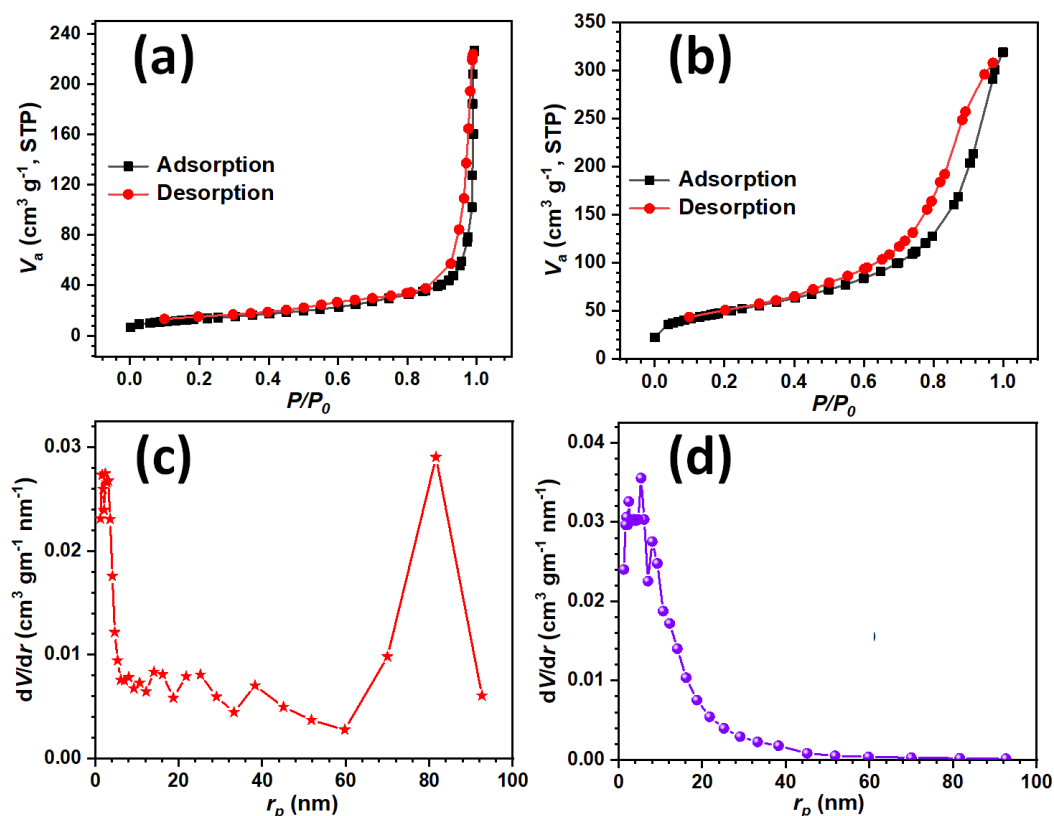


Figure 4.11: N₂ adsorption graphs of a) CuSe₂, and b) CuSe₂@rGO and pore size distribution of c) CuSe₂, and d) CuSe₂@rGO samples.

The average pore diameter of the electrodes was analyzed by Barrett-Joyner-Halend (BJH) method and results are provided in Figures 4.11c and d. The BET specific surface areas of CuSe₂ and CuSe₂@rGO samples are found to be 24 m² g⁻¹ and 84 m² g⁻¹, respectively. These results indicate that the composition of pseudocapacitive material with rGO sheets enhances the specific surface area. The observed average pore diameter for CuSe₂ is 32 nm and for CuSe₂@rGO sample 13 nm. The average pore diameter is decreased after composition. The decrease in average pore size for CuSe₂@rGO may cause in the rise of specific capacitance compared to CuSe₂ [26]. From the XRD, SEM, and BET studies, it is observed that the incorporation of rGO with copper selenide film affects structural and topographical properties.

4.3.3 Electrochemical characterizations of CuSe₂ and CuSe₂@rGO thin films

4.3.3.1 CV studies

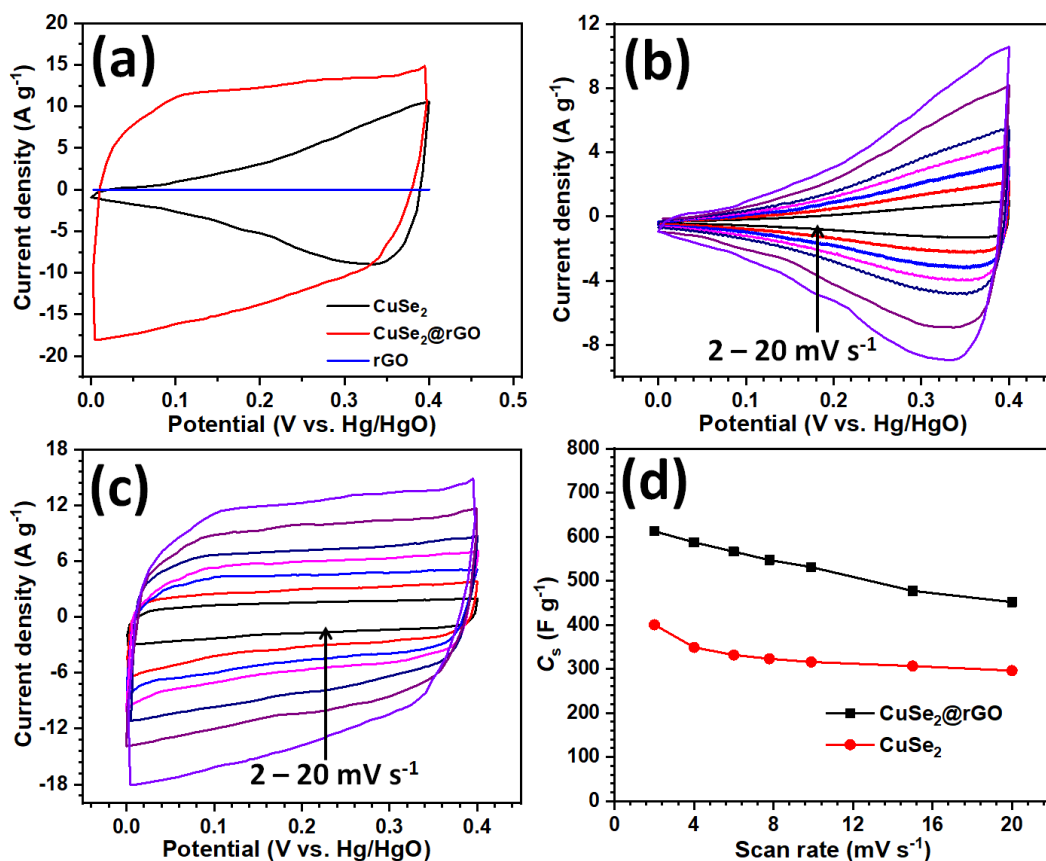


Figure 4.12: a) Comparative CV curves of CuSe₂, CuSe₂@rGO, and rGO at a scan rate of 20 mV s⁻¹, the CV curves of b) CuSe₂, and c) CuSe₂@rGO at various scan rates from 2-20 mV s⁻¹, and d) variation of C_s with the scan rate for CuSe₂ and CuSe₂@rGO thin film electrodes.

To figure out the effect of composition of CuSe₂ with rGO on the electrochemical charge storage performance of electrodes, CV curves of CuSe₂ and CuSe₂@rGO were measured in 1 M KOH electrolyte using half cell (three electrodes) system. The comparative CV curves of CuSe₂, CuSe₂@rGO and rGO thin films at a scan rate of 20 mV s⁻¹ is shown in Figure 4.12a. The current response for the rGO thin films is very low compared CuSe₂ and CuSe₂@rGO thin films. With introduction of rGO in CuSe₂, an improvement in the electrochemical properties is observed from the CV curves (Figure 4.12a). The CV curves of CuSe₂ thin film electrode at scan rates between 2 to 20 mV s⁻¹ are shown in Figure 4.12b and that of CuSe₂@rGO in Figure 4.12c. For composite electrode, shape of CV curves changes to near rectangle due to the presence of rGO as confirmed by XRD, EDAX, and XPS studies. Change in CV curves with rGO indicates difference in the charge storage mechanism. Shape of CV curves indicates transformation in charge storage mechanism from intercalation pseudocapacitor to surface redox pseudocapacitor [27, 28]. The values of C_s for

CuSe₂ and CuSe₂@rGO are 400 and 612 F g⁻¹, respectively at the scan rate of 2 mV s⁻¹. As the scan rate increases, C_s decreased due to time constraint at a higher scan rate for reversible redox reactions. The variation in C_s with the scan rate is shown in Figure 4.12d.

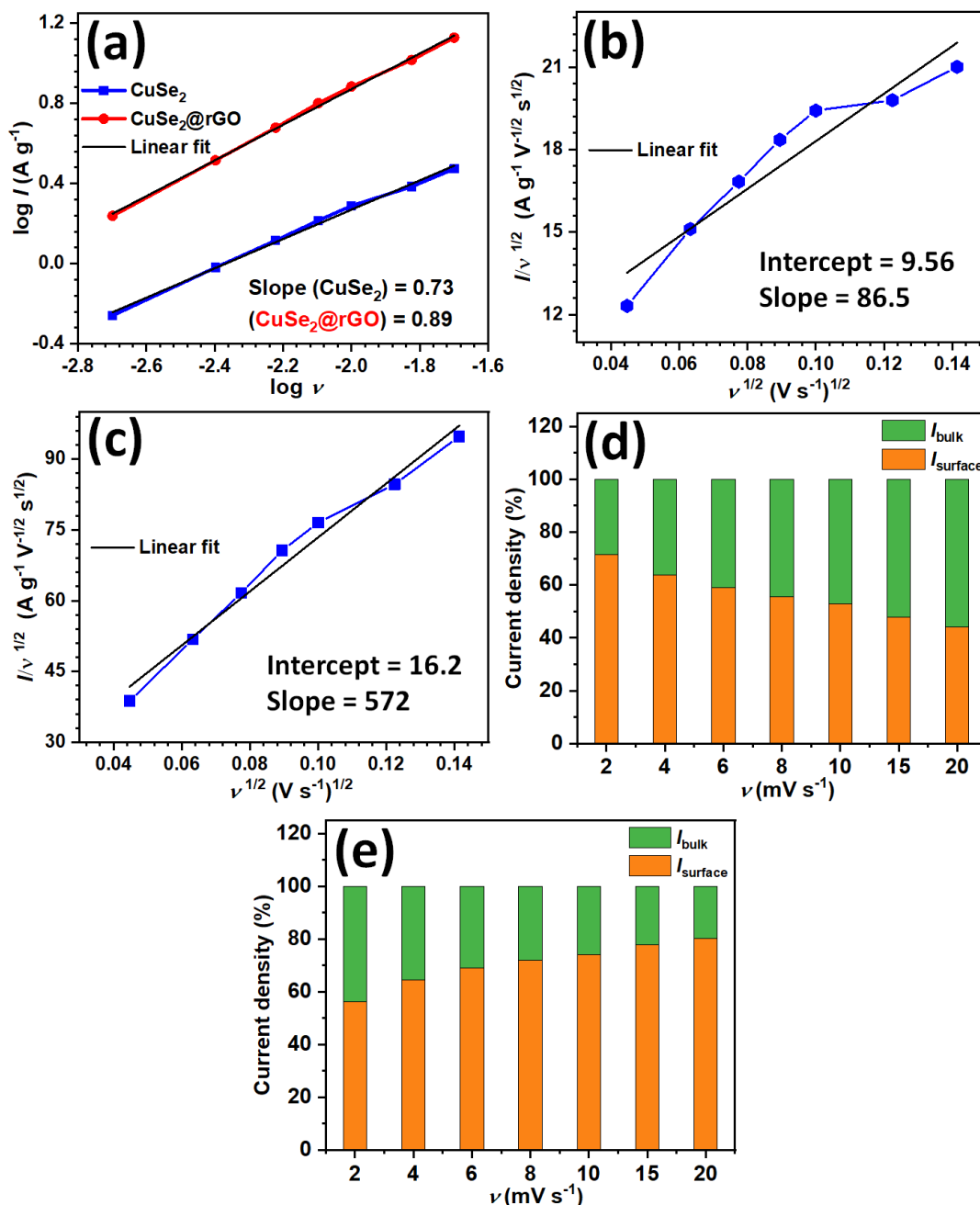


Figure 4.13: a) Plots of $\log I$ versus $\log \nu$, b) plots of $I/\nu^{1/2}$ versus $\nu^{1/2}$ of CuSe₂, and CuSe₂@rGO thin film electrodes, and calculated charge storage by capacitive and diffusion processes for d) CuSe₂, and e) CuSe₂@rGO thin film electrodes.

The charge storage process is controlled by two kinds of mechanisms, the capacitive (charge storage on the outer surface) process and the diffusion controlled

(charge storage inside bulk electrode) process [29, 30]. The peak current (I_p) obtained in CV curves is related to potential scan rate (v) according to the Eq. 3.2. The actual contribution of both processes can be separated using Eq. 3.3. The estimated value of constant b from plot of $\log I$ versus $\log v$ (Figure 4.13a) is 0.73 for CuSe_2 and changes to 0.89 for $\text{CuSe}_2@\text{rGO}$ film electrode. Such deviation in b value indicates a rise in charge storage through a capacitive controlled process. These are expected results as depicted in the change in topography observed through FE-SEM images and rise in specific surface area of $\text{CuSe}_2@\text{rGO}$ compared to CuSe_2 thin film electrode. This indicates that the composition of rGO with CuSe_2 facilitates more active sites to electrolyte ions for reversible electrochemical reactions [31]. In Figures 4.13b and c, the graphs of $I/v^{1/2}$ versus $v^{1/2}$ for the cathodic current at potential of 0.4 V vs. Hg/HgO give values of constants k_1 (slope) and k_2 (y-axis intercept) for CuSe_2 and $\text{CuSe}_2@\text{rGO}$ thin film electrodes, respectively.

The specific current contribution from capacitive and diffusive processes calculated from Eq. 3.3 is presented in Figures 4.13d and e for both electrodes. For CuSe_2 electrode, the charge storage through the diffusion process is higher, about 66% of the total current due to diffusion process at the scan rate of 20 mV s^{-1} . On the other hand, for $\text{CuSe}_2@\text{rGO}$ composite electrode, the value of the current due to diffusion process is approximately 20% at scan rate of 20 mV s^{-1} . This interprets that, for $\text{CuSe}_2@\text{rGO}$ electrode the current contribution through diffusion process decreased as compared to CuSe_2 electrode at the same scan rate and the most current contribution is the result of the capacitive controlled process. The analysis of the CV study using power law shows that charge storage in CuSe_2 electrode is more diffusion controlled than $\text{CuSe}_2@\text{rGO}$ electrode [32].

4.3.3.2 GCD studies

The GCD curves of CuSe_2 and $\text{CuSe}_2@\text{rGO}$ are shown in Figures 4.14a and b, respectively. The GCD curves show transformation of charge storage mechanism due to the composition of CuSe_2 with rGO. The C_s values from GCD plots are 404 and 471 F g^{-1} at the current density of 2 A g^{-1} for CuSe_2 and $\text{CuSe}_2@\text{rGO}$, respectively. Variation of C_s with the applied current density is shown in Figure 4.14c. As C_s decreases with the increasing scan rate, in the same way, it decreases with the rising current density. From the CV and GCD studies, it is concluded that the charge storage

for CuSe₂@rGO electrode is mainly attributed to surface faradaic charge transfers as a result of the insertion of electrolyte ions into layer structured CuSe₂@rGO electrode [33].

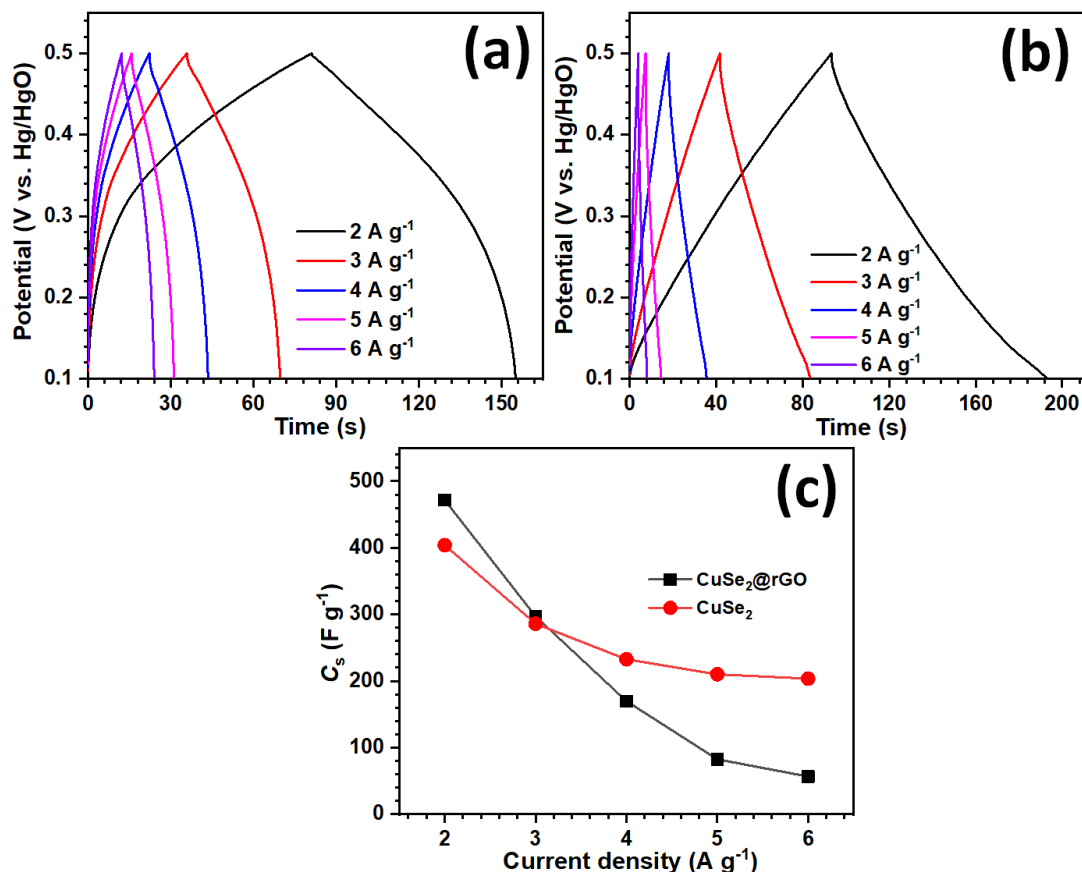


Figure 4.14: The GCD curves of a) CuSe₂, b) CuSe₂@rGO at different current densities from 2-6 A g⁻¹, and c) variation of C_s with charge-discharge current density.

4.3.3.3 EIS studies

The Nyquist plots of CuSe₂ and CuSe₂@rGO electrodes are shown in Figure 4.15a. The sections of Nyquist plots at a higher frequency are shown in inset of Figure 4.15a. The R_s given by intercept of Nyquist plot on real axis is 1.39 and 0.83 $\Omega \text{ cm}^{-2}$ for CuSe₂ and CuSe₂@rGO electrodes, respectively. The decrease in R_s is due to better contact of electrolyte with CuSe₂@rGO electrode due to various functional groups attached to rGO sheets [34, 35]. Furthermore, the reduction in diameter of semicircle arose at middle frequencies of Nyquist plot suggests a decrease in R_{ct} . The lower value of R_{ct} (1.50 $\Omega \text{ cm}^{-2}$) for CuSe₂@rGO electrode compared to that of CuSe₂ (3.50 $\Omega \text{ cm}^{-2}$) suggests that CuSe₂@rGO electrode provides good conductivity in 1 M KOH aqueous electrolyte. The low R_s and R_{ct} values for CuSe₂ and CuSe₂@rGO electrodes may be due to binder free synthesis and better electron transferability from

electrolyte to electrode and reciprocally. The electrolytic ion diffusion in the active material is responsible for the straight line in the low frequency region and it corresponds to W . The EIS data reveals that CuSe_2/rGO film electrode has lower resistance and better electrochemical performance. This proves that resistive parameters of electrodes are modified due to lateral paths provided by rGO in CuSe_2/rGO composite electrode [36].

The fitted equivalent circuit from the EIS data of both film electrodes is shown in Figure 4.15b. The circuit consists of R_s , R_{ct} , W , and C_{dl} . The values of each fitted circuit parameter are tabulated in Table 4.1.

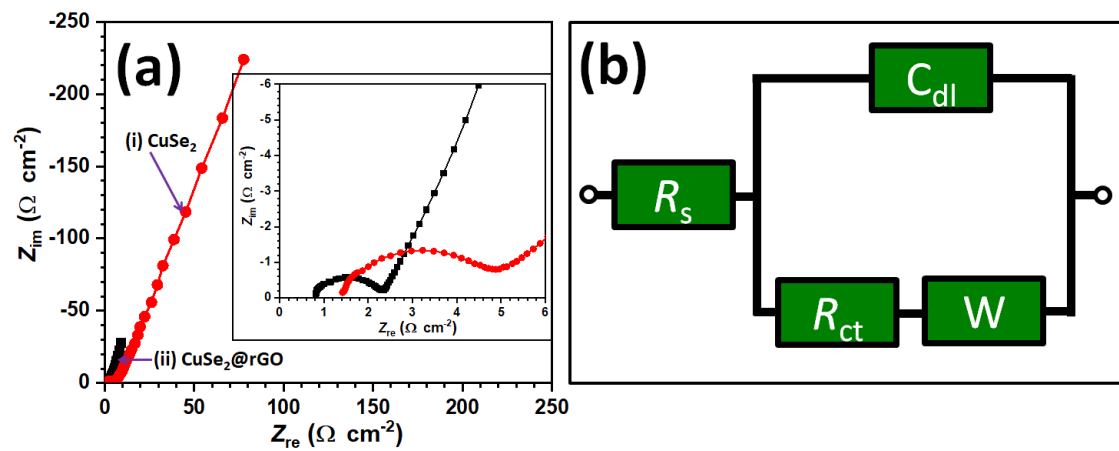


Figure 4.15: a) Nyquist plots of i) CuSe_2 and ii) CuSe_2/rGO thin film electrodes (Inset shows magnified Nyquist plots in higher frequency region), and b) the fitted equivalent circuit from the EIS data.

Table 4.1: Electrochemical impedance fitted circuit parameters for Nyquist plots of CuSe_2 and CuSe_2/rGO thin film electrodes.

Sample	R_s ($\Omega \text{ cm}^{-2}$)	R_{ct} ($\Omega \text{ cm}^{-2}$)	C_{dl} (mF)	W (Ω)
CuSe_2	1.39	3.50	0.68	1.04
CuSe_2/rGO	0.83	1.50	0.73	0.57

4.3.3.4 Stability studies

The electrochemical stability of electrode material is one of the decisive parameters to determine applicability of synthesized thin film electrode for SC device fabrication [37, 38]. The GCD studies at a current density of 6 A g^{-1} were carried out to examine electrochemical stability of both electrodes for 10,000 cycles. The retention of C_s for CuSe_2 and CuSe_2/rGO electrodes for 10,000 GCD cycles are

shown in Figure 4.16. In comparison, $\text{CuSe}_2@\text{rGO}$ (78%) electrode exhibits better electrochemical stability than CuSe_2 (57%). $\text{CuSe}_2@\text{rGO}$ thin film electrode shows improved cycling stability as compared to CuSe_2 thin film electrode as rGO sheets assist rapid electron mobility in $\text{CuSe}_2@\text{rGO}$ composite to accelerate the reversible electrochemical redox reactions. Increased electrical conductivity also results in improved stability of the composite electrode material [39].

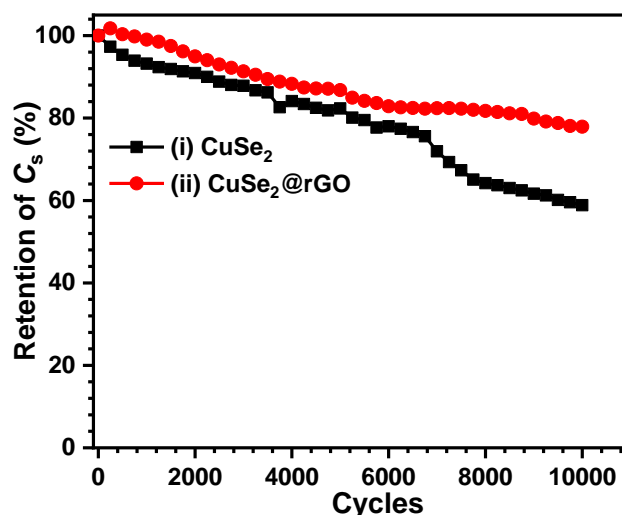


Figure 4.16: Stability curves of i) CuSe_2 and ii) $\text{CuSe}_2@\text{rGO}$ thin film electrodes.

4.4 Conclusions

In summary, $\text{CuSe}_2@\text{rGO}$ composite thin film electrode was prepared on a flexible SS substrate using SILAR method at room temperature and implemented as an anode material for supercapacitive charge storage. This study concludes that the binder less composition of CuSe_2 with rGO affects the structural, morphological, and electrochemical properties of CuSe_2 . The composite $\text{CuSe}_2@\text{rGO}$ electrode exhibited an excellent specific surface area of $84 \text{ m}^2 \text{ g}^{-1}$ compared to that of $24 \text{ m}^2 \text{ g}^{-1}$ for bare CuSe_2 . The C_s of CuSe_2 and $\text{CuSe}_2@\text{rGO}$ films were 400 and 612 F g^{-1} , respectively at the scan rate of 2 mV s^{-1} . The stability of the composite electrode (78%) was more than that of the bare electrode (57%) after 10,000 GCD cycles. Based on the experimental results, preparing a composite material via SILAR method is an auspicious strategy to enhance specific surface area and electrochemical performance of the electrode for SC applications.

References:

- [1] B. Zhao, D. Chen, X. Xiong, B. Song, R. Hu, Q. Zhang, B. Rainwater, G. Waller, D. Zhen, Y. Ding, Y. Chen, C. Qu, D. Dang, C. Wong, M. Liu, A high-energy,

-
- long cycle-life hybrid supercapacitor based on graphene composite electrodes, *Energy Storage Mater.*, 7 (2017) 32-39, DOI: 10.1016/j.ensm.2016.11.010.
- [2] C. Jinga, X. Guo, L. Xia, Y. Chen, X. Wang, X. Liu, B. Dong, F. Dong, S. Li, Y. Zhang, Morphologically confined hybridization of tiny CoNi_2S_4 nanosheets into S, P co-doped graphene leading to enhanced pseudocapacitance and rate capability, *Chem. Eng. J.*, 379 (2020) 122305, DOI: 10.1016/j.cej.2019.122305.
- [3] A. Fouda, A. Salem, F. El-Tantawy, H. Salem, E. Duraia, Hydrothermal synthesis of high quality graphene nanosheets anchored by uniform and well distributed silicon nanoparticles, *Superlattices Microstruct.*, 124 (2018) 240-247, DOI: 10.1016/j.spmi.2018.08.025.
- [4] P. Ren, D. Yan, X. Ji, T. Chen, Z. Li, Temperature dependence of graphene oxide reduced by hydrazine hydrate, *Nanotechnology*, 22 (2011) 055705, DOI: 10.1088/0957-4484/22/5/055705.
- [5] M. Gilic, M. Petrovic, R. Kostic, D. Stojanovic, T. Barudzija, M. Mitric, N. Romcevic, U. Ralevic, J. Trajic, M. Romcevic, I. S. Yahia, Structural and optical properties of CuSe_2 nanocrystals formed in thin solid Cu–Se film, *Infrared Phys. Technol.*, 76 (2016) 276–284, DOI: 10.1016/j.infrared.2016.03.008.
- [6] M. Xue, Y. Zhou, B. Zhang, L. Yu, H. Zhang, Z. Fu, Fabrication and electrochemical characterization of copper selenide thin films by pulsed laser deposition, *J. Electrochem. Soc.*, 153 (2006) A2262-A2268, DOI: 10.1149/1.2358854.
- [7] P. P. J. Helan, K. Mohanraj, G. Sivakumar, Doping of Sn transition metal in CuSe_2 thin films and its effect on structural evolution and opto-electrical properties, *Appl. Phys. A*, 122 (2016) 718-8, DOI: 10.1007/s00339-016-0249-7.
- [8] A. Viswanathan, A. Shetty, Facile in-situ single step chemical synthesis of reduced graphene oxide-copper oxide-polyaniline nanocomposite and its electrochemical performance for supercapacitor application, *Electrochim. Acta*, 257 (2017) 483-493, DOI: 10.1016/j.electacta.2017.10.099.
- [9] M. Senthilkumar, C. I. Mary, S. M. Babu, Morphological controlled synthesis of hierarchical copper selenide nanocrystals by Oleic acid, 1-Dodecanethiol and 1-Octadecene as surfactants, *J. Cryst. Growth*, 468 (2017) 169-174, DOI: 10.1016/j.jcrysgro.2016.11.001.
- [10] C. Gopi, R. Vinodh, S. Sambasivam, I. M. Obaidat, R. M. N. Kall, H. Kim, One-pot synthesis of copper oxide–cobalt oxide core–shell nanocactus-like heterostructures as binder-free electrode materials for high-rate hybrid supercapacitors, *Mater. Today Energy*, 14 (2019) 100358-9, DOI: 10.1016/j.mtener.2019.100358.
- [11] F. Qiao, J. Wang, S. Ai, L. Li, As a new peroxidase mimetics: The synthesis of selenium doped graphitic carbon nitride nanosheets and applications on colorimetric detection of H_2O_2 and xanthine, *Sens. Actuators B Chem.*, 216 (2015) 418-427, DOI: 10.1016/j.snb.2015.04.074.
-

- [12] G. Deniau, L. Azoulay, P. Je'gou, G. Chevallier, S. Palacin, Carbon-to-metal bonds: Electrochemical reduction of 2-butenitrile, *Surf. Sci.*, 600 (2006) 675–684, DOI: 10.1016/j.susc.2005.11.021.
- [13] S. M. Peiris, T. T. Pearson, D. L. Heinz, Compression of klockmannite, CuSe, *J. Chem. Phys.*, 109 (1998) 634-636, DOI: 10.1063/1.476601.
- [14] T. C. S. Girisun, M. Saravanan, V. R. Soma, Wavelength-Dependent Nonlinear Optical Absorption and Broadband Optical Limiting in Au-Fe₂O₃-rGO Nanocomposites, *ACS Appl. Nano Mater.*, 1 (2018) 6337-6348, DOI: 10.1021/acsanm.8b01544.
- [15] W. Wang, Y. Liu, H. Zhang, Y. Qian, Z. Guo, Re-investigation on reduced graphene oxide/Ag₂CO₃ composite photocatalyst: An insight into the double-edged sword role of RGO, *Appl. Surf. Sci.*, 396 (2017) 102-109, DOI: 10.1016/j.apsusc.2016.11.030.
- [16] V. Fesenko, G. Dovbeshko, A. Dementjev, R. Karpicz, T. Kaplas, Y. Svirko, Graphene-enhanced Raman spectroscopy of thymine adsorbed on single-layer graphene, *Nanoscale Res. Lett.*, 10 (2015) 163-7, DOI: 10.1186/s11671-015-0869-4.
- [17] X. Liu, X. Duan, P. Peng, W. Zheng, Hydrothermal synthesis of copper selenides with controllable phases and morphologies from an ionic liquid precursor, *Nanoscale*, 3 (2011) 5090-5095, DOI: 10.1039/c1nr10833f.
- [18] M. Monte, G. Munuera, D. Costa, J. C. Conesa, A. Martínez-Arias, Near-ambient XPS characterization of interfacial copper species in ceria-supported copper catalysts, *Phys. Chem. Chem. Phys.*, 17 (2015) 29995-30004, DOI: 10.1039/C5CP04354A.
- [19] L. Qiao, H. Wang, Y. Shen, Y. Lin, C. Nan, Enhanced photocatalytic performance under visible and near-infrared irradiation of Cu_{1.8}Se/Cu₃Se₂ composite via a phase junction, *Nanomaterials*, 7 (2017) 19, DOI: 10.3390/nano7010019.
- [20] L. Ran, L. Yin, Double-walled heterostructured Cu_{2-x}Se/Cu₇S₄ nanoboxes with enhanced electrocatalytic activity for quantum dot sensitized solar cells, *CrystEngComm*, 19 (2017) 5640-5652, DOI: 10.1039/C7CE01112A.
- [21] R. Al-Gaashani, A. Najjar, Y. Zakaria, S. Mansour, M. A. Atieh, XPS and structural studies of high quality graphene oxide and reduced graphene oxide prepared by different chemical oxidation methods, *Ceram. Int.*, 45 (2019) 14439-14448, DOI: 10.1016/j.ceramint.2019.04.165.
- [22] Z. Huang, Z. Li, L. Zheng, L. Zhou, Z. Chai, X. Wang, W. Shi, Interaction mechanism of uranium(VI) with three-dimensional graphene oxide-chitosan composite: Insights from batch experiments, IR, XPS, and EXAFS spectroscopy, *Chem. Eng. J.*, 28 (2017) 1066-1074, DOI:10.1016/j.cej.2017.07.067.
- [23] H. Wang, L. Ma, M. Gan, T. Zhou, X. Sun, W. Dai, H. Wang, S. Wang, Design and assembly of reduced graphene oxide/polyaniline/urchin-like mesoporous TiO₂ spheres ternary composite and its application in supercapacitors,

-
- Composites, Part B, 92 (2016) 405-412, DOI: 10.1016/j.compositesb.2016.02.047.
- [24] P. Avasthi, A. Kumar, V. Balakrishnan, Paradoxical observance of “intrinsic” and “geometric” oxygen evolution electrocatalysis in phase-tuned cobalt oxide/hydroxide nanoparticles, *ACS Appl. Nano Mater.*, 2 (2019) 1484-1495, DOI: 10.1021/acsanm.9b01990.
- [25] X. Lin, Q. Lü, Q. Li, M. Wu, R. Liu, Fabrication of low-cost and eco-friendly porous biocarbon using konjaku flour as the raw material for high-performance supercapacitor application, *ACS Omega*, 3 (2018) 13283–13289, DOI: 10.1021/acsomega.8b01718.
- [26] A. Gupta, S. Sardana, J. Dalal, S. Lather, A. S. Maan, R. Tripathi, R. Punia, K. Singh, A. Ohlan, Nanostructured Polyaniline/Graphene/Fe₂O₃ composites hydrogel as a high-performance flexible supercapacitor electrode material, *ACS Appl. Energy Mater.*, 3 (2020) 6434-6446, DOI: 10.1021/acsaem.0c00684.
- [27] N. R. Chodankar, H. D. Pham, A. K. Nanjundan, J. F. S. Fernando, K. Jayaramulu, D. Golberg, Y. Han, D. P. Dubal, True meaning of pseudocapacitors and their performance metrics: asymmetric versus hybrid supercapacitors, *Small*, 16 (2020) 2002806-35, DOI: 10.1002/sml.202002806.
- [28] A. J. C. Mary, C. I. Sathish, A. Vinu, A. C. Bose, Electrochemical performance of rGO/NiCo₂O₄@ZnCo₂O₄ ternary composite material and the fabrication of an all-solid-state supercapacitor device, *Energy & Fuels*, 34 (2020) 10131-10141, DOI: 10.1021/acs.energyfuels.0c01427.
- [29] N. Priyadharsini, R. K. Selvan, Nano-sheet-like KNiPO₄ as a positive electrode material for aqueous hybrid supercapacitors, *Electrochim. Acta*, 246 (2017) 963-970, DOI: 10.1016/j.electacta.2017.06.100.
- [30] B. Mei, O. Munteshari, J. Lau, B. Dunn, L. Pilon, Physical interpretations of nyquist plots for EDLC electrodes and devices, *J. Phys. Chem. C*, 122 (2018) 194–206, DOI: 10.1021/acs.jpcc.7b10582.
- [31] F. Li, Z. Sun, H. Jiang, Z. Ma, Q. Wang, F. Qu, Ion-exchange synthesis of ternary feconi-layered double hydroxide nanocage toward enhanced oxygen evolution reaction and supercapacitor, *Energy & Fuels*, 34 (2020) 11628-11636, DOI: 10.1021/acs.energyfuels.0c02533.
- [32] Q. Wu, Y. Xu, Z. Yao, A. Liu, G. Shi, Supercapacitors Based on flexible graphene/polyaniline nanofiber composite films, *ACS Nano*, 4 (2010) 1963-1970, DOI: 10.1021/nn1000035.
- [33] N. Choudhary, C. Li, H. Chung, J. Moore, J. Thomas, Y. Jung, High-performance one-body core/shell nanowire supercapacitor enabled by conformal growth of capacitive 2D WS₂ layers, *ACS Nano*, 10 (2016) 10726-10735, DOI: 10.1021/acsnano.6b06111.
- [34] A. Joshi, S. Lalwani, G. Singh, R. K. Sharma, Highly oxygen deficient, bimodal mesoporous silica based supercapacitor with enhanced charge storage
-

- characteristics, *Electrochim. Acta*, 297 (2019) 705-714, DOI: 10.1016/j.electacta.2018.12.033.
- [35] S. Ayaz, P. K. Mishra, R. K. Sharma, S. Kamal, S. Sen, Structural, optoelectronic, and electrochemical properties of $\text{Zn}_{1-x}(\text{Ga}_{0.5}\text{Al}_{0.5})_x\text{O}$ nanoparticles for supercapacitor applications, *ACS Appl. Nano Mater.*, 3 (2020) 4562–4573, DOI: 10.1021/acsanm.0c00636.
- [36] D. Cai, D. Wang, B. Liu, Y. Wang, Y. Liu, L. Wang, H. Li, H. Huang, Q. Li, T. Wang, Comparison of the electrochemical performance of NiMoO_4 nanorods and hierarchical nanospheres for supercapacitor applications, *ACS Appl. Mater. Interfaces*, 5 (2013) 12905-12910, DOI: 10.1021/am403444v.
- [37] E. S. Agudosi, E. C. Abdullah, A. Numan, N. M. Mubarak, S. R. Aid, R. Benages-Vilau, P. Gómez-Romero, M. Khalid, N. Omar, Fabrication of 3D binder-free graphene NiO electrode for highly stable supercapattery, *Sci. Rep.*, 10 (2020) 11214-13, DOI: 10.1038/s41598-020-68067-2.
- [38] M. M. Vadiyar, S. S. Kolekar, J. Chang, Z. Ye, A. V. Ghule, Anchoring ultrafine $\text{ZnFe}_2\text{O}_4/\text{C}$ nanoparticles on 3D ZnFe_2O_4 nanoflakes for boosting cycle stability and energy density of flexible asymmetric supercapacitor, *ACS Appl. Mater. Interfaces*, 9 (2017) 26016–26028, DOI: 10.1021/acsami.7b06847.
- [39] Y. Yang, P. Zhu, L. Zhang, F. Zhou, T. Li, R. Bai, R. Sun, C. Wong, Electrodeposition of $\text{Co}(\text{OH})_2$ improving carbonized melamine foam performance for compressible supercapacitor application, *ACS Sustainable Chem. Eng.*, 7 (2019) 16803–16813, DOI: 10.1021/acssuschemeng.9b04321.

CHAPTER – V

Synthesis and characterization of MnO₂ thin films

CHAPTER-V

Synthesis and characterization of MnO₂ thin films

5.1	Introduction.....	129
5.2.	Experimental details.....	130
5.2.1	Chemicals	130
5.2.2	Synthesis of MnO ₂ thin films.....	130
5.3	Material characterizations.....	131
5.4	Results and discussion.....	132
5.4A	Physico-chemical characterizations.....	132
5.4B	Electrochemical characterizations.....	135
5.5	Conclusions.....	137
	References.....	137

5.1 Introduction

A simple assembly of SC consists of two electrodes (anode and cathode) separated by an electrolyte (aqueous or organic) and a separator that permits transfer of ions while keeping electrodes electrically insulated from each other [1, 2]. There are two types of SCs based on configuration, one such simple design is SSCs, which, consist of two similar electrodes. Another configuration made of two dissimilar electrodes is ASCs. The working voltage of SCs depends on the thermodynamic breakdown potential of water molecules when aqueous electrolytes are used. In comparison between SSC and ASC, due to the advantages of different work functions and potential windows of electrode materials, the operating potential of SSCs is lower than ASCs [3, 4].

Recently, different electrode materials have been used as a counterpart to fabricate ASCs. Carbon allotropes like AC, graphene, CNTs are the most used materials for this purpose [5, 6]. High electrical conductivity, high surface area, easy to modulate surface texture, and abundance make them favorable for this purpose. Some of the best examples of the ASCs consisting of one of the carbon electrodes are AC//PPy/MnO₂ [7], CNT-G//Mn₃O₄-G [8], and CNT//CNT@MnO₂ [9]. But, the restacking of graphene sheets and aggregation of CNTs as well as AC are the problems faced while using the carbon allotropes as an electrode material. The low specific capacitance is another issue for the graphene based electrodes, which obstructs its practical applications. To overcome these issues, in recent times, ASCs consisting of two pseudocapacitive electrodes have been fabricated and evaluated for electrochemical performance. Fe₂O₃/CF// α -MnO₂/CF [10], Fe₂O₃//CuO [11], MnO₂//CoSe [12] are some of the representative examples of ASCs utilizing pseudocapacitive or battery type material as both electrodes.

Manganese dioxide (MnO₂) is a largely explored transition metal oxide for its pseudocapacitive nature in different electrolytes due to its better electrochemical properties such as high theoretical capacitance of about 1370 F g⁻¹, environment friendly nature, low cost, and simple processing [13-15]. The structure of birnessite MnO₂ features a layered structure composed of edge-sharing MnO₆ octahedra and can incorporate various types of cations and molecules within its interlayer spacing. The fabrication of nanocrystalline and mesoporous MnO₂ directly on the current collector by various methods is a new concept [16]. The deposition of MnO₂ have been previously reported using various methods such as SILAR [17], electrodeposition

[18], spray pyrolysis [19], CBD [20], atomic layer deposition [21], etc., to overcome the problem of dead volume generated by the use of less conductive binder and substantially improve electroactive sites while reducing R_{ct} . To prepare a binder less MnO_2 electrode, CBD is one of the best choice due to its simplicity and cost effectiveness. Adherent, uniform, and large area deposition is possible using this method. Therefore, CBD is used to prepare large scale deposition of different inorganic materials with diverse surface morphologies and architectures [22].

The MnO_2 stores charges through the surface or bulk redox reactions in between Mn^{4+} and Mn^{3+} oxidation states of Mn. The charge storage mechanism of MnO_2 has been extensively investigated in aqueous electrolytes, and two mechanisms have been proposed [23]. The charge storage reaction mechanism can be written as,



The second mechanism involves the surface adsorption of cations on MnO_2 :



In the above reaction mechanisms, H^+ implies proton involved in the interaction process, the symbol A denotes an alkali metal cation e.g. Na^+ , Li^+ , and K^+ [24].

Few metal sulfides have negative potential window such as copper sulfide (CuS) [25] and molybdenum sulfide (MoS) [26] with greater electrochemical performance as compared to carbon based materials. A combination of MnO_2 thin film as a cathode and CuS@rGO thin film electrode as an anode will ensure one, of getting enhanced electrochemical performance in terms of C_s , S_E , S_P , and cycling stability of ASC device. So, the combination of CuS@rGO electrode with MnO_2 could become a promising approach to enhance S_E of FSS-ASCs device. This section deals with the synthesis, characterization, and electrochemical performance evaluation of MnO_2 thin film electrode deposited by CBD method.

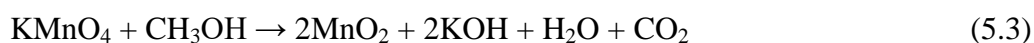
5.2. Experimental details

5.2.1. Chemicals

The AR grade potassium permanganate ($KMnO_4$), methanol (CH_3OH), and lithium perchlorate ($LiClO_4$) were purchased from Thomas Baker Chemicals Pvt. Ltd., India, and used without further purification. Flexible SS substrate of thickness 0.03 mm was used for film deposition. The DDW was used as a solvent throughout the experiment.

5.2.2 Synthesis of MnO_2 thin films

The deposition of MnO₂ thin film on SS substrate was carried out using CBD method. For this purpose, KMnO₄ was used as a source of manganese. 50 mL, 0.02 M KMnO₄, and 10 mL CH₃OH solutions were mixed under constant stirring for 15 minutes. The solution was kept at room temperature (300 K) throughout the deposition. The clean SS substrates were immersed vertically in it. The deposition time, concentration of reactants, and pH of the solution are crucial parameters in the CBD deposition method. In this study, the concentration and deposition time were optimized to get adherent and uniform thin film. The deposition of MnO₂ thin films was carried out for 6 h. After 6 h, dark brown colored thin films of MnO₂ were deposited on SS substrate. The reaction mechanism of MnO₂ formation is as follows,



The thickness of MnO₂ thin film was calculated by the gravimetric weight difference method, assuming the density of the prepared material equal to the bulk density of MnO₂ (5.03 g cm⁻³). For this purpose, analytical balance from Contech Instruments Ltd. (Modal CAL-35) with the least count of 0.00001 g was used. The thickness of MnO₂ thin film found to be 0.25 μm.

5.3 Material characterization

5.3.1 Physico-chemical characterizations

All physico-chemical characterizations of MnO₂ thin films were performed similarly to that of CuS thin films, mentioned in section 3.3.1.

5.3.2 Electrochemical characterizations

The three electrode system was used for the investigation of the electrochemical properties. The electrochemical setup consists of MnO₂ thin film as a working electrode, SCE, and Pt sheet as a reference and counter electrodes, respectively. All the electrochemical measurements were carried out in a 1 M LiClO₄ aqueous electrolyte. The unit (1 cm²) area of the working electrode was exposed to the electrolyte. The CV, GCD, and EIS measurements were carried out using an electrochemical workstation (ZIVE MP1). The supercapacitive behavior of electrodes was evaluated in terms of C_s , electrochemical stability, R_s , and R_{ct} . The optimized potential window of 0 to 1 V/SCE was used to evaluate all the electrochemical parameters. The CV analysis was carried out at different scan rates in between 5 mV s⁻¹ to 100 mV s⁻¹. The Eq. 2.10 was used to calculate the C_s of electrode material from CV studies. The GCD analysis of MnO₂ thin film electrode was performed at various current densities. The values of C_s from GCD curves were calculated using Eq. 2.12.

The EIS study was performed in the frequency range of 0.1 Hz and 0.1 MHz at an amplitude of 5 mV and open circuit bias potential. The electrochemical equivalent circuit for measured EIS data was obtained through The Zview software. Electrochemical cyclic stability of MnO₂ thin film was evaluated by performing 5000 CV cycles at the scan rate of 50 mV s⁻¹.

5.4. Results and discussion

5.4A Physico-chemical characterizations

5.4A.1 XRD study

The charge storage characteristics of MnO₂ are strongly influenced by its crystallographic structures and crystallinity. The XRD pattern of MnO₂ thin film electrode is shown in Figure 5.1a. The MnO₂ thin film shows small peaks corresponding to crystallographic planes (101), (111), and (312) of δ phase of MnO₂, respectively. The peak positions and intensities are well matched with JCPDS card no. 00-44-0141. The diffraction peaks from SS were denoted by sign *; confirm the nanocrystalline nature of the film [27, 28]. This nature of the thin film is beneficial to enhance electrochemical activities because more active sites will be available due to irregular arrangement of the particles and as it enables easy and fast intercalation/deintercalation of electrolyte ion in the interior of the electrode material [29, 30].

5.4A.2 FT-IR study

The FT-IR spectrum of MnO₂ film displayed in Figure 5.1b shows a broad absorption band in between 3100 to 3450 cm⁻¹ corresponding to the stretching vibrations of hydroxyl (-OH) group from adsorbed water [31]. The absorption band at 1590 cm⁻¹ corresponds to the bending modes of -OH of adsorbed water molecules. The bands at 1417 cm⁻¹, 1072 cm⁻¹ match with C=O vibrations, and the absorption band at 540 cm⁻¹ represents Mn-O vibrations in MnO₂ [32].

5.4A.3 Raman study

To identify nanocrystalline nature of MnO₂ thin film, Raman spectroscopy was used and the Raman spectrum of MnO₂ film is presented in Figure 5.1c. Broad peaks confirm the nanocrystalline nature of the films. The Raman spectrum of MnO₂ shows three broad and distinct peaks at 504, 577, and 643 cm⁻¹. The first two peaks correspond to Mn-O-Mn deformation mode and the latter to Mn-O stretching mode [33, 34].

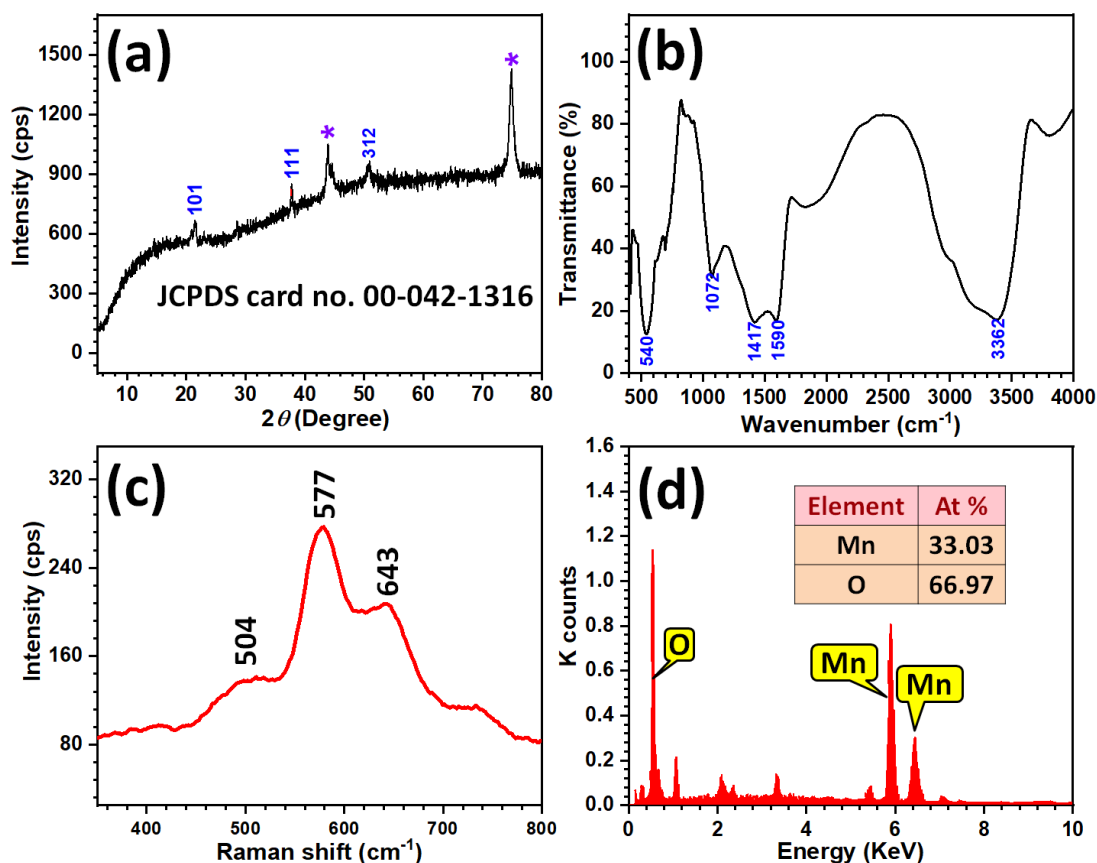


Figure 5.1: a) The XRD pattern, b) FT-IR spectrum, c) Raman spectrum, and d) EDAX spectrum of MnO_2 thin film (Inset shows atomic percentage of constituent elements).

5.4A.4 EDAX study

The EDAX spectrum acts as a supplementary characterization of XRD analysis in the identification of the material. The EDAX spectrum of MnO_2 thin film is shown in Figure 5.1d. The atomic ratio of elements Mn:O is 1:2.02 which is very much closer to the ideal value of Mn:O ratio (1:2) in MnO_2 . From the EDAX spectrum, the stoichiometric formation of MnO_2 thin film was confirmed.

5.4A.5 FE-SEM study

The surface topography of MnO_2 thin film observed by FE-SEM at the magnifications of 10,000 X and 70,000 X are shown in Figure 5.2a and b, respectively; which reveal formation of irregularly packed nanospheres. The random arrangement of particles is attributed to the higher reaction rate in the alkaline bath in which nucleation and grain growth take place simultaneously.

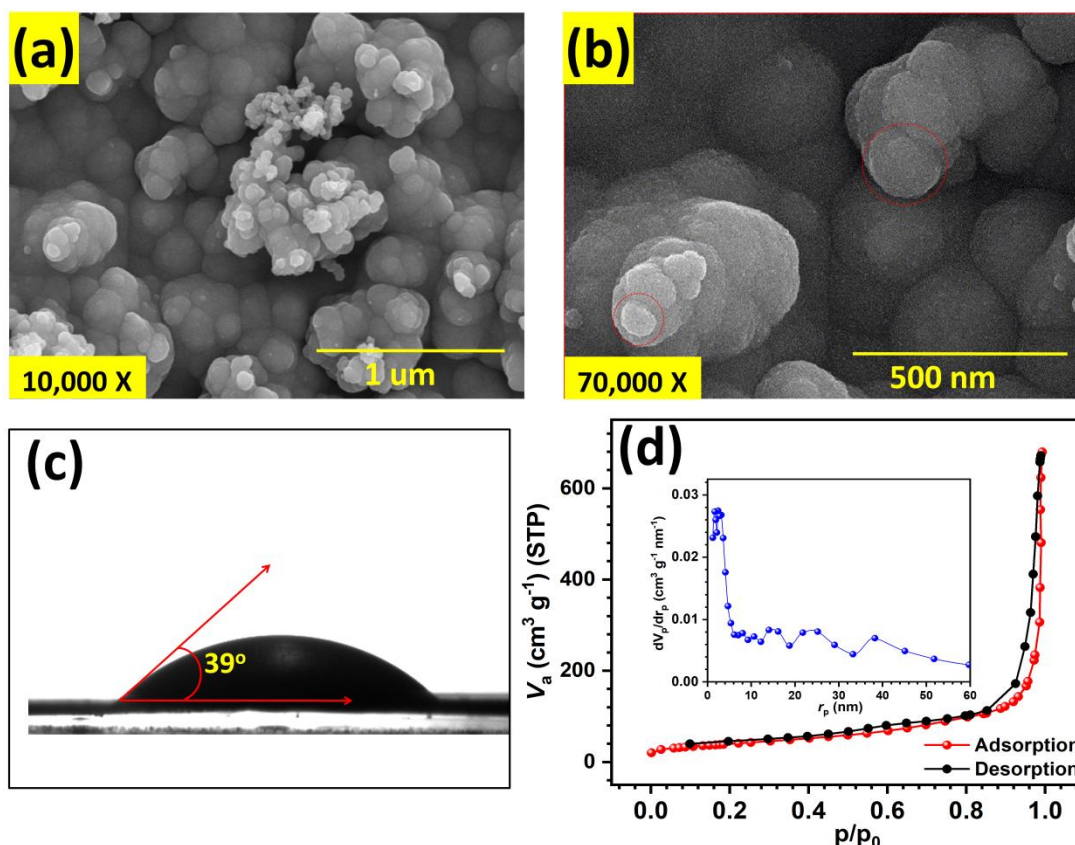


Figure 5.2: The FE-SEM images at a) 10,000 X, and b) 70,000 X magnifications, c) contact angle photograph, and d) N₂ sorption curves of MnO₂ film (Inset shows pore size distribution curve).

5.4A.6 Contact angle study

Figure 5.2c shows photograph of water contact angle of MnO₂ thin film. The value of contact angle (39°) indicates hydrophilic nature of MnO₂ film. This type of surface helps in reducing resistance in the electrochemical reactions.

5.4A.7 BET and BJH study

The specific surface area of MnO₂ material was measured by N₂ sorption and the obtained isotherm is shown in Figure 5.2d. The physical adsorption isotherm of MnO₂ is of type IV which often attributed to the mesoporosity and high energy of adsorptions [35]. The hysteresis of adsorption and desorption can be classified as H2 hysteresis loop [36]. Such a type of hysteresis loop is the characteristic of the formation of pores with narrow and wide sections and possible interconnecting channels. The specific surface area of MnO₂ is 140.5 cm² g⁻¹. The inset image of Figure 5.2d presents the pore size distribution of MnO₂ with an average pore radius of 27.8 nm. Small average pore size is achieved due to the restricted process of material growth on SS substrate.

5.4B Electrochemical characterizations

5.4B.1 CV study

The electrochemical properties of MnO₂ thin film were evaluated in 1 M LiClO₄ electrolyte using three electrode system comprised of the reference electrode (SCE), counter (Pt), and working (MnO₂) electrode. The CV curves at different scan rates ranging between 5 to 100 mV s⁻¹ are shown in Figure 5.3a. The values of C_s as 702, 688, 636, 548, and 493 F g⁻¹ correspond to the scan rates of 5, 10, 20, 50, and 100 mV s⁻¹, respectively. The reaction mechanism of charge storage could be written as,



The variation of C_s with the scan rate is shown in Figure 5.3b. At higher scan rates, the time available for Faradaic reactions is limited; hence overall charge stored at the electrode surface is less causing lower C_s [37, 38].

5.4B.2 GCD study

The GCD curves of MnO₂ thin film are shown in Figure 5.3c at the current densities of 1, 0.5, and 0.25 A g⁻¹. The triangular shape of GCD curves closely resembling to those of carbon based materials, is the signature of the surface redox pseudocapacitor nature of electrode material which stores charges at the interface of electrode/electrolyte rather than intercalation of the ions inside the electrode material. The charge stored on the electrode is linearly dependent on the applied potential [39]. The values of C_s of MnO₂ thin film electrode varied from 688 to 490 F g⁻¹ as the current density varies from 1 to 0.25 A g⁻¹.

5.4B.3 EIS study

The EIS study was carried out to find out the resistive behavior of MnO₂ film electrode in the frequency range of 0.01 Hz to 0.1 MHz at the potential amplitude of 5 mV. The Nyquist plot of MnO₂ film electrode shown in Figure 5.3d is composed of a small semicircle at higher frequencies and a straight line in the lower frequency region. The intercept of the observed plot with the abscissa gives a value of R_s and the radius of the subsequent circle provides a value of the R_{ct} [40]. In case of MnO₂, the observed values of R_s (1.94 Ω cm⁻²) is independent of the potential applied, as it is related to the formation of a fine layer on the surface of the electrode by the electrolyte ions. The semicircle in high and medium frequency regions can be fitted using an equivalent circuit (inset of Figure 5.3d) which is composed of parallel resistances (R_s and R_{ct}) and imperfect capacitor (Q , when $n=1$ $Q=C$) [41, 42]. The

value of R_{ct} is $5.81 \Omega \text{ cm}^{-2}$. The linear part of the Nyquist plot in the lower frequency range, inclining with the real axis of the impedance corresponds to W . The value of W (0.89Ω) is related to the diffusion of electrolyte ions inside the pores on the surface of the electrode [43].

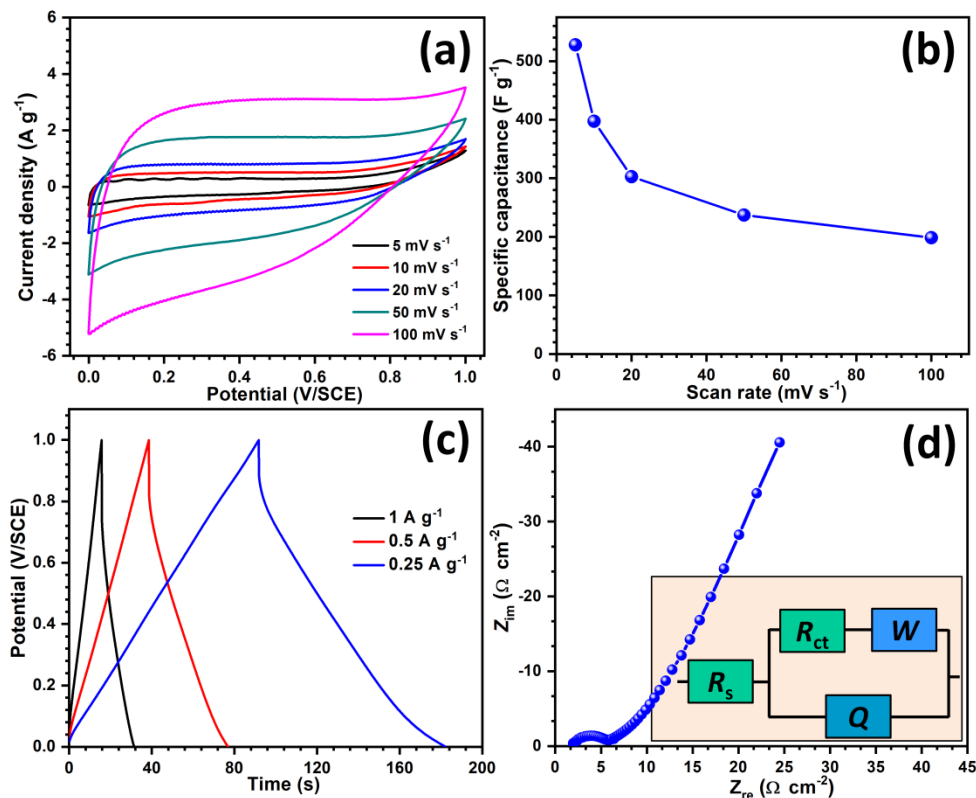


Figure 5.3: a) The CV curves, b) variation of the C_s with the scan rate, c) GCD plots, and d) Nyquist plot (Inset shows fitted equivalent circuit for the EIS data) of MnO_2 thin film electrode.

5.4B.4 Stability study

The electrochemical stability of electrode material plays an important role in deciding the life span of SC devices. With the increased durability of SCs, the cost of maintenance of any system utilizing SCs as an energy storage device will be reduced substantially [44]. The stability of the electroactive material depends on the number of things such as material composition/chemistry, applied potential window, charging-discharging current density, type and concentration of electrolyte [45]. To evaluate electrochemical stability of MnO_2 thin film electrode, 5000 CV cycles were performed at a scan rate of 50 mV s^{-1} . The retention of 93% is observed for MnO_2 thin film electrode (Figure 5.4). The inset image shows 2nd and 5000th cycles of the CV.

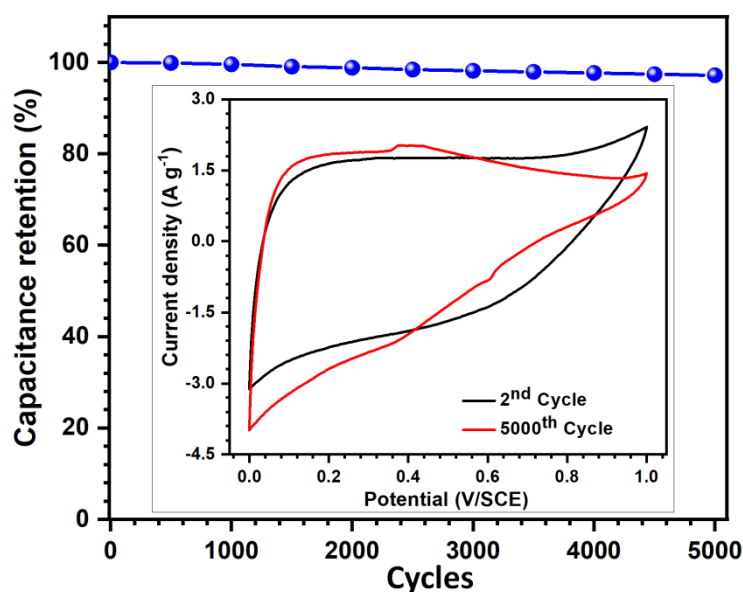


Figure 5.4: Capacitance retention of MnO₂ thin film electrode (Inset shows CV curves of 2nd and 5000th cycles).

5.5 Conclusions

In summary, the nanocrystalline MnO₂ thin films are successfully prepared on SS substrate using CBD method at room temperature. The surface texture of thin film was composed of a cluster of nanospheres, possessing a specific surface area of 140.5 cm² g⁻¹ and an average pore radius of 27.8 nm. The mesoporous surface showed a hydrophilic nature. In addition to this, MnO₂ thin film exhibited C_s of 702 F g⁻¹ at a scan rate of 5 mV s⁻¹. Lower resistive parameters such as R_s (1.94 Ω cm⁻²) and R_{ct} (1.94 Ω cm⁻²) as well as capacitive retention of 93% after 5000 CV cycles of MnO₂ thin film electrode are ascribed to its nanostructured morphology consisting of nanospheres provides easy access for electrolyte ions. The present strategy provides a new opportunity for promoting further development of SCs by enhancing the involvement of the nanocrystalline and mesoporous materials. As the CBD method is useful for large scale deposition, it can be scaled up for the large scale production of MnO₂ films.

Reference

- [1] S. W. Bokhari, Y. Hao, A. H. Siddique, Y. Ma, M. Imtiaz, R. Butt, P. Hui, Y. Li, S. Zhu, Assembly of hybrid electrode rGO-CNC-MnO₂ for a high performance supercapacitor, *Results Mater.*, 1 (2019) 100007, DOI: 10.1016/j.rinma.2019.100007.
- [2] Y. Qiu, X. Li, M. Bai, H. Wang, D. Xue, W. Wang, J. Cheng, Flexible full-solid-state supercapacitors based on self-assembly of mesoporous MoSe₂

- nanomaterials, *Inorg. Chem. Front.*, 4 (2017) 675-682, DOI: 10.1039/C6QI00569A.
- [3] A. M. Zardkhoshoui, S. S. H. Davarani, A. A. Asgharinezhad, Designing graphene-wrapped NiCo_2Se_4 microspheres with petal-like FeS_2 toward flexible asymmetric all-solid-state supercapacitors, *Dalton Trans.*, 48 (2019) 4274-4282, DOI: 10.1039/C9DT00009G.
- [4] P. Pazhamalai, K. Krishnamoorthy, S. Sahoo, S. Kim, Two-dimensional molybdenum diselenide nanosheets as a novel electrode material for symmetric supercapacitors using organic electrolyte, *Electrochim. Acta*, 295 (2019) 591-598, DOI: 10.1016/j.electacta.2018.10.191.
- [5] E. Frackowiak, Carbon materials for supercapacitor application, *Phys. Chem. Chem. Phys.*, 9 (2007) 1774-1785, DOI: 10.1039/B618139M.
- [6] L. Borchardt, M. Oschatz, S. Kaskel, Tailoring porosity in carbon materials for supercapacitor applications, *Mater. Horiz.*, 1 (2014) 157-168, DOI: 10.1039/c3mh00112a.
- [7] J. Tao, N. Liu, L. Li, J. Su, Y. Gao, Hierarchical nanostructures of polypyrrole@ MnO_2 composite electrodes for high performance solid-state asymmetric supercapacitors, *Nanoscale*, 6 (2014) 2922-2928, DOI: 10.1039/C3NR05845J.
- [8] H. Gao, F. Xiao, C. B. Ching, H. Duan, Flexible all-solid-state asymmetric supercapacitors based on free-standing carbon nanotube/Graphene and Mn_3O_4 nanoparticle/graphene paper electrodes, *ACS Appl. Mater. Interfaces*, 4 (2012) 7020-7026, DOI: 10.1021/am302280b.
- [9] F. Su, M. Miao, Asymmetric carbon nanotube- MnO_2 two-ply yarn supercapacitors for wearable electronics, *Nanotechnology*, 25 (2014) 135401, DOI: 10.1088/0957-4484/25/13/135401.
- [10] P. Yang, Y. Ding, Z. Lin, Z. Chen, Y. Li, P. Qiang, M. Ebrahimi, W. Mai, C. P. Wong, Z. L. Wang, Low-cost high-performance solid-state asymmetric supercapacitors based on MnO_2 nanowires and Fe_2O_3 nanotubes, *Nano Lett.*, 14 (2014) 731-736, DOI: 10.1021/nl404008e.
- [11] A. V. Shinde, N. R. Chodankar, V. C. Lokhande, A. C. Lokhande, T. Ji, J. H. Kim, C. D. Lokhande, Highly energetic flexible all-solid-state asymmetric supercapacitor with Fe_2O_3 and CuO thin films, *RSC Adv.*, 6 (2016) 58839-58843, DOI: 10.1039/C6RA11896H.
- [12] N. Yu, M.-Q. Zhu, D. Chen, Flexible all-solid-state asymmetric supercapacitors with three-dimensional CoSe_2 /carbon cloth electrodes, *J. Mater. Chem. A*, 3 (2015) 7910-7918, DOI: 10.1039/C5TA00725A.
- [13] G. S. Gund, D. P. Dubal, N. R. Chodankar, J. Y. Cho, P. Gomez-Romero, C. Park, C. D. Lokhande, Low-cost flexible supercapacitors with high-energy density based on nanostructured MnO_2 and Fe_2O_3 thin films directly fabricated onto stainless steel, *Sci. Rep.*, 5 (2015) 12454, DOI: 10.1038/srep12454.

- [14] N. R. Chodankar, D. P. Dubal, A. C. Lokhande, C. D. Lokhande, Ionically conducting PVA-LiClO₄ gel electrolyte for high performance flexible solid state supercapacitors, *J. Colloid Interface Sci.*, 460 (2015) 370-376, DOI: 10.1016/j.jcis.2015.08.046.
- [15] P. Iamprasertkun, C. Tangarnjanavalukul, A. Krittayavathananon, J. Khuntilo, N. Chanlek, P. Kidkhunthod, M. Sawangphruk, Insight into charge storage mechanisms of layered MnO₂ nanosheets for supercapacitor electrodes: In situ electrochemical X-ray absorption spectroscopy, *Electrochim. Acta*, 249 (2017) 26-32, DOI: 10.1016/j.electacta.2017.08.002.
- [16] N. R. Chodankar, D. P. Dubal, G. S. Gund, C. D. Lokhande, Flexible all-solid-state MnO₂ thin films based symmetric supercapacitors, *Electrochim. Acta*, 165 (2015) 338-347, DOI: 10.1016/j.electacta.2015.02.246.
- [17] D. P. Dubal, D. S. Dhawale, R. R. Salunkhe, C. D. Lokhande, A novel chemical synthesis of Mn₃O₄ thin film and its stepwise conversion into birnessite MnO₂ during super capacitive studies, *J. Electroanal. Chem.*, 647 (2010) 60-65, DOI: 10.1016/j.jelechem.2010.05.010.
- [18] D. Sun, Z. Wang, K. Huang, X. Wang, H. Wang, C. Qing, B. Wang, Y. Tang, A sandwich-structured porous MnO₂/polyaniline/MnO₂ thin film for supercapacitor applications, 638 (2015) 38-42, DOI: 10.1016/j.cplett.2015.08.030.
- [19] S. Balamurugan, A. Rajalakshmi, D. Balamurugan, Acetaldehyde sensing property of spray deposited β -MnO₂ thin films, *J. Alloys Compd.*, 650 (2015) 863-870, DOI: 10.1016/j.jallcom.2015.08.063.
- [20] N. R. Chodankar, D. P. Dubal, G. S. Gund, C. D. Lokhande, A symmetric MnO₂/MnO₂ flexible solid state supercapacitor operating at 1.6 V with aqueous gel electrolyte, *J. Energy Chem.*, 25 (2016) 463-471, DOI: 10.1016/j.jechem.2016.01.020.
- [21] S. P. Zankowski, L. Hoecke, F. Mattelaer, M. Raedt, O. Richard, C. Detavernier, P. M. Vereecken, Redox layer deposition of thin films of MnO₂ on nanostructured substrates from aqueous solutions, *Chem. Mater.*, 31 (2019) 4805–4816, DOI: 10.1021/acs.chemmater.9b01219.
- [22] S. M. Pawar, B. S. Pawar, J. H. Kim, O. Joo, C. D. Lokhande, Recent status of chemical bath deposited metal chalcogenide and metal oxide thin films, *Curr. Appl Phys.*, 11 (2011) 117-161, DOI: 10.1016/j.cap.2010.07.007.
- [23] N. R. Chodankar, H. D. Pham, A. K. Nanjundan, J. F. S. Fernando, K. Jayaramulu, D. Golberg, Y. Han, D. P. Dubal, True meaning of pseudocapacitors and their performance metrics: asymmetric versus hybrid supercapacitors, *small*, 16 (2020) 2002806, DOI: 10.1002/smll.202002806.
- [24] J. P. Tafur, J. Abad, E. Román, A. J. F. Romero, Charge storage mechanism of MnO₂ cathodes in Zn/MnO₂ batteries using ionic liquid-based gel polymer electrolytes, *Electrochem. Commun.*, 60 (2015) 190-194, DOI: 10.1016/j.elecom.2015.09.011.

- [25] M. Jayalakshmi, M. M. Rao, B. M. Choudary, Identifying nano SnS as a new electrode material for electrochemical capacitors in aqueous solutions, *Electrochem. Commun.*, 6 (2004) 1119-1122, DOI: 10.1016/j.elecom.2004.09.004.
- [26] K. Krishnamoorthy, G. K. Veerasubramani, P. Pazhamalai, S. J. Kim, Designing two dimensional nanoarchitected MoS₂ sheets grown on Mo foil as a binder free electrode for supercapacitors, *Electrochim. Acta*, 190 (2016) 305-312, DOI: 10.1016/j.electacta.2015.12.148.
- [27] Y. Munaiah, B. G. S. Raj, T. P. Kumar, P. Ragupathy, Facile synthesis of hollow sphere amorphous MnO₂: the formation mechanism, morphology and effect of a bivalent cation-containing electrolyte on its supercapacitive behavior, *J. Mater. Chem. A*, 1 (2013) 4300-4306, DOI: 10.1039/C3TA01089A.
- [28] E. Guneri, A. Kariper, Optical properties of amorphous CuS thin films deposited chemically at different pH values, *J. Alloys Compd.*, 516 (2012) 20-26, DOI: 10.1016/j.jallcom.2011.11.054.
- [29] S. Ghosh, R. Santhosh, S. Jeniffer, V. Raghavan, G. Jacob, K. Nanaji, P. Kollu, S. K. Jeong, A. N. Grace, Natural biomass derived hard carbon and activated carbons as electrochemical supercapacitor electrodes, *Sci. Rep.*, 9 (2019) 16315, DOI: 10.1038/s41598-019-52006-x.
- [30] S. Zhang, P. Shi, Electrochemical impedance study of lithium intercalation into MCMB electrode in a gel electrolyte, *Electrochim. Acta*, 49 (2004) 1475-1482, DOI: 10.1016/j.electacta.2003.10.033.
- [31] F. Meng, X. Yan, Y. Zhu, P. Si, Controllable synthesis of MnO₂/polyaniline nanocomposite and its electrochemical capacitive property, *Nanoscale Research Letters*, 8 (2013) 179, DOI: 10.1186/1556-276X-8-179.
- [32] T. D. Schladt, K. Koll, S. Prüfer, H. Bauer, F. Natalio, O. Dumele, R. Raidoo, S. Weber, U. Wolfrum, L. M. Schreiber, M. P. Radsak, H. Schild, W. Tremel, Multifunctional superparamagnetic MnO@SiO₂ core/shell nanoparticles and their application for optical and magnetic resonance imaging, *J. Mater. Chem.*, 22 (2012) 9253-9262, DOI: 10.1039/C2JM15320C.
- [33] N. G. Bretesche, O. Crosnier, G. Buvat, F. Favier, T. Brousse, Electrochemical study of aqueous asymmetric FeWO₄/MnO₂ supercapacitor, *J. Power Sources*, 326 (2016) 695-701, DOI: 10.1016/j.jpowsour.2016.04.075.
- [34] D. P. Dubal, J. G. Kim, Y. Kim, R. Holze, W. B. Kim, Demonstrating the highest supercapacitive performance of branched MnO₂ nanorods grown directly on flexible substrates using controlled chemistry at ambient temperature, *Energy. Technol.*, 1 (2013) 125-130, DOI: 10.1002/ente.201200040.
- [35] S. Bernardini, F. Bellatreccia, A. C. Municchia, G. D. Ventura, A. Sodo, Raman spectra of natural manganese oxides, *J. Raman Spectrosc.*, 50 (2019) 873-888, DOI: 10.1002/jrs.5583.

-
- [36] A. Phuruangrat, T. Thongtem, S. Thongtem, Characterization of copper sulfide hexananoplates, and nanoparticles synthesized by a sonochemical method, *Chalcogenide Lett.*, 8 (2011) 291-295.
- [37] M. Toupin, T. Brousse, D. Be' langer, Charge storage mechanism of MnO_2 electrode used in aqueous electrochemical capacitor, *Chem. Mater.*, 16 (2004) 3184-3190, DOI: 10.1021/cm049649j.
- [38] P. R. Deshmukh, S. N. Pusawale, V. S. Jamadade, U. M. Patil, C. D. Lokhande, Microwave assisted chemical bath deposited polyaniline films for supercapacitor application, *J. Alloys Compd.*, 509 (2011) 5064-5069, DOI: 10.1016/j.jallcom.2010.12.009.
- [39] R. B. Pujari, A. C. Lokhande, A. R. Shelke, J. H. Kim, C. D. Lokhande, Chemically deposited nano grain composed MoS_2 thin films for supercapacitor application, *J. Colloid Interface Sci.*, 496 (2017) 1-7, DOI: 10.1016/j.jcis.2016.11.026.
- [40] B. Zheng, T. Huang, L. Kou, X. Zhao, K. Gopalsamy, C. Gao, Graphene fiber-based asymmetric micro-supercapacitors, *J. Mater. Chem. A*, 2 (2014) 9736-9743, DOI: 10.1039/C4TA01868K.
- [41] K. J. Huang, J. Z. Zhang, K. Xing, One-step synthesis of layered CuS /multi-walled carbon nanotube nanocomposites for supercapacitor electrode material with ultrahigh specific capacitance, *Electrochim. Acta*, 149 (2014) 28-33, DOI: 10.1016/j.electacta.2014.10.079.
- [42] L. Zhang, W. Zheng, H. Jiu, C. Ni, J. Chang, G. Qi, The synthesis of NiO and NiCo_2O_4 nanosheets by a new method and their excellent capacitive performance for asymmetric supercapacitor, *Electrochim. Acta*, 215 (2016) 212-222, DOI: 10.1016/j.electacta.2016.08.099.
- [43] P. Wen, M. Fan, D. Yang, Y. Wang, H. Cheng, J. Wang, An asymmetric supercapacitor with ultrahigh energy density based on nickle cobalt sulfide nanocluster anchoring multi-wall carbon nanotubes hybrid, *J. Power Sources*, 320 (2016) 28-36, DOI: 10.1016/j.jpowsour.2016.04.066.
- [44] B. G. Choi, S. J. Chang, C. P. Park, H. W. Kang, H. J. Kim, W. H. Hong, S. Lee, Y. S. Huh, High performance of a solid-state flexible asymmetric supercapacitor based on graphene films, *Nanoscale*, 4 (2012) 4983-4988, DOI: 10.1039/C2NR30991B.
- [45] L. Nyholm, G. Nystrom, A. Mihranyan, M. Stromme, Toward flexible polymer and paper-based energy storage devices, *Adv. Mater.*, 23 (2011) 3751-3769, DOI: 10.1002/adma.201004134.
-

CHAPTER – VI

**Fabrication and performance evaluation
of FSS–ASCs devices based on CuS@rGO
and CuSe₂@rGO thin films**

CHAPTER-VI

Fabrication and performance evaluation of FSS–ASCs devices based on CuS@rGO and CuSe₂@rGO thin films

6.1	Introduction.....	143
6.2	Experimental details	143
6.2.1	Introduction	143
6.2.2	Electrode preparation.....	144
6.2.3	Preparation of polymer gel electrolytes.....	144
6.2.4	Fabrication of FSS–ASCs devices.....	144
6.2.5	Electrochemical characterizations of FSS-ASC devices.....	144
6.3	Results and discussion.....	145
6.3A	Electrochemical studies of MnO ₂ //CuS@rGO FSS–ASC device.....	145
6.3B	Electrochemical studies of CuSe ₂ @rGO//CuS FSS-ASC device.....	149
6.4	Conclusions.....	153
	References.....	154

6.1 Introduction:

The portable and small size SCs are required in the fabrication of recent energy storage devices [1, 2]. The mechanical flexibility, lightweight, inexpensive, and environment friendly energy storage of SCs provides uses in portable, wearable, and commercialized pocket electronic devices [3, 4]. There is a need to increase S_E and S_P of energy storage devices using different electrode materials and electrolytes. The asymmetric design of SC is an effective method to enhance the operating voltage of the device [5]. The S_E and C_s of ASCs are higher as compared to the SSCs [6-9]. Various combinations of the anode and cathode have been reported in literature as, $\text{MnO}_2//\text{Fe}_3\text{O}_4$ [10], $\text{CoMoO}_4//\text{MnO}_2$ [11], $\text{FeWO}_4//\text{MnO}_2$ [12], $\text{NiO}//\alpha\text{-Fe}_2\text{O}_3$ [13], NiO and NiCo_2O_4 [14]. The solid electrolyte based SC holds many advantages such as small size, lightweight, excellent reliability, and a wider range of operating temperature. The polymer based gel electrolytes offer mechanical flexibility to the SC devices [15, 16].

The transition metal based electrode chalcogenides such as copper sulfide and copper selenide can be operated in the wide potential window. Therefore, the combination of polymeric gel electrolytes with these electrode materials will be a good contribution to the FSC devices. The MnO_2 holds great attention as a positive electrode to fabricate the FSS–ASCs device due to higher C_s and operating voltage as compared to carbon based materials. In addition, the low cost, large abundance, higher conductive and nontoxic nature of copper based chalcogenides makes them possible to develop the FSS–ASCs devices [17-19].

In this chapter, FSS–ASC device is fabricated using MnO_2 thin film as an anode and $\text{CuS}@r\text{GO}$ thin film as a cathode with ionically conducting PVA– LiClO_4 gel as an electrolyte as well as a separator. Another FSS–ASC device is fabricated using $\text{CuSe}_2@r\text{GO}$ as an anode and CuS as a cathode with PVA–KOH as an electrolyte. This chapter deals with the fabrication and electrochemical performance evaluation of FSS–ASCs devices with configuration $\text{MnO}_2//\text{CuS}@r\text{GO}$ and $\text{CuSe}_2@r\text{GO}//\text{CuS}$.

6.2 Experimental details

6.2.1 Introduction

The present section describes the electrode preparation (MnO_2 and $\text{CuS}@r\text{GO}$, $\text{CuSe}_2@r\text{GO}$, and CuS), polymer gel electrolytes (PVA– LiClO_4 and PVA–KOH)

preparation and fabrication of $\text{MnO}_2//\text{CuS@rGO}$ and $\text{CuSe}_2@\text{rGO}//\text{CuS}$ FSS-ASCs devices.

6.2.2 Electrode preparation

The CBD method was employed to prepare MnO_2 thin films and SILAR method to prepare CuS, CuS@rGO , and $\text{CuSe}_2@\text{rGO}$ thin films on flexible SS substrates. The optimized preparative parameters of CuS, CuS@rGO , and MnO_2 thin film electrodes are described in chapters III and V, respectively, and that of $\text{CuSe}_2@\text{rGO}$ in chapter IV.

6.2.3 Preparation of polymer gel electrolytes

To fabricate FSS-ASCs device, water soluble PVA polymer was selected to prepare gel electrolyte using salt of LiClO_4 and KOH. The optimized amount (6 g) of PVA was separately dissolved in 60 mL DDW at a temperature of 343 K under vigorous stirring. The solution was continuously stirred until the polymer dissolved in water to form a clear solution. Further, 25 mL of 1 M LiClO_4 solution was added to the prepared polymer matrix and stirred for 1 h to get a transparent viscous gel like solution [20]. This viscous solution was used as a gel electrolyte to fabricate $\text{MnO}_2//\text{CuS@rGO}$ FSS-ASCs device. A similar process is followed to prepare PVA-KOH gel electrolyte.

6.2.4 Fabrication of FSS-ASCs devices

The FSS-ASCs device was fabricated using MnO_2 (anode) and CuS@rGO (cathode) flexible electrodes. The electrodes of size $5 \times 5 \text{ cm}^2$ were used and edges of electrodes were sealed with plastic tape to avoid short circuit. The polymer gel electrolyte was painted on each electrode and dried at room temperature. After drying one more time polymer gel electrolyte was painted on electrodes for proper contact between electrode and electrolyte. Then electrodes were packed together using transparent plastic strips to avoid leakage. Thereafter, whole device was placed in a hydraulic press with a pressure of 1 ton for 6 h. A similar process was followed to assemble $\text{CuSe}_2@\text{rGO}//\text{CuS}$ ASC device.

6.2.5 Electrochemical characterization of FSS-ASC devices

To optimize operating voltage of FSS-ASC devices, CV and GCD studies of ASC devices were carried out at various scan rates and current densities, respectively. The S_E (Wh kg^{-1}) and S_P (W kg^{-1}) of ASC device were calculated from Eq.1.2 and 1.3, respectively. To evaluate flexible nature of ASC device, CV curves were repeated at different bending positions. The stability study of ASC devices performed for 5000 cycles using GCD technique.

6.3. Results and discussion

6.3A Electrochemical studies of $\text{MnO}_2/\text{CuS@rGO}$ FSS-ASC device

To explore the application of CuS@rGO thin films in SC, the ASC device was fabricated using CuS@rGO and MnO_2 thin film as electrodes and PVA- LiClO_4 gel as an electrolyte. The final working voltage was decided from the CV curves taken at different working voltages ranging from 0 to +1.6 V at the scan rate of 100 mV s^{-1} as shown in Figure 6.1a. At a working voltage of +1.6 V, the device shows greater area enclosed by CV curve resulting in a possible enhancement in S_E and S_P . The GCD curves at a applied current of 5 A g^{-1} having a different working voltages are presented in Figure 6.1b. The maximum possible working voltage for water based electrolyte depends on electrode materials [21]. So, from analysis of CV and GCD curves, a suitable working voltage of +1.6 V was decided and further electrochemical characterizations were carried out in that working voltage (0 to +1.6 V).

The CV curves at different scan rates ranging from 5 to 100 mV s^{-1} is shown in Figure 6.1c. The values of C_s are 109.3, 103.7, 98.4, 92.1, and 80.3 F g^{-1} , at scan rates 5, 10, 20, 50, and 100 mV s^{-1} , respectively. The GCD curves at different current densities ranging from 2 to 5 A g^{-1} presented in Figure 6.1d suggest the possible versatile applications of the fabricated $\text{MnO}_2/\text{CuS@rGO}$ device. The values of C_s are 102.9, 96.8, 89.1, and 81.5 F g^{-1} at current densities 2, 3, 4, and 5 A g^{-1} , respectively.

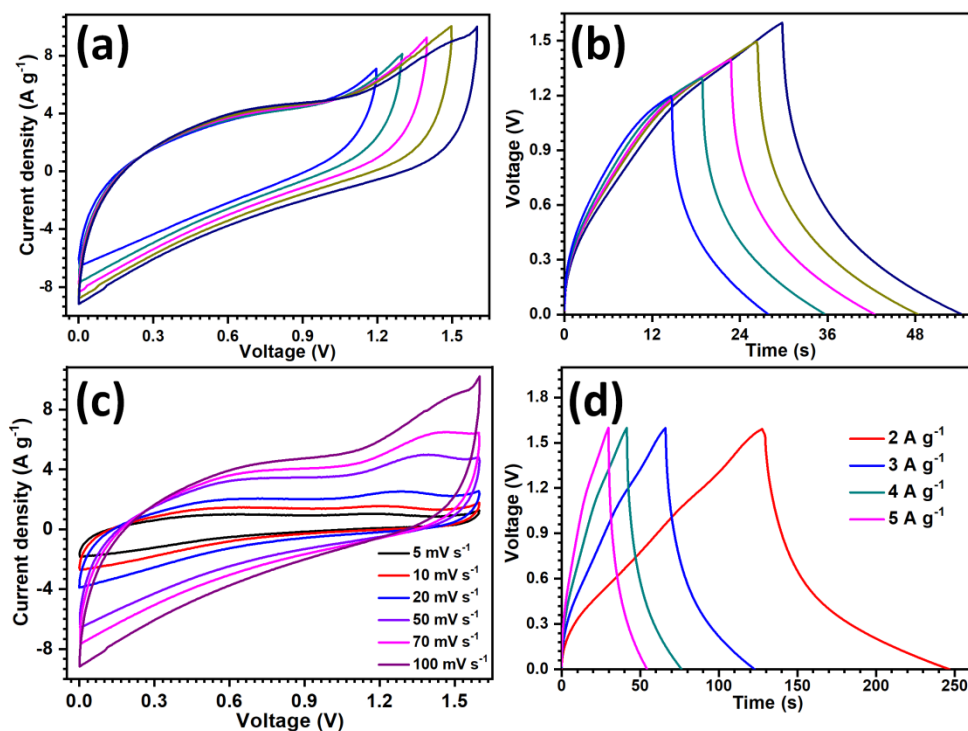


Figure 6.1: a) The CV curves, b) the GCD curves at different voltage ranges (0 V to 1.6 V), c) the CV curves at various scan rates, and d) the GCD curves at various current densities of $\text{MnO}_2/\text{CuS}@r\text{GO}$ ASC device.

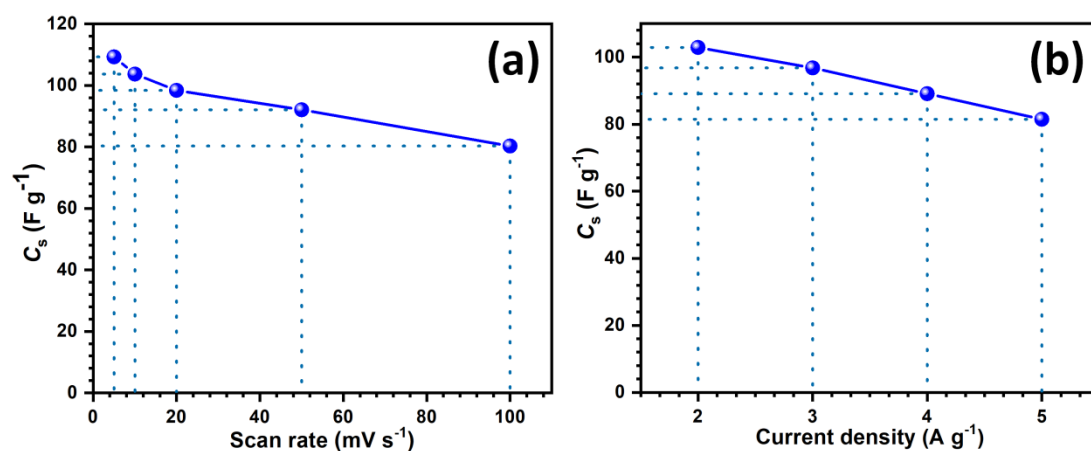


Figure 6.2: Variation of specific capacitance with a) the scan rate and b) the current density.

The C_s of device declines with the rise in scan rate as presented in Figure 6.2a due to time constraints for the interaction of electrolyte ions with the active sites of the respective electrodes at the higher scan rates [22]. The unchanged shape of CV curves indicates the sustainability of device against higher current ratings. The variation of C_s with the current density is shown in Figure 6.2b. The rate capacity of ASC device at a current of 5 A g⁻¹ is 73%. The excellent rate capacity indicates

synergistic effect of layered structure of faradic rGO and pseudocapacitive CuS nanoparticles.

The values of S_E and S_P are 40.5 W kg^{-1} and 1087 Wh kg^{-1} , respectively. Variation of S_E with S_P is shown in Ragone plot (Figure 6.3a). The mechanical flexibility of the ASC without losing its electrochemical performance is significantly important for the relevance of device in different portable electronic appliances. Therefore, CV measurements of $\text{MnO}_2/\text{CuS@rGO}$ device were performed at different bending angles at a scan rate of 100 mV s^{-1} . The small increase in C_s at the bending angle of 30° may be due to compression-decompression of porous CuS@rGO electrodes. Figure 6.3b shows the percent C_s retention versus bending angle and it is observed that the device retains 90% of initial C_s even at the twisting of the device at an angle of 165° .

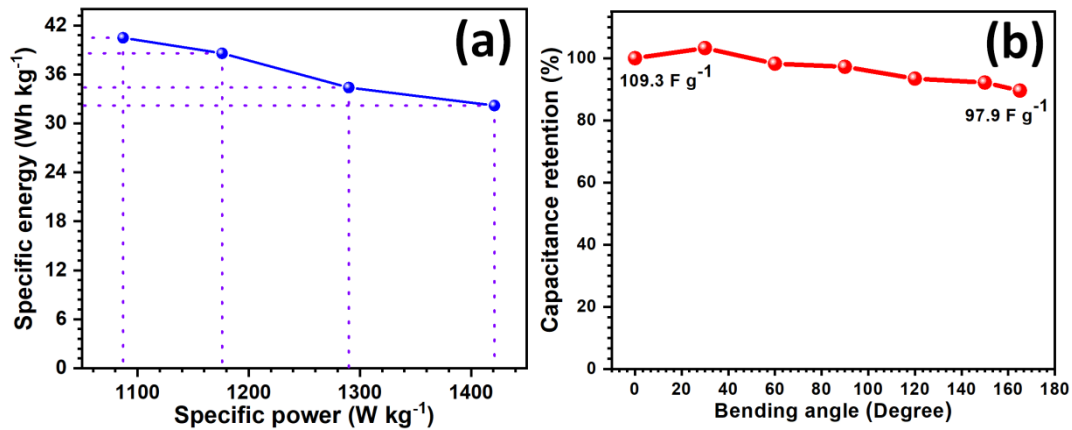


Figure 6.3: a) Ragone plot, and b) change in specific capacitance with different bending angles of $\text{MnO}_2/\text{CuS@rGO}$ ASC device.

The resistive characteristics of $\text{MnO}_2/\text{CuS@rGO}$ device were evaluated by EIS measurement in the frequency range of 0.01 Hz to 0.1 MHz. The Nyquist plot of the device is shown in Figure 6.4a (Inset shows an equivalent circuit of fitted impedance data). The R_s and R_{ct} of the device are 0.24Ω and 2Ω , respectively. At low frequencies, the straight line with 45° angle indicates W caused by the diffusion of the electrolyte in the bulk of the electrode, the value of W is 30Ω [23, 24]. Figure 6.4b shows variation of phase angle with the frequency. The relaxation time constant ($\tau_0=1/f_0$) is estimated to be 0.83 s; where, f_0 is the frequency at which phase angle is 45° . The lower relaxation time promotes fast ions transport rate to the interior of electrode material; which may enhance GCD efficiency of the device. This suggests the efficient nature of FSS-ASC device towards various applications [25].

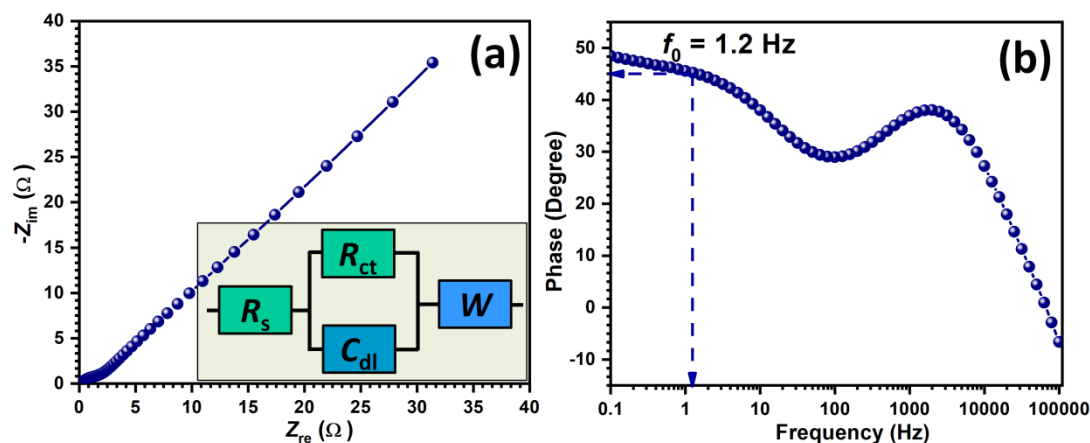


Figure 6.4: a) The Nyquist plot (Inset shows equivalent circuit), and b) phase angle as a function of frequency of FSS-ASC device.

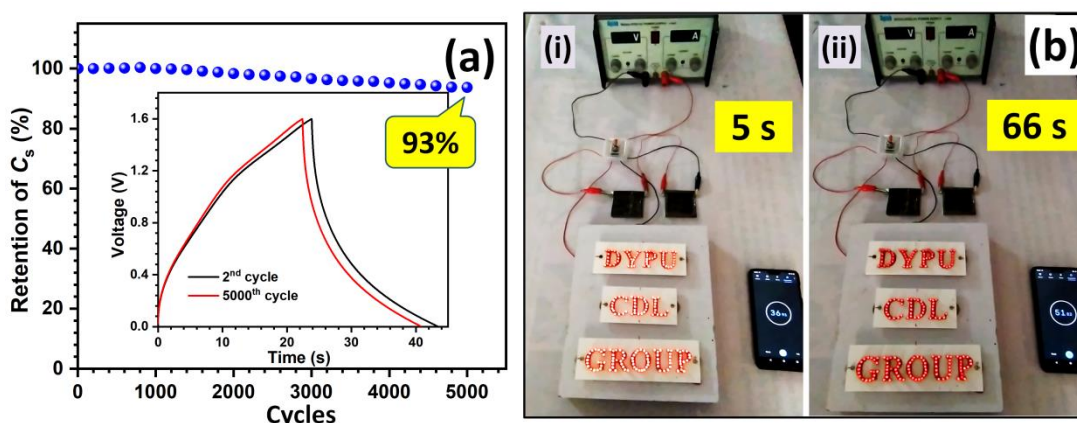


Figure 6.5: a) Variation of specific capacitance with GCD cycles (Inset show 2nd and 6000th cycles), and b) practical application of MnO₂//CuS@rGO device to glow 201 red LEDs panel.

The life span of SC is considered a core parameter that reduces the cost of maintenance of any portable electronic device that leads to economically affordable appliances. Stability of MnO₂//CuS@rGO device evaluated for 5000 cycles at a current density of 2.5 A g⁻¹ is presented in Figure 6.5a. Inset shows 2nd and 5000th GCD curves. The excellent electrochemical stability (93%) can be accredited to a proper combination of faradic and pseudocapacitive electroactive material forming a porous hybrid electrode with an appropriate pore size.

To demonstrate the practical applicability of MnO₂//CuS@rGO device, two devices were connected in series and charged for 30 s by applying the voltage of 3.2 V. The series combinations of two MnO₂//CuS@rGO devices easily glow up 201 light emitting diodes (LEDs) for 66 s (Figure 6.5b). This revealed the practical application of MnO₂//CuS@rGO device in different portable electronic device. The

measured initial output power of 31.04 mW cm^{-2} signifies excellent charge storing capability.

6.3.B Electrochemical studies of $\text{CuSe}_2\text{@rGO//CuS}$ FSS-ASC device

The schematic of assembly of $\text{CuSe}_2\text{@rGO//CuS}$ FSS-ASC device is shown in Figure 6.6a, where, $\text{CuSe}_2\text{@rGO}$ electrode is used as an anode and CuS as a cathode. The image of $\text{CuSe}_2\text{@rGO//CuS}$ ASC device is shown in Figure 6.6b. The CuS electrode was prepared as described in chapter-III.

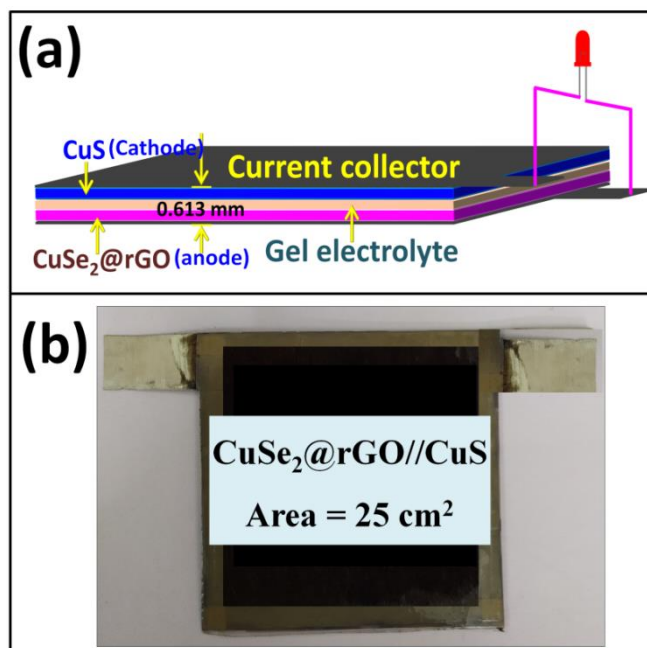


Figure 6.6: a) Schematic of assembly, and b) photograph of $\text{CuSe}_2\text{@rGO//CuS}$ ASC device.

To identify suitable operating voltage, CV curves of the device in various operating voltages ranging between 0 to +1.4 V are shown in Figure 6.7a. As operating voltage increases, the area enclosed under CV curve increases and as a result C_s also increases from 21 to 37 F g^{-1} . The symmetric nature of CV curve at +1.4 V indicates good capacitive performance of ASC device. As no visible water splitting was observed, it was concluded that ACS device can be charged up to +1.4 V.

The GCD plots of the device at charging current density of 13.3 A g^{-1} for various operating voltages range between 0 to +1.4 V are shown in Figure 6.7b. Large time of charge-discharge indicates more charge storage at +1.4 V and symmetric GCD plot suggests excellent charge storage behavior of ASC device. Therefore, further characterizations of ASC device are carried out in voltage range of 0 to +1.4 V.

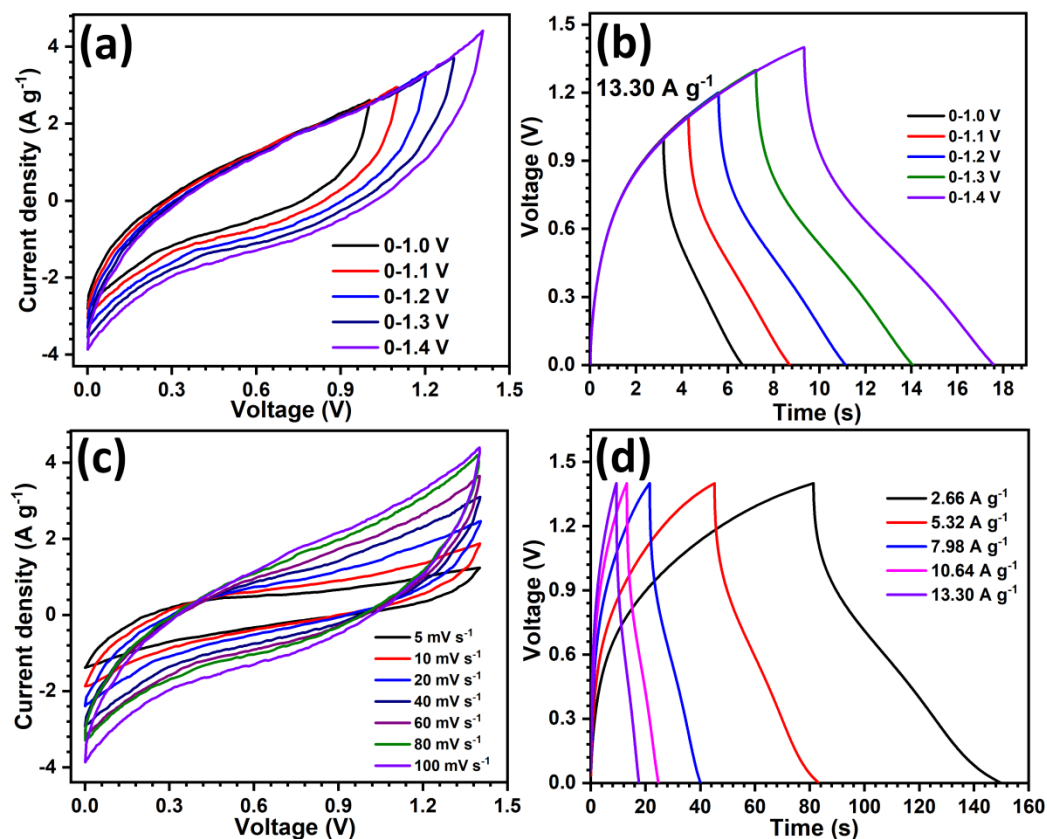


Figure 6.7: a) The CV curves, and b) the GCD plots at various voltages, c) the CV curves at different scan rates, and d) the GCD curves at various charging current densities of $\text{CuSe}_2@\text{rGO}//\text{CuS}$ ACS device.

The CV curves of FSS-ASC device at different scan rates are presented in Figure 6.7c. The shapes of all CV curves are similar, indicating good reversibility of SC device. The maximum C_s of 112 F g^{-1} at the scan rate of 5 mV s^{-1} was obtained. The GCD curves for various charging current densities ($2.66\text{--}13.30 \text{ A g}^{-1}$) are shown in Figure 6.7d. The C_s of 104 F g^{-1} was obtained at charge-discharge current density of 2.66 A g^{-1} .

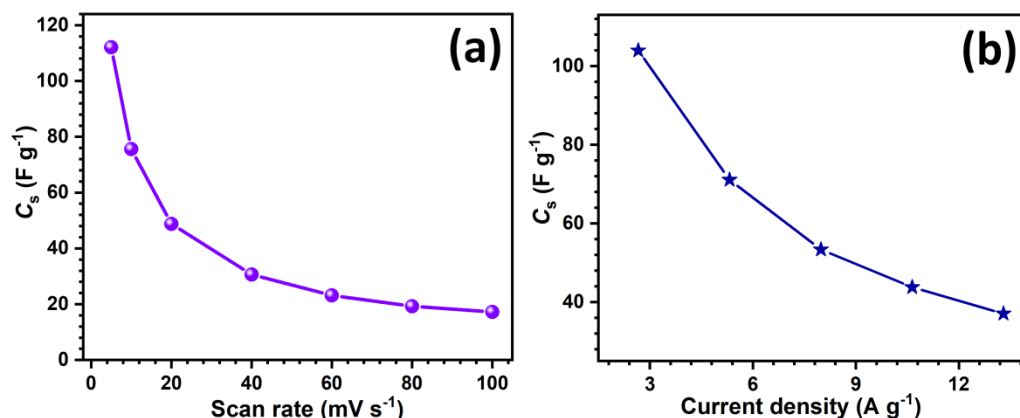


Figure 6.8: a) Variation of C_s with a) the scan rate and b) current density.

The variation of C_s of ASC with the scan rate is presented in Figure 6.8a and with charging current densities is presented in Figure 6.8b. With rising scan rate and current density, the discharging time (t_d) of the device drops, which resulted into decrease in C_s of the device due to insufficient electrode-electrolyte interaction.

The S_E and S_P values decide practical applications of energy storage devices. The S_E (29.6 Wh kg⁻¹) and S_P (1498 W kg⁻¹) of CuSe₂@rGO//CuS ASC device are suitable for practical application. The Ragone plot of ASC device is shown in Figure 6.9a.

To understand the electrochemical behavior of SC device the EIS is one of the excellent nondestructive technique. The Nyquist plot obtained through the EIS study is shown in Figure 6.9b. The R_s of 0.32 Ω and R_{ct} of 20.1 Ω are observed for the ASC device. The higher value of R_{ct} is due to the gel form of electrolyte (PVA-KOH) [26, 27]. The data of fitted equivalent circuit is shown in the inset of Figure 6.9b. The circuit consists of R_s , R_{ct} , W , and a double layer capacitor (C_{dl}). The W evaluated from the equivalent circuit is 0.194 Ω and the value of C_{dl} is 0.814 F. From the Bode plot (Figure 6.9c), the observed characteristics frequency (f_0) at the phase angle of 45° is 0.17 Hz. The t_0 of 5.88 s suggests that the device can be charged within a short time and delivers excellent power easily [28-31].

For commercial purposes, along with high performance, long term stability of ACS devices is very important. The stability of the ASC device is tested for 5,000 GCD cycles at a charging current density of 13.3 A g⁻¹. The 83.5% stability is shown in Figure 6.9d. The selected GCD plots (2nd and 5000th cycles) are presented in the inset of Figure 6.9d. The better electrochemical stability is due to the result of binder less electrode preparation, the composition of CuSe₂ with rGO, and use of solid state polymer gel (PVA-KOH) electrolyte.

The electrode materials were deposited on the flexible SS substrate of thickness 0.03 mm. To figure out the usefulness of the device in wearable and bendable appliances, CV curves of the device were examined at different bending positions from 0 to 165°. In Figure 6.10a, CV curves at different bending angles demonstrate structural integrity of the device after folded. About 89% of C_s was retained after 165° bending (Figure 6.10b) and it confirms that ASC device can be bent without sacrificing the electrochemical performance. It is observed that there was no obvious shape change of CV plots at various bending angles. The flexible

nature of SS substrate accompanied by layered structure of $\text{CuSe}_2@\text{rGO}$ film helps good mechanical flexibility.

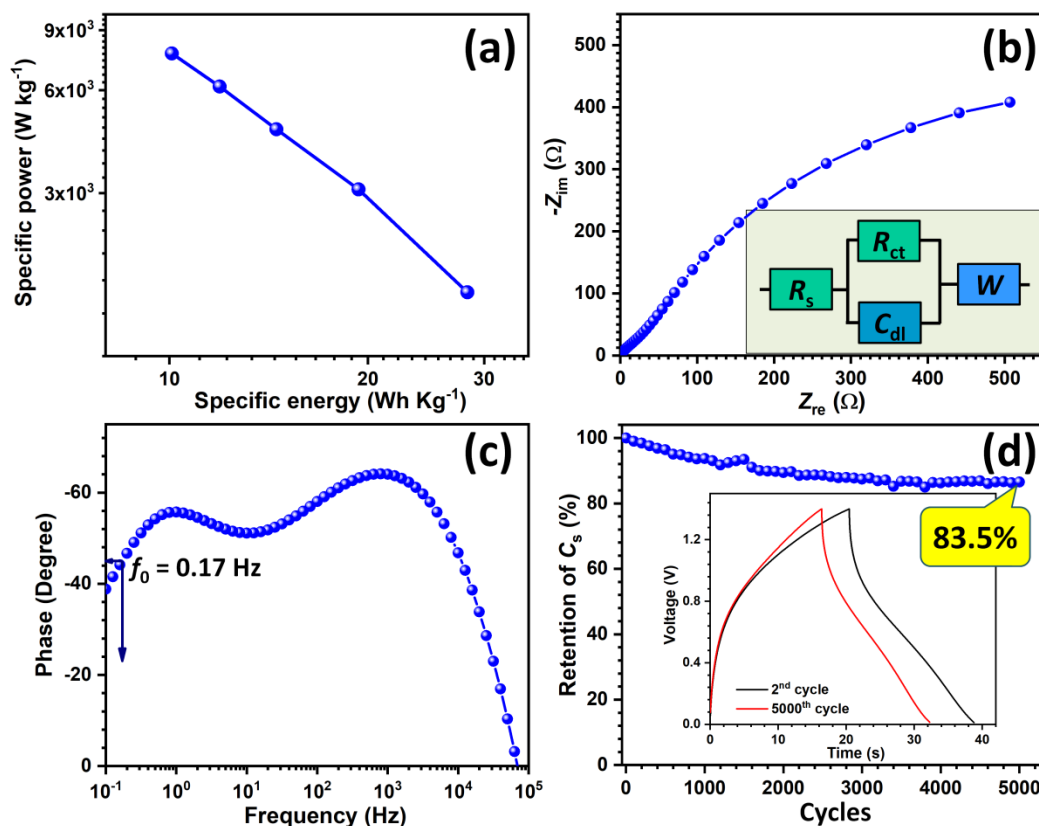


Figure 6.9: a) Ragone plot, b) Nyquist plot (Inset shows equivalent circuit), c) Bode plot, and d) plot of C_s retention over 5000 GCD cycles (Inset shows 2nd and 5000th GCD cycles) of ASC device.

Furthermore, the practical applicability of the ASC device is demonstrated by lightning LED by two series connected ASC devices. After 30 s of charging, ASC devices light up 201 red LEDs for 150 s. Figure 6.10c shows photographs while discharging ASC devices. Initially, 19.6 mW cm^{-2} power was stored in through two series connected ASC devices.

Overall, a simple and effective approach was developed to the synthesis of $\text{CuSe}_2@\text{rGO}$ and $\text{CuSe}_2@\text{rGO}$ composite thin film flexible electrodes with excellent electrochemical properties. The composition of rGO with copper chalcogenides offers high specific surface area and low R_{ct} . The fabricated ASC devices is useful as potent flexible energy storage systems.

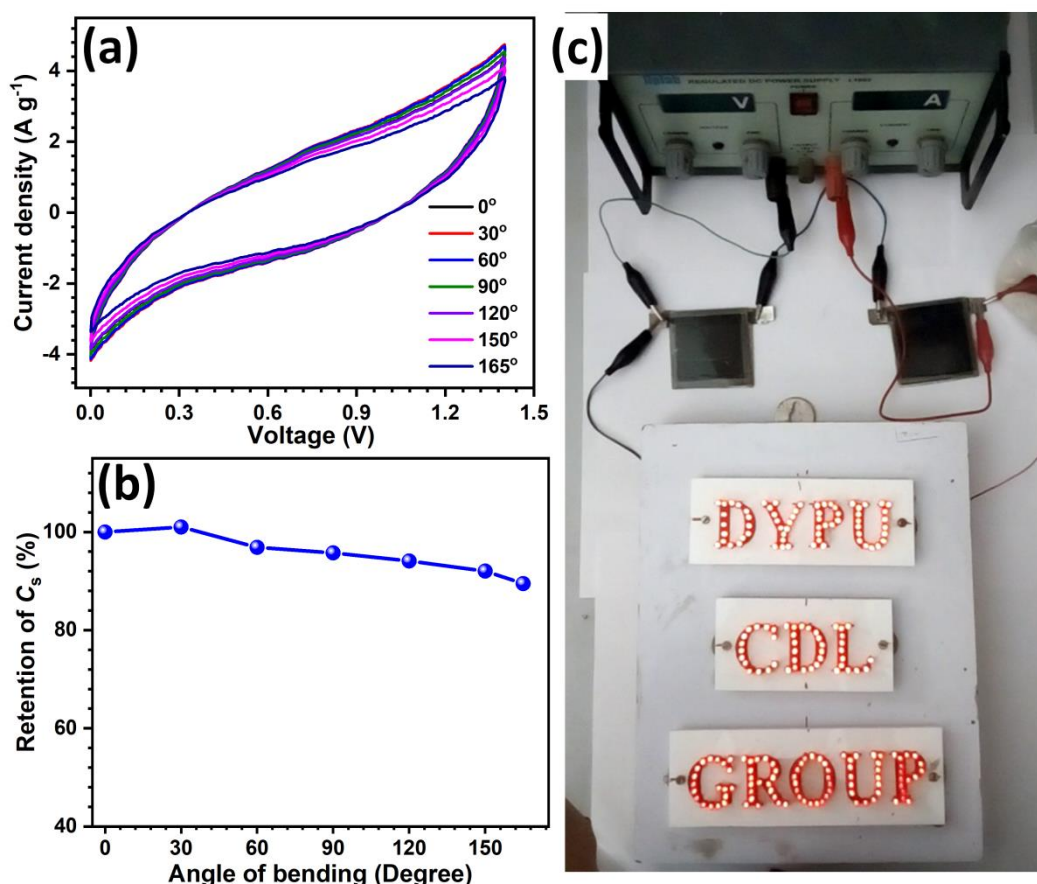


Figure 6.10: a) The CV curves at various bending angles, b) retention of specific capacitance with the bending angle, and c) demonstration of two series connected CuSe₂@rGO//CuS ASC devices to illuminate 201 red LEDs.

6.4 Conclusions

In summary, MnO₂//CuS@rGO FSS-ASCs device was fabricated using MnO₂ as a positive and CuS@rGO as a negative electrode using PVA-LiClO₄ gel electrolyte. In the same way, CuSe₂@rGO//CuS FSS-ASCs device was also assembled using PVA-KOH gel electrolyte. The MnO₂//CuS@rGO FSS-ASCs device exhibited excellent electrochemical performance with maximum C_s of 102.9 F g⁻¹, S_E of 40.5 Wh kg⁻¹, and S_P of 1087 W kg⁻¹. The C_s, S_E, and S_P of CuSe₂@rGO//CuS FSS-ASCs device were 104 F g⁻¹, 28.3 Wh kg⁻¹, and 1538 W kg⁻¹, respectively. Furthermore, MnO₂//CuS@rGO FSS-ASCs device revealed excellent cycling stability of 93% with an operating voltage of +1.6 V for 5000 GCD cycles and that of CuSe₂@rGO//CuS ASC device 83.5% after 5000 GCD cycles. Both FSS-ASC devices displayed outstanding mechanical flexibility and high rate capability. In an actual demonstration, both MnO₂//CuS@rGO and CuSe₂@rGO//CuS FSS-ASC devices light up 201 red LEDs using a series

combination of two devices (area of $5 \times 5 \text{ cm}^2$). This shows the possible use of both copper chalcogenide based FSS-ASC devices for practical applications.

References:

- [1] D. P. Dubal, J. G. Kim, Y. Kim, R. Holze, W. B. Kim, Demonstrating the highest supercapacitive performance of branched MnO_2 nanorods grown directly on flexible substrates using controlled chemistry at ambient temperature, *Energy Technol.*, 1 (2013) 125-130, DOI: 10.1002/ente.201200040.
- [2] S. Shi, C. Xu, C. Yang, J. Li, H. Du, B. Li, F. Kang, Flexible supercapacitors, *Particuology*, 11 (2013) 371, DOI: 10.1016/j.partic.2012.12.004.
- [3] L. Nyholm, G. Nystrom, A. Mihranyan, M. Stromme, Toward flexible polymer and paper-based energy storage devices, *Adv. Mater.*, 23 (2011) 3751-3769, DOI: 10.1002/adma.201004134.
- [4] P. Wen, M. Fan, D. Yang, Y. Wang, H. Cheng, J. Wang, An asymmetric supercapacitor with ultrahigh energy density based on nickel cobalt sulfide nanocluster anchoring multi-wall carbon nanotubes hybrid, *J. Power Sources*, 320 (2016) 28-36, DOI: 10.1016/j.jpowsour.2016.04.066.
- [5] B. G. Choi, S. J. Chang, C. P. Park, H. W. Kang, H. J. Kim, W. H. Hong, S. Lee, Y. S. Huh, High performance of a solid-state flexible asymmetric supercapacitor based on graphene films, *Nanoscale*, 4 (2012) 4983-4988, DOI: 10.1039/C2NR30991B.
- [6] B. Zheng, T. Huang, L. Kou, X. Zhao, K. Gopalsamy, C. Gao, Graphene fiber-based asymmetric micro-supercapacitors, *J. Mater. Chem. A*, 2 (2014) 9736-9743, DOI: 10.1039/C4TA01868K.
- [7] M. Jayalakshmi, M. M. Rao, B. M. Choudary, Identifying nano SnS as a new electrode material for electrochemical capacitors in aqueous solutions, *Electrochem. Commun.*, 6 (2004) 1119-1122, DOI: 10.1016/j.elecom.2004.09.004.
- [8] K. Krishnamoorthy, G. K. Veerasubramani, P. Pazhamalai, S. J. Kim, Designing two dimensional nanoarchitected MoS_2 sheets grown on Mo foil as a binder free electrode for supercapacitors, *Electrochim. Acta*, 190 (2016) 305-312, DOI: 10.1016/j.electacta.2015.12.148.
- [9] Y. Munaiah, B. G. S. Raj, T. P. Kumar, P. Ragupathy, Facile synthesis of hollow sphere amorphous MnO_2 : the formation mechanism, morphology and effect of a bivalent cation-containing electrolyte on its supercapacitive behavior, *J. Mater. Chem. A*, 1 (2013) 4300-4306, DOI: 10.1039/C3TA01089A.
- [10] T. Brousse and D. Belanger, A hybrid Fe_3O_4 - MnO_2 capacitor in mild aqueous electrolyte, *Electrochem. Solid-State Lett.*, 6 (2003) A244, DOI: 10.1149/1.1614451.
- [11] J. Wang, S. Liu, X. Zhang, X. Liu, X. Liu, N. Li, J. Zhao, Y. Li, A high energy asymmetric supercapacitor based on flower-like $\text{CoMoO}_4/\text{MnO}_2$ heterostructures

- and activated carbon, *Electrochim. Acta*, 213 (2016) 663-671, DOI: 10.1016/j.electacta.2016.07.155.
- [12] N. G. Bretesche, O. Crosnier, G. Buvat, F. Favier, T. Brousse, Electrochemical study of aqueous asymmetric $\text{FeWO}_4/\text{MnO}_2$ supercapacitor, *J. Power Sources*, 326 (2016) 695-701, DOI: 10.1016/j.jpowsour.2016.04.075.
- [13] S. Zhang, B. Yin, Z. Wang, F. Peter, Super long-life all solid-state asymmetric supercapacitor based on NiO nanosheets and $\alpha\text{-Fe}_2\text{O}_3$ nanorods, *Chem. Eng. J.*, 306 (2016) 193-203, DOI: 10.1016/j.cej.2016.07.057.
- [14] L. Zhang, W. Zheng, H. Jiu, C. Ni, J. Chang, G. Qi, The synthesis of NiO and NiCo_2O_4 nanosheets by a new method and their excellent capacitive performance for asymmetric supercapacitor, *Electrochim. Acta*, 215 (2016) 212-222, DOI: 10.1016/j.electacta.2016.08.099.
- [15] E. Guneri, A. Kariper, Optical properties of amorphous CuS thin films deposited chemically at different pH values, *J. Alloys Compd.*, 516 (2012) 20-26, DOI: 10.1016/j.jallcom.2011.11.054.
- [16] S. Bernardini, F. Bellatreccia, A. C. Municchia, G. D. Ventura, A. Sodo, Raman spectra of natural manganese oxides, *J. Raman Spectrosc.*, 50 (2019) 873-888, DOI: 10.1002/jrs.5583.
- [17] A. Phuruangrat, T. Thongtem, S. Thongtem, Characterization of copper sulfide hexanano plates, and nanoparticles synthesized by a sonochemical method, *Chalcogenide Lett.*, 8 (2011) 291-295.
- [18] P. R. Deshmukh, S. N. Pusawale, V. S. Jamadade, U. M. Patil, C. D. Lokhande, Microwave assisted chemical bath deposited polyaniline films for supercapacitor application, *J. Alloys Compd.*, 509 (2011) 5064-5069, DOI: 10.1016/j.jallcom.2010.12.009.
- [19] K. J. Huang, J. Z. Zhang, K. Xing, One-step synthesis of layered CuS/multi-walled carbon nanotube nanocomposites for supercapacitor electrode material with ultrahigh specific capacitance, *Electrochim. Acta*, 149 (2014) 28-33, DOI: 10.1016/j.electacta.2014.10.079.
- [20] N. R. Chodankar, D. P. Dubal, A. C. Lokhande, C. D. Lokhande, Ionically conducting PVA- LiClO_4 gel electrolyte for high performance flexible solid state supercapacitors, *J. Colloid Interf. Sci.*, 460 (2015) 370-376, DOI: 10.1016/j.jcis.2015.08.046.
- [21] T. Brousse, D. Belanger, J. W. Long, To be or not to be pseudocapacitive? *J. Electrochem. Soc.*, 162 (2015) A5185-A5189, DOI: 10.1149/2.0201505jes.
- [22] D. P. Dubal, O. Ayyad, V. Ruiz, P. Gomez-Romero, Hybrid energy storage: the merging of battery and supercapacitor chemistries, *Chem. Soc. Rev.*, 44 (2015) 1777-1790, DOI: 10.1039/C4CS00266K.
- [23] V. Pototskaya, O. Gichan, On the origin of phase angle in warburg finite length diffusion impedance, *Int. J. Electrochem. Sci.*, 14 (2019) 8195-8205, DOI: 10.20964/2019.08.97.

- [24] W. Choi, H. Shin, J. M. Kim, J. Choi, W. Yoon, Modeling and applications of electrochemical impedance spectroscopy (EIS) for Lithium-ion batteries, *J. Electrochem. Sci. Technol.*, 11 (2020) 1-13, DOI: 10.33961/jecst.2019.00528.
- [25] D. G. Moye, P. L. Moss, D. R. R. Kannan, X. Chen, O. Bolufawi, W. Cao, S. Y. Foo, Improvements to temperature, warburg impedance, and voltage computations for a design-based predictive model for lithium-ion capacitors, *Mater. Sci. Appl.*, 11 (2020) 347-369, DOI: 10.4236/msa.2020.116024.
- [26] A. M. Patil, V. C. Lokhande, U. M. Patil, P. A. Shinde, C. D. Lokhande, High performance all-solid-state asymmetric supercapacitor device based on 3d nanospheres of β -MnO₂ and nanoflowers of O-SnS, *ACS Sustainable Chem. Eng.*, 6 (2018) 787–802, DOI: 10.1021/acssuschemeng.7b03136.
- [27] M. Tripathi, S. M. Bobade, A. Kumar, Nanocomposite polymer gel with dispersed alumina as an efficient electrolyte for application in supercapacitors, *J. Phys. Chem. Solids*, 152 (2021) 109944, DOI: 10.1016/j.jpcs.2021.109944.
- [28] X. Li, H. Li, X. Fan, X. Shi, J. Liang, 3D-printed stretchable micro-supercapacitor with remarkable areal performance, *Adv. Energy Mater.*, 10 (2020) 1903794, DOI: 10.1002/aenm.201903794.
- [29] N. K. Sidhu, A. C. Rastogi, Bifacial carbon nanofoam-fibrous PEDOT composite supercapacitor in the 3-electrode configuration for electrical energy storage, *Synth. Met.*, 219 (2016) 1-10, DOI: 10.1016/j.synthmet.2016.04.012.
- [30] A. Nashim, S. Pany, K. M. Parida, J. Nanda, La₂Ti₂O₇ as nanometric electrode material: an emerging candidate for supercapacitor performance, *ChemistrySelect*, 4 (2019) 12037-12042, DOI: 10.1002/slct.201903227.
- [31] R. Bhujel, S. Rai, U. Deka, B. P. Swain, Electrochemical, bonding network and electrical properties of reduced graphene oxide-Fe₂O₃ nanocomposite for supercapacitor electrodes applications, *J. Alloys Compd.*, 792 (2019) 250-259, DOI: 10.1016/j.jallcom.2019.04.004.

CHAPTER – VII

Summary and conclusions

Summary and conclusions

The electrical energy storage systems such as battery, capacitor and SCs are available in recent years. In which SC have ability to store charge rapidly and it has higher power density than batteries. The tremendous use of SCs in the flexible and wearable electronics has been intended for a number of applications like medical bio-monitoring devices for military equipment. The batteries have limited service lifetime, safety issue and small-scale power which restrict applications of batteries in portable electronic devices. In contradict, SCs offers higher power density, electrochemical cycling stability, better energy density and environmental energy storage. Therefore, SC technology is rising rapidly to substitute capacitors and batteries. Currently, SCs are being used in several applications such as telecommunications, hybrid electric vehicles, power back up sources, flash camera's, etc. In hybrid electric vehicles, the higher power during start is required.

The SCs give high power and energy to hybrid electric vehicles during start and so hybrid electric vehicles use SCs. Nevertheless, SCs have limitations with aqueous electrolytes, lower reduction potential of metal cations and higher resistivity of metal oxides. The FSS-ASCs device is the innovative member of energy storage SC and attracted due to their high power density, long cycle life, environmental friendliness and safety. To overcome these drawbacks of device, further electrode material investigation is necessary to enhance performance of SCs. Temporarily, the combination of best active electrode materials with supportable electrolyte efficiently raises both the energy and power capability of the FSS-SCs device.

The previous reports suggest that the materials like metal oxides, conducting polymers and carbon based materials enhance the electrochemical performance of SC device. The electrical conductivity and thermal stability of metal oxides are comparatively lower than metal sulfides. Therefore, the low cost and high performance electrode material preparation in transition metal sulfide family is required.

The present work deals with the synthesis of copper chalcogenide (CuS , CuSe_2) thin films by simple, cost effective and binder-free chemical approach. The number of preparative parameters were optimised to get highly porous surface

morphology with higher specific surface area, which successfully increase the electrochemical features of CuS and CuSe₂ thin films. The composite thin films showed better SC performance than CuS and CuSe₂ thin films. Therefore, the composite thin films with excellent electrochemical features were used as one electrode for fabrication of FSS-ASCs device. Furthermore, MnO₂ was selected as positive electrode with a wide potential window. The work has been distributed in six chapters.

Chapter I deals with a general introduction and literature survey of different transition metal sulfides and selenides for SC application. Additionally, it covers a literature survey on copper chalcogenide electrode materials. It displays information regarding mechanisms of energy exploitation from different energy sources. Consequently, the importance of energy storage from renewable energy sources is noted. It clarifies the most simple energy storage devices specifically capacitor, battery, and SC. The different types of SCs along with their energy storage capabilities are discussed. The benefits of SCs over capacitors and batteries in terms of energy and power densities are mentioned.

The significance of thin film and different nanostructure morphologies of material is explained in brief. The different electrode materials such as carbon based materials, metal oxides/hydroxides, and conducting polymers are discussed. The significance of metal chalcogenides for SC application is described concerning a contribution from non-faradaic reactions in addition to faradaic reactions. The literature survey of transition metal sulfides and selenides includes preparation methods, properties, and applications. Furthermore, the literature survey of CuS and CuSe based electrode materials for supercapacitive applications is carried out and finally, the orientation and purpose of the thesis are described.

Chapter II presents thin film preparation method and the advantages of chemical methods over physical thin film deposition methods. Out of chemical methods, the SILAR method is deemed to be more controllable on thin film deposition process. This method is comprised of three processes, i) adsorption, ii) reaction, and iii) rinsing. To evaluate the structural, morphological, and elemental compositional parameters different characterization techniques such as XRD, FE-SEM, FT-IR and Raman spectroscopy, XPS, contact angle measurement and BET

were used. The basic principle and working mechanism of these techniques are discussed in chapter II in order to understand obtained results. Further, fundamental aspects and applications of various electrochemical techniques for energy storage application were studied in this chapter.

Thickness affects the charge storage, cycling stability, resistive parameters of the film electrode material. Considering this, the optimization of thin film thickness or mass loading is necessary which can be done by varying deposition cycles in SILAR method.

From this perspective, **Chapter III** presents the study of the effect of mass loading on the physico-chemical properties and electrochemical performance of copper sulfide. Chapter III deals with the synthesis of CuS thin films by SILAR method and their characterization for electrochemical performance evaluation. This chapter also deals with the synthesis of CuS@rGO thin films using SILAR method. Since the ratio of rGO in the composite film decides the overall electrochemical performance of the film, the effect of amount of rGO on the electrochemical performance of CuS@rGO thin films was evaluated. The crystalline nature of CuS thin films changes with the composition of rGO. With mass loading $0.0126(\pm 0.001)$ mg cm⁻², CuS100 thin film (CuS film prepared at 100 cycles) exhibited the specific capacitance of 687 F g⁻¹ at the scan rate of 2 mV s⁻¹ and stability of 89% after 10000 GCD cycles.

The mass loading of CuS@rGO5 thin film of $0.0137(\pm 0.001)$ mg cm⁻², indicated an increase in mass loading with the introduction of rGO. The C_s of the composite film was 1201.8 F g⁻¹ at the scan rate of 2 mV s⁻¹ and stability of 94% over 10000 GCD cycles. The values of R_s and R_{ct} for CuS100 thin film were 1.34 and 3.54 Ω cm⁻² and that of CuS@rGO5 were 2.78 and 20.80 Ω cm⁻², respectively. Thus the composition of CuS with rGO in proper ratio can be used to modify structural and morphological properties and able to improve specific capacitance. Due to higher mass loading R_s of CuS@rGO composite thin film was more. This chapter highlights superiority of CuS@rGO thin film over CuS and rGO thin films.

Chapter IV deals with the preparation and characterization of CuSe₂ and CuSe₂@rGO thin films by the SILAR method. The mass loading of CuSe₂ and CuSe₂@rGO thin films was $0.091 (\pm 0.01)$ mg cm⁻² and $0.106 (\pm 0.01)$ mg cm⁻², respectively. The effect of rGO on chemical composition, crystal structure, surface

morphology, and electrochemical properties was studied. The chemical composition of rGO with copper selenide orients crystal growth from (200) to (221) crystallographic plane. The petal-like morphology of CuSe₂ thin film modified to randomly distributed sheet-like morphology. The nanospheres of CuSe₂ coated on rGO sheets were observed in CuSe₂@rGO thin film. This mesoporous structure exhibited specific surface area of 84 m² g⁻¹ compared to 24 m² g⁻¹ of CuSe₂ material. Shift in average pore radius to lower dimension side (32 nm for CuSe₂ to 13 nm for CuSe₂@rGO) was the main cause of increased specific surface area.

The supercapacitive properties of CuSe₂ thin film were assessed using CV, charge-discharge, and electrochemical stability and EIS study. The maximum C_s of 400 F g⁻¹ was achieved at the scan rate of 2 mV s⁻¹. The charge-discharge curves were non-linear indicating pseudocapacitive behavior of CuSe₂ electrode. The CuSe₂@rGO thin film exhibited maximum C_s of 612 F g⁻¹ at the scan rate of 2 mV s⁻¹. The stability of CuSe₂@rGO thin film increased impressively from 57 to 78% after composition. The values of R_s and R_{ct} for CuSe₂ thin film were 1.39 and 3.50 Ω cm⁻² and that of CuSe₂@rGO were 0.83 and 1.50 Ω cm⁻², respectively. In conclusion, the highest specific surface area offered by CuSe₂@rGO material helps to reduce ion diffusion resistance and maximum active sites exposed to the electrolyte improves the infiltration of electrolyte ions (OH⁻) in the electrode.

Chapter V deals with the synthesis of MnO₂ thin films using CBD method and their characterization for electrochemical performance evaluation. MnO₂ thin film exhibited a specific surface area of 140.5 cm² gm⁻¹ and an average pore radius of 27.8 nm. The mesoporous surface showed a hydrophilic nature. In addition to this, MnO₂ thin film exhibited C_s of 702 F g⁻¹ at a scan rate of 5 mV s⁻¹. Low resistive parameters such as R_s (1.94 Ω cm⁻²) and R_{ct} (1.94 Ω cm⁻²) and capacitive retention of 93% after 5000 CV cycles of MnO₂ thin film electrode ascribed to its nanostructured morphology consisting nanospheres.

Chapter VI contains the fabrication and electrochemical evaluation of MnO₂//CuS@rGO and CuSe₂@rGO//CuS FSS-ASC devices. For ASC device fabrication high performance positive electrode material is required. Furthermore, this chapter includes the preparation of solid-state PVA-LiClO₄ and PVA-KOH gel electrolytes. The MnO₂//CuS@rGO FSS-ASC device exhibited the operating voltage

of +1.6 V, which is due to different operating potential windows of CuS@rGO and MnO₂ thin films. It exhibited the excellent C_s of 102.9 F g⁻¹ with a maximum S_E of 40.5 Wh kg⁻¹ at the power density of 1087 W kg⁻¹. The MnO₂//CuS@rGO FSS-ASC device showed capacitance retention of 93% after 5000 GCD cycles and robust mechanical flexibility by retaining 90% of capacitance at a bending angle of 165°.

Similarly, CuSe₂@rGO//CuS FSS-ASC device working at a voltage of 1.4 V exhibited C_s of 104 F g⁻¹ at a current density of 2.6 A g⁻¹. Outstanding S_E (26.9 Wh kg⁻¹) and S_P (1498 W kg⁻¹) of the device underlined its possible practical applications. CuSe₂@rGO//CuS FSS-ASC device showed capacitance retention of 83.5% after 5000 GCD cycles and 89% at the bending angle of 165°.

Finally, two FSS-ASC devices connected in series were able to glow a panel of 201 red LEDs efficiently. The initial power dissipated through MnO₂//CuS@rGO FSS-ASC was 31 mW cm⁻² and for CuSe₂@rGO//CuS FSS-ASC device was 19.6 mW cm⁻². The electrochemical parameters of CuS, CuS@rGO, CuSe₂, CuSe₂@rGO are summarised in Table. 7.1. In this table, methods of material preparation, surface morphology, electrolytes, C_s , R_s , R_{ct} , and cycling stability of the electrodes are mentioned. The electrochemical parameters of MnO₂//CuS@rGO and CuSe₂@rGO//CuS FSS-ASC devices are summarised in Table 7.2. Finally, the observed results conclude that the copper chalcogenide based FSS-ASCs can power up small electronic equipment requiring power in the range of 0.01 mW to 0.1 mW.

In this study, copper chalcogenide thin films and their composites with rGO were synthesized using automated SILAR method. The introduction of rGO improves electrical conductivity, specific surface area, and overall electrochemical performance of pristine material. Instead of rGO, other carbon allotropes like fullerene, CNTs, carbon aerogel, and carbon foam for the composition will be used. Along with this, the composition of other transition metals (Ni, Co, Cr) to form a bimetallic compound will also enhance the electrochemical energy storage properties of the electrode material. To understand the process of energy storage in copper chalcogenide based compounds, physical characterization of these materials should be performed to analyze changes in the crystal structure, surface morphology, and chemical composition using techniques such as XRD, SEM, TEM, and XPS. Further, in situ

characterization of ASC devices through TEM and NMR analyses could give a better understanding of actual processes involved in charge storage.

Table 7.1: The electrochemical parameters of CuS, CuS@rGO, CuSe₂, and CuSe₂@rGO thin film electrodes deposited using SILAR method in three electrode system.

Material	Surface morphology	Electrolyte	C_s (F g ⁻¹)	R_s (Ω cm ⁻²)	R_{ct} (Ω cm ⁻²)	Stability (%) (after 10000 cycles)
CuS60	Spong-like	1 M LiClO ₄	550	1.77	1.20	74
CuS80	Nanoflakes		639	1.36	5.91	79
CuS100	Nanoflakes		687	1.34	3.54	89
CuS120	Nanoflowers		660	2.92	13.82	80
CuS@rGO3	Spherical nanoparticles on sheet like structure		902	3.34	22.21	76
CuS@rGO4			1109	2.75	21.30	81
CuS@rGO5			1202	2.78	20.80	94
CuS@rGO6			1023	4.13	43.90	87
CuSe ₂	Petal-like	1 M KOH	400	1.39	3.50	57
CuSe ₂ @rGO	Spherical nanoparticles on sheet-like structure		612	0.83	1.50	78

Table 7.2: The electrochemical parameters of FSS-ASC devices evaluated using two electrode system.

Configuration of FSS-ASC device	C_s (F g ⁻¹)	Specific energy (Wh kg ⁻¹) at specific power (W kg ⁻¹)	R_s (Ω)	R_{ct} (Ω)	Stability (%) (cycles)	Flexibility (%) at 165°
MnO ₂ //CuS@rGO	102.9 at 2 A g ⁻¹	40.5 at 1087	0.24	2	93 (5000)	90
CuSe ₂ @rGO//CuS	104 at 2.6 A g ⁻¹	26.9 at 1498	0.32	20	83 (5000)	89



Figure 7.1: a) Photograph in twisted position, and b) thickness measurement of CuS@rGO//MnO₂ ASC device. Demonstration to illuminate c) table lamp consisting 12 white LEDs, and d) LEDs panel made of 201 red LEDs using two series connected CuS@rGO//MnO₂ ASC devices.

80-Recommendations

8.1 Recommendations:

In the presented research work, thin films of copper chalcogenides mainly copper sulphide and copper selenide were prepared using SILAR method. The charge storage capacity of these thin film was improved by means of improvement in surface area. To achieve this rGO was composited with the copper chalcogenides using SILAR method. The objective of the preparation of composite electrode was to improve specific capacitance and stability of the material than pristine materials. The solid state supercapacitor fabricated using these thin films delivered energy density of 40.5 Wh kg⁻¹ at 1087 W kg⁻¹.

Finally, it is recommended that, at 100 SILAR cycles, CuS thin film show best electrochemical performance and for CuSe₂ it is 40 SILAR cycles. To get best electrochemical performance optimized concentration of rGO is 0.5 mg mL⁻¹. Due to the simplicity, scalable nature of the deposition method, it can be potentially translated at industrial level with minimum modification.

8.2 Conclusions

The conclusions from the present research work are listed as follows:

1. The mass loading per unit area of electrode is controlled through variation of deposition cycles. Optimum mass loading of electrode was essential for highest electrochemical performance.
2. At the optimum mass loading charge transfer resistance per unit mass is minimum and thereafter it increased. Copper sulfide thin film deposited at 100 SILAR cycles showed best electrochemical performance. And CuSe₂, thin film deposited at 40 SILAR cycles showed best electrochemical performance.
3. Composition of rGO with copper chalcogenides improve specific surface area. This leads to increase in electrochemical active sites and improvement in charge storage through capacitive assisted mechanism. As the pristine rGO has very low specific capacitance, optimization of composition of each material need to be considered. For copper chalcogenides 0.5 mg mL⁻¹ concentration of rGO suspension provide better effect on electrochemical properties.
4. Composition of copper chalcogenides with the rGO increased in electrochemical stability of the electrodes. Stability of CuS was improved from 89% to 94%

(CuS@rGO) and that for CuSe₂@rGO it was reached up to 78% from 57% (CuSe₂).

5. Compared to composite electrodes of copper sulfide (CuS@rGO) electrochemical performance of composite electrodes of copper selenide (CuSe₂@rGO) is lower.
6. Asymmetric solid-state supercapacitor fabricated using MnO₂ and CuS@rGO delivers energy density of 40.5 Wh kg⁻¹ at the power density of 1087 W kg⁻¹.

8.3 Summary

The present work deals with the synthesis of copper chalcogenide (CuS, CuSe₂) thin films by simple, cost effective and binder-free chemical approach. The numbers of preparative parameters were optimized to get highly porous surface morphology with higher specific surface area, which successfully increase the electrochemical features of CuS and CuSe₂ thin films. The composite thin films showed better SC performance than CuS and CuSe₂ thin films. Therefore, the composite thin films with excellent electrochemical features were used as one electrode for fabrication of FSS-ASCs device. Furthermore, MnO₂ was selected as positive electrode with a wide potential window.

The significance of thin film and different nanostructure morphologies of material is explained in brief. The different electrode materials such as carbon based materials, metal oxides/hydroxides, and conducting polymers are discussed. The significance of metal chalcogenides for SC application is described concerning a contribution from non-faradaic reactions in addition to faradaic reactions. The literature survey of transition metal sulfides and selenides includes preparation methods, properties, and applications. Furthermore, the literature survey of copper sulfide and copper selenide based electrode materials for supercapacitive applications is carried out and finally, the orientation and purpose of the thesis are described.

The thin film preparation method and the advantages of chemical methods over physical thin film deposition methods are discussed. Out of chemical methods, the SILAR method is deemed to be more controllable on thin film deposition process. This method is comprised of three processes, i) adsorption, ii) reaction, and iii) rinsing. To evaluate the structural, morphological, and elemental compositional parameters different characterization techniques such as XRD, FE-SEM, FT-IR and

Raman spectroscopy, XPS, contact angle measurement and BET were used. The basic principle and working mechanism of these techniques are discussed to understand obtained results. Further, fundamental aspects and applications of various electrochemical techniques for energy storage application are discussed.

Thickness affects the charge storage, cycling stability, resistive parameters of the film electrode material. Considering this, the optimization of thin film thickness or mass loading is necessary which can be done by varying deposition cycles in SILAR method.

From this perspective, the study of the effect of mass loading on the physico-chemical properties and electrochemical performance of copper sulfide were evaluated. Since the ratio of rGO in the composite film decides the overall electrochemical performance of the film, the effect of amount of rGO on the electrochemical performance of CuS@rGO thin films was evaluated. The crystalline nature of CuS thin films changes with the composition of rGO. With mass loading $0.0126(\pm 0.001) \text{ mg cm}^{-2}$, CuS100 thin film (CuS film prepared at 100 cycles) exhibited the specific capacitance of 687 F g^{-1} at the scan rate of 2 mV s^{-1} and stability of 89% after 10000 GCD cycles.

The mass loading of CuS@rGO5 thin film of $0.0137(\pm 0.001) \text{ mg cm}^{-2}$, indicated an increase in mass loading with the introduction of rGO. The C_s of the composite film was 1201.8 F g^{-1} at the scan rate of 2 mV s^{-1} and stability of 94% over 10000 GCD cycles. The values of R_s and R_{ct} for CuS100 thin film were 1.34 and $3.54 \Omega \text{ cm}^{-2}$ and that of CuS@rGO5 were 2.78 and $20.80 \Omega \text{ cm}^{-2}$, respectively. Thus the composition of CuS with rGO in proper ratio can be used to modify structural and morphological properties and able to improve specific capacitance. Due to higher mass loading R_s of CuS@rGO composite thin film was more. This highlights superiority of CuS@rGO thin film over CuS and rGO thin films.

The preparation of CuSe₂ and CuSe₂@rGO thin films by the SILAR method, the mass loading of CuSe₂ and CuSe₂@rGO thin films was $0.091 (\pm 0.01) \text{ mg cm}^{-2}$ and $0.106 (\pm 0.01) \text{ mg cm}^{-2}$, respectively. The effect of rGO on chemical composition, crystal structure, surface morphology, and electrochemical properties was studied. The chemical composition of rGO with copper selenide orients crystal growth from (200) to (221) crystallographic plane. The petal-like morphology of CuSe₂ thin film modified to randomly distributed sheet-like morphology. The nanospheres of CuSe₂

coated on rGO sheets were observed in CuSe₂@rGO thin film. This mesoporous structure exhibited specific surface area of 84 m² g⁻¹ compared to 24 m² g⁻¹ of CuSe₂ material. Shift in average pore radius to lower dimension side (32 nm for CuSe₂ to 13 nm for CuSe₂@rGO) was the main cause of increased specific surface area.

The supercapacitive properties of CuSe₂ thin film were assessed using CV, charge-discharge, and electrochemical stability and EIS study. The maximum C_s of 400 F g⁻¹ was achieved at the scan rate of 2 mV s⁻¹. The charge-discharge curves were non-linear indicating pseudocapacitive behavior of CuSe₂ electrode. The CuSe₂@rGO thin film exhibited maximum C_s of 612 F g⁻¹ at the scan rate of 2 mV s⁻¹. The stability of CuSe₂@rGO thin film increased impressively from 57 to 78% after composition. The values of R_s and R_{ct} for CuSe₂ thin film were 1.39 and 3.50 Ω cm⁻² and that of CuSe₂@rGO were 0.83 and 1.50 Ω cm⁻², respectively. In conclusion, the highest specific surface area offered by CuSe₂@rGO material helps to reduce ion diffusion resistance and maximum active sites exposed to the electrolyte improves the infiltration of electrolyte ions (OH⁻) in the electrode.

The thin films of MnO₂ were prepared using CBD method and characterized for electrochemical performance evaluation. MnO₂ thin film exhibited a specific surface area of 140.5 cm² gm⁻¹ and an average pore radius of 27.8 nm. The mesoporous surface showed a hydrophilic nature. In addition to this, MnO₂ thin film exhibited C_s of 702 F g⁻¹ at a scan rate of 5 mV s⁻¹. Low resistive parameters such as R_s (1.94 Ω cm⁻²) and R_{ct} (1.94 Ω cm⁻²) and capacitive retention of 93% after 5000 CV cycles of MnO₂ thin film electrode ascribed to its nanostructured morphology consisting nanospheres.

The FSS-ASC devices with configuration of MnO₂//CuS@rGO and CuSe₂@rGO//CuS were fabricated. The MnO₂//CuS@rGO FSS-ASC device exhibited the operating voltage of +1.6 V, which is due to different operating potential windows of CuS@rGO and MnO₂ thin films. It exhibited the excellent C_s of 102.9 F g⁻¹ with a maximum S_E of 40.5 Wh kg⁻¹ at the power density of 1087 W kg⁻¹. The MnO₂//CuS@rGO FSS-ASC device showed capacitance retention of 93% after 5000 GCD cycles and robust mechanical flexibility by retaining 90% of capacitance at a bending angle of 165°.

Similarly, CuSe₂@rGO//CuS FSS–ASC device working at a voltage of 1.4 V exhibited C_s of 104 F g⁻¹ at a current density of 2.6 A g⁻¹. Outstanding S_E (26.9 Wh kg⁻¹) and S_P (1498 W kg⁻¹) of the device underlined its possible practical applications. CuSe₂@rGO//CuS FSS–ASC device showed capacitance retention of 83.5% after 5000 GCD cycles and 89% at the bending angle of 165°.

Finally, two FSS–ASC devices connected in series were able to glow a panel of 201 red LEDs efficiently. The initial power dissipated through MnO₂//CuS@rGO FSS–ASC was 31 mW cm⁻² and for CuSe₂@rGO//CuS FSS–ASC device was 19.6 mW cm⁻². Finally, the observed results conclude that the copper chalcogenide based FSS–ASCs can power up small electronic equipment requiring power in the range of 0.01 mW to 0.1 mW.

8.4 Future findings

In this study, copper chalcogenide thin films and their composites with rGO were synthesized using automated SILAR method. The introduction of rGO improves electrical conductivity, specific surface area, and overall electrochemical performance of pristine material. Instead of rGO, other carbon allotropes like fullerene, CNTs, carbon aerogel, and carbon foam for the composition can be used. Along with this, the composition of other transition metals (Ni, Co, Cr) to form a bimetallic compound will also enhance the electrochemical energy storage properties of the electrode material. To understand the process of energy storage in copper chalcogenide based compounds, physical characterization of these materials should be performed to analyze changes in the crystal structure, surface morphology, and chemical composition using techniques such as XRD, SEM, TEM, and XPS. Further, in situ characterization of ASC devices through TEM and NMR analyses could give a better understanding of actual processes involved in charge storage.